

GRAN SASSO SCIENCE INSTITUTE
ASTROPARTICLE PHYSICS DOCTORAL PROGRAMME
CYCLE XXXIII 2017-2021

STUDY OF COSMIC-RAY INTERACTIONS IN
CANDIDATE SOURCES. APPLICATIONS TO THE
INTERPRETATION OF THE ENERGY SPECTRUM
AND MASS COMPOSITION DATA OF THE PIERRE
AUGER OBSERVATORY

Ph.D. Candidate:
Antonio Condorelli

Advisors:

Prof. Sergio Petrerá
Dr. Denise Boncioli



**Study of cosmic-ray interactions in
candidate sources. Applications to the
interpretation of the energy spectrum
and mass composition data of the
Pierre Auger Observatory**

PhD Candidate:

Antonio Condorelli

Advisor:

Prof. Sergio Petrera

Gran Sasso Science Institute

Advisor:

Dr. Denise Boncioli

University of L'Aquila

Thesis submitted for the degree of Doctor of Philosophy

May 7, 2021

GSSI Gran Sasso Science Institute

Viale Francesco Crispi, 7 - 67100 L'Aquila - Italy

Abstract

In the last decades significant progresses in the understanding of Ultra-High-Energy Cosmic rays (UHECRs) have been made, thanks to the measurements provided by very large ground-based experiments such as the Pierre Auger Observatory. However, it is still a mystery what the sources of UHECRs are and by which processes they are accelerated.

This thesis has been developed inside the Auger Collaboration and was devoted to study astrophysical models capable to describe the UHECRs measurements, in particular the energy spectrum and mass composition, in order to infer information about the properties of UHECRs sources.

As a first approach, an astrophysical scenario with a population of identical extra-galactic point-like sources homogeneously and isotropically distributed has been tested, thanks to the use and the implementation of a software for the fit of the energy spectrum and mass composition, with the aim to describe the Auger data above the so-called *ankle* feature ($E = 10^{18.7}$ eV). At this stage only the extra-galactic propagation has been taken into account (“propagation model”). In order to extend the analysis below the ankle, two populations of sources capable to accelerate cosmic-ray nuclei with different spectral parameters have been considered. To this purpose, the software previously used within the Auger Collaboration has been reorganized and improved. The results suggest that, within this scenario, a reasonable description of the measurements over a large energy range can be found, in terms of spectral parameters and mass composition at the escape from the sources.

In the second part, the hypothesis of point-like sources has been abandoned and a study of the UHECRs interactions in the environment surrounding the sources has been performed (“source-propagation model”), applied in particular to Starburst Galaxies. This could be helpful to explain the origin of some features observed in the UHECR measurements, therefore motivating the results found with the “propagation model”. As an additional novelty, we have been included the hadronic interactions in the source environment. By exploring several configurations of source characteristics, we demonstrate that it is possible to accommodate the Auger measurements with the scenario of cosmic rays accelerated and processed in Starburst Galaxies. Secondary messengers directly produced in these sources and along the UHECR travel to the Earth have been computed, in order to complete the multi-messenger picture and improve the constraining capability of our model.

*A Mamma, Papà, Elena e Ciacco, alla mia famiglia
Ogni mio (piccolo) successo sarà sempre il vostro.*

Introduction	1
1 Cosmic ray physics	3
1.1 Historical background	3
1.2 The Cosmic Ray Spectrum	4
1.3 Cosmic ray acceleration	5
1.3.1 The Fermi acceleration mechanism	5
1.3.2 Source candidates	7
1.4 Propagation of Ultra-High-Energy-Cosmic-Rays	10
1.4.1 Adiabatic energy loss	10
1.4.2 Photo-interaction with background photons	11
1.4.3 Pair production loss	12
1.4.4 Photo-disintegration of nuclei	13
1.4.5 Photo-pion production	13
1.5 Extensive Air Shower	14
1.5.1 Electromagnetic shower	15
1.5.2 Heitler model for hadronic showers	16
1.5.3 The superposition model	18
1.6 Detection techniques	19
1.6.1 Geometry estimation	19
1.6.2 Energy estimation	20
1.6.3 Composition estimation	21
2 The Pierre Auger Observatory	24
2.1 The SD	24
2.1.1 Cherenkov stations	25
2.1.2 Data communication and maintenance	26
2.1.3 The SD reconstruction	27
2.2 The FD	28
2.2.1 Fluorescence telescopes	29
2.3 FD event reconstruction	30
2.3.1 Atmospheric monitoring	31

2.3.2	SD energy calibration	31
2.4	Auger enhancements	32
2.4.1	Low-energy extension	32
2.4.2	Radio and Microwave detection	34
2.5	Auger Prime	35
2.6	Highlights from Pierre Auger Observatory	36
2.6.1	Energy Spectrum	36
2.6.2	Mass composition studies	38
2.6.3	Anisotropies	39
3	Combined fit of energy spectrum and composition of the Pierre Auger Observatory, at energies above the “ankle”	41
3.1	Scientific motivation	41
3.2	Simulation of extra-galactic propagation	47
3.2.1	The SimProp software	47
3.2.2	Propagation matrix	48
3.3	Combined fit above the ankle	50
3.3.1	Models and experimental data	50
3.3.2	Fit procedure	51
3.3.3	Main results	53
3.4	A new combined fit package	55
3.5	Results	58
3.5.1	Validation	58
3.5.2	Update of the dataset	59
3.5.3	Including overdensity in the combined fit	62
3.5.4	Combined fit using ICRC2019 dataset	63
4	Extension of the combined fit below the ankle	67
4.1	Hints of a second component	67
4.2	Implementation of the extended combined fit	69
4.2.1	Combined fit using two extra-galactic components	69
4.2.2	Technical issues	71
4.3	Results	71
4.3.1	Combined fit using two extra-galactic populations	71
4.3.2	Including the galactic component	76
4.3.3	Low energy component made of protons	79
4.4	Quality of the fit	82
4.5	Crosscheck on the errors	84
4.6	Expected neutrino fluxes	86
5	Source effect mechanism	90
5.1	Source interaction model	90
5.2	The UFA model	91
5.2.1	Comparison to UFA model	93
5.3	Astrophysical input: application of the source interaction model to starburst galaxies	97

5.3.1	Motivation	97
5.3.2	Escape time	99
5.3.3	Interaction time	101
5.3.4	Source injection interface	103
5.3.5	The benchmark case: M82	103
5.3.6	Scan over the parameter space	106
5.3.7	Injecting light and heavy masses	109
5.4	Hadronic interaction input: Including spallation mechanism	112
5.4.1	Comparison with Sibyll	116
5.4.2	Scan over the parameter space	118
5.5	Expected neutrino fluxes	122
	Conclusions and future prospects	125
	Appendix A: Detector effects	129
	Bibliography	132
	Aknowledgements	148

1.1	Cosmic rays flux.	4
1.2	Schematic view of Fermi acceleration mechanism	6
1.3	Hillas plot.	7
1.4	Active Galactic Nuclei scheme.	9
1.5	Schematic Spectral Energy Distributions of the most important backgrounds in the Universe.	12
1.6	Fractional energy loss rate for protons and nuclei.	13
1.7	Photo-meson cross section.	14
1.8	Sketch of the development of an extensive air shower.	15
1.9	Sketch of the model for the development of a hadronic cascade.	17
1.10	Geometrical shower reconstruction from the observables of a fluo- rescence detector.	20
2.1	Map of the Pierre Auger Observatory.	25
2.2	Schematic view of a tank [49].	26
2.3	CIC procedure.	28
2.4	A schematic view of an FD telescope [55].	29
2.5	Fundamental patterns for the second level FD trigger [55].	29
2.6	An example of FD trace.	30
2.7	The energy deposit as a function of the atmospheric depth.	31
2.8	Correlation between SD energy estimators and the FD energy values.	32
2.9	Schematic view of HEAT telescope.	33
2.10	Schematic view of the two physical process responsible for radio emission of an extensive air shower.	34
2.11	3-D view of a Water Cherenkov Detector with a SSD unit.	36
2.12	Combined spectrum from ICRC2019 datasets.	37
2.13	Vertical spectrum measured by the Auger observatory.	37
2.14	Measurements of $\langle X_{\max} \rangle$ (left) and $\sigma(X_{\max})$ (right) at the Pierre Auger Observatory.	38
2.15	Sky map in Galactic coordinates showing the cosmic ray flux for $E > 38$ EeV	39

2.16	Maximum likelihood-ratio as a function of energy threshold for the models based on different catalogues.	40
3.1	Combined energy spectrum presented at the last International Cosmic Rays Conference (ICRC) in 2019 [53].	42
3.2	X_{max} predictions for the transition model compared to the Auger data.	43
3.3	Theoretical modification factor computed for different values of the injection power law index	44
3.4	The predicted pair-production dip in comparison with Akeno-AGASA, HiRes, Yakutsk and Telescope Array data.	45
3.5	Modification factors for protons, helium and iron, as labelled in the picture.	46
3.6	Fluxes of protons and nuclei with primary injected particles from [84].	47
3.7	Intensity of EBL at different redshift.	48
3.8	Deviance of the combined fit above the ankle as a function of γ and R_{cut}	54
3.9	Schematic view of the new organization of the code used for the combined fit.	55
3.10	Fraction fit results.	57
3.11	The psuedo standard deviation $\sqrt{(D - D_{min})}$ as a function of $(\gamma, \log_{10}(R_{cut}))$ for two different dataset.	60
3.12	Injection spectra at the best fit for two different datasets.	61
3.13	Overdensity factor as a function of distance.	62
3.14	Weights applied to a new overdensity function.	66
4.1	Spectrum and composition at the best fit in the reference scenario.	68
4.2	Spectrum and composition using an additional component as shown in sec. 6 in [2].	69
4.3	Spectra at Earth assuming two extra-galactic component.	73
4.4	Mass composition at Earth assuming two extra-galactic components.	74
4.5	Injection spectra for the two extra-galactic component	75
4.6	KASKADE-GRANDE data for different hadonic interaction model.	77
4.7	Spectrum and composition of two extra-galactic component fitting the galactic contribution.	79
4.8	Spectrum and composition assuming a second component made of protons and a galactic contribution	82
4.9	Distributions of D_J , $D_{X_{max}}$ and D_{tot} in the mock data sets generated from the best-fit model predictions. The vertical red lines represent the corresponding values of D_J , $D_{X_{max}}$ and D_{tot} of the found best fit.	83
4.10	Distribution of spectral parameters in the mock traces for the extended combined fit.	84
4.11	Predicted neutrino fluxes for different value of maximum redshift and different evolution for the combined fit above the ankle.	87

LIST OF FIGURES

4.12	The predicted spectrum of neutrinos obtained with $m = 5$ for the combined fit above the ankle.	87
4.13	Deviance as a function of different evolution of two extra-galactic components.	88
4.14	Neutrino fluxes associated with two different scenario for the extended combined fits	89
5.1	Sketch of the source model.	91
5.2	Photon Spectra and interaction time used in a reference paper. . .	92
5.3	Interaction and escape times for different nuclei.	93
5.4	Spectrum and composition at Earth according to the reference paper (UFA).	94
5.5	Photon fields and interaction times as implemented in in-source-SimProp.	95
5.6	Comparison between the interaction times and the escaping fluxes with the reference scenario.	95
5.7	Comparison between spectra at Earth in the reference scenario and in this work.	96
5.8	Comparison between the galactic component used in the reference scenario and the KASCADE-Grande fluxes.	97
5.9	Picture of M82.	98
5.10	Implemented diffusion and advection time.	101
5.11	Implemented interaction times.	102
5.12	Scheme of source interaction steps.	103
5.13	Multiwavelength spectrum of M82.	104
5.14	Timescale and escaping fluxes in M82 scenario.	104
5.15	M82 fluxes at Earth	105
5.16	Scan in $\gamma - R_{\text{cut}}$ space	108
5.17	Spectrum and composition at Earth after scanning parameter . .	109
5.18	Scan in $\gamma - R_{\text{cut}}$ space using protons and silicon nuclei at the injection	110
5.19	Spectrum and composition at Earth injecting two primary particles	111
5.20	Spallation cross section in Sibyll2.3d	113
5.21	Fit of the cross section outcomes from Sibyll2.3d	113
5.22	Sketch of disintegration due to hadronic interaction.	114
5.23	Fit of the cross section outcomes from Sibyll2.3d	114
5.24	Fit of the charged secondary particles from Sibyll2.3d	115
5.25	x_{Lead} distributions of secondary particles in p-p interactions. . . .	116
5.26	Rapidity and energy distribution for secondary of a $p-p$ interaction.	117
5.27	Comparison of hadrons and neutrinos distributions in Sibyll and in the used parametric model.	118
5.28	Interaction times after the inclusion of spallation.	119
5.29	Kennicutt-Schmidt law.	119
5.30	$\gamma - R_{\text{cut}}$ space including spallation processes.	120
5.31	Spectrum and composition at Earth including spallation process for a flat evolution of the source	121

LIST OF FIGURES

5.32	Spectrum and composition at Earth including spallation process for a SFR evolution of the source	122
5.33	Neutrino fluxes for M82 case (left) and best case (right) according to a SFR evolution of the sources.	123
5.34	Neutrino fluxes for M82 case (left) and best case (right) according to a flat evolution of the sources.	124
5.35	Detector acceptance and resolution functions in three different $\log_{10}(E/eV)$ bins.	130

3.1	Best fit parameters for the two minima discussed in the combined fit paper [2].	54
3.2	Effect of the unfolded combined spectrum in the combined fit results.	58
3.3	Combined fit results for different datasets, JCAP2017 and ICRC2017.	60
3.4	Comparison of fit results with and without overdensity for the JCAP2017 and ICRC2017 dataset.	63
3.5	Effect of the overdensity correction to the combined fit.	64
3.6	Effect of the different photo-disintegration cross sections in the combined fit.	65
4.1	Best fit values for the extended combined fit with and without overdensity correction.	72
4.2	Best fit parameters for the electron-poor component of KASKADE-GRANDE.	77
4.3	Best fit parameters for the extended combined fit using two extragalactic components and including the galactic one.	78
4.4	Best fit parameters for the extended combined fit using a sub-ankle contribution made of protons.	81
4.5	Errors obtained with the bootstrap methods for the case presented in section 4.3.1.	85
5.1	Parameter space for M82 case	107
5.2	Gumbel distribution parameters for the X_{\max} distributions with different hadronic interaction models. The meaning of the parameters can be found in [107].	131

One of the most exciting astrophysical discoveries of the last century is the existence of a diffuse flux of cosmic particles which extends in energy up to values greatly exceeding every Earth-based accelerator. Decades of observations have allowed us to explore its spectral behavior and composition in terms of atomic nuclei. However its nature and origin remain a mystery. This makes the puzzle of Ultra-High-Energy Cosmic Rays (UHECRs) one of the most intriguing open questions of modern astrophysics. The mysteries of UHECRs can be captured in a few fundamental questions:

- What are the sources of high-energy cosmic rays?
- By which processes are they accelerated?
- What is their mass composition?
- How do they propagate towards Earth?
- Is our understanding on their interaction in atmosphere satisfactory?

To answer these questions, the Pierre Auger Observatory [1], the largest facility to detect cosmic rays built so far, has combined different experimental techniques. The key to unravelling these questions could be to combine different information about the nature of cosmic rays in order to infer properties of their sources.

In a study published by the Pierre Auger Collaboration [2], a combined fit of energy spectrum and composition measurements above $5 \cdot 10^{18}$ eV was performed using a simple astrophysical model, consisting of a population of identical point-like sources distributed uniformly. Monte Carlo simulations to take into account the processes occurring during the propagation of particles through the intergalactic medium are used (“propagation model”).

The main part of my work during the course of my PhD involved contributions to the analyses within the Cosmic Rays Phenomenology task of the Pierre Auger Collaboration. In the first part of my work, I re-organized the software for the combined fit analysis, making it more flexible for other phenomenological analyses.

In the second part, I developed an extension of the combined fit analysis in order to take into account the region below the energy in which a change of slope in the energy spectrum, the so-called *ankle*, is observed ($E \sim 5 \cdot 10^{18}$ eV). This analysis required the use of two independent components, corresponding to two different classes of sources. In addition, the role of the galactic contribution has also been studied. This work contributes to the understanding of UHECR data in the largest possible energy range.

The final part of my work concerned the abandonment of the hypothesis of point-like sources, and the study instead of the UHECR interactions in the environment surrounding the sources (“source-propagation model”). Within the sources capable of accelerating UHECRs, the region surrounding the source could act as a high-pass filter, permitting the highest energy cosmic rays to escape freely while the lower energy ones are disintegrated inside the source region, generating nucleons at lower energies. The overlap of these two contributions can explain the features observed in the UHECRs spectrum and composition [3], as well as motivate the results of the “propagation model”. We have explored this scenario extending SimProp, a simulation code for UHECR extra-galactic propagation, allowing us to compute the interactions inside and outside the source.

A potentially interesting class of sources have been studied: starburst galaxies. Considering interactions with background photons in the starburst nucleus, a study of the parameter space has been performed in order to directly link parameters at the source to the experimental data on Earth. Taking into account interactions with the Interstellar medium (ISM), a detailed treatment of the hadronic interactions inside a source has been performed, using the hadronic interaction model Sibyll2.3d [4] as a reference.

To complete this procedure, the secondary fluxes are computed, comparing the expected fluxes with the experimental results and providing a multi-messenger approach to our analysis.

This approach can be exploited in future works with a systematic scan of the parameter space of the source environment, applied to different source candidates.

The thesis is organized as follows: in the chapter 1, I introduce the history of cosmic rays, acceleration and propagation, including also extensive air showers physics. In chapter 2, I mainly focus on the Pierre Auger Observatory, describing the detection techniques and commenting the most important results. In chapters 3 and 4, I focus on the combined fit analysis, first above the ankle and then extending the analysis to lower energies. In chapter 5, I study the source interaction model: in the first part of the chapter, I focus on a generic source and in the second part, I study processes happening inside starburst galaxies. Finally, I summarize the results and possible future developments are discussed.

1.1 Historical background

Even if the discovery of cosmic rays is used to be attributed in the first half of the 20th centuries, the first evidences of an unexplained natural radiation dates back to the end of 18th century, when it was proved that a leaf electroscope spontaneously discharges overtime due to the ionization of the air surrounding it. At the beginning of the 20th century, the discovery of spontaneous radioactivity allowed to find a source of air ionization in the natural decay processes. At that time, many believed that almost all the natural radiation was coming from the ground. To proof this hypothesis, experiments were performed comparing the rate of discharge of an electroscope at ground level with the rate at higher level, such as the Father Wulf experiment [5]. The results of these first experiences were unclear and taken as a confirmation of the dominant opinion: radioactivity came from the soil. A new point of view was shown independently by Domenico Pacini [6] and Victor Hess [7], between 1907 and 1912. Hess highlighted an increase of air ionization with altitude using balloons, while Pacini measured a decrease with deepness in water due to absorption of the ionizing radiation. Both these results confirmed that a penetrating radiation must come from outside the Earth, producing a noticeable ionization in the atmosphere. Robert Millikan in the 20's named this radiation "cosmic rays", believing it was composed mainly of γ rays. However, in the following years, it was understood that such radiation originates in the interaction of energetic particles with the atmosphere molecules: such particles are nowadays designated as cosmic rays. The origin of cosmic rays is still a mystery, even if likely connected with the most catastrophic events in the Universe, such as SuperNovae explosions in the Milky Way, or Active Galactic Nuclei and Gamma Ray Bursts in extra-galactic space (since the most energetic cosmic rays are disfavoured to be produced in our Galaxy, as shown in the following).

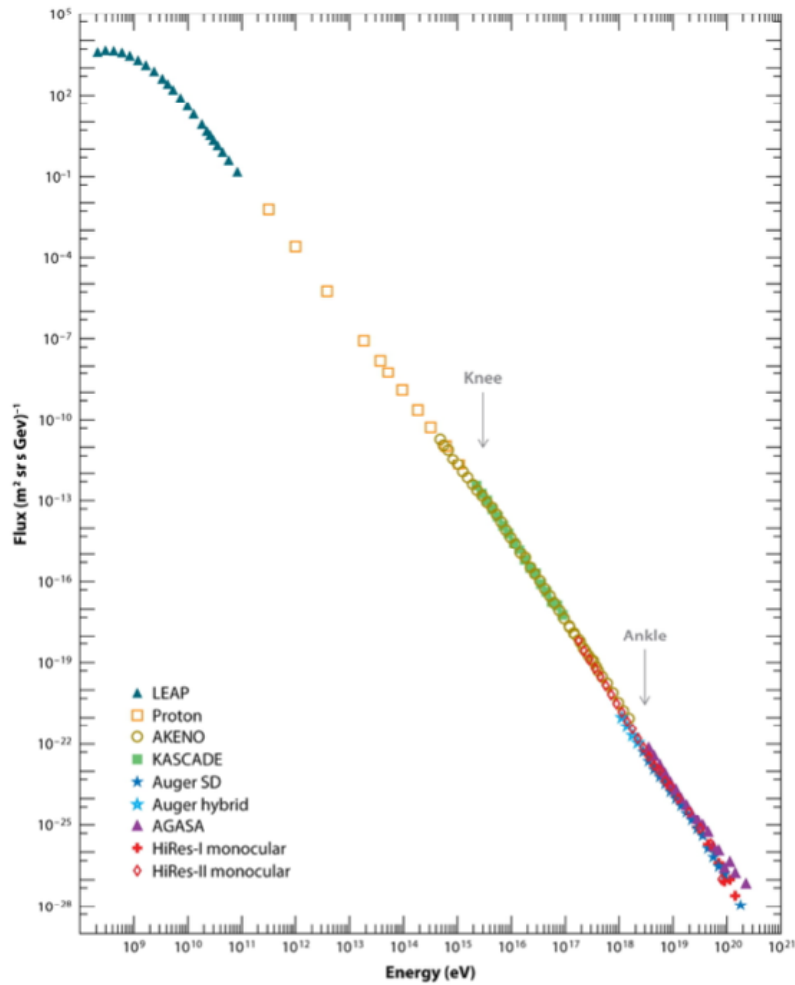
1.2 The Cosmic Ray Spectrum

The behaviour of the differential flux of the cosmic rays measured at Earth as function of the energy E is a power law:

$$\frac{dN}{dE} \propto E^{-\gamma} [\text{m}^{-2} \text{s}^{-1} \text{sr}^{-1} \text{eV}^{-1}] \quad (1.1)$$

where γ is the spectral index. It is necessary to point out that below 10^9 eV cosmic rays are modulated by the Solar activity and deviated by the magnetic fields in the Solar System, so this energy range is not considered in the following.

As can be seen from fig. 1.1, the energy spectrum spans over 12 orders of



 Beatty JJ, Westerhoff S. 2009. Annu. Rev. Nucl. Part. Sci. 59:319–45

Figure 1.1: Cosmic rays flux as a function of energy, as measured by different experiments. Data from LEAP [8], Proton [9], AKENO [10], KASCADE [11], Auger surface detector and Auger hybrid [12], AGASA [13], HiRes-I monocular and HiRes-II monocular [14]. From [15].

magnitude in energy (from 10^9 eV to 10^{20} eV) and above 30 orders of magnitude

in flux (from about 1 particle/m²/s at low energies, to 1 particle/km²/century at the highest), giving an overall idea of the enormous number of phenomena that contribute in the production, propagation and observation of these particles. The spectrum can be roughly divided into three parts depending on the γ value, which is supposed to change because of different origin, acceleration mechanisms and propagation of the primary particles:

- **low energy region:** from above 10⁹ eV to the “knee” ($E \simeq 10^{15}$ eV): the spectral index is roughly $\gamma \sim 2.7$ and the primaries of this region are supposed to be galactic;
- **intermediate region:** from the “knee” to the “ankle” ($E \simeq 10^{18}$ eV): the spectral index becomes softer $\gamma \sim 3.1$; in this region the transition between galactic and extra-galactic cosmic rays is expected;
- **high energy region,** above the ankle the spectral index decreases ($\gamma \sim 2.6$) approximately to the value before the knee; moreover, a flux suppression is observed above 10¹⁹ eV.

For the low energy cosmic rays a direct detection is possible, while for the energies above the knee many techniques of indirect detection have been developed.

1.3 Cosmic ray acceleration

In order to explain the observed energies, it seems reasonable to take the most energetic astrophysical objects in the Universe as perfect candidates. Those objects are characterized by surrounding matter in the state of plasma and by the presence of intense, strongly variable magnetic fields. Such environments are perfect to accelerate charged particles, as proposed by Enrico Fermi [16], based on the concept of collision-less magnetic diffusion. Currently, the most widely accepted model for cosmic ray acceleration is an evolution of the Fermi model, based on diffusive shock acceleration. Both scenarios are illustrated in the following.

1.3.1 The Fermi acceleration mechanism

A first acceleration mechanism was originally proposed by Fermi in 1949. Nowadays it is known as second order mechanism. This is a toy model in which the interstellar medium is assumed to be filled with moving clouds of magnetic fields, being their speed small. In this model, a charged particle bounces off these clouds in an elastic way. The net change of energy of the particle is then [17]:

$$\left\langle \frac{\Delta E}{E} \right\rangle = \frac{8}{3} \beta^2, \quad (1.2)$$

Where β is the ratio between the speed of the cloud and the speed of light. This mechanism is a second order (in β), making this acceleration method highly

inefficient for particle acceleration. If, however, the interaction happens in a shock area, things change drastically: it is possible to have enough energy gain in a regime of diffusive shock acceleration (figure 1.2), where the charged particles interact with a shock wave front of magnetized matter. In particular, in the context of SuperNova (SN) explosions, the ejected material moves a thousand times faster than the sound speed, the shock-wave being just a disturbance of the interstellar medium (ISM) that conveys the signal of the explosion. In order to develop a shock-wave there must be some interaction: in air, it is molecular interactions, and the thickness of the shockwave is of the order of a few interaction lengths. In astrophysics, since the rate of collisions is very small due to the low density of the ISM (1 particle per cubic centimetre), the shockwave can only be formed through excitation of electromagnetic instabilities. In this case:

$$\left\langle \frac{\Delta E}{E} \right\rangle \simeq \frac{V_{\text{shock}}}{c} \quad (1.3)$$

where $V_{\text{shock}} = 4/3 V$, with V speed of the cloud. Because the shock front can reach sub-relativistic velocities ($V_{\text{shock}} \simeq 0.1 c$) this result is acceptable to explain the observations.

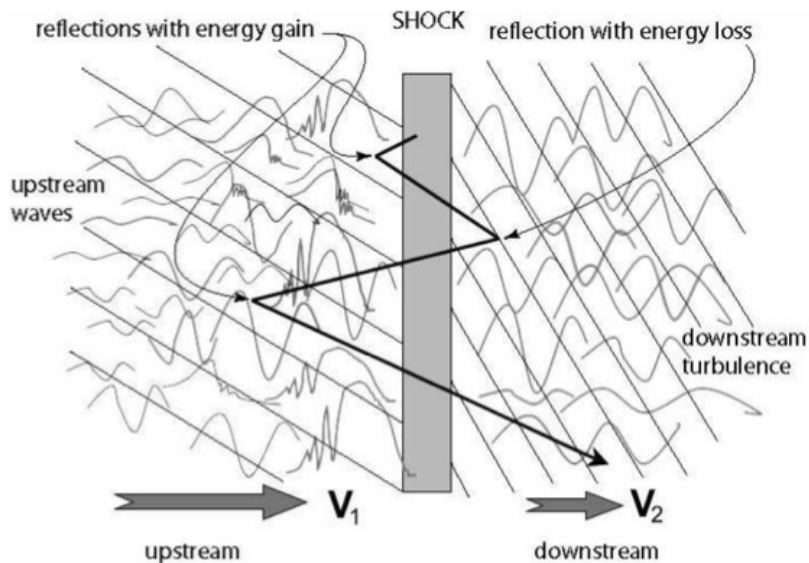


Figure 1.2: Schematic view of Fermi acceleration mechanism

A focus on the detection techniques for the the cosmic ray of the highest energies will be provided in the next chapter.

In this work, the focus will be on Ultra-High-Energy Cosmic Rays (UHECRs). Which astrophysical objects have the possibility to accelerate cosmic rays up to such high energies? We will present here the most plausible candidates, discussing the interactions they suffer in the extra-galactic propagation and, in addition, presenting the experimental techniques for indirect detection.

1.3.2 Source candidates

In order to estimate what sources could accelerate cosmic rays, one can look at the size and the magnetic field. By estimating the residence time of a particle within a source, one can demonstrate [18] that :

$$\left(\frac{E}{10^{18} \text{ eV}} \right) < \frac{Z\beta}{2} \left(\frac{L}{\text{kpc}} \right) \left(\frac{B}{\mu\text{G}} \right) \quad (1.4)$$

where L is the size of the acceleration site.

This relation provides an upper limit of the energy to which particles of a certain charge can be accelerated, given the size of a source and its magnetic field. For cosmic rays of the highest energies, exceedingly vast sources or extremely powerful magnetic fields are required to accelerate them. Particles with higher charge are easier to confine in the magnetic fields, so they can be accelerated to higher energies. Using the relation 1.3 it is possible to build the so-called **Hillas Plot**: an overview of potential astronomical sources of cosmic rays, which can be seen in figure 1.4.

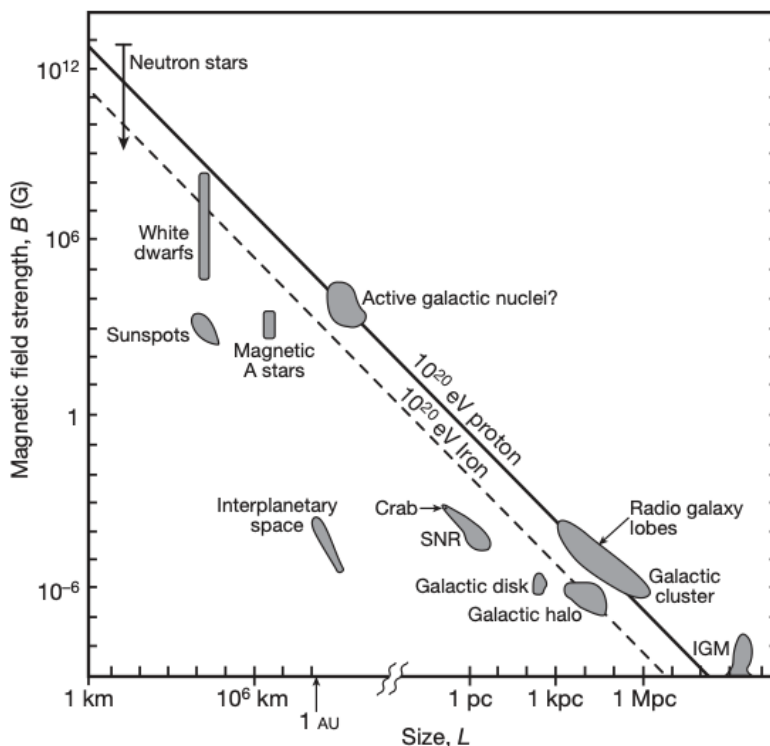


Figure 1.3: Hillas plot with several different astronomical sources of cosmic rays and diagonal lines illustrating the minimum size and magnetic field of cosmic rays of 10^{20} eV, assuming $\beta = 1$ [18].

Below the knee ($\simeq 10^{15}$ eV) possible source candidates are the Supernovae. In fact, considering a magnetic field of intensity $B \simeq 3 \mu\text{G}$ and a Larmor radius of ~ 1 pc, the maximal reachable energy as function of Z is $E_{\text{max}} \simeq Z \cdot 10^{15}$ eV.

Another argument supporting the galactic origin for cosmic rays below the knee is the comparison between the luminosity of the Supernovae in our Galaxy and the luminosity of low energy cosmic rays, as emphasized long ago by Ginzburg and Syrovatskii [19]. They have shown that only $\sim 1\%$ of the energy emitted by Supernovae is needed to accelerate all the cosmic rays produced inside the Milky Way, supporting the hypothesis that low energy cosmic rays (below the ankle) can be produced in our Galaxy.

In the following a list of the astrophysical candidate sources, that have been proposed for the acceleration of the highest energy cosmic rays, is provided. The first two candidates are both related to Active Galactic Nuclei (AGNs), Galaxies with a nuclear super-massive black hole with accretion processes running.

- **AGN:** AGNs have been considered as appealing candidate sources of cosmic rays for the last 50 years [20]. In this case the engine of the acceleration is the accretion disk of matter orbiting around a super-massive black hole ($10^6 - 10^{10}$ solar masses) in the nucleus of the Galaxy, as sketched in figure 1.4. Those accreting disks are known to have magnetic fields of the order of few Gauss. These parameters are marginally consistent with acceleration up to 100 EeV. The high radiation field around the central engine of an AGN is likely to interact with the accelerated protons while energy losses, due to synchrotron radiation, Compton processes, and adiabatic losses, will also take place. The situation is worse for nuclei that will photo-disintegrate even faster. For this reason, it is now believed that the inner part of AGN galaxies could only contribute to accelerating particles up to small fractions of EeV [21].
- **FR radio Galaxy lobes:** in Fanaroff-Riley (FR) radio-loud active galaxies, extended lobes of magnetized plasma originate from the central black hole. The lobes are observed mainly in radio through synchrotron emission, and may slowly vanish with distance from the nucleus or show high density areas called hot-spots at the lobe edges [20]. Lobes usually exceed in size the Galaxy itself with dimensions up to hundreds of kpc. In the lobes, magnetic fields are usually of less than a μG . On the other hand, hot spots are usually of the order of few kpc and show magnetic fields of the order of hundreds of μG . Both the lobes and the hot spots are candidates to accelerate protons up to hundreds of EeV. If the jets are oriented towards the Earth, these objects are usually called "blazars". Blazars are much brighter and can be detected at higher distances than radiogalaxies; but, since the jet is collimated, they are much rarer than radiogalaxies. Nevertheless, blazars and radiogalaxies are the same objects and can be equally considered as candidates for UHECR acceleration.
- **Galaxy clusters:** in Galaxy clusters, magnetic fields of the order of μG are thought to be present. Those magnetic fields may extend to large dimensions (up to 500 kpc). This should allow acceleration of UHECRs up to 100 EeV [23]. Actually, the fact that long paths in the Galaxy cluster are needed increases the probability of interacting with cosmic backgrounds

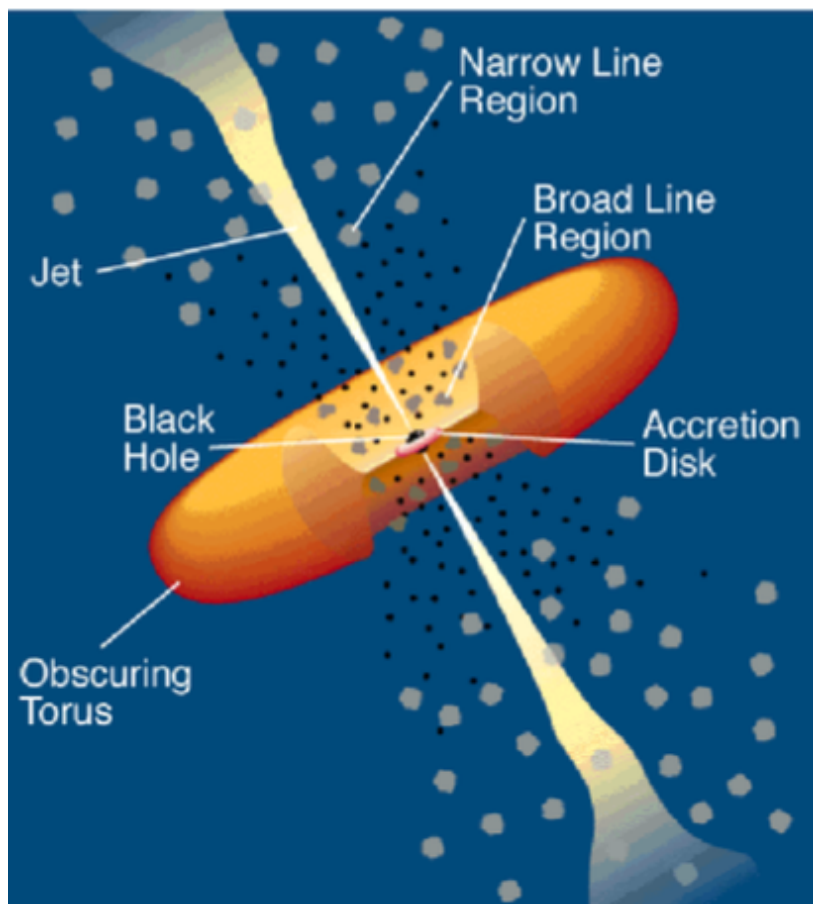


Figure 1.4: Active Galactic Nuclei scheme. It is possible to see the supermassive black hole surrounded by its accreting disk. The jets here represented are typical of Radio Loud AGN and Blazars, and are not present in every active Galaxy. Figure from [22].

and lowers the maximum energy expectation to some tens of EeV.

- **Compact objects:** cosmic rays could be accelerated directly by compact objects such as neutron stars, in particular pulsars and magnetars. In this case the maximum achievable energy should be $E_{\max} = \omega \cdot Z \cdot B \cdot R^2$ where ω is the spinning velocity of the object, Z the charge of the accelerated particle, B the magnetic field at the surface and R the radius of the object. For example, using values from the Crab Nebula Pulsar: $B \sim 10^{12}$ G , $R \sim 10$ km, $\omega \sim 200$ Hz, we obtain a maximum energy of about 10^{18} eV for a proton. Objects with more “extreme” characteristics such as magnetars, where magnetic fields up to 10^{16} G are thought to be present, are then necessary to explain UHECRs [24].
- **Gamma Rays Burst:** Gamma Ray Bursts (GRB) are prompt explosions in the γ band. GRBs duration distributions show two different populations which are thought to have different origins: short (< 1 s) GRBs are possibly the result of the merge of two neutron stars of a binary system into a black

hole, while long ($> 1 - 2$ s) ones have been associated to hypernovae. Some GRBs may be also single Soft Gamma-ray Repeaters (SGR), a class of γ -emitting neutron stars. In particular, the accreting disk around the neutron star binary system could be a good site for particles acceleration. GRBs are though disfavored as primary UHECR source since the major fraction of them were observed at high redshifts (up to $z = 5$) and the few GRBs observed within the GZK horizon would not explain the observed flux [25].

1.4 Propagation of Ultra-High-Energy-Cosmic-Rays

During the travel from the source to the Earth, UHECRs suffer interactions that can change their characteristics as the kind of particle and the energy that will be detected at Earth. This is caused by both the expansion of the Universe and the interaction with the extra-galactic photon fields. Regarding the electromagnetic interactions, as can be the Compton or inverse-Compton scattering and the synchrotron radiation, these processes are mostly important for the propagation of photons and electrons than for protons and nuclei. The remaining interaction processes of interest for our applications are the interactions of UHECR particles with cosmic photons, with the consequent production of secondary particles.

1.4.1 Adiabatic energy loss

In order to describe that the adiabatic energy losses is due to the expansion of the Universe, a general recall about the metric that describes a homogeneous and isotropic expanding Universe is needed. The metric that describes a homogeneous and isotropic expanding Universe is the Robertson-Walker metric [26]; it is used to calculate the modification of the Euclidean distance due to expansion of the Universe.

$$ds^2 = dt^2 - cR^2(t) \left(\frac{dr^2}{1 - kr^2} + r^2(d\theta^2 + \sin^2\theta d\phi^2) \right) \quad (1.5)$$

where (t, r, θ, ϕ) are co-moving coordinates, $0 \leq r \leq 1$ and the scale factor $R(t)$ has dimension of length and depends only on t . The k parameter can be chosen to be > 0 , < 0 and $= 0$, which corresponds respectively to a spatial curvature which can be positive, negative or zero. Observations are compatible with a flat evolution, therefore $k = 0$. The k parameter depends on whether the total energy density of the Universe ρ is greater, less or equal than the critical density $\rho_c = 3H^2/8\pi G$, where $H = \frac{\dot{R}(t)}{R(t)}$ is the Hubble constant, i.e. the rate of expansion of the Universe (at present $H_0 \simeq 70 \text{ km s}^{-1}\text{Mpc}^{-1}$). In this work I will consider $\Omega = \Omega_m + \Omega_\Lambda$, where Ω_m is the ratio between total matter density and critical density and Ω_Λ is the ratio between dark energy density and critical density (at the current time $\Omega_m \simeq 0.26$ and $\Omega_\Lambda \simeq 0.74$).

Because the moment of a photon changes with R , the wavelength received at

time t_0 , denoted as λ_0 , will differ from that at time t_1 , denoted as λ_1 , by:

$$\frac{\lambda_1}{\lambda_0} = \frac{R(t_1)}{R(t_0)} \quad (1.6)$$

The observed wavelength is increased with respect to the emitted one; this effect is called **cosmological redshift** and expresses the fact that the Universe was smaller when the photon was emitted. The redshift parameter z is defined as

$$z = \frac{\Delta\lambda}{\lambda} = \frac{\lambda_1}{\lambda_0} - 1 \quad (1.7)$$

It can be proved that the quantity $\frac{dt}{dz}$ can be written such as:

$$\left(\frac{dt}{dz}\right)^{-1} = -H_0(1+z)\sqrt{(1+z)^3\Omega_m + \Omega_\Lambda} \quad (1.8)$$

and the adiabatic energy loss can be expressed as:

$$\beta_{ad}(A, Z) = -\frac{1}{E} \frac{dE}{dz} \left(\frac{dt}{dz}\right)^{-1} = H_0\sqrt{(1+z)^3\Omega_m + \Omega_\Lambda} = H(z) \quad (1.9)$$

1.4.2 Photo-interaction with background photons

Hereafter the interaction with background photons are discussed. In fact, during the travel from the source to the Earth, UHECRs could interact changing their energy and mass. The background photons usually taken into account are the Cosmic Microwave Background radiation (CMB) and the radiations in the infrared, optical and ultraviolet bands, called Extra-galactic Background Light (EBL). The spectral energy distribution of the two photon fields are sketched in figure 1.5. At this stage it is necessary to describe the interactions of UHECRs with these photon fields, namely pair production, photo-disintegration and photo-meson production. For all of these processes, the interaction rate, given in [27], is shown in equation 1.10, considering high-energy cosmic-ray nuclei traversing an isotropic radiation field of arbitrary energy spectrum $n_\gamma(\epsilon')$.

$$\frac{1}{\tau(\Gamma)} = \frac{c}{2\Gamma^2} \int_{\epsilon_{thr}}^{\infty} d\epsilon' \sigma(\epsilon') K(\epsilon') \epsilon' \int_{\epsilon'/2\Gamma}^{\infty} d\epsilon \frac{n_\gamma(\epsilon)}{\epsilon^2} \quad (1.10)$$

In equation 1.10 Γ is the Lorentz factor of the particle, ϵ_{thr} the threshold in the rest frame of the particle, $\sigma(\epsilon')$ the relevant cross section and $K(\epsilon')$ the inelasticity of the reaction. Note that primed symbols (e.g. ϵ') refer to quantities in the nucleus rest frame (NRF), while unmarked symbols refer to quantities in the laboratory frame.

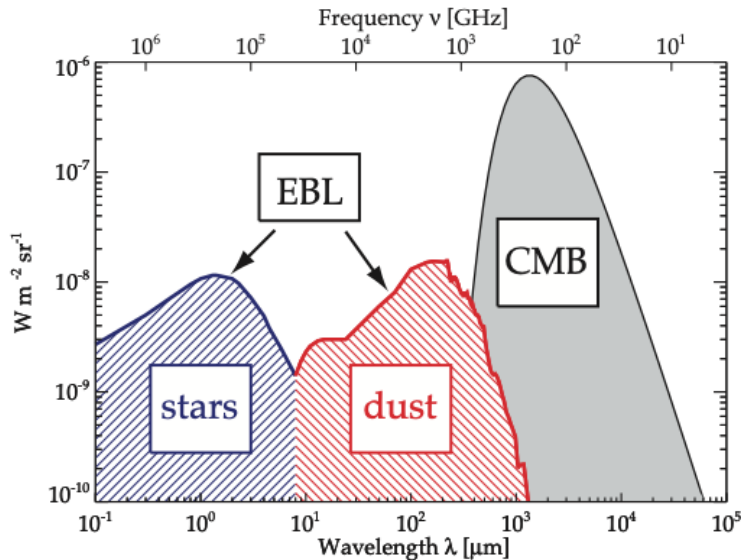


Figure 1.5: Schematic Spectral Energy Distributions of the most important backgrounds in the Universe. From right to left: the cosmic microwave background (CMB), the cosmic infrared background (CIB) and the cosmic optical background (COB). The last two components together are called EBL. From [28].

1.4.3 Pair production loss

The interaction between a charged particle and a background photon can produce a positron-electron pair.

$$N + \gamma \longrightarrow N + e^- + e^+ \quad (1.11)$$

This interaction has a very short mean free path, but it leads to a very small fractional energy loss, with inelasticity $\simeq 0.1\%$ at the energy threshold $\epsilon'_{min} = 2m_e + (2m_e)^2/2m \sim 1.02$ MeV and monotonically decreasing from higher energies [29]. In the case of nuclei, since the photon energies in the extra-galactic space are much smaller than nuclear binding energies, the nucleus behaves as a point particle; the cross section is proportional to Z^2 and the inelasticity to $1/A$, so the fractional energy loss rate is Z^2/A times that for a single proton with the same Lorentz factor.

This process can happen both on a CMB or a EBL photon. However, the density of EBL photons is considerably lower compared to the CMB, as shown in fig. 1.5. In addition, at higher energies, the pair production on CMB photons is strongly dominant, hence the EBL contribution to pair production can usually be neglected [30].

1.4.4 Photo-disintegration of nuclei

Photons with $\epsilon' > 8$ MeV can interact with nuclei stripping them of one or more fragments



Since the energies involved are smaller than the rest mass of the nucleus, nuclear recoil is negligible and all the fragments inherit the Lorentz factor of the parent nucleus. As a result, the energy losses for nuclei can be separated with good approximation into processes that decrease the Lorentz factor but not A (adiabatic and pair production) and those that decrease A but not Γ (photo-disintegration). These contributions are shown in fig. 1.6. Total photo-disintegration cross sections have been measured for many nuclides, but exclusive cross sections for the individual channels are hard to measure, especially in the case of charged particles ejected. Phenomenological models are used to describe these cross sections, but they are not always in agreement with the few measurements available, as for instance reported in [31].

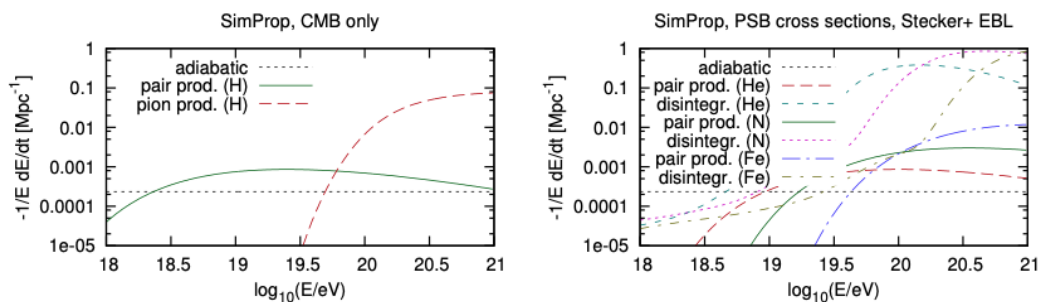


Figure 1.6: Fractional energy loss rate for protons (left) and nuclei (right) for various processes. Figure from [32].

1.4.5 Photo-pion production

Photons with energy in the nucleus rest frame above ~ 145 MeV can interact with nucleons producing pions



At higher energies, processes where several pions or heavier mesons are produced are also possible. Since the involved photon energies are much greater than nuclear binding energies, nuclei behave approximately as collections of free nucleons in these processes.

The fraction of energy lost by a nucleon in this process is 13% at $\epsilon' = 145$ MeV and higher at higher photon energies. The total cross section for these processes has a peak at $\epsilon' \sim 340$ MeV [33] where $\sigma \sim 0.5$ mb, corresponding to the Δ resonance, some lower peaks and an almost constant plateau at higher energies, as can be seen by fig. 1.7.

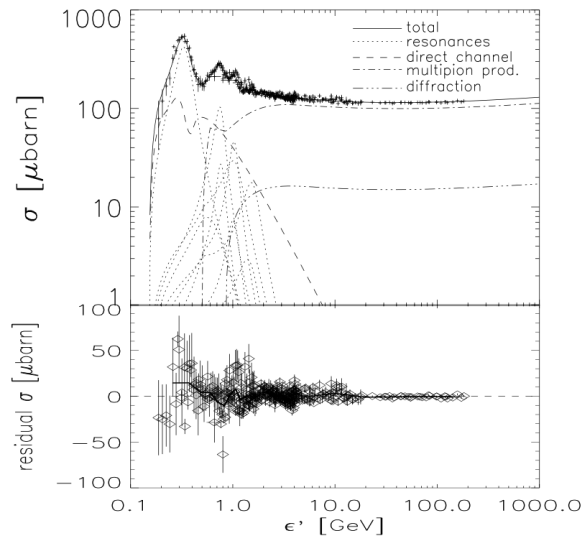


Figure 1.7: Top panel: total cross section $\gamma\pi$ (solid line) compared to different partial contributions (dashed lines). Bottom panel: Residuals of the total cross section data to the sum of all partial cross sections implemented in SOPHIA [33].

1.5 Extensive Air Shower

Cosmic rays in different energy ranges require different types of detectors. For cosmic rays of energy lower than 10^{14} eV the flux is high enough for direct detection: this can be performed by satellites or high-altitude balloons in order to avoid atmosphere absorption. At higher energies, given the much lower fluxes, cosmic ray detection is performed indirectly. For their detection we aim to detect the particle cascades, or Extensive Air Showers (EAS) that the cosmic rays produce in the Earth’s atmosphere. In order to reconstruct the characteristics of the primary particle, it is necessary to analyse the interaction processes that govern the atmospheric development of a cascade.

The development of a cascade can be manly divided in three components:

- **hadronic:** mainly composed by pions and mesons in the initial phase of the shower, rapidly decreasing during the development.
- **electromagnetic:** composed by photons, electron and positrons, it becomes predominant from an energetic point of view when the shower reaches its maximum.
- **hard:** composed by muons and neutrinos originating by the decay of mesons. It is called “hard” because it reaches the ground with almost no interaction.

During the propagation of the shower in atmosphere, the number of particles produced in the cascade grows while the average energy per particle lowers. In order to quantify what happens from the top of the atmosphere to a certain

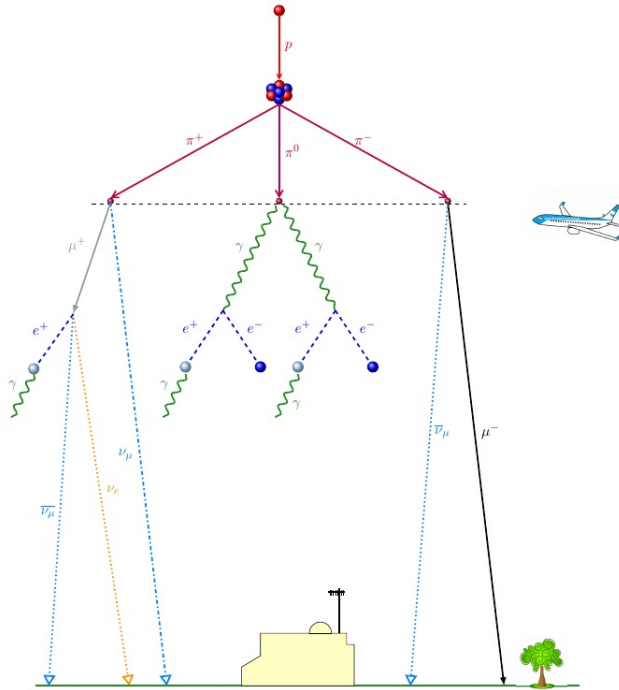


Figure 1.8: Sketch of the development of an extensive air shower.

altitude h , the atmospheric depth X is defined as:

$$X = X_v / \cos\theta \text{ with } X_v = \int_h^\infty \rho(z) dz \quad (1.14)$$

where θ is the zenith angle of the shower axis with respect to the vertical direction and $\rho(z)$ is the density profile as function of the height in atmosphere.

When a shower starts, the particles produced interact continuously up to a certain critical value, an energy threshold below which the particle creation stops. At this energy, the maximum number of particles in the shower is reached, and therefore, the atmospheric depth corresponding at which the shower has the maximum number of particles is called X_{\max} . In the following, we are going to describe the showers dividing the description in electromagnetic and hadronic shower. For the first case, cross sections and multiplicity of particles produced are well known. Instead, for the hadronic shower, more complicated and approximated models have to be taken into account.

1.5.1 Electromagnetic shower

A simple model was elaborated by Heitler in the '40s [34], taking into account the stochastic nature of the shower development. In a purely electromagnetic shower, the most important processes are bremsstrahlung and pair production. The Heitler model considers a primary particle with energy E_0 which splits into secondary particles after passing through an amount of atmosphere λ_r , called *radiation length* and defined as the quantity of atmospheric depth in which an

electron gets its energy reduced of a factor $1/e \simeq 0.37$. This process is repeated thereafter. So, after n steps, the average energy per particle can be written as:

$$\langle E \rangle = \frac{E_0}{2^n} \quad (1.15)$$

By definition, the average energy at which the shower reaches its maximum is given by $\langle E \rangle = \epsilon_c$, with ϵ_c called critical energy and defined as the value when energy losses through radiation are equal to those in ionization processes. Replacing this condition in equation 1.15 we find:

$$n_{\max} = \frac{\ln(E_0/\epsilon_c)}{\ln(2)} \quad (1.16)$$

and, taking the interaction step length equal to $d = \ln 2 \cdot \lambda_r$ [35], consequently the depth of shower maximum X_{\max} increases logarithmically with energy:

$$X_{\max} = X_0 + \lambda_r \ln(E_0/\epsilon) \quad (1.17)$$

where X_0 is the atmospheric depth of the first interaction of the primary cosmic ray. From this expression we can also obtain the evolution rate of the depth of the maximum as function of primary energy. This quantity is called *elongation rate*.

$$D_{10} \equiv \frac{dX_{\max}}{d \log_{10} E_0} \simeq 2.3 \lambda_r \quad (1.18)$$

The Heitler model for the electromagnetic shower is just a first approach in the EAS analysis; nonetheless, it correctly reproduces the proportionality between the shower **size**, defined as the maximum number of particle N_{\max} during the shower propagation, and the primary energy E_0 . Furthermore, it provides a logarithmic relation between X_{\max} and E_0 .

1.5.2 Heitler model for hadronic showers

Even if it is simplistic, the Heitler model can be generalized in order to describe an extensive air shower generated by a nucleon. An important difference between electromagnetic and hadronic showers is the development of a significant muon component whereas there are very few muons in purely electromagnetic showers. Furthermore, hadronic multi-particle production is characterized by large event-to-event fluctuations. An important result of the generalized Heitler model for hadronic showers is that, traversing a layer of target, each hadron interacts producing 2 charged pions and a neutral one; the energy is shared in equal parts. In this way, at each interaction, one third of the primary energy is transferred to the electromagnetic shower component. Generalizing for an arbitrary number of step n we get:

$$E_{\text{had}} = (2/3)^n E_0 \quad E_{\text{e.m.}} = [1 - (2/3)^n] E_0 \quad (1.19)$$

One can also study the dependence of the number of muons from the energy of the primary.

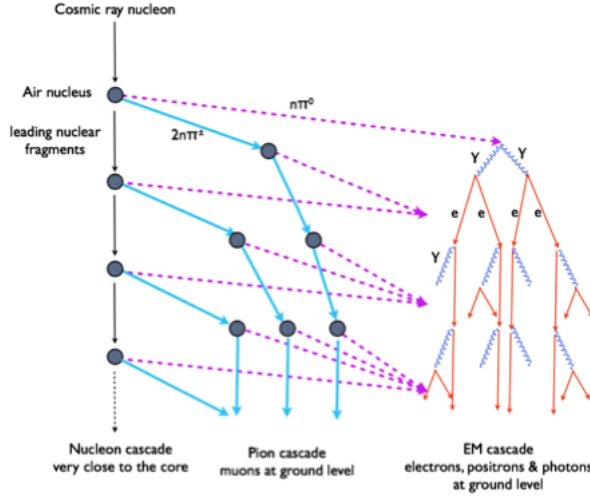


Figure 1.9: Sketch of the model for the development of a hadronic cascade. From [35].

Assuming that all the charged pions decay into muons when the critical energy E_c^π is reached, we can calculate the average energy of charged pions after n interactions:

$$\langle E_{\pi^\pm} \rangle = \frac{(2/3)^n E_0}{(2N_\pi)^n} \quad (1.20)$$

where the number of charged particles produced at each steps and the repartition of the energy between electromagnetic and hadronic components are taken into account. The critical energy for pion decay is reached after n_c interactions, where

$$n_c = \frac{\ln(E_0/E_c^\pi)}{\ln(3N_\pi)} \quad (1.21)$$

And in this way, the total number of muons N_μ can be written as:

$$N_\mu = (2N_\pi)^{n_c} = \left(\frac{E_0}{E_c^\pi} \right)^\alpha \quad \text{with} \quad \alpha = \frac{\ln(2N_\pi)}{\ln(3N_\pi)} \sim 0.9 \quad (1.22)$$

Therefore the muonic size of the shower increases with the primary energy. This result depends on the multiplicity (i.e. the effective number of charged and total particles produced in each interaction, which leads to the value of α), that is taken here as constant as a function of the energy.

Finally, it is possible to estimate the atmospheric depth corresponding to the maximum number of particles produced in an hadronic shower. Because in this case the cascade has two components, X_{\max} is defined such as maximum of the electromagnetic component, being the cascade numerically dominated by that component. Assuming that the X_{\max} value is influenced only by the starting generation of electromagnetic sub-shower produced by the decay of π^0 [36], we get:

$$X_{\max}^n \sim X_0 + \lambda_I \ln 2 + X_{\max}^{e.m.} \left(\frac{(1/3)E_0}{2N_\pi} \right) \quad (1.23)$$

where λ_I is the interaction length for strongly interactive particles and $X_{\max}^{\text{e.m.}}$ is the atmospheric depth of each sub-shower calculated for a cascade with an initial energy equal to $1/3$ of the primary proton energy shared among $(2N_\pi)$ particles. Substituting 1.17 in 1.23:

$$X_{\max}^n(E_0) \sim X_0 + \lambda_I \ln 2 + \lambda_r \ln \left(\frac{E_0}{6N_\pi \epsilon_c} \right) \quad (1.24)$$

Even if simplistic, from 1.24 we can evaluate the elongation rate for an hadronic shower:

$$D_{10}^p = \frac{d X_{\max}^n}{d \log_{10} E_0} \sim D_{10}^{\text{e.m.}} \left[1 - \frac{d \log_{10}(6N_\pi)}{d \log_{10} E_0} \right] + \ln 2 \cdot \frac{d \lambda_I}{d \log_{10} E_0} \quad (1.25)$$

The elongation rate per energy of nucleon-initiated showers is always smaller than the corresponding value for e.m. showers. This result is a direct consequence of the larger number of particles produced in hadronic EAS for each step, which gives a much higher conversion rate of the primary energy into secondary particles.

1.5.3 The superposition model

The superposition model allows us to extend the generalized model for nucleon initiated showers to the case of primary nucleus.

Since the binding energy per nucleon is much smaller than the interaction energy for cosmic rays interaction, a primary nucleus of mass A and energy E_0 can be considered as a bunch of A primary nucleons with energy E_0/A which independently interact in the atmosphere. The behaviour of every sub-shower follows the Heitler model but the total shower development results as a superposition of the cascade generated by each nucleon. Averaging over many showers, the superposition model expectation coincided with that of more realistic calculations. Therefore the superposition model provides good results, such as the mean depth of the shower maximum and the number of muons. Under the superposition assumption it is possible to write, starting from 1.23:

$$X_{\max}^A(E_0) = X_{\max}^p(E_0/A) - \lambda_r \ln A \quad (1.26)$$

which means that heavier nuclei develop earlier in the atmosphere than lighter ones. In addition, the shower-to-shower fluctuation are reduced for heavy nuclei with respect to the light ones, as result of combination of several cascades.

Furthermore, the superposition model predicts a fast development of the shower, meaning that the pions reach their critical energy sooner. So the number of muons with respect to the electromagnetic component will be larger, as can be obtained from 1.22:

$$N_\mu^A(E_0) = \left(\frac{E_0}{AE_c^\pi} \right)^\alpha = A^{1-\alpha} N_\mu^p(E_0) \quad (1.27)$$

For example, an iron-initiated shower contains $\sim 50\%$ more muons than a proton-initiated one.

In the end, it is important to highlight that all the described trends for atmospheric depth and number of muons and their dependence on the energy are reproduced by detailed MonteCarlo simulations [37]. Unfortunately our poor knowledge of the nuclear and subnuclear reactions at extreme high energy cause some uncertainties and makes the fully reproduction of the UHECR observations more challenging.

1.6 Detection techniques for Extensive Air Showers initiated by UHECRs

Several detection techniques for extensive air showers initiated by UHECRs have been developed; in this chapter we are focusing only on the two most important ones.

The first one, developed by Pierre Auger in 1938, consists in distributing a certain number of detectors across a large area and detecting directly particles of the shower surviving at ground level. Using this technique, the particles are detected with an array of detectors deployed, often in a regular grid, over an area of many square kilometers. All the arrays built to measure cosmic rays above 10^{19} eV must be located between 800 g/cm^2 and the sea level. This is because the average maximum depth of the showers is about 750 g/cm^2 and it is effective to study showers close to the shower maximum. Usually the detectors used for this purpose are called **Surface Detectors** (or **SD**).

The second technique, complementary to the sampling with many detectors on a grid, consists in measuring the fluorescence lights associated to an EAS and measures the energy dissipated by shower particles in the atmosphere. This method exploits the excitation of nitrogen molecules by the particles in the shower and the associated fluorescence emission of light in \sim hundreds of nanometers band. The fluorescence light is emitted isotropically along the trajectory of the shower; experimentally, mirrors are used for receiving the light and collecting it into photomultipliers. In this way it is possible to follow directly the development of the shower in atmosphere. In this case the detectors are called **Fluorescence Detectors** (or **FD**).

At this stage we can focus on how it is possible to have information about the geometry of the shower and about the features of the primary particle, such as energy and composition, for both detection techniques.

1.6.1 Geometry estimation

- *Fluorescence Detectors*: The first step in the analysis of a shower is the determination of the shower-detector plane (SDP) [39]. The SDP is the plane that includes the location of the eye of the telescope and the line of the shower axis. This is the plane through the eye which most nearly contains the pointing directions of the Fluorescence Detector pixels centered on the shower axis. Next, the timing information of the pixels are used for

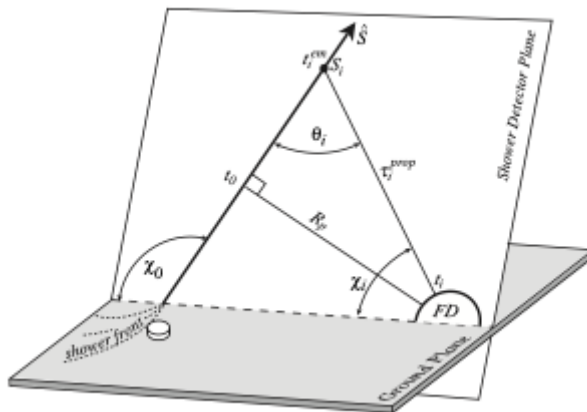


Figure 1.10: Illustration of the geometrical shower reconstruction from the observables of a fluorescence detector [38].

reconstructing the shower axis within the SDP. As show in 1.10, the shower axis can be characterized by two parameters: the perpendicular distance R_p from the camera to the track, and the angle χ_0 that the track makes with the horizontal line in the SDP. Each pixel which observes the track has a pointing direction which makes an angle χ_i with the horizontal line. Let t_0 be the time when the shower front on the axis passes the point of closest approach R_p to the camera. The light arrives at the i -th pixel at the time

$$t_i = t_0 + \frac{R_p}{c} \tan[(\chi_0 - \chi_i)/2]; \quad (1.28)$$

this is obtained assuming instantaneous emission of light and straight propagation with vacuum speed.

- *Surface Detectors*: With an array of particle detectors, the direction of the shower axis, and hence of the primary cosmic ray, is deduced from the relative arrival times of signals at a minimum of three non collinear detectors.

The shower disk is assumed to sweep across the array at the velocity of light and the relative arrival times are measured. As a first approximation, the extreme front of the disc is treated as if it was planar. The shower disk has a thickness that increases from a few nanoseconds close to the shower core up to several microseconds at distances beyond 1 km. Thus a large area detector is more likely to intercept a particle or photon arriving early in the shower front and so enhance the accuracy of directional reconstruction.

1.6.2 Energy estimation

- *Fluorescence Detectors*: If the track geometry is determined, the number of photons N_γ received by a photo-multiplier can be calculated. An important quantity for these measurements is the fluorescence yield Y_f , that is the

number of photons produced by a charged particles per unit of length crossed in air. Knowing the fluorescence yield Y_i^f at a certain depth in the atmosphere, and being X_i the slant depth in which the fluorescence light is emitted at the time t_i , the number of photons produced at the shower in the slant depth interval ΔX_i is

$$N_\gamma^f(X_i) = Y_i^f \omega_i \Delta X_i \quad (1.29)$$

where ω_i is the energy deposited per unit depth at slant depth X_i . From the number of photons it is then possible to infer something about the the primary energy. Further details will be provided in the next chapter.

- *Surface Detectors*: The estimation of the energy using a ground array can be done looking at the measured signals in surface detectors.

Once the size of the shower is reconstructed, we can use the Lateral Distribution Function (LDF), which describes the fall of the signal size with the distance from the shower core. In order to avoid large fluctuations, it was proposed to use the signal at a certain distance r_{opt} to classify the size and therefore the energy of the primary particle. This distance have to be chosen in order to minimize the fluctuations; it can change with different experimental setup, energy range and array spacing.

In addition, the attenuation caused by the zenith angle θ should be taken into account. In fact, an inclined shower traverses about twice the amount of atmosphere if compared to a vertical one, and this produces an important difference in the absorption of electromagnetic particles. So showers initiated by the same primary particle present increasing signal for decreasing zenith angles. The problem of this attenuation is solved normalizing the shower size to a particular zenith angle θ_{opt} . This correction is called **Constant Intensity Cut** (CIC) [40] and will be described in the next chapter. Finally it is possible to establish a relation between the primary energy and the size of the shower.

$$E = kS(r_{opt}, \theta_{opt})^\beta \quad (1.30)$$

where where $S(r_{opt}, \theta_{opt})$ is the signal evaluated at r_{opt} using the LDF parameterization and renormalized at θ_{opt} through the CIC technique, while k and β are parameters to be obtained with independent methods.

Further details will be provided in the next chapter.

1.6.3 Composition estimation

A measurement that could be crucial to solve the mystery behind UHECRs is their composition as a function of energy observed at Earth. For energy up to ~ 100 TeV the composition can be directly measured with space-based experiments. For higher energies, composition is derived from the observed development and particle content of the EAS.

- *Fluorescence detectors*: in this case, to estimate the mass of the shower-inducing primary particle, the depth of the shower maximum X_{\max} is used. In fact, the maximum number of particles in a shower is reached at a certain depth, which depends on mass and energy of the primary particle. The most used technique in the indirect measurement of primary mass composition is based on the “elongation rate theorem”, firstly proposed by Linsley in 1977 [41]. The elongation rate denotes the increase in atmospheric depth of maximum development that results from increased primary energy, as already written in equation 1.25. The slant depth position X_{\max} at which the maximum of the longitudinal shower profile occurs is one of the most sensitive observable to the composition.

In addition, also the width of the X_{\max} distribution in a narrow range of energies is another parameter sensitive to composition since heavy nuclei are expected to produce shower-to-shower fluctuations smaller than for protons.

The X_{\max} parameter is a very powerful observable for mass composition studies. In order to have independent measurements to cross-check the results, observables measured with surface detectors are also used for mass composition studies.

- *Surface detectors*: in this case the parameter used is the *Electron-to-muon number ratio*. After the interaction of a hadronic cosmic ray with a molecule in atmosphere, charged pion π^{\pm} can be created; the π can interact or decay according to the density of the atmosphere and the Lorentz factor of the π . Muons produced in the decay of pions lose energy via ionization processes and their number decreases less rapidly than the number of electrons, because for those bremsstrahlung and pair production processes are more important. For this reason, showers induced by heavy primaries generate more secondary particles and lead to an earlier attenuation of the electromagnetic component after the shower maximum. This reduces the average pion energy in the early stages of the cascade relative to a proton shower of the same energy and, as a result, the number of muons is larger and the number of electrons is smaller.

Another important parameter is the *arrival time distribution of particles*. The collection of particles in an air shower that first hits the ground at any location make up the front of an air shower. This front is curved since the particle production started at the point where the first interaction took place and particles in the shower travel at the speed of light. The first particle at ground is therefore the one for whom the path length of it and its parent particles is shortest between the first interaction point and a detector station at the ground. These are mainly muons that are the products of the earliest pion decays in the shower. The shape of the curved front is approximately spherical as it is made up out of the particles that travelled on the shortest path. The center of this sphere is the location where these particles have been produced and its distance from the impact point of the shower core at the surface of the Earth: the center of the sphere is corre-

lated to the location of the first interaction, and therefore to the primary mass.

Another approach consists in measuring the rise time of the signal at 1000 m from the shower axis. The time distribution of the signals recorded by the surface detector contains implicitly the information of the shower development, therefore timing parameters can be used as primary composition discriminator. This fact can be explained on the basis of the dominance in the different time regions of the signal of the electromagnetic and muonic component. Both approaches were studied and discussed in [42].

CHAPTER 2

The Pierre Auger Observatory

The Pierre Auger Observatory [1] is the largest cosmic rays observatory, first experiment capable of observing ultra-high energy cosmic rays with both an array of particle detectors at the ground and fluorescence telescopes. The Observatory is located in Argentina, in the province of Mendoza, in the so-called pampa amarilla, a large plateau at 1400 m above sea level. The height is crucial because the Earth atmosphere can be considered as a part of the detector itself. The optimal altitude was chosen to allow the observation of the average shower maximum above the ground at the energies of interest. A map of the observatory is shown in figure 2.1; in addition, in the city of Malargue there is the office building that is the center of operation, where the local permanent staff works. The building is equipped with an assembly hall and a laboratory where broken parts of the detectors can be repaired. It also houses for the Central Data Acquisition System (CDAS).

The two most important detectors in the Pierre Auger Observatory are the surface detector (SD) and the fluorescence detector (FD). The SD occupies an area of $\sim 3000 \text{ km}^2$, which is also observed by the FD, composed by four buildings with six telescopes each, as can be seen in the picture 2.1.

The hybrid design is a key feature of the Pierre Auger Observatory, since the two detection techniques allow to measure air showers in complementary ways, providing important cross-check and reducing the need of simulations.

2.1 The Surface Detector (SD)

The Surface Detector [47] of the Pierre Auger Observatory is composed of 1660 detectors, each spaced by 1500 m resulting in a total surface $\sim 3000 \text{ km}^2$. The SD samples the particle components of extensive air showers with a duty cycle of nearly 100%. It has fully efficiency in the detection of Extensive Air Showers (EAS) generated by primary with energy greater than $\sim 3 \cdot 10^{18} \text{ eV}$ [48]. Starting from 2008, part of the array was filled with more detectors in order to have a denser one, which is able to detect events down to $3 \cdot 10^{17} \text{ eV}$ [44]. The infill

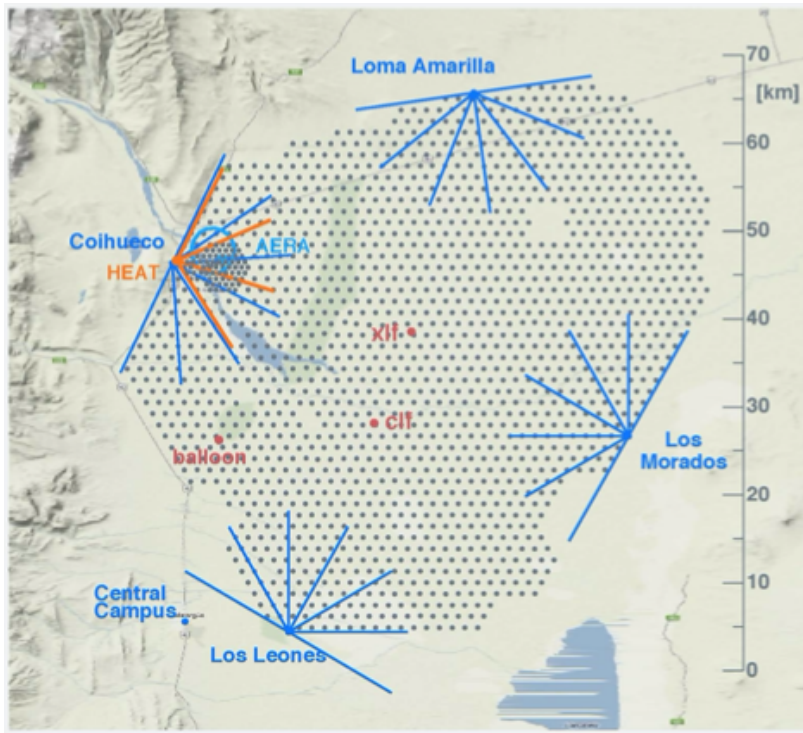


Figure 2.1: The Pierre Auger Observatory: dots represent stations of the surface detector while blue lines represent the fields of view of the fluorescence detector telescopes. Orange lines represent the field of view of the HEAT [43] telescopes. In front of them, the AMIGA detector [44] is visible as a denser array. The two red dots at the center of the array are the two laser facilities used to monitor the atmosphere [45]. The blue circle near Coihueco is the location of the AERA array of radio detectors [46].

detector and the Auger enhancements will be described later.

2.1.1 Cherenkov stations

Each detector is composed of a roughly cylindrical polyethylene tank filled with 1200 litres of ultra-pure water, which ensure an high level of transparency, overlooked by three PMTs. The water volume height is 1.2 m, chosen as a compromise between offering a large effective surface for horizontal showers (which is useful in particular for UHE neutrino search) and logistic necessities. Inside the polyethylene structure, the water is contained in a circular cylinder, called *liner*, made of a flexible plastic material conforming approximately to the inside surface of the tank. The liner prevents water from contamination and loss, it provides a barrier against any light that enters the closed tank; in addition, it diffusely reflects the light that is produced in the water. The liner is composed by many layers, the innermost one being made of *Tyvek*, a peculiar material which is excellent for the reflection of the Cherenkov light in the near ultraviolet. Each part of the station was designed for a lifetime of 20 years. The purification of the water prevents the growth of micro-organisms that can affect the water transparency and therefore

the signal stability.

The light produced by particles in water is detected by three PMTs looking downward in the water; they are positioned at 1.2 m from the tank center axis in an equilateral triangle pattern. The signals, coming from the dynode and the anode are read using front-end electronics by Fast Analog to Digital Converters (FADCs). The digitized signals are sent to a programmable logic board, which is used to implement the various triggering decisions. The time at which a local station triggers is crucial for the reconstruction of the events: it is measured using a commercial Motorola GPS board with a precision of ~ 8 ns . Each station is powered by two 12 V batteries that are recharged by two solar panels. For this reason the electronics was designed in order to have a low power consumption (less than 10 W). The Cherenkov light recorded by a tank is measured in units of the signal produced by a muon traversing the tank on a vertical trajectory, a unit called *Vertical Equivalent Muon* (VEM).

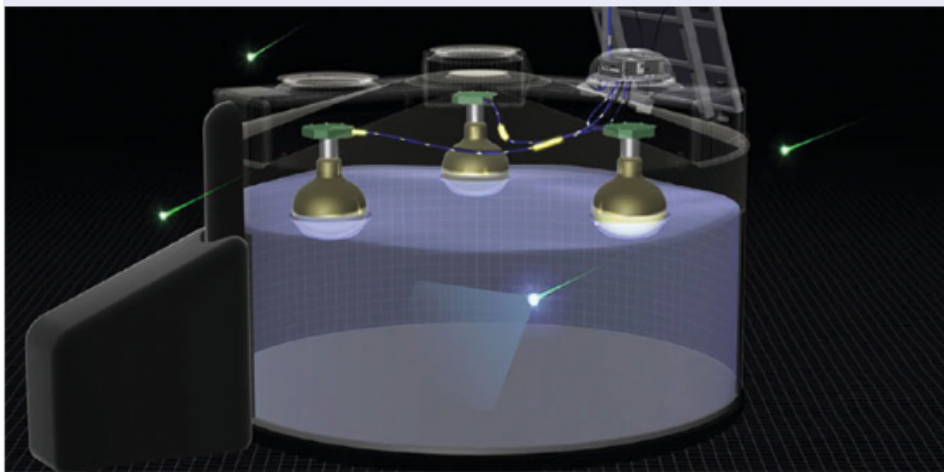


Figure 2.2: Schematic view of a tank [49].

2.1.2 Data communication and maintenance

The data communication system of the Pierre Auger Observatory consists of two radio networks. The first one, operating in the microwave band, is a high capacity network and it provided communication from the FD sites to the central campus. It also re-transmits data that are sent to and from the FD sites by individual SD stations via the second network, a wireless Local Area Network (LAN). All the data are transmitted to the Central Data Acquisition System (CDAS). The CDAS assembles the triggers from the surface array detectors, checks for SD-FD coincidences, called **hybrid** events and organizes the storage of data.

Concerning the maintenance of the SD station, this is performed regularly by the local staff. Each tank sends constantly diagnostic data, which are collected by a monitoring system. Thanks to this continuous monitoring and repairing, less than 1 % of the stations are inactive on average over the whole array.

2.1.3 The SD reconstruction

In the reconstruction of the events measured by the surface array the most important information are the integrated signals and the timing information from the detectors hit by the shower particles. In the previous chapter it was shown how to infer information about the shower geometry. In the subsection 1.5.1 we have already introduced an important energy estimator, called shower *size*.

First of all, it is necessary to select only the events in the stations corresponding to EAS events; for this purpose the physics triggers, based on the time correlation between adjacent detectors, guarantee the selection of good quality data for physics analysis.

The shower geometry is reconstructed by fitting the start times (t_i) of the signal of each detectors. For events with enough triggered stations, a concentric-spherical model can reproduce these times according to the following equation:

$$c(t_i - t_0) = |\vec{x}_{sh} - \vec{x}_i| \quad (2.1)$$

where t_0 and \vec{x}_{sh} identify a virtual origin (in space and time) of the shower development, while t_i and \vec{x}_i are the position and trigger time of each tank.

An important quantity which has to be determined is the shower core, thanks to a fit of the Lateral Distribution Function (LDF) of the signals measured by each station $S(r)$ involved in the event. A modified Nishimura-Kamata-Greisen function is employed:

$$S(r) = S(r_{\text{opt}}) \left(\frac{r}{r_{\text{opt}}} \right)^\beta \left(\frac{r + r_1}{r_{\text{opt}} + r_1} \right)^{\beta + \gamma} \quad (2.2)$$

where $r_1 = 700$ m, β and γ are slope parameters functions of the zenith angle, r_{opt} is the optimal distance at which the shower-to-shower fluctuation are minimal and $S(r_{\text{opt}})$ the corresponding signal. For the surface detector of the Pierre Auger Observatory, the optimum distance was estimated to be $r_{\text{opt}} = 1000$ m [50].

The main outcome of the LDF fit is the determination of the shower impact point at the ground (\vec{x}_{gr}) and of the shower size $S(1000)$. At this point the shower axis \hat{a} can be calculated using the virtual shower origin \vec{x}_{sh} (from equation 2.1) and \vec{x}_{gr} (from the LDF reconstruction):

$$\hat{a} = \frac{\vec{x}_{sh} - \vec{x}_{gr}}{|\vec{x}_{sh} - \vec{x}_{gr}|} \quad (2.3)$$

The angular resolution achieved reach less than 0.9° for events detected by more than six stations [51].

Finally, the value of $S(1000)$ is converted in an energy estimator. This is performed using the Constant Intensity Cut method (CIC) [52, 40] (already introduced in section 1.6.1), in the assumption of an isotropic flux of primaries at the top of the atmosphere. This method provides an attenuation curve $f_{\text{CIC}}(\theta)$, such that can be written as a third degree polynomial in $x = \cos^2\theta - \cos^2\bar{\theta}$, where $\bar{\theta} = 38^\circ$ is the median of the zenith distribution for the vertical events measured by the surface detector. The fitted function can be written as:

$$f_{\text{CIC}}(\theta) = 1 + ax + bx^2 + cx^3 \quad (2.4)$$

where $a = 0.952$, $b = -1.636$ and $c = -0.978$ (for the International Cosmic Rays Conference (ICRC) 2019 analysis [53]). Choosing $\bar{\theta} = 38^\circ$ as reference angle, the energy estimator can be written as:

$$S_{38} = \frac{S(1000)}{f_{\text{CIC}}(\theta)} \quad (2.5)$$

which can be considered as signal that a shower with certain size $S(1000)$ would have produced arriving with an inclination of 38° instead of θ , as shown in figure 2.3.

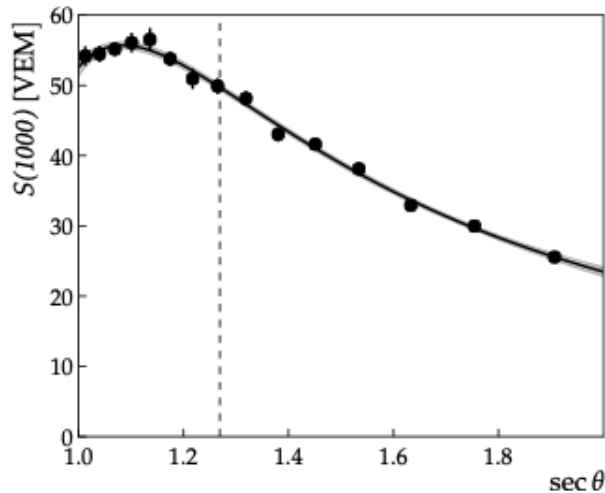


Figure 2.3: Signal attenuation with increasing zenith angle for showers of approximately equal energy, according with the CIC procedure. In particular, it is represented the signal evaluated at 1000 m from the core. The solid line is the function $f_{\text{CIC}}(\theta)$ used to fit the data Image from [54].

2.2 The fluorescence detector

The fluorescence detector is designed to detect extensive air showers in a complementary way with respect to the SD. The charged particles in the EAS excite atmospheric nitrogen molecules, causing them to emit fluorescence light in the 300-450 nm range. This light can be observed during clear and moonless nights and provides us information about the longitudinal development profile of the EAS. Because the observation periods are limited to dark nights with good weather, the FD duty cycle is $\sim 15\%$. The integral of the longitudinal development profile give the total energy dissipated electromagnetically. This energy accounts for $\sim 90\%$ of the primary cosmic ray, the remaining $\sim 10\%$ is the so-called “invisible energy”, carried away by neutrinos and high energy muons not depositing all their energy in atmosphere.

2.2.1 Fluorescence telescopes

The FD is composed by 27 telescopes distributed in four sites (Los Leones, Los Morados, Loma Amarilla, Coihueco) overlooking the surface array [55]. Each building hosts six independent telescopes with field of view of approximately $30^\circ \times 30^\circ$ in azimuth and elevation, providing a 180° coverage in azimuth. In addition there are three additional telescopes, named *High Elevation Auger Telescopes* (HEAT), which will be described in the next section.

Each telescope has a 3.6 m diameter mirror illuminating a camera composed of 440 PMTs, as can be seen in 2.4. Each PMT (or pixel) has a field of view of

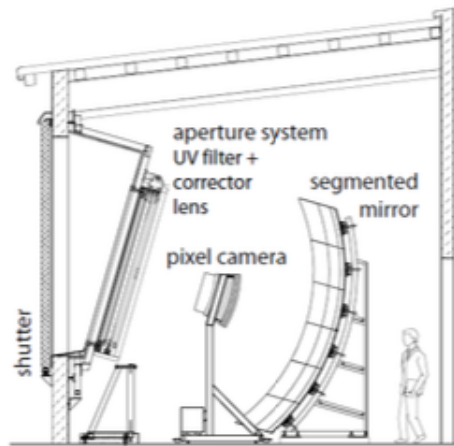


Figure 2.4: A schematic view of an FD telescope [55].

$1.5^\circ \times 1.5^\circ$. A UV-transmitting filter is installed at the aperture to improve the signal-to-noise ratio in the fluorescence emission band. Furthermore, corrector lenses are arranged in a ring around the aperture diaphragm in order to reduce optical aberration, as can be seen in figure 2.4.

The selection of candidate events is performed by a three-stage trigger system. The first level selects the PMT signal over a certain threshold value, that is adjusted in order to keep the trigger rate of each pixel around 100 Hz. At the second level, the trigger searches for track segments long at least $4/5$ pixels, shown in figure 2.5, resulting in a rate between 0.1 and 10 Hz.

The third level trigger is a more complicate software algorithm, design to reject noise events which appears to be uncorrelated in time or space. Once per year,

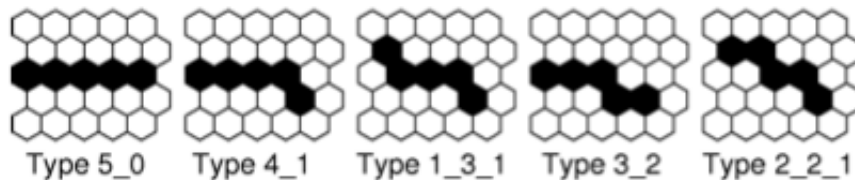


Figure 2.5: Fundamental patterns for the second level FD trigger [55].

an absolute calibration of the telescopes is performed with a uniform source posi-

tioned at the telescope aperture. This calibration ensures that the response of the PMTs is uniform. In addition to that, a relative calibration is done during each night of shift (data-taking), before and after each run, illuminating the camera with optical fibers. In this way also the long-term variations in the telescopes calibration can be monitored.

2.3 FD event reconstruction

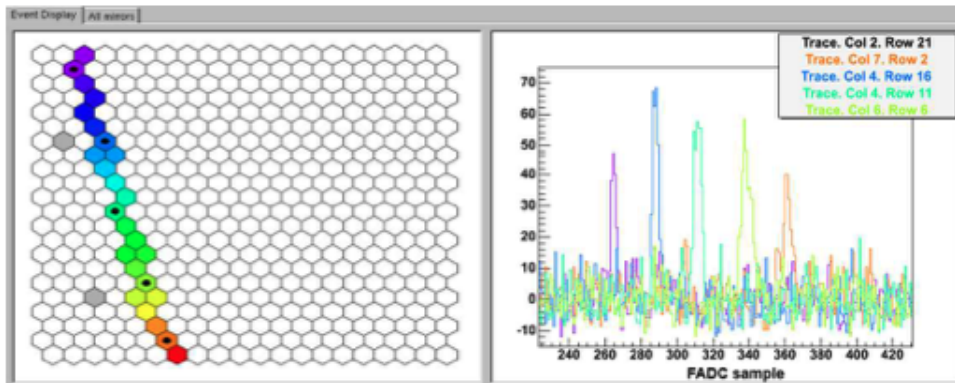


Figure 2.6: An example of FD trace. The color code indicates the timing of the trigger in each pixel (early=red, late=violet) [55].

When a signal is recorded in the FD, what we get is a trace such as in picture 2.6. The signal and timing of each pixel is recorded and used in the event reconstruction. It starts with the determination of the shower-detector plane, as already shown in the equation 1.28. This allows to know the geometry of the shower. The resolution of the geometry reconstruction can be improved if the same event is seen by two or more FD stations (so-called stereo, triple or quadruple event). Therefore, the light collected as a function of time can be converted to energy deposit as a function of slant depth. The calorimetric energy E_{FD} of a shower is estimated by fitting the Gaisser-Hillas function [40] to the reconstructed energy deposit profile and by integrating it.

$$f_{\text{GH}} = \left(\frac{dE}{dX} \right)_{\text{max}} \left(\frac{X - X_0}{X_{\text{max}} - X_0} \right)^{(X_{\text{max}} - X_0)/\lambda} \exp\left(\frac{X_{\text{max}} - X_0}{\lambda} \right) \quad (2.6)$$

An example of fit is shown in figure 2.7. A correction for the invisible energy has been estimated from hybrid data and is of the order of 10-15 %. The systematic uncertainty on the energy estimation is $\sim 14\%$ [54]. The main contributions are the uncertainties on the fluorescence yield estimate (3.6 %), on the absolute calibration of the fluorescence telescopes ($\sim 9\%$), on the reconstruction method ($\sim 6.5\%$) and on the atmospheric monitoring (6.2%). From the fit of equation 2.6 also the most important mass-sensitive parameter, named the depth of the shower maximum (X_{max}) can be extracted.

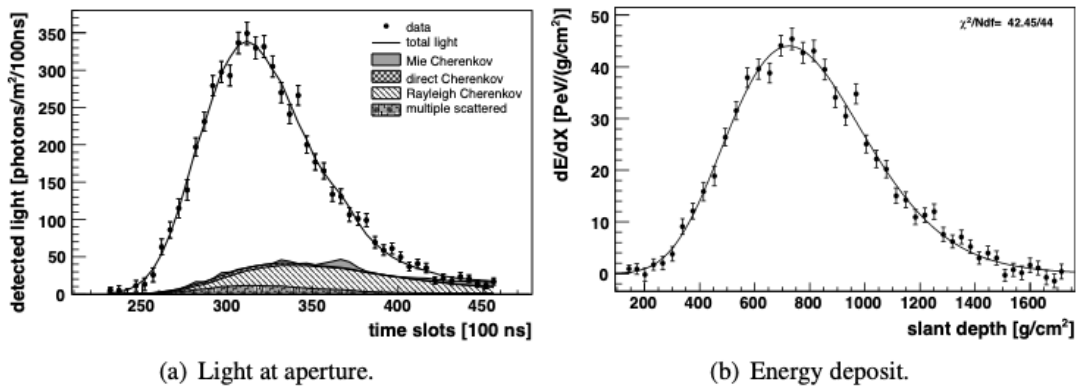


Figure 2.7: Left panel: the light collected at the aperture as a function of time, where the different light contributions are shown. Right panel: the energy deposit as a function of the atmospheric depth; the line is the resulting Gaisser-Hillas fitting function. Images from [54].

2.3.1 Atmospheric monitoring

An accurate reconstruction of the longitudinal profile with FD requires continuous monitoring of the atmosphere conditions. For this purpose, an ensemble of instrument was designed and deployed to monitoring the atmosphere at the Observatory [45]. The monitoring of the attenuation of the light due to aerosol scattering uses two lasers placed near the center of the array, called Central Laser Facility (CLF) and eXtreme Laser Facility (XLF). In total, four elastic scattering lidar stations and two optical telescope, that determine the wavelength dependence of the aerosol attenuation, have been used, together with four infra-red cameras for cloud detection.

The aerosol content of atmosphere during data taking is continuously monitored. For this purpose, the vertical aerosol optical depth (VAOD) is measured each hour using laser shots by CLF and XLF and cross-checked by lidars operated at each FD site.

2.3.2 SD energy calibration

The estimation of the primary energy for events recorded by an array of ground detectors requires the comparison with an independent measurement. In fact, the energy scale can be determined only through a calibration of the energy estimator.

The advantage of the Pierre Auger Observatory is the possibility of **hybrid detection**, so the same shower is seen independently by both the SD and the FD. In the particular case of event separately reconstructed with both procedures, the energy estimator for the SD S_{38} can be therefore compared with the almost-calorimetric E_{FD} value from the FD reconstruction.

The SD energy calibration is performed using a sub-set of the hybrid events,

called **golden** hybrid dataset. These are selected according with several quality cuts. The final step consists on a fit on this relation, which seems to be well described by a power-law function:

$$E_{\text{FD}} = A \left(\frac{S_{38}}{\text{VEM}} \right)^B \quad (2.7)$$

where A and B are free parameters of the fit. In figure 2.8 it is possible to see the calibration curves for different datasets. From ICRC 2019 results $A = (1.86 \pm 0.03) \cdot 10^{17}$ eV and $B = 1.031 \pm 0.04$ [56].

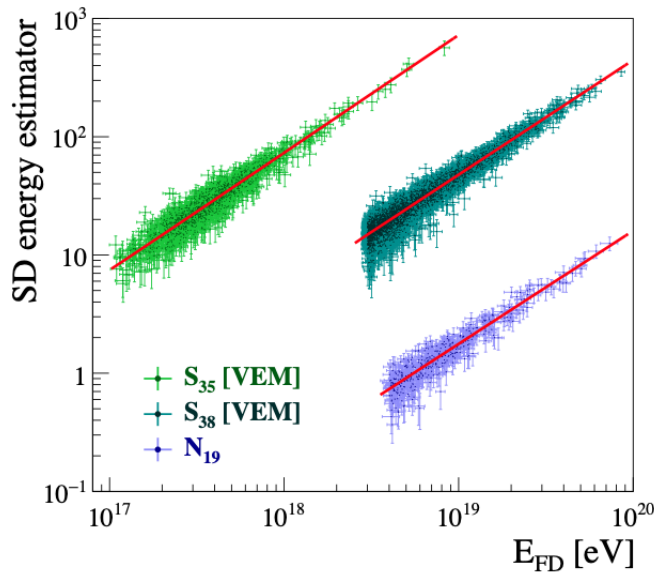


Figure 2.8: Correlation between SD energy estimators and the FD energy values. Each point represents a single event. S_{38} is the estimator for the SD-1500 vertical dataset, while S_{35} is a similar estimator employed for the events measured by the infill array (750 m spacing). Instead, the N_{19} estimator is used for the calibration of inclined events. Image from [56].

2.4 Auger enhancements

2.4.1 Low-energy extension

The main target of the Pierre Auger Observatory is to detect cosmic rays in the EeV region and above. Nonetheless, the energy range between 10^{17} and few 10^{18} eV is very important to understand the origin of cosmic rays and in particular the transition energy between galactic and extra-galactic cosmic rays, which is expected to take place in this energy range. In order to explore it, two low-energy enhancements were deployed: HEAT and AMIGA.

HEAT

HEAT (High Elevation Auger Telescope) [43] is a FD enhancement for low energy study. It is composed by three additional telescopes placed at the Coihueco FD site. Their peculiarity is that they can look at the atmosphere from 0° to 30° as standard FD, but in addition they can also tilt upwards. The main target of this enhancement is to lower the energy threshold for the shower detection. In fact, in the upward tilted mode, HEAT can observe events down to 10^{17} eV, that develop higher in the atmosphere. An accurate hybrid reconstruction can be accomplished in combination with the infill, a denser array with 750 m spacing nested within the standard SD one in an area inside the field of view of the HEAT telescopes.

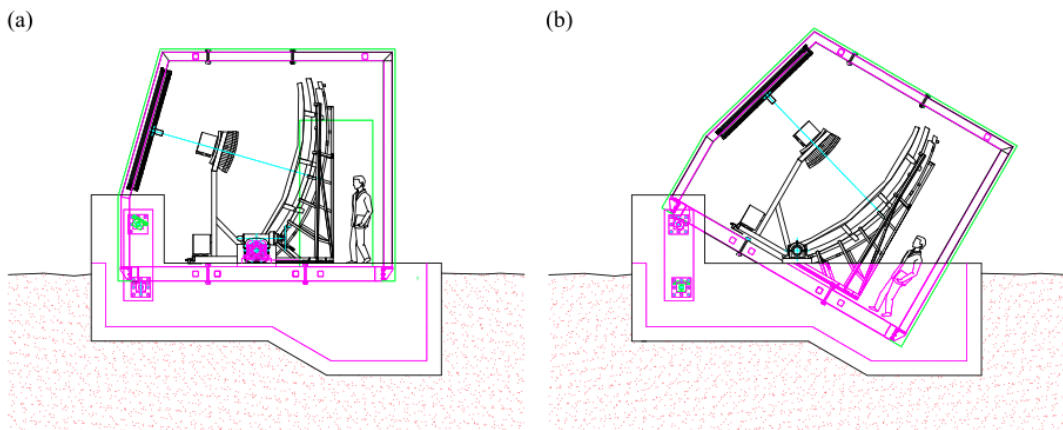


Figure 2.9: Schematic view of HEAT telescope: horizontal (a) for cross-calibration, tilted (b) mode for data taking. From [1].

AMIGA

AMIGA (Auger Muons and Infill for the Ground Array) is the SD enhancement for low energy studies [44]. Inside it, two different parts can be distinguished: the first part is a denser sub-array of the SD built adding 60 stations near the Coihueco eye (see figure 2.1). This infill array has a spacing of 750 m (half of the standard) and an area of 23.5 km^2 . This denser array is able to detect events above $3 \cdot 10^{17}$ eV. The reconstruction of the infill events is similar to the 1500 m array with small differences in the trigger implementation and the energy estimator.

In addition, the AMIGA enhancement will include also muon detectors, consisting of 30 m^2 plastic scintillators buried at a depth of 2.3 m aside the SD station. The aim is to measure GeV muons to extract relevant information on the mass composition of cosmic rays.

2.4.2 Radio and Microwave detection

In the last years, another detection technique was improved, in order to provide complementary information to FD and SD, namely the *Radio detection*. It was known that an extensive air shower, travelling through the atmosphere, induces radio and microwave emission.

The primary process producing radio emission is the geomagnetic mechanism, or current excess, described by Kahn and Lerche [57]. The local geomagnetic field accelerates electrons and positrons in the shower front in opposite directions; this leads to a net drift of the electrons and positrons, which can be interpreted as a current. This current varies with the amount of charge present in the air shower and increases until the shower reaches its shower maximum and starts to decrease from there. This effect is either being referred as the *geomagnetic effect* or *time varying transverse currents*. A secondary effect is called *Askarian mechanism* or *charge excess mechanism* [58]. A schematic view of the two physical processes is provided in figure 2.10. As the shower develops in air, electrons are dragged from molecules in air along with all the shower particles leaving positively charged ions behind. This results in a charge separation along the shower axis. During the shower development, the number of particles first increases and afterwards decreases and both effects can be seen as a changing dipole moment. The radiation emitted by the dipole is coherent as long as the wavelength is larger than the thickness of the shower front. The polarization of the radiation is determined by the dipole moment and is parallel to the shower axis.

The potential of detecting in such way the EAS is high since this could allow

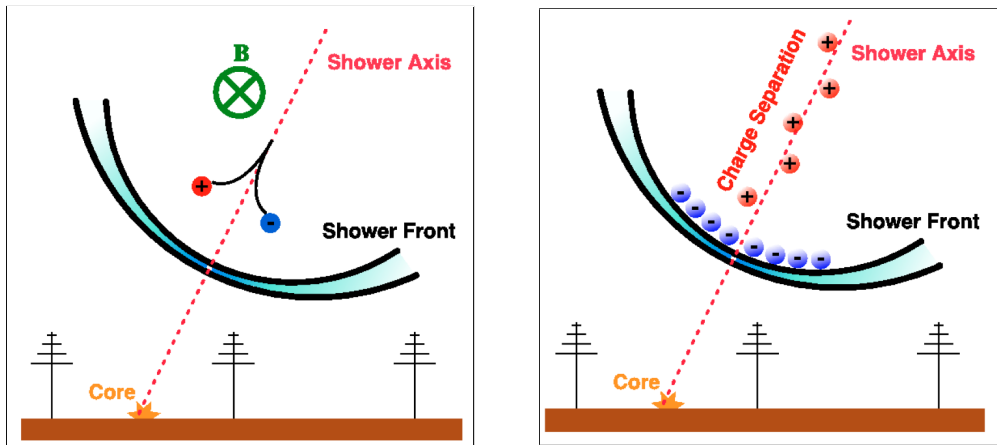


Figure 2.10: Schematic view of the two physical processes responsible for radio emission: geomagnetic effect (left) and Askarian (or charge-excess) mechanism (right). Picture from [59].

the study of the shower longitudinal profile as a fluorescence detector does, but with $\sim 100\%$ duty cycle as surface array.

At this point we can focus on the radio detectors deployed in the Pierre Auger Observatory.

AERA

AERA (Auger Engineering Radio Array) is an array of 153 radio antennas, sensitive in the MHz domain, deployed close to Coihueco eye [46]. It combined different hardware, electronics, triggers and even spacing between the antennas. The advantages of using AERA consist in $\sim 100\%$ duty cycle and negligible attenuation, since the atmosphere is transparent to radio waves. The main disadvantage concerns the high level of background, both natural and anthropogenic.

Microwaves

Cosmic ray detection in the GHz band is being pursued at the Pierre Auger Observatory with two different approaches. **MIDAS** (Microwave Detector of Air Showers) and **AMBER** (Air shower Microwave Bremsstrahlung Experimental Radiometer) are composed by imaging parabolic dish detectors, while **EASIER** (Extensive Air Shower Identification with Electronic Radiometer) is composed of radio receivers installed on the SD detectors. EASIER was able to perform the first detection ever of an air shower in microwaves in 2011 [60].

2.5 Auger Prime

In order to answer to the open questions in the UHECR field, recently an upgrade of the observatory is undergoing, called *AugerPrime* [61, 62]. The most important goal of the upgrade is to improve the mass composition measurements for primary energies above 10^{19} eV. Unfortunately, it is not possible to perform this measurements using fluorescence detectors due to its limited duty cycle ($\sim 15\%$). In order to measure the mass composition using the SD, a new detector will be added at each station. This is called Surface Scintillator Detector (SSD) and it is installed on the top of each SD, as shown in figure 2.11.

The great advantage of using two detectors looking at the same events consist in the different responses: a thin scintillation detector and a water-Cherenkov tank present very different responses to the shower particles. In particular, the comparison between simultaneous measurements could allow to disentangle the muonic and electromagnetic components of the signal, providing a direct information about the mass of the primary particle, as shown in subsection 1.6.3. Therefore the possibility of new studies of the mass composition at the highest energies are foreseen.

In addition of the SSD, the SD has been upgraded with a faster electronics and with an additional PMT, called *small photomultiplier* (SPMT). The small PMT is designed [63] to extend the dynamic range from 600 to 30,000 VEM, trying to fix the problem of the saturation of the signal near the shower core. In fact, more than 40 % of events with energies above $3 \cdot 10^{19}$ eV present at least one saturated station. With the new configuration is expected to deliver less than 2% of the saturated events.

Furthermore, Radio antennas on top of each SD stations are being deployed. The Observatory upgrade also includes the finalization of AMIGA. In fact, an

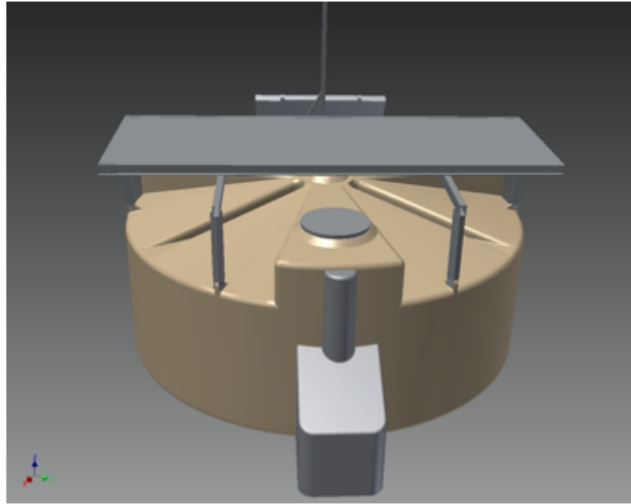


Figure 2.11: 3-D view of a Water Cherenkov Detector with a SSD unit. From [62].

underground Muon Detector is necessary to provide direct measurements of the shower muon content.

2.6 Highlights from Pierre Auger Observatory

A review of the most relevant results presented by the Pierre Auger Observatory is shown in the following; in particular, the key results to unravel UHECR open questions are energy spectrum measurements, mass composition studies and arrival direction analyses.

2.6.1 Energy Spectrum

The precise measurement of the flux of ultra-high-energy cosmic rays has been one of the main motivation for building the Pierre Auger Observatory. In fact, the measurement from two previous experiments, AGASA and HiRes, led to controversial conclusions on the presence of a suppression at the highest energies. Auger data at energy greater than $10^{16.6}$ eV have achieved an unprecedented precision. Several independent datasets have been presented, as shown in left panel of figure 2.12. The four spectra, in agreement within uncertainties, are combined into a global one, called *combined* spectrum. The Pierre Auger collaboration have shown an updated combined spectrum for the ICRC in 2019 (right panel of figure 2.12) [53], presenting an exposure of $80.000 \text{ km}^2 \text{ sr yr}$. The features are found fitting the combined spectrum with a model which takes into account the change of spectral index and the smoothing.

I want also to cite the latest energy spectrum result published by the Pierre Auger Observatory [64, 65] and shown in figure 2.13 concerning the vertical

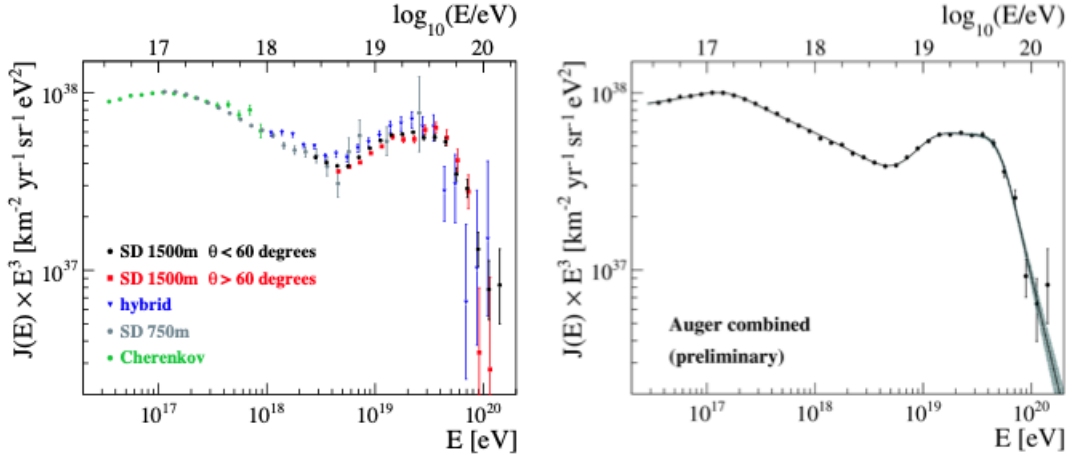


Figure 2.12: On the left, four different spectra coming from SD or hybrid data. On the right, the combined spectrum. Image from [53].

dataset. Because the spectrum behaviour can be approximated to a power law $J(E) \propto E^{-3}$, the measured flux is multiplied by a factor E^3 (right panel of figure 2.13), in order to put in evidence the observed features. Beyond any doubt,

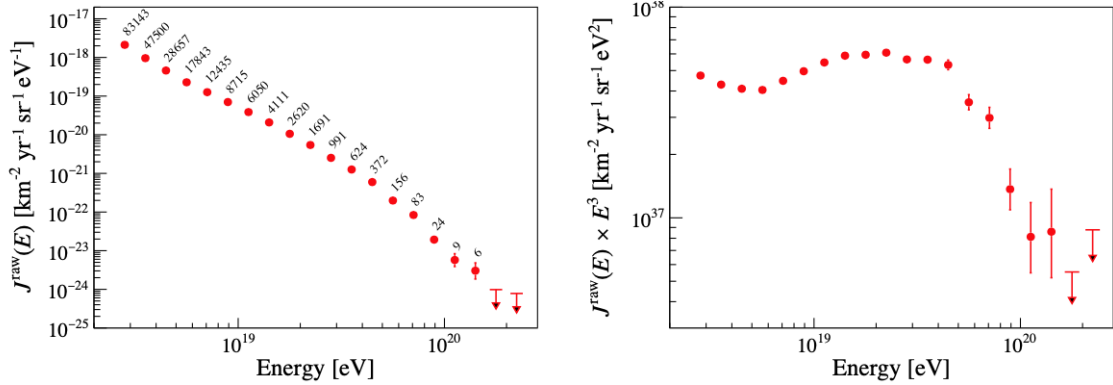


Figure 2.13: Left: Vertical spectrum measured by the Pierre Auger Observatory. Right: Vertical spectrum multiplied by E^3 . Image from [65].

two spectral features are confirmed: the hardening of the spectrum at about 5×10^{18} eV (ankle) and a strong suppression at 4×10^{19} eV. In addition to that, a new features at $E = 1.4 \cdot 10^{19}$ eV is a new observation and can be addressed to astrophysical processes [64].

2.6.2 Mass composition studies

The most accessible and reliable mass-related variable that can be observed at the Pierre Auger Observatory is the depth of shower maximum (X_{\max}) through the FD telescopes. This is related to the logarithm of the primary mass, as it was described in equation 1.26. Due to fluctuations of the properties of the first few hadronic interactions in the cascade, the primary mass cannot be measured on an event-by-event basis but must be inferred statistically from the distribution of shower maxima of an ensemble of air showers. The recent results presented at the last ICRC [66] represent the mean and the standard deviation of the X_{\max} distribution, as shown in figure 2.14. Among the X_{\max} measurements, two datasets can be distinguished. One is composed by hybrid events above $10^{17.8}$ eV collected by standard FD telescopes. Few years ago the measurements have been extended down to $10^{17.2}$ eV using data collected by HEAT in coincidence with Coihueco telescopes: for this reason this addition dataset is called *HeCo*. Considering the mean of the distributions (left panel of figure 2.14) two different trends can be observed: data from heavy to light mass composition are observed up to $10^{18.3}$ eV, while a second trend at higher energies suggests a transition to intermediate-heavy masses.

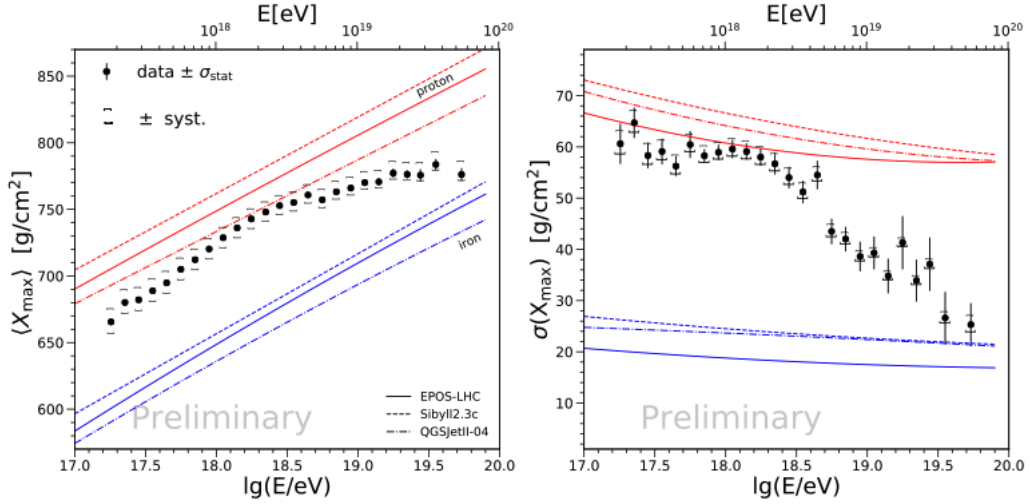


Figure 2.14: Measurements of $\langle X_{\max} \rangle$ (left) and $\sigma(X_{\max})$ (right) at the Pierre Auger Observatory compared to the predictions for proton and iron nuclei of the hadronic models EPOS-LHC, Sibyll 2.3c and QGSJetII-04. Image from [66].

Taking into account the X_{\max} mean and standard deviation of the distributions is useful and can give an overall view of the mass as a function of energy. Nonetheless, studying directly the X_{\max} distributions provides more information and reduces the degeneracy, because different mass composition can generate X_{\max} distributions with the same mean and the same standard deviation. For this reason it was chosen in this work to study the X_{\max} distributions and not only their means and standard deviations.

2.6.3 Anisotropies

To understand the origin of UHECRs, the study of the distribution of their arrival directions has always been of capital importance, despite the difficulties that arise from the deflection they suffer due to magnetic fields. In particular, the highest-energy region, above a few tens of EeV, which extends beyond the observed flux suppression, is of particular interest because of the high rigidities. The Pierre Auger Observatory has found a significant dipolar large-scale anisotropy in the arrival direction for cosmic rays above 8 EeV [67, 68]. The extra-galactic origin of UHECRs was claim due to the measurements of a total dipolar amplitude of $d = 0.066 \pm 0.012$ pointing to 125° away from the direction of the Galaxy center.

An important step forward is a model-independent blind search for overdensities over the whole field of view [69]. The map of the local significance for $E > 38$ EeV over the whole sky is shown in figure 2.15. In this analysis, the Pierre Auger Collaboration has found a significant excess of events in a 27° window centered in the direction of *Centaurus A* (*Cen A*) with a significance $\sigma \simeq 4$.

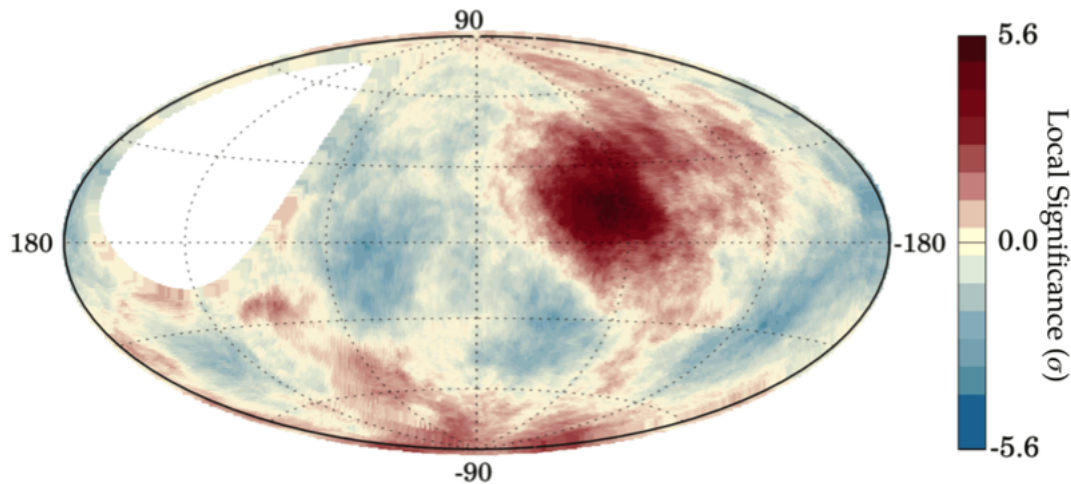


Figure 2.15: Sky map in Galactic coordinates showing the cosmic ray flux for $E > 38$ EeV; it shows the local significance of overdensities in an angular window of 27 degrees (red spot). The Galactic center is at the origin. Image from [69].

The analysis is extended taking into account catalogs of different source candidates.

- **2RMS** catalog, taking out sources closer than 1 Mpc [70].
- **Swift-BAT AGNs**, which includes both radio loud and quiet AGNs [71].
- $\gamma - AGN$ [72].
- **Starburst galaxies** [73, 74].

Each object in every catalog is weighted based on its relative flux, measured in an appropriate band different for each catalog, and on its distance. The attenuation is computed based on the composition scenario at sources that best reproduces the average composition and spectrum measured at the Auger Observatory. An isotropic fraction of events was added to the probability maps obtained this way in order to model the diffuse component of UHECRs due to highly deflected events and faint sources not included in the catalogs.

The statistics tests are shown in figure 2.16, left for starburst and γ -AGN and right for Swift-BAT and 2MRS. It is possible to see that the maximum likelihood-ratio is found with starburst galaxies, for which the fit parameters provide a correlation of 4.5σ . This result makes starburst galaxies interesting objects to study if we want to provide an astrophysical interpretation to the Auger data.

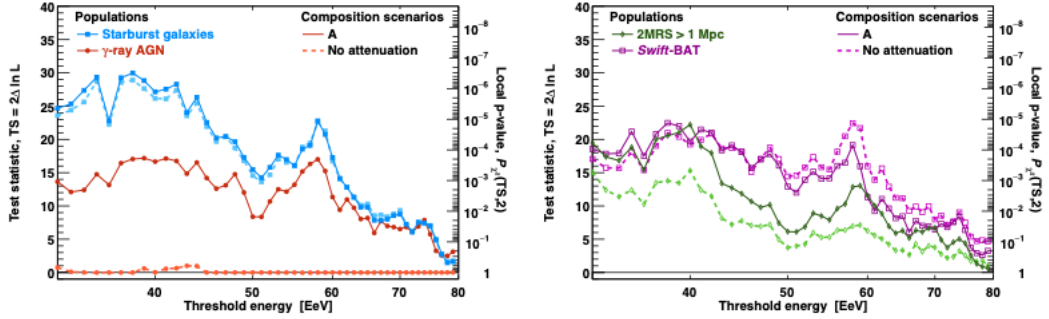


Figure 2.16: Maximum likelihood-ratio as a function of energy threshold for the models based on starburst galaxies and γ -AGN (left) and Swift-BAT and 2MRS (right). The dashed lines are the same obtained in the no-attenuation scenario. From [69].

CHAPTER 3

Combined fit of energy spectrum and composition of the Pierre Auger Observatory, at energies above the “ankle”

3.1 Scientific motivation

The observed energy spectrum of cosmic rays has an approximate power-law behavior over several orders of magnitude in energy with several features that can be linked with particle propagation and acceleration. This power-law behavior is most probably indicative of a power-law acceleration spectra, while spectral features may be assigned to changes in the origin of particles, their propagation and acceleration.

In the energy spectrum measured by Auger, in the energy region of interest of this work, some features can be recognized: a hardening of the spectrum at the energy of $\simeq 5$ EeV, called the **ankle**, and a softening of the spectrum with a suppression of the flux at $\simeq 40$ EeV ¹ (see figure 3.1).

The interpretation of the ankle is still under debate. A dedicated picture explaining this feature was already put forward by Linsley [77], affirming that the ankle may be the spectral feature marking the transition between galactic and extra-galactic cosmic rays. The reason for supporting this hypothesis was the following: since the strength of the magnetic field is of the order of microgauss, galactic cosmic rays might be confined in the galactic disk up to energies of $Z \cdot 10^{17}$ eV, with Z the charge of the particles. Once particles are not confined anymore, which should happen at an energy which depends on the charge Z , the time they spent in the disk tends to the constant free escape time due to the direct escape from the Galaxy. If cosmic rays up to the highest energies were produced by the same sources in the Galaxy responsible for the bulk of low-energy cosmic rays, the energy spectrum of each mass group element should thus show a prominent

¹In literature, this feature was initially called the *cutoff*, referring explicitly to the GZK model [75, 76]. Following the latest results of the UHECR mass composition provided by the Auger collaboration, this term loses its meaning because mass composition is dominated by nuclei at these energies and further it might be related to a limit in the acceleration at the sources rather than propagation effects.

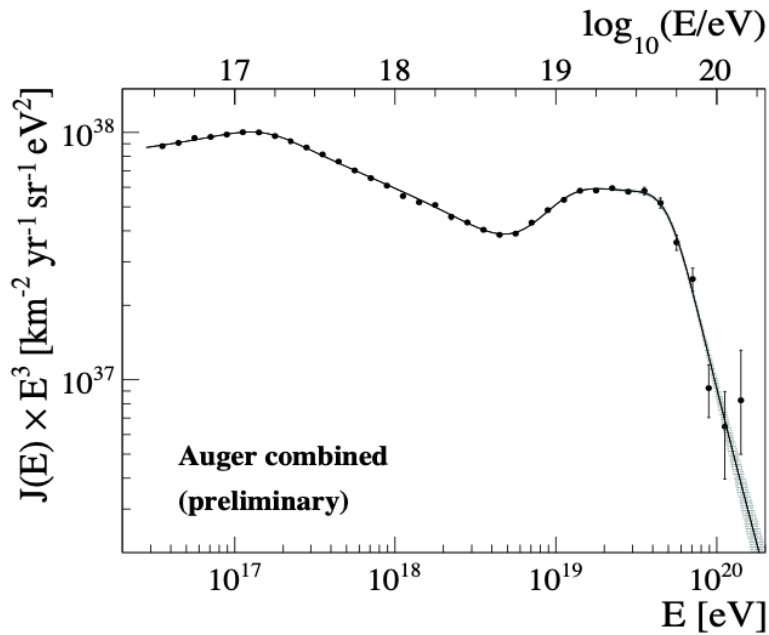


Figure 3.1: Combined energy spectrum presented at the last International Cosmic Rays Conference (ICRC) in 2019 [53].

hardening around each charge-dependent energy at which the free escape starts.

Also, for energies at which particles escape freely from the Galaxy, the observed intensity should be naturally much stronger towards the disk compared to other directions. Due to their high level of isotropy, cosmic rays in excess of $\simeq 10^{18}$ eV have previously been thought to be of extra-galactic origin [78]. Because a hardening in the energy spectrum is a natural feature expected from the intersection of a steep component with a flatter one, the ankle was widely considered as the onset in the energy spectrum marking the transition between galactic and extra-galactic cosmic rays. This model has several issues: as a first point, it is not clear how it is possible to accelerate particles in our Galaxy above energies of 10^{17} eV [79]. Another problem of this model is the contradiction with the Auger X_{\max} measurement in the energy range (1 - 4) EeV. In fact, the data would admit proton or light nuclei composition around the ankle energy [80], while the ankle model predicts a combination of a heavy galactic component (due to rigidity dependent acceleration) and the emerging lighter extra-galactic component. Such a model is shown with continuous lines in figure 3.2. As observed [81], this model is not in agreement with the experimental data. One may conclude that this model is excluded or very strongly disfavoured.

The dip model

A change of slope at energies around $10^{18.7}$ eV would naturally appear in the spectrum of extra-galactic proton Cosmic Rays (CRs) due to the combination of the energy losses due to the expansion of the Universe and pair production processes due to interactions with CMB photons, the so-called **dip-model**, the-

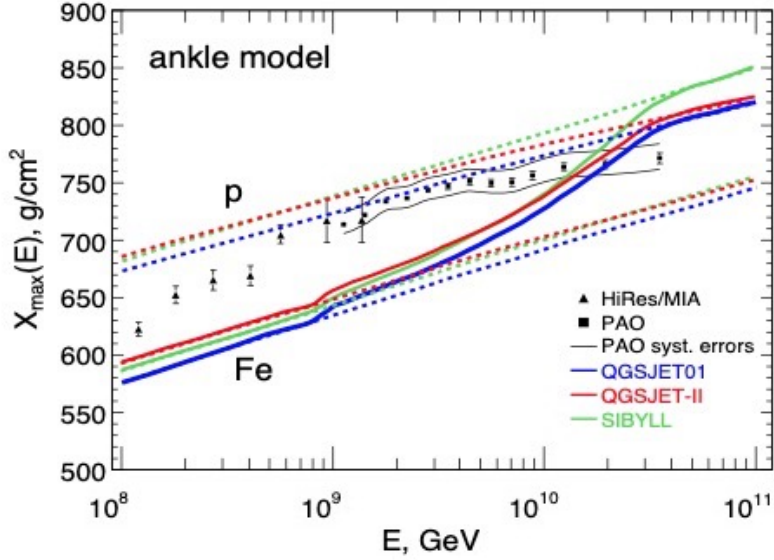


Figure 3.2: X_{\max} prediction for transition model (coloured solid lines for different hadronic interaction models) compare to the Auger dataset. The lines “p” and “Fe” present the elongation curves for proton and Iron which are used for calculations of the model elongation curves. Image from [81]. Readapted from [82].

orized by Berezhinski et al. [83]. In the hypothesis of pure proton composition at the highest energies, two main features are predicted by the model: the proton spectrum must show a steepening which begins at $E_{\text{GZK}} \sim 50 \text{ EeV}$. This is the famous Greisen, Zatsepin and Kuzmin cutoff, referred to as **GZK** [75, 76], caused by energy losses from photopion-production in collisions of protons with the CMB photons:

$$p + \gamma_{\text{CMB}} \longrightarrow N + \pi \quad (3.1)$$

In addition, a feature at energies near the ankle region is foreseen in this model, called the **dip**. The dip is a feature in the spectrum of protons in the energy range $1 \cdot 10^{18} - 4 \cdot 10^{19} \text{ eV}$, which, as in case of the GZK cutoff, can be directly linked to the interaction of CRs with the Cosmic Microwave Background (CMB), as outlined in sec 1.4.2. The dip arises due to electron-positron production energy loss by extra-galactic protons interacting with the CMB photons:

$$p + \gamma_{\text{CMB}} \longrightarrow p + e^+ + e^- \quad (3.2)$$

Note that in the case of a pure proton composition, the only relevant astrophysical background is the CMB due to its higher density with respect to the EBL (see figure 1.5). This fact makes the propagation of Ultra-High-Energy (UHE) protons free from uncertainties related to the background, being that the CMB is exactly known as a pure black body spectrum that evolves with redshift through its temperature.

In order to isolate the effects of energy losses in the propagated proton spectrum, it is useful to use the so-called modification factor $\eta(E)$ defined as the ratio:

$$\eta(E) = \frac{J_p(E)}{J_{\text{unm}}(E)} \quad (3.3)$$

where $J_p(E)$ is the proton spectrum, computed with all energy losses taken into account, and $J_{\text{unm}}(E)$ is the unmodified spectrum computed taking into account only adiabatic energy losses due to the expansion of the Universe. Assuming an

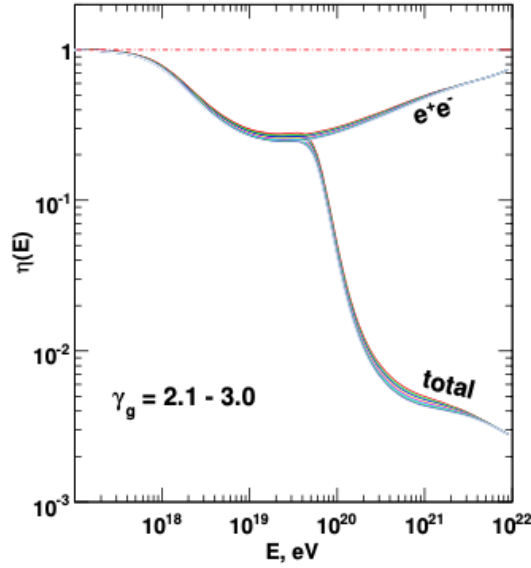


Figure 3.3: Theoretical modification factor computed for different values of the injection power law index as labeled [83].

injection spectrum at the source with a power law form $\propto E^{-\gamma_g}$, the modification factor $\eta(E)$ is computed and plotted for different values of the injection power law γ_g as labeled in figure 3.3. From figure 3.3, it is evident that $\eta(E)$ shows the signatures of energy losses suffered by protons, being almost independent of the injection. At low energy, losses are dominated by the adiabatic expansion of the Universe, the spectrum at Earth keeps the injection shape, and the modification factor is therefore $\eta(E) = 1$. Taking into account only the pair production process (relevant above the pair production threshold $\sim 2 \cdot 10^{18}$ eV), the propagated spectrum hardens. Above the photo-pion threshold ($\sim 5 \cdot 10^{19}$ eV) the propagated spectrum steepens in correspondence with the GZK feature (curves labeled with *total* take into account all relevant energy losses).

Remarkably, the dip model explains the observed flux with only one extragalactic component of pure protons, directly linking the flux behaviour to energy losses. The characteristic energy of the pair-production dip is rigidly fixed by interaction with CMB and it was proposed in [83] to be used as energy calibrator for different detectors, as can be seen in figure 3.4.

Hence, in the case of the dip model, the transition between galactic and extragalactic cosmic rays should occur at energies below the pair-production threshold,

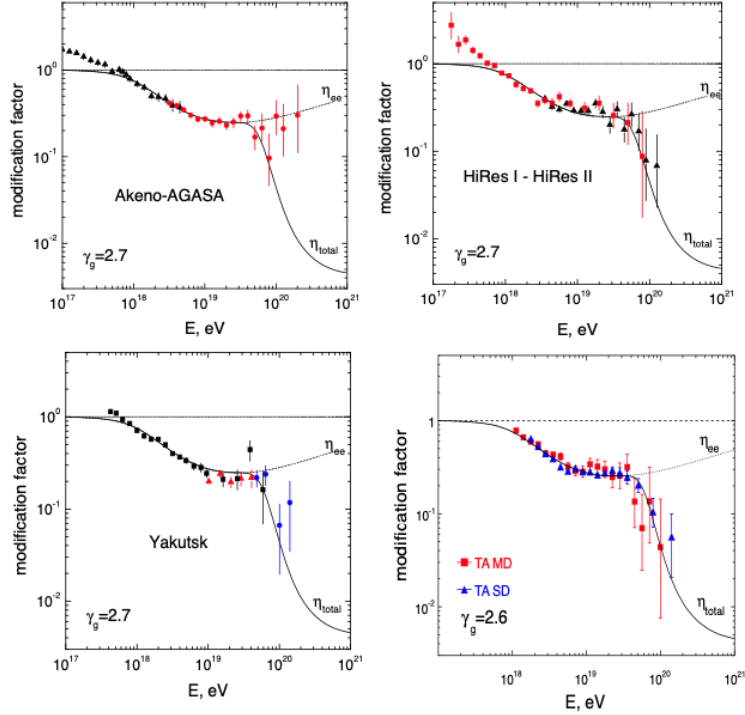


Figure 3.4: The predicted pair-production dip in comparison with Akeno-AGASA, HiRes, Yakutsk and Telescope Array data [10, 14]. All these experiments confirm the dip behavior with good accuracy [83].

i.e. $E_{\text{tr}} < 2 \cdot 10^{18}$ eV, in agreement with the diffusive shock acceleration.

The mixed composition model

An alternative explanation of the UHECR spectrum can be provided assuming that nuclei heavier than protons are accelerated. This is due to the fact that the Pierre Auger Observatory has measured a composition not compatible with protons (see figure 2.14) [66].

In this case, the propagation of UHE nuclei cannot explain the features in the UHECR spectrum, in particular the pair production for nuclei does not produce the ankle-like feature, as shown in figure 3.5. In addition to the pair production and photo-meson production processes, the photo-disintegration for nuclei, described in section 1.4.2, must also be included.

The photo-disintegration process occurs when a nucleus with atomic mass number A loses one or more nucleons through interaction with a photon. In the energy range we are interested in, the photon energy spectrum includes the CMB and the EBL:

$$A + \gamma_{\text{CMB,EBL}} \longrightarrow (A - nN) + nN \quad (3.4)$$

being n the number of nucleons lost by the nucleus. The photo-disintegration of nuclei leads to a steepening in the observed spectrum compared with the injected one. The suppression can be explained by the photo-disintegration of the

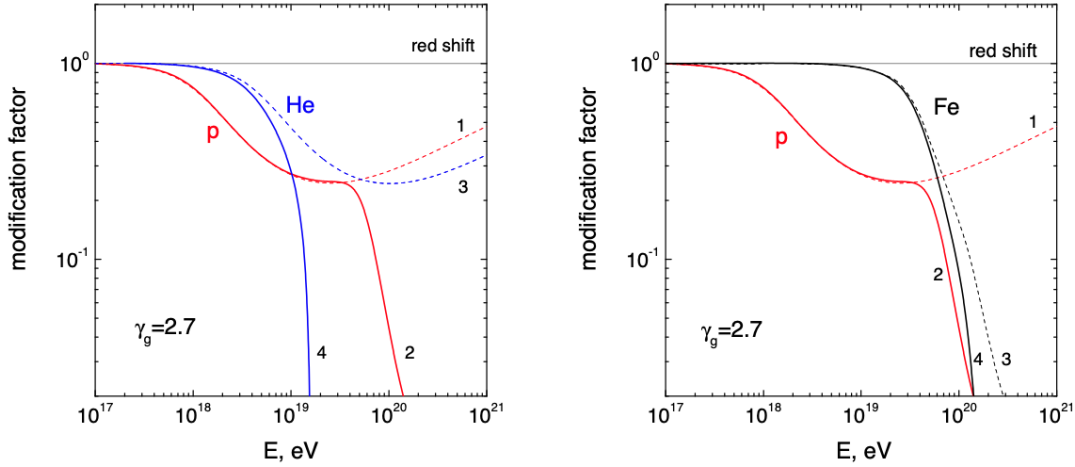


Figure 3.5: Modification factors for protons, helium and iron, as labelled. The dashed lines (1 and 3) refer to the spectra computed taking into account only adiabatic energy losses due to the expansion of the Universe, while the solid lines (2 and 4) refer to the spectra computed with all the energy losses taken into account. Plot from [29].

nuclei.

Considering nuclei, a rigidity-dependent acceleration mechanism is assumed: at the galactic energy scales, the mass composition becoming heavier with increasing energy appears as a natural consequence of the rigidity dependent scenario for particle acceleration. The maximum energy that a single species can be accelerated to is proportional to the particle charge: if E_{\max}^p is the maximum energy reached by protons, it is reasonable to expect for a nucleus with charge Z an $E_{\max}^Z = Z \cdot E_{\max}^p$ [18].

Under these assumptions, in Aloisio et al. [84], the spectrum and composition measurements are reproduced, as shown in figure 3.6, for energies $E \geq 5 \cdot 10^{18}$ eV. The results indicate that the maximum rigidity should not exceed a few EeV at the price of requiring very hard injection spectrum at the sources.

This model is able to explain the Auger data above the ankle; if we want to give an astrophysical explanation to the data below the ankle, an additional cosmic-ray component is required by the Auger data in the energy range $E < 5 \cdot 10^{18}$ eV, as done for instance in [84]. To summarize: in the pure proton scenario, the features of the energy spectrum are due primarily to the interactions with the CMB. In the mixed composition scenario, the suppression of the flux at the highest energies would be due to the photo-disintegration of nuclei, while the ankle feature cannot be easily accommodated.

If we want to fit the Auger spectrum only above the ankle, both the pure proton and mixed composition scenarios could describe the data, provided the fact that the suppression of the flux is a combination of both acceleration and propagation effects.

Instead, fitting both the spectrum and composition, one can remove this degeneracy and infer information about the source scenarios which are compatible

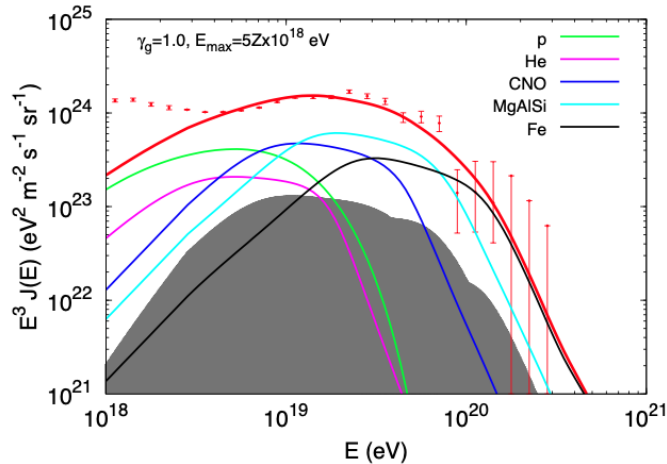


Figure 3.6: Fluxes of protons and nuclei with primary injected particles as labelled. Curves with different colors show the sum of the flux of primaries with given mass number and all secondaries produced by the same nuclear species. The shaded area shows the flux of all secondaries alone. Experimental data are the flux measurements by Auger. From [84].

with data. This was done in some works [84, 85, 86]; in addition, the Auger Collaboration has published a comprehensive study regarding the astrophysical implications from the combined fit of both spectrum and composition data [2], hereinafter called “combined fit paper”.

3.2 Simulation of extra-galactic propagation

To interpret the measured spectrum and mass composition data in terms of astrophysical scenarios, some tools are needed in order to take into account the role of the propagation. Some public codes available for our purposes are *SimProp* [87, 88, 89, 90] and *CRPropa* [91, 92, 93]. I here provide a description of the *SimProp* code, as it represents the propagation code I use for all of my analyses.

3.2.1 The *SimProp* software

SimProp is a Monte Carlo simulation code for the propagation of UHECRs through the Universe. A *SimProp* run consists of N events, each including the generation of a primary particle with mass number A_{inj} , initial energy E_{inj} sampled from a flat distribution from E_{min} to E_{max} and source redshift z_{inj} uniformly distributed from z_{min} to z_{max} . The propagation of particles is followed, along with that of the secondary particles produced during propagation. The injection parameters N , A_{inj} , E_{min} , E_{max} , γ , z_{min} and z_{max} can be chosen by the user at the beginning of the run.

During the propagation, a particle can interact, decay or arrive at Earth. In the interaction with the background photons, many assumptions have to be made:

- **EBL models:** the extra-galactic background light has several uncertainties concerning its spectrum and its evolution with redshift, based on the time evolution of Galaxy populations as estimated using different approaches. The results of these methods are not always compatible with each other, even in the case of recent models, especially for long wavelengths (far IR) and at large redshifts, as seen in figure 3.7. There are different models of the EBL available for use in SimProp, with the most common being those of Dominguez et al. [94] and Gilmore et al. [95]. A more complete comparison between the two models is performed in [96];

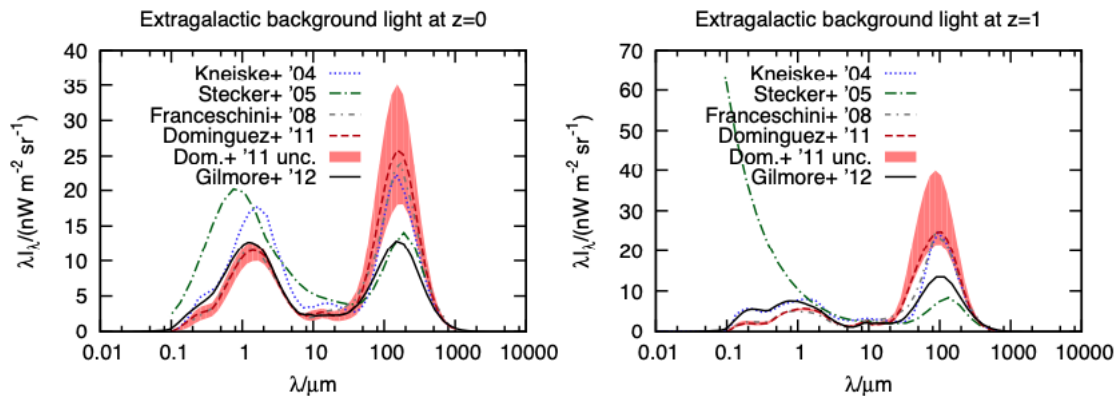


Figure 3.7: Intensity of EBL at $z = 0$ (left) and $z = 1$ (right) as a function of wavelength for different models. From [96].

- **Photo-disintegration model:** in nuclear physics, measurements of the photo-disintegration cross section are not available for all nuclei, and when they are, sometimes only the total absorption and/or the one-neutron ejection cross sections have been measured. Cross sections for exclusive channels in which charged fragments are ejected are hard to measure, since they tend to undergo multiple scattering in the target. For this reason, various phenomenological models have been used in UHECR propagation studies to treat these processes. In my analysis, I consider two models: the treatment by Puget–Stecker–Brekamp hereinafter called **PSB** model [97, 98] and the **TALYS** program [99, 100, 101], both of which are implemented in SimProp. TALYS is a more sophisticated photo-disintegration cross section model and it is more efficient, having different photo-disintegration channels. Nonetheless, many of the cross section in TALYS appear to be overestimated with respect to experimental data [31].

3.2.2 Propagation matrix

After properly taking into account the possible interactions during the extragalactic propagation, we can calculate the propagated flux under certain source hypothesis, using the SimProp Monte Carlo code.

The first step of this procedure involves the consideration the number of injected particles at the source, $n(E_{\text{inj}}, A_{\text{inj}})$, of mass A_{inj} and of energy within $[E_{\text{inj}}; E_{\text{inj}} + \Delta E_{\text{inj}}]$ per unit co-volume and unit energy,

$$n(E_{\text{inj}}, A_{\text{inj}}) dE_{\text{inj}} = \int_{t_{\text{min}}}^{t_0} dt \mathcal{Q}(E_{\text{inj}}, A_{\text{inj}}) dE_{\text{inj}} \quad (3.5)$$

where $\mathcal{Q}(E_{\text{inj}}, A_{\text{inj}})$ can be written as $\mathcal{Q}(E_{\text{inj}}, A_{\text{inj}}) = q_{\text{gen}}(E_{\text{inj}}, A_{\text{inj}}) \cdot S(z)$. $q_{\text{gen}}(E_{\text{inj}}, A_{\text{inj}})$ represents the production rate of a nucleus of mass A_{inj} per unit co-volume and per unit energy, with E_{inj} energy at the source, while the evolution term, $S(z)$, describes the cumulative intensity of UHECR sources at a given cosmic time t and can be written as $S(z) = (1 + z)^m$. In the hypothesis of a homogeneous distribution of identical sources, $m = 0$.

The second step involves the calculation of the expected flux at Earth J^{exp} of nuclei with energy E_{det} assuming a certain production rate $q_{\text{gen}}(E_{\text{inj}}, A_{\text{inj}})$. We can write:

$$J^{\text{exp}}(E_{\text{det}}) \propto c \int_0^{z_{\text{max}}} dz \left| \frac{dt}{dz} \right| \sum_{A_{\text{inj}}} q_{\text{gen}}(E_{\text{inj}}, A_{\text{inj}}) \cdot S(z) \frac{dE_{\text{inj}}}{dE_{\text{det}}} \quad (3.6)$$

where the term $\frac{dE_{\text{inj}}}{dE_{\text{det}}}$ describes the energy losses of injected nuclei due to adiabatic expansion and interactions with photons from both the CMB and EBL. While this procedure is valid in an analytical approach, in this case, events are simulated with a Monte Carlo code. Therefore, we first simulate the cosmic ray events with a uniform distribution in redshift. For practical reasons, the simulation is divided in several shells in redshift and, in each shell, five injected mass (H^1 , He^4 , N^{14} , Si^{28} , Fe^{56}) have been simulated.

To each Monte Carlo event, originated at z , we associate a weight

$$w = S(z) \cdot \left| \frac{dt}{dz}(z) \right| \quad (3.7)$$

All the events are stored, with weight w , in a 4D histogram, the **propagation matrix**, whose elements are N_{ijkm} , with indexes i, j, k, m defined as follows

$$\begin{cases} i \longrightarrow E_{\text{inj}} \\ j \longrightarrow E_{\text{det}} \\ k \longrightarrow A_{\text{inj}} \\ m \longrightarrow A_{\text{det}} \end{cases} \quad (3.8)$$

Energy intervals are equally spaced in log-energy with bin size $\Delta \log_{10}^{\text{exp}}(E/\text{eV}) = 0.01$, while mass intervals have $\Delta A = 1^2$.

If the injected flux is $J^{\text{inj}}(E_{\text{inj}}, Z(A_{\text{inj}}) \cdot R_{\text{cut}})$ and J_{ik}^{inj} is its value calculated at

² The $\Delta \log_{10}^{\text{exp}}(E/\text{eV})$ in the expected spectrum is chosen in order to be sub-multiple of the $\Delta \log_{10}^{\text{obs}}(E/\text{eV})$ of the observed spectrum.

$E_{\text{inj}} \in \text{bin } i$ for mass $A_{\text{inj}} = A_k$, the expected elemental flux at Earth can be computed as:

$$J_{A_{\text{det}}}^{\text{exp}}(E_{\text{det}}) = J_{j_m}^{\text{exp}} \propto \sum_{k \geq m} \sum_{i \geq j} N_{ijkm} \cdot J_{ik}^{\text{inj}} \quad (3.9)$$

and of course the all-particle flux can be written as:

$$J^{\text{exp}}(E_{\text{det}}) = J_j^{\text{exp}} = \sum_m J_{j_m}^{\text{exp}}(E_j) \quad (3.10)$$

The fluxes in equations (3.9) and (3.10) are normalized “a-posteriori”; they are compared to the experimental data and normalized in order to minimize the χ^2 . The propagation matrices are stored in .txt files and can be read by the “combined fit program” that we will introduce in sec. 3.4. In this way, it is possible to disentangle the propagation through the Universe from the fit of the experimental data. One can choose a certain SimProp configuration and then store the simulated events N_{ijkl} into the propagation matrix described above, which takes into account the propagation effects. This approach has been already successfully used in [2] and will be exploited in this work. Further applications of this procedure will be provided in chapter 5.

3.3 Combined fit above the ankle

In this section, a detailed description of the combined fit published by the Auger Collaboration [2] is provided. The astrophysical model as well as the main assumptions are described; following this, the fit procedure is formalized and, in the end, the main results are discussed.

3.3.1 Models and experimental data

In the published work, for the reasons described in section 3.1, a combined fit of the Auger spectrum and X_{max} measurements for energy $E > 5$ EeV was performed, assuming a simple model of UHECR sources. In this analysis, five nuclear species at the source were assumed: Hydrogen (^1H), Helium (^4He), Nitrogen (^{14}N), Silicon (^{28}Si) and Iron (^{56}Fe).

The injected flux for each mass can be written as:

$$J_k(E_i) = f_k J_0 \left(\frac{E_i}{E_0} \right)^{-\gamma} \cdot f_{\text{cut}}(E_i, Z \cdot R_{\text{cut}}) \quad (3.11)$$

where f_k is the fraction of injected element of mass k so that $\sum_k f_k = 1$, J_0 is the spectrum normalization at energy E_0 , E_{cut} is the cutoff energy and γ is the spectral index at escape from the sources and $f_{\text{cut}}(E_i, Z \cdot R_{\text{cut}})$ is the cutoff function, which fix the weight that we include after the propagation, as reported in the previous section.

In the absence of information about the nature of the UHECR acceleration mechanism, the choice of shape for the cutoff function is mostly arbitrary. In this

study, it was chosen to use a broken exponential cutoff (the effect of a different cutoff shape was investigated in [2]):

$$f_{\text{cut}}(E_i, Z \cdot R_{\text{cut}}) = \begin{cases} 1 & E_i < Z R_{\text{cut}} \\ \exp\left(1 - \frac{E_i}{Z \cdot R_{\text{cut}}}\right) & E_i > Z R_{\text{cut}} \end{cases} \quad (3.12)$$

As outlined in section 3.2.1, it is necessary to consider the uncertainties in the EBL and the photo-disintegration cross section when modelling of the extragalactic propagation.

In [2], simulations based on CRpropa [91, 92, 93] and SimProp [88, 89, 90, 87] are used, along with the Gilmore [95] and Dominguez [94] models of EBL and the PSB [97, 98], TALYS [99, 100, 101], and Geant4 [102] models of photo-disintegration in various combinations.

Another parameter which influences the result of the fit is the Hadronic Interaction Model (HIM). There are several models available to simulate the hadronic interactions involved in the shower development, as shown in chapter 1. The simulated mass compositions from the propagation simulations are converted to X_{max} distributions assuming EPOS-LHC [103], QGSJetII-04 [104] and Sibyll 2.1 [105] as the hadronic interaction models.

Concerning the data-set used in [2], it consists of the SD event distribution in 15 bins of 0.1 of $\log_{10}(E/\text{eV})$, ($18.7 \leq \log_{10}(E/\text{eV}) \leq 20.2$) and X_{max} distributions (in bins of 20 g/cm²) in the same bins of energy up to $\log_{10}(E/\text{eV}) = 19.5$ and a final bin from 19.5 to 20.0, for a total of 110 non zero data points. In total, we count 47767 events in the part of the spectrum we use in the fit and 1446 in the X_{max} distributions.

For the spectrum, a forward-folding procedure is applied: this is due to the fact that measurements of UHECR energies are affected by uncertainties of the order of 10%, due to both shower-to-shower fluctuations and detector effects. These uncertainties can cause detected events to be reconstructed in the wrong energy bin. As a consequence of the true spectrum being a decreasing function of energy, most of the events with a given reconstructed energy E_{rec} have a true energy $E_{\text{true}} < E_{\text{rec}}$ than $E_{\text{true}} > E_{\text{rec}}$. The net effect of this is that the reconstructed spectrum is shifted to higher energies and smoothed compared to the true spectrum. To avoid this problem, the forward-folding procedure allows the simulated true spectrum $J(E)$ to be obtained from each source model (spectral index, maximum rigidity and composition at the sources, from equation 3.11) in order to compute the expected event count in each energy bin, and directly compare them to the observed counts.

3.3.2 Fit procedure

The free parameters of the fit can be found in equation 3.11: $J_{0,\gamma}$, R_{cut} and $N - 1$ fractions, with f_k number of injected masses (the last one is given by $f_{\text{last}} = 1 - \sum_k f_k$). Because $N - 1$ mass fractions are fitted, they were expressed

as a function of the director cosines c_i in a $N - 1$ dimensional space; the parameters c_i can vary between $[0, 1]$. Writing the following equations:

$$\begin{aligned}
 f_{\text{H}} &= c_1^2 \\
 f_{\text{He}} &= (1 - c_1^2) \cdot c_2^2 \\
 f_{\text{N}} &= (1 - c_1^2) \cdot (1 - c_2^2) \cdot c_3^2 \\
 f_{\text{Si}} &= (1 - c_1^2) \cdot (1 - c_2^2) \cdot (1 - c_3^2) \cdot c_4^2 \\
 f_{\text{Fe}} &= (1 - c_1^2) \cdot (1 - c_2^2) \cdot (1 - c_3^2) \cdot (1 - c_4^2)
 \end{aligned} \tag{3.13}$$

we can express 5 mass fractions as a function of 4 independent cosines.

The quantity we minimize is the deviance, given by $D = -2\ln(\mathcal{L}/\mathcal{L}_{\text{sat}})$, where \mathcal{L} is the likelihood of the model under consideration and \mathcal{L}_{sat} is the likelihood of a hypothetical model perfectly describing the observed data. Since \mathcal{L}_{sat} is a function of the observed data but not of the model parameters, minimizing D is equivalent to maximizing \mathcal{L} . According to Wilks’s theorem [106], in the limit of large statistics, the probability distribution of D_{min} if the model is correct is a χ^2 distribution whose number of degrees of freedom equals the number of data points minus the number of fitted parameters. The total deviance is computed as the sum of two independent deviances: $D_{\text{tot}} = D_{\text{J}} + D_{X_{\text{max}}}$.

The deviance of the spectrum can be written as:

$$D_{\text{J}} = \sum_m = \frac{(J_m^{\text{obs}} - J_m^{\text{exp}})^2}{\sigma_m^2} \tag{3.14}$$

where J_m^{obs} and J_m^{exp} are the observed and expected spectrum in the m -th energy bin and σ_m is the mean of upper and lower uncertainties for that energy bin.

Concerning the X_{max} deviance, the X_{max} distributions at each log energy bin and for each mass are parameterized using Gumbel probability distribution functions [107]. These functions are denoted as $g(X_{\text{max}} | \lg E_m, A)$:

$$g(X_{\text{max}} | \lg E, A) = \frac{\lambda^\lambda}{\sigma \Gamma(\lambda)} \exp\left(-\lambda \frac{X_{\text{max}} - \mu}{\sigma} - \lambda \exp\left(-\frac{X_{\text{max}} - \mu}{\sigma}\right)\right) \tag{3.15}$$

The values of μ , σ , and λ were obtained by fitting this Gumbel parametrization to X_{max} distributions obtained via CONEX simulations [108]. Afterwards, each Gumbel function is corrected for the detector effects (see Appendix A). Then these distributions, denoted as $\mathcal{G}_m^{\text{model}}(X_{\text{max}} | \lg E)$, are mixed with relative weights given by fractions $p_A^{\text{exp}}(E)$, defined as $p_A^{\text{exp}}(E) = \frac{J_A^{\text{exp}}(E)}{J^{\text{exp}}(E)}$, where $J^{\text{exp}}(E)$ is the expected flux at Earth at energy E and $J_A^{\text{exp}}(E)$ is the expected flux of a mass A at the same energy. The mixed distributions are written as:

$$G_m^{\text{model}}(X_{\text{max}} | \lg E) = \sum_A p_A^{\text{exp}} \cdot \mathcal{G}(X_{\text{max}} | \lg E, A) \tag{3.16}$$

For the likelihood of the X_{max} distributions, we used a multinomial distribution:

$$D_{X_{\max}} = \sum_m D_m = \sum_m -2 \ln \frac{L_{X_{\max}}}{L_{X_{\max}}^{\text{sat}}} = -2 \sum_m \sum_x k_{mx} \left(\ln G_{mx} - \ln \frac{k_{mx}}{N_m} \right) \quad (3.17)$$

where G_{mx} is the probability $G_m^{\text{model}}(X_{\max}|E)$ calculated at bin x of X_{\max} , k_{mx} is the event content of the experimental X_{\max} distribution at X_{\max} bin x and log energy bin m ; $N_m = \sum_x k_{mx}$ is the total number events in the log energy bin m . The quantity that it has to be minimized is the sum of the equations 3.14 and 3.17.

In this approach a uniform scan over $(\gamma, \log_{10}(R_{\text{cut}}/V))$ binned pairs was performed and for each pair the deviance is minimized as a function of the fractions (p_A^{exp}) of masses ejected at the source. The minimisation as a function of J_0 can be performed analytically solving $\delta D_J / \delta J_0 = 0$.

The Minuit [109] package is used. A scan is performed in the $\gamma \in [-1.5, 2.5]$, $\log_{10}(R_{\text{cut}}/V) \in [17.5, 20.5]$ intervals, on a grid with 0.01 spacing in γ and $\log_{10}(R_{\text{cut}}/V)$.

3.3.3 Main results

In this section I am going to present the results of the fit, taking as reference SimProp propagation with PSB cross sections, and using the Gilmore EBL model (hereafter this combination is going to be called **SPG**). The hadronic interaction model used to describe UHECR-air interactions for this fit is EPOS-LHC. An important result of this work is shown in 3.8, where the value of the pseudo standard deviation $\sqrt{(D - D_{\min})}$ as a function of $(\gamma, \log_{10}(R_{\text{cut}}/V))$ is shown. In the inset the behaviour of the deviance along the valley line connecting $(\gamma, \log_{10}(R_{\text{cut}}/V))$ minima (dashed line in the figure), corresponding in each point to the best fit of the other parameters is shown.

It is evident from figure 3.8 that the best fit solutions present a marked correlation between γ and $\log_{10}(R_{\text{cut}}/V)$, and two local minima regions:

- An elongated region at $R_{\text{cut}} \leq 5 \cdot 10^{18}$ V, $\gamma \leq 1$, where the best minimum falls. In this region both the spectrum and the X_{\max} data are reproduced reasonably well, but the precise location of the best fit strongly depends on the propagation model (i.e. Monte Carlo code, EBL spectrum, photo-disintegration cross sections and air interaction models).
- A smaller region at $R_{\text{cut}} \simeq 7 \cdot 10^{19}$ V, $\gamma \simeq 2$, where the spectrum is well reproduced but there are too many high-energy protons at strong variance with the X_{\max} data, while the position of the local minimum does not vary much among the various propagation models.

As already expressed, with different hypotheses the source parameters can change considerably and for some of them well outside the statistical uncertainties of the fit with other assumptions. However, the low spectral index and low rigidity solution is generally preferred. The best fit parameters are shown in tab 3.1.

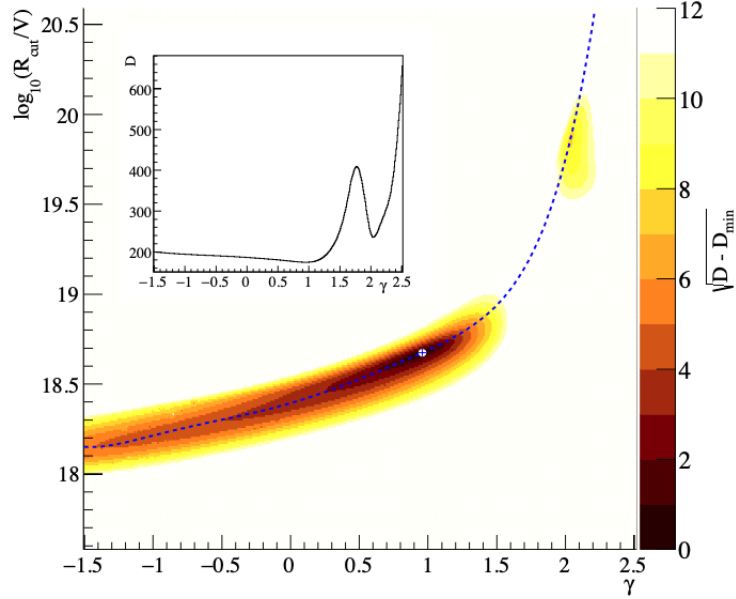


Figure 3.8: Deviance as a function of γ and R_{cut} . In the box the plot of the Deviance as a function of γ . The best fit was found at $\gamma = 0.96$ and $\log_{10}(R_{\text{cut}}/V) = 18.68$ [2].

Parameter	Best fit	2nd minimum
$f_{\text{H}}(\%)$	0.00	0.00
$f_{\text{He}}(\%)$	67.3	0.00
$f_{\text{N}}(\%)$	28.1	79.8
$f_{\text{Si}}(\%)$	4.6	20.2
$f_{\text{Fe}}(\%)$	0.00	0.00
γ	$0.96^{+0.08}_{-0.04}$	2.04 ± 0.01
$\log_{10}(R_{\text{cut}}/V)$	$18.68^{+0.02}_{-0.04}$	19.88 ± 0.02
D_{J}	13.3(15)	19.3(15)
$D_{X_{\text{max}}}$	161.1 (110)	216.2 (110)
D_{tot}	174.4(125)	235.7 (125)

Table 3.1: Best fit parameters for the two minima discussed in the combined fit paper [2]. The numbers in brackets refers to the fitted number of points.

A hard spectral index ($\gamma \simeq 1$), as found, is not what we expect according to Fermi acceleration, as shown in chapter 1.

This is largely due to the fact that with a low spectral index and a low cutoff rigidity, the partial spectra for the various mass groups are clearly separated. This is what the mass composition data, in particular the $\sigma(X_{\text{max}})$, require, due to the pronounced decreasing as a function of the energy, as can be seen in figure 2.14. On the contrary, for a soft injection, the spectra at the source are less separated and produce a larger $\sigma(X_{\text{max}})$.

As explained in sec. 3.1, fitting spectrum and composition is crucial to determine the parameters at the source. For larger changes in the position along the “valley”, the main effect is that, the lower γ and R_{cut} are, the less the propagated energy spectra for individual mass groups overlap, and therefore the least mixed the mass composition is at each energy. This explains why the local minimum at $\gamma \sim 2$ is so strongly disfavoured by the narrowness of the observed X_{max} distributions.

3.4 A new combined fit package

After the published work [2], it was a goal of the collaboration to extend this analysis to lower energy. My thesis project includes rewriting the original combined fit code in order to make it more flexible for further analysis. For this reason, it was chosen to reorganize the internal structure of the code, dividing it and organizing it according to a logic structure. The code itself has been divided in several different classes in C++, trying to follow the path of a single particle, from its emission until its detection. Nowadays, thanks to my work, the combined fit code is organized in six different classes as shown in the scheme in figure 3.9. Each class has been designed to carry out specific tasks:

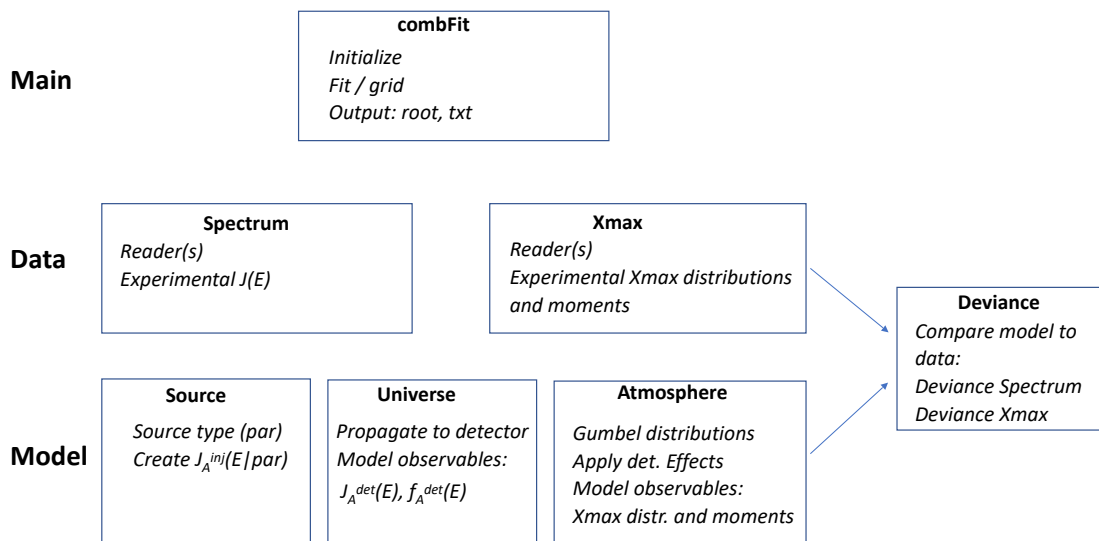


Figure 3.9: Schematic view of the new organization of the code used for the combined fit.

- **Source:** this class contains methods to simulate the emission of Ultra-High-Energy Cosmic Ray (UHECR) nuclei from sources. Nuclei (A, Z) , are injected in the extra-galactic space with a power-law energy spectrum having spectral index γ and rigidity cutoff R_{cut} . Alternately, it is possible to consider sources from two different populations. In this case, different nuclei (A^a, Z^a) , (A^b, Z^b) can be accelerated with different spectral indexes γ^a and γ^b and different rigidity cutoff R_{cut}^a and R_{cut}^b . This will be exploited in the next chapter. In addition, the code provides the possibility to read a specific source injection spectra: in this case the spectral parameters (γ, R_{cut}) are not needed. This will be used for the source-propagation model in chapter 5.
- **Universe:** starting from the injected spectra at the source, methods within this class can be used to propagate nuclei through the Universe, considering sources uniformly distributed in a comoving volume up to a certain z_{max} , up to the atmosphere. UHECRs travel through the extra-galactic environment and interact with photon backgrounds changing their energy and, in the case of nuclei, their species too. The propagated spectra are obtained as written in the eq. 3.9, where the interface between the propagation code and the combined fit code is the propagation matrix, as detailed in section 3.2.2.
- **Atmosphere:** This class deals with the effects of the CR cascade production in the atmosphere, which due to stochastic effects, introduces shower to shower fluctuations in particular for the position of the shower maximum (X_{max}). The expected X_{max} distributions are calculated making use of the generalized Gumbel probability distribution functions, as shown in the previous section, and then corrected for the detector effects. A great advantage of using this parametric function is that it allows us to evaluate the model X_{max} distribution for any mixture of nuclei without the need to simulate showers for each primary. In this analysis the nuclei from $A = 1$ up to $A = 56$ are taken into account. The spectra are unaffected by atmosphere, so they are not managed in this class.
- **Spectrum** and X_{max} : These classes are designated to read in the experimental data according to the chosen dataset. The codes and data are largely based on material available from the Auger spectrum, mass composition and Cosmic Ray Phenomenology wikispaces [110].
- **Deviance:** This class implements the methods for calculating the deviances of the spectrum and X_{max} , as written in the equations 3.14 and 3.17. The deviances are calculated comparing experimental data with model expectations, where the latter depend on fit parameters. The X_{max} deviance calculation is performed at each energy bin of the corresponding X_{max} distribution.

The new organization of the combined fit classes expands significantly its power and makes it more flexible to be used. The specific usage is managed by

a user main (“combFit” in figure 3.9) and an input configuration.

Being each class independent, they can be utilized also for different purposes, e.g. for fitting separately spectrum and mass composition. We call these approaches “vertical”, because for them we use just a single model class and its respective data class, moving along the vertical line in our scheme (see figure 3.9).

Furthermore, “horizontal” usages are also possible; for example, making a particular choice for the initial parameters (γ , R_{cut} and the mass fractions at the source), we can propagate the injected spectra through the Universe and get the expected spectrum and composition at Earth, eventually calculating the deviances with respect to data.

One possible application, allowed thanks to this new organization, is the **FractionFit**, which uses only three classes, namely *Atmosphere*, X_{max} and *Deviance*, in which the mass fractions on the top of the atmosphere are fitted. The results are show in figure 3.10, in which we found consistent results compared to those one presented by the collaboration in the ICRC2017 [111] using an independent code.

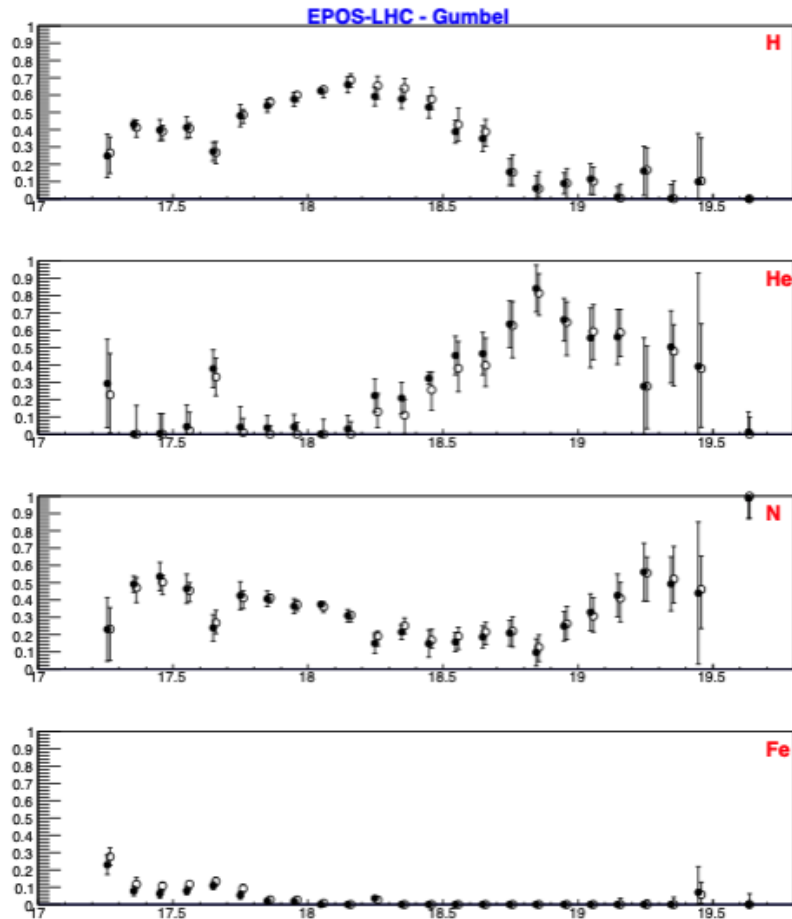


Figure 3.10: FractionFit results: the white dots refer to the ICRC2017 analysis, carried out with an independent code. Black dots refer to this analysis. Error bars are calculated using Minuit.

3.5 Results

3.5.1 Validation

After the publication of the combined fit paper [2] and before my work on the code described in the previous section, two important modifications have been done in the original combined fit code.

- The first one concerns the use of the experimental spectrum. In the combined fit paper the SD vertical and inclined measured data corrected for the detector effect through a forward folding procedure are used, as already outlined in section 3.3.1. In order not to incur in an underestimation of the systematic uncertainties that could arise from the model choice, in [2] it was decided to use the raw spectra as input, implementing the forward-folding in the combined fit routine.

Successively, we have chosen to directly fit the combined spectrum, which allows to easily extend the energy range without the need for performing the forward-folding of each raw spectrum in the combined fit routine. The consistency of the results thus obtained has been verified and it is shown in the first two columns of table 3.2. Hereinafter, the combined spectrum will be used for all the further analyses.

Parameter	Published results	Combined Spectrum	New param. of Gumbel functions
$f_{\text{H}}(\%)$	0.00	0.00	0.00
$f_{\text{He}}(\%)$	67.3	74.1	81.5
$f_{\text{N}}(\%)$	28.1	22.0	16.1
$f_{\text{Si}}(\%)$	4.6	3.9	2.4
$f_{\text{Fe}}(\%)$	0.00	0.00	0.00
γ	$0.96^{+0.08}_{-0.04}$	$0.88^{+0.09}_{-0.1}$	$0.67^{+0.12}_{-0.12}$
$\log_{10}(R_{\text{cut}}/V)$	$18.68^{+0.02}_{-0.04}$	$18.63^{+0.02}_{-0.03}$	$18.59^{+0.03}_{-0.03}$
D_{J}	13.3(15)	15.8(15)	21.1(15)
$D_{X_{\text{max}}}$	161.1 (110)	163.3(110)	174.6 (110)
D_{tot}	174.4(125)	179.1 (125)	195.7(125)

Table 3.2: Best fit parameters from [2] (second column), results obtained fitting the unfolded combined spectrum from ICRC 2015 (third column) and changing the Gumbel parametrization (forth column). From [112].

- The second one concerns an update of the Gumbel parametrization of X_{max} moments and distributions previously published in [113, 107]. The new parametrization are reported in Appendix A. How the combined fit changes according to the Gumbel parametrization correction is shown in the last two columns of table 3.2.

The best fit parameters reported in the last column of table 3.2 are taken as benchmark case for my work. As shown in the previous section, many modifications on the internal structure and on the organization of the classes have been applied. Using the same dataset of the benchmark case, a combined fit using the new version of the code has been performed: this is reported in the second column of 3.3. Comparing the two results one can affirm, as it is expected, that the modification of the structure does not change the fit result.

3.5.2 Update of the dataset

After the publication of the combined fit paper, new data have been available during the last years. We list here the three possible dataset nowadays available for the combined fit analysis:

- **JCAP2017**: the dataset used for the results in the last column of table 3.2.
- **ICRC2017**: spectrum and composition data presented by the collaboration at the International Cosmic Rays Conference (ICRC) in 2017 [114, 111].
- **ICRC2019**: spectrum and composition data presented by the collaboration at the ICRC in 2019 [56].

We firstly use the **ICRC2017** dataset reproducing the reference scenario chosen in the combined fit paper: SimProp simulations with PSB disintegration cross sections and the Gilmore EBL model (SPG) are used for propagation from sources to Earth; the events have been simulated up to a redshift value $z = 1$, corresponding to a comoving distance of approximately 3 Gpc. This is due to the fact that most particles reaching Earth with an energy above $10^{18.7}$ eV are expected to originate from sources with $z \leq 1$. The interactions with atmosphere are modelled with EPOS-LHC. Note that we are taking into account the modifications on the spectrum and composition described in the previous section (unfolded spectrum and change of Gumbel parametrizations). In addition, the two spectral parameters γ and R_{cut} are included in the fit as free parameters. The uncertainties of the parameters are the ones provided by MINUIT [109], as the minimizer successfully converges to the minimum and the covariance matrix appears to be accurately computed.

The updated results are shown in table 3.3, while in figure 3.11 in the values of the pseudo standard deviance $\sqrt{(D - D_{\text{min}})}$ are shown as a function of $(\gamma, \log_{10}(R_{\text{cut}}/V))$ for both the ICRC2017 and JCAP2017 datasets.

The fractions of injected elements are calculated to an energy that is lower than the fitted energy range ($E_0 = 10^{18}$ eV); they strongly depend on the estimated γ value. For this reason, starting from an arbitrary energy $E_{\text{min}} = 10^{17}$ eV, it can be useful to write the fractions in terms of total emissivity $\mathcal{L}_0 = \sum_A \mathcal{L}_A = \sum_A \int_{E_{\text{min}}}^{\infty} J_A^{\text{exp}}(E) E dE$, where \mathcal{L}_A is the energy density of the partial spectrum

CHAPTER 3. COMBINED FIT OF ENERGY SPECTRUM AND
COMPOSITION OF THE PIERRE AUGER OBSERVATORY, AT
ENERGIES ABOVE THE “ANKLE”

Parameter	JCAP2017	ICRC2017
$f_{\text{H}}(\%)$	0.00	75.5 ± 8
$f_{\text{He}}(\%)$	80.6 ± 3	24.2 ± 7
$f_{\text{N}}(\%)$	16.8 ± 3	0.3 ± 0.1
$f_{\text{Si}}(\%)$	2.4 ± 0.5	$O(10^{-4})$
$f_{\text{Fe}}(\%)$	0.00	0.00
γ	$0.69^{+0.12}_{-0.12}$	-1.15 ± 0.27
$\log_{10}(R_{\text{cut}}/V)$	$18.59^{+0.03}_{-0.03}$	18.27 ± 0.04
\mathcal{L}_0 (erg · Mpc ⁻³ · yr ⁻¹)	$4.8 \cdot 10^{44}$	$5.37 \cdot 10^{44}$
$I_{\text{H}}(\%)$	$O(10^{-6})$	11.9
$I_{\text{He}}(\%)$	41.4	44.7
$I_{\text{N}}(\%)$	43.3	29.3
$I_{\text{Si}}(\%)$	15.2	14.4
$I_{\text{Fe}}(\%)$	0.00	0.00
D_J	21.1(15)	14.9(15)
$D_{X_{\text{max}}}$	174.6 (110)	237.9 (109)
D_{tot}	195.7(125)	252.8(124)

Table 3.3: Best fit parameters estimated by fitting the unfolded combined spectrum and the X_{max} distributions above $\log_{10}(E/\text{eV}) = 18.7$ for the two data sets.

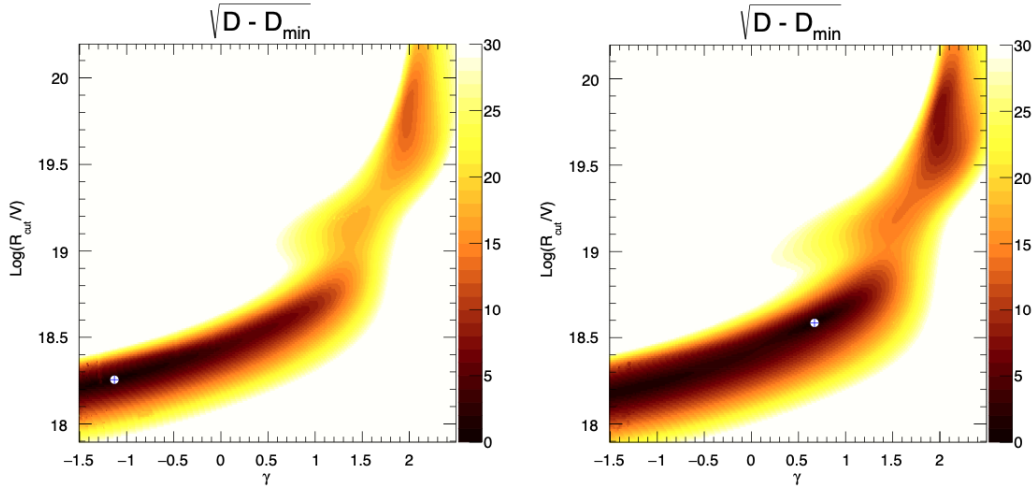


Figure 3.11: The pseudo standard deviation $\sqrt{(D - D_{\text{min}})}$ as a function of $(\gamma, \log_{10}(R_{\text{cut}}/V))$ obtained from two different datasets: ICRC2017 on the left and JCAP2017 on the right.

$J_A^{\text{exp}}(E)$.

Therefore the mass fractions can be written such as $I_A = \mathcal{L}_A/\mathcal{L}_0$.

In case we choose $E_{\text{min}} \ll E_0$, this expression can be approximated as $I_A = \mathcal{L}_A/\mathcal{L}_0 = f_A Z_A^{2-\gamma} / \sum_A (f_A Z_A^{2-\gamma})$ as already done in the combined fit work [2]. Hereinafter, in the following tables I_A will be shown instead of f_A . The mass fractions written in terms of luminosity ratio are reported in the second part of

table 3.3.

Comparing the two plots in figure 3.11, it appears evident that there are still two regions of local minima already outlined in the combined fit paper. However, even if the plots are similar, some significant differences in the fit results are observed when ICRC2017 data are fitted. First of all, the best fit minimum, even if still located in the extended minimum region, is found at a negative value of γ for this dataset.

The estimated composition at sources is lighter with respect to JCAP2017 results: it is dominated by hydrogen and, to a lesser extent, by helium, with a much smaller contribution from nitrogen and silicon.

It is worth noting that if we move along the “stability line” (the line in the (γ, R_{cut}) space that joins all the local minima) towards the low- γ region, the rigidity cutoff gets lower too, becoming more significant in shaping each injected spectrum, so that for $\gamma \leq 1$ the injection fluxes are not as superimposed as it would happen for larger (positive) γ (see figure 3.12). The total flux is then reproduced by hierarchically ordering the partial fluxes rather than modifying the injection spectral index. As a consequence, for low (and especially negative) values of γ the fit becomes less and less sensitive to the slope of the injection spectrum and the spectral parameters appear to be degenerate [2]. In the negative- γ region, the fit is dominated by propagation effects rather than by source properties, hence it is expected to be strongly dependent on the chosen models for the EBL spectrum and for the photo-disintegration cross sections, as already explained in the previous section and in [2].

Furthermore we see that the updated results provided a worse fit if compared to

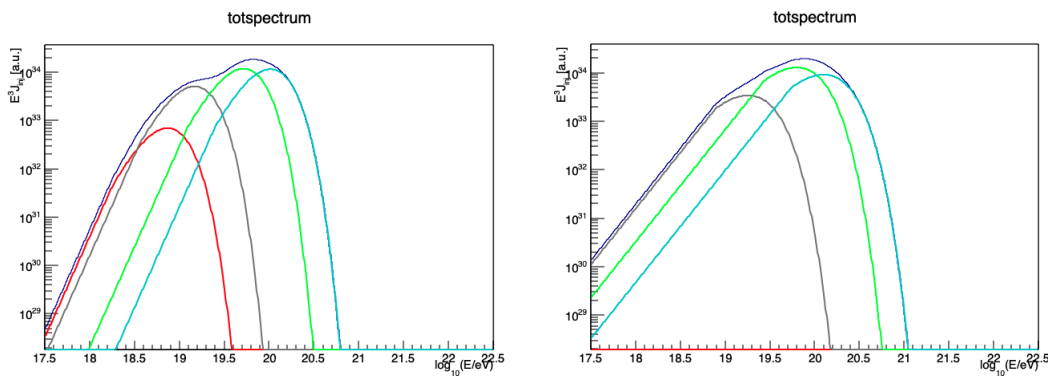


Figure 3.12: Injection spectra multiplied by E^3 for the ICRC2017 (left) and JCAP2017 (right) best fit solution. Each curve corresponds to one representative injected mass: ^1H (red), ^4He (grey), ^{14}N (green), ^{28}Si (cyan), ^{56}Fe (blue).

that one using the JCAP2017 data. This is probably due to the fact that some assumptions in our model are too simplistic to describe the experimental data, which have become more constraining with ICRC2017 dataset. In order to make our model more realistic, it was chosen to take into account the local overdensity around our Galaxy and evaluate how the fit is affected by a more realistic distribution of the sources.

3.5.3 Including overdensity in the combined fit

In the combined fit paper [2] the simplest astrophysical model is considered, in which the sources are assumed to be uniformly distributed in a comoving volume. However, as outlined few years ago inside the collaboration and detailed in Q. Luce PhD thesis [115], it is important to take into account the local overdensity of the sources.

In fact, since the Milky Way belongs to a cluster of Galaxies, the space density of local sources, ρ_{local} , is larger than the average density in the Universe, ρ_{Universe} . A cluster centered around our Galaxy can be described by the correlation function expressed in eq. 3.18, where r is the comoving distance, $r_0 = 5.4$ Mpc and $\gamma = 1.66$ [116]. Hence the weight of each event accelerated at a redshift $z < 0.007$ (29.5 Mpc) has been multiplied by this correction factor:

$$\frac{\rho_{\text{local}}}{\rho_{\text{Universe}}} = 1 + \left(\frac{r_0}{r}\right)^{-\gamma} \quad (3.18)$$

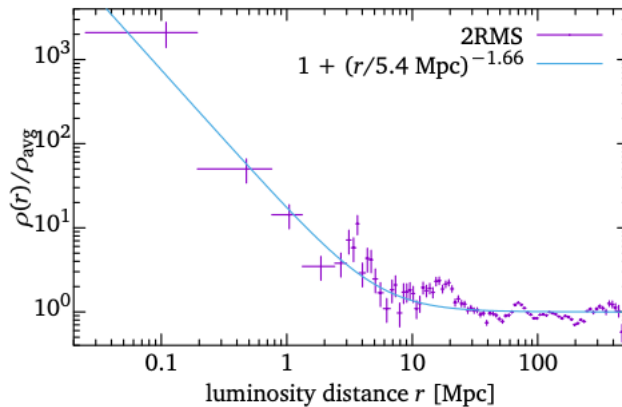


Figure 3.13: The overdensity factor of eq. 3.18 as a function of distance (light blue curve), compared to that of objects in the 2MRS catalog using the procedure outlined in [117] to compensate the exclusion of objects with low apparent luminosity (violet crosses). (The peaks visible at $D < 1$ Mpc, $D \sim 4$ Mpc, $D \sim 20$ Mpc and $D \sim 70$ Mpc correspond respectively to the Local Group, the Council of Giants, the Virgo Cluster, and the Hydra–Centaurus Supercluster). Plot from [112]

In [116], this function is fitted taking into account only Galaxies at distances above 5 Mpc, but it happens to be approximately correct also for closer distances, as shown in figure 3.13, which is reassuring because most of the flux from starburst galaxies with which Auger data are found to correlate originates from within 5 Mpc. The impact of the overdensity correction can be quantified comparing the best fit results using the two different datasets.

Including the overdensity correction, one can notice that this has almost no effect on the dataset JCAP2017; this slightly decreases the deviance, even if the spectral parameters and the mass fractions are almost the same. Instead, the

overdensity correction plays an important role for the dataset ICRC2017, because, once it is included, the minimum found is more similar to the JCAP one. The results is consistent to the one presented in [115].

In particular, the spectral index is shifted to a positive value, the composition at sources is dominated by intermediate-mass species, namely by helium and nitrogen with also a small fraction of silicon. In fact, since the contribution of local sources is more important, there is less room for photo-disintegration processes during propagation, hence the composition is more similar to the one observed at Earth. The overdensity correction produces an improvement of the X_{\max} distributions fit and, even if the energy spectrum fit worsens, the total deviance value decreases. So the overdensity correction will be taken into account in the future analysis.

Parameter	JCAP2017	JCAP2017 OD	ICRC2017	ICRC2017 OD
$I_{\text{H}}(\%)$	0.00	0.00	13.4 ± 1	0.00
$I_{\text{He}}(\%)$	41.4 ± 1	39 ± 1	42.1 ± 12	45.5 ± 1
$I_{\text{N}}(\%)$	43.3 ± 9	61 ± 1	32.6 ± 16	48.4 ± 7
$I_{\text{Si}}(\%)$	15.2 ± 4	$O(10^{-4})$	9.9 ± 16	5.9 ± 2
$I_{\text{Fe}}(\%)$	0.00	0.00	2 ± 2	0.00
γ	$0.69^{+0.12}_{-0.12}$	0.74 ± 0.08	-1.12 ± 0.28	0.45 ± 0.09
$\log_{10}(R_{\text{cut}}/V)$	$18.59^{+0.03}_{-0.03}$	18.59 ± 0.01	18.23 ± 0.04	18.53 ± 0.02
D_{J}	21.1(15)	28.6(15)	14.9(15)	32.5(15)
$D_{X_{\max}}$	174.6(110)	153.9(110)	237.9(109)	202.6(109)
D_{tot}	195.7(125)	182.5(125)	252.8(124)	235.1(124)

Table 3.4: Comparison of fit results with and without overdensity for the JCAP2017 and ICRC2017 dataset.

3.5.4 Combined fit using ICRC2019 dataset

In 2019 a new update of the data was available. In this section we present the fit performed with the following dataset:

- **Spectrum:** we use the unfolded ICRC2019 combined spectrum, including data from January 2004 to August 2018 for the SD1500 and SD750 arrays, from January 2007 to December 2017 for the Hybrids and from June 2012 to December 2015 for the Cherenkov sample [56].
- **Composition:** The selection is performed exactly as for that of JCAP2017 [118], except that below $10^{18.1}$ eV events that belong to the *HeCo* (HEAT

and Coihueco eyes, see chapter 2) data set are excluded. Acceptance and resolution are those used for the X_{\max} of JCAP2017.

It was chosen to use the same setting of the two previous scenarios: SimProp simulations with PSB disintegration cross sections and the Gilmore EBL model (SPG) are used for propagation from sources to Earth. The interaction with the atmosphere is modelled on EPOS-LHC. The results are shown in the central column of table 3.5.

The best fit solution estimates a very hard injection spectrum, providing an

Parameter	ICRC2019	ICRC2019 OD
$I_{\text{H}}(\%)$	11.2 ± 9	0.00
$I_{\text{He}}(\%)$	44.7 ± 12	46.5 ± 1
$I_{\text{N}}(\%)$	28.7 ± 15	46.8 ± 6
$I_{\text{Si}}(\%)$	15.4 ± 12	6.7 ± 0.1
$I_{\text{Fe}}(\%)$	0.00	0.00
γ	-1.1 ± 0.25	0.36 ± 0.09
$\log_{10}(R_{\text{cut}}/V)$	18.5 ± 0.01	18.5 ± 0.01
D_{J}	23(15)	49.5(15)
$D_{X_{\max}}$	293.7 (121)	259.7 (121)
D_{tot}	316.7(136)	309.2(136)

Table 3.5: Best minimum parameters estimated fitting the unfolded combined spectrum from ICRC2019 dataset with and without including the overdensity correction.

accurate description of the features in the observed energy spectrum, which are more and more pronounced because of the increased number of events. As concerns the mass composition at the sources, it is largely dominated by hydrogen and helium, with a relatively small amount of nitrogen.

The fit is a worse if compared to the previous dataset. Also including the overdensity correction the fit does not improve significantly, as shown on the second column of table 3.5. This means that some assumption in our model is not accurate enough to describe the experimental data, and this is as more evident as the data become more constraining.

All the results that have been presented so far are obtained in the reference scenario. Of course, other models can be chosen and it is interesting to verify how much such choices can affect the fit results. One can find a more complete treatment of this in [112]. We show, as an example, how changing photo-disintegration model, from PSB to TALYS, and including overdensity correction we significantly improve the value of the deviance using ICRC2019 dataset (see table 3.6).

Parameter	TALYS	PSB
$I_{\text{H}}(\%)$	13.9 ± 0.5	0.00
$I_{\text{He}}(\%)$	22.8 ± 5	46.5 ± 1
$I_{\text{N}}(\%)$	60 ± 25	46.8 ± 6
$I_{\text{Si}}(\%)$	2 ± 2	6.7 ± 0.1
$I_{\text{Fe}}(\%)$	1.3 ± 1.3	0.00
γ	-1.19 ± 0.11	0.36 ± 0.09
$\log_{10}(R_{\text{cut}}/\text{V})$	18.2 ± 0.02	18.5 ± 0.01
D_{J}	14.5(15)	49.5(15)
$D_{X_{\text{max}}}$	261.2 (121)	259.7 (121)
D_{tot}	275.7(136)	309.2(136)

Table 3.6: Best minimum parameters estimated fitting the unfolded combined spectrum from ICRC2019 dataset for two different photo-disintegration cross section models. In both cases the over-density correction is taken into account.

In order to show how the fit can improve taking into account the source distribution, I want to cite an ongoing work [119] in the collaboration in which they improve the result of the fit shown in table 3.5 using astrophysical model. They study the impact of a source evolution following the stellar mass density (SMD) and they account for density variations on distance scales ranging from few Mpc to tens of Gpc. This approach is motivated by the 4.5σ preference of the “starburst” model over isotropy at energies larger than 40 EeV. Instead of a slow source evolution on Gpc scales, such as $S(z) = (1 + z)^m$ with $m = \{-3; 0; 3\}$, they study the SMD accounting for the over-density of matter surrounding the Milky Way. The cosmic SMD, ρ^{cosmo} , is the integral over time of the cosmic star formation history (CSFH), which describes the star formation rate on cosmological scales.

They model the luminosity evolution term as:

$$S(z) = \rho_*(z) = \rho^{\text{cosmo}}(z) \cdot (1 + \varepsilon(z)) \quad (3.19)$$

where ε is the correction for the overdensity.

Including this correction, shown in figure 3.14, their deviance improves by 70-80 units compared to the case presented in table 3.6 and the best fit is found at $\gamma \simeq 1$. Moreover, an overall good consistency is found between the parameters obtained with PSB and TALYS, indicative of the robustness of the inferred parameters within the SMD scenario.

In the next two chapters we are going to extend the combined fit analysis to lower energies: in a first moment duplicating this approach for energies below the ankle (in chapter 4), and then taking into account interactions in the environment surrounding the sources within the source-propagation model (in chapter 5).

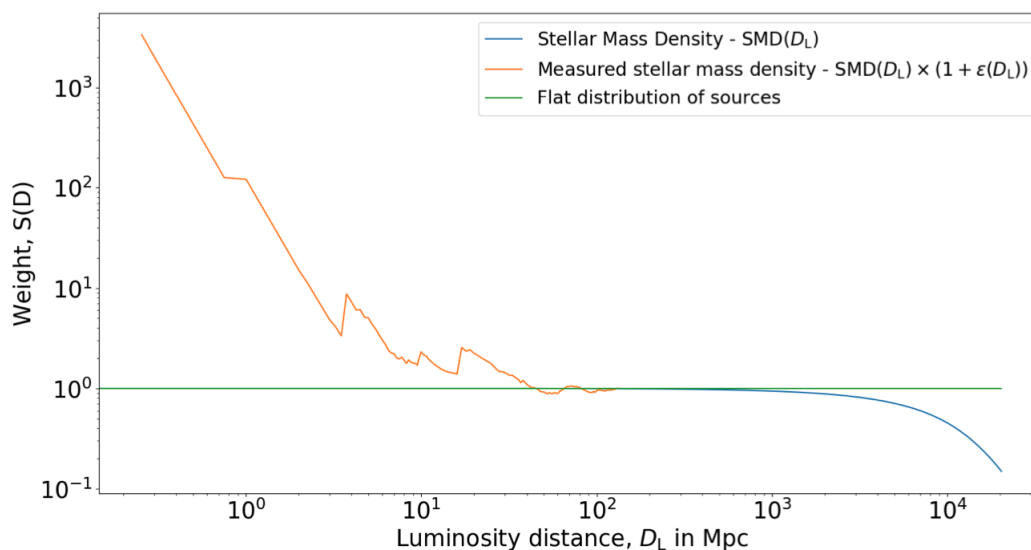


Figure 3.14: Weights applied to each simulated event regarding its distance on injection in [119]. In blue, the weights are computed from the SMD. In orange, the weights are computed from the SMD accounting for the local over-density. For comparison, the weights applied in a flat-distribution scenario are shown in green. Plot from [119].

CHAPTER 4

Extension of the combined fit below the ankle

4.1 Hints of a second component

In the previous chapter, we have shown the results of the combined fit of the spectrum and composition data in the energy region above the ankle. In section 3.1 it was discussed how, taking into account only propagation effects, it is impossible to generate the ankle feature using nuclei rather than protons (see figure 3.5).

In order to extend the combined fit at energies below the ankle ($E = 10^{18.7}$ eV), two explanations could be provided to interpret the Auger measurements below the ankle:

- A second extra-galactic component, independent of the one used to fit the data above the ankle;
- A source mechanism effect, which provides a low energy component as a product of photo-disintegration of heavier nuclei. These heavy nuclei would be accelerated at the source and confined within a region surrounding the source with magnetic and photon fields present.

I choose to explore the first mechanism in this chapter, while the second one is investigated in the following chapter.

A second extra-galactic component can originate from different sources and mechanisms. An exclusive galactic origin is difficult to accommodate up to the ankle energy in the standard paradigm of acceleration in SNRs, as already discussed in section 3.1. Therefore, extra-galactic CR sources are expected to contribute to the low energy component that generates the ankle feature. These sources should reasonably belong to a different class with respect to the one used in our fit above the ankle.

Some hints of the necessity of a second component are provided in the previous chapter: from the best fit plots referring to the table 3.5, we can see from the spectrum that an additional component is needed to describe the experimental data (black dots) in the orange boxes. In particular, an important observation can be

done looking at the mass composition measurement: this additional component cannot be composed only of protons, but must also include heavier elements in order to fit the X_{\max} measurements shown in figure 4.1. This is due to the fact that, assuming the hadronic interaction model which best fits the Auger data, EPOS-LHC, the mean value of X_{\max} is close to the one generated by pure He, but the dispersion is closer to that of H.

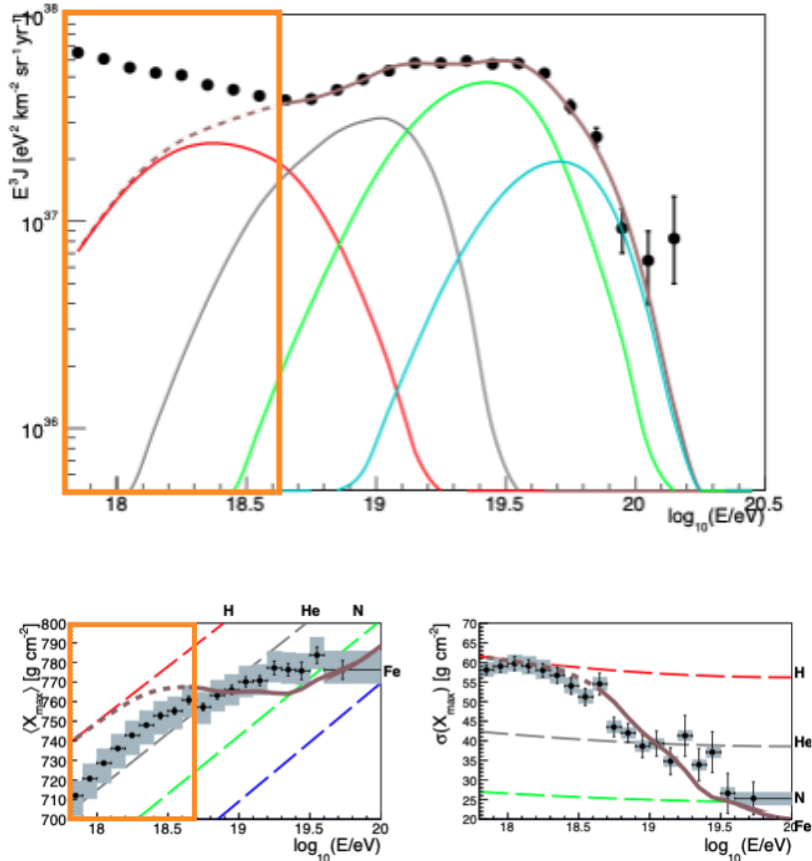


Figure 4.1: Best fit for the spectrum and composition in the reference scenario, as discussed in section 3.5.4. The orange boxes highlight the region below $10^{18.7}$ eV, where the model does not converge with the data.

A first analysis of the features that must be present in a second component was previously shown in section 6 of the combined fit paper [2].

In order to see if a sub-ankle component could influence their results at higher energies, they include the sub-ankle flux obtained by subtracting from the experimental data the lower energy continuation of the all-particle flux fitted or $\log_{10}(E/eV) < 18.7$. Under this assumption, a reasonable description of the sub-ankle component was found for a spectral index $\gamma = 3.6$, a rigidity cutoff $\log_{10}(R_{\text{cut}}/V) = 18.4$ and a mix of about 56% H, 35% N and 9% Si. The result of this procedure is shown in figure 4.2.

Inspired by this, as a natural extension of the combined fit in the following section I use an independent component below the ankle in order to describe the

Pierre Auger measurements down to $17.8 \log_{10}(E/\text{eV})$.

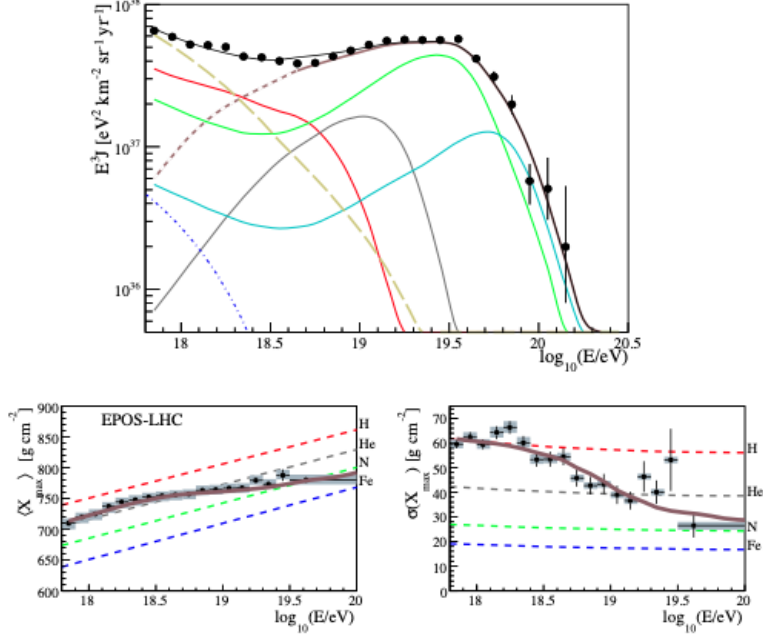


Figure 4.2: Top: simulated energy spectrum of UHECRs (multiplied by E^3) at the top of Earth’s atmosphere, best-fit parameters along with Auger data points. The dashed (yellowish) line shows the sub-ankle component obtained as described in the text. The dot-dashed (blue) shows the galactic cosmic rays flux, here assumed to be composed only of iron.

Bottom: average and standard deviation of the X_{max} distribution as predicted. From [2].

4.2 Implementation of the extended combined fit

4.2.1 Combined fit using two extra-galactic components

In this scenario, the fit of the Auger spectrum and X_{max} data is performed at energies greater than $10^{17.8}$ eV. In the extended combined fit, the architecture of the combined fit above the ankle is duplicated. In particular:

- The injection spectrum is a power law with rigidity dependent cutoff. Because the two components are independent, we are going to consider two different spectral indexes and two different rigidity cutoffs, generalizing the

equation 3.11:

$$\begin{aligned} J_k^{\text{LE}}(E) &= J_0^{\text{LE}} f_k^{\text{LE}} \left(\frac{E}{E_0} \right)^{-\gamma^{\text{LE}}} \cdot f_{\text{cut}}(E, Z \cdot R_{\text{cut}}^{\text{LE}}) \\ J_k^{\text{HE}}(E) &= J_0^{\text{HE}} f_k^{\text{HE}} \left(\frac{E}{E_0} \right)^{-\gamma^{\text{HE}}} \cdot f_{\text{cut}}(E, Z \cdot R_{\text{cut}}^{\text{HE}}) \end{aligned} \quad (4.1)$$

The superscripts “LE” and “HE” refer to the low energy and high energy components. The hypothesis of two independent components means also that $\sum_k f_k^{\text{LE}} = 1$ and $\sum_k f_k^{\text{HE}} = 1$.

In this scenario, the combined fit uses several free parameters:

- f_k^{LE} : $N - 1$ fractions (see section 3.3.2) for the low energy component;
- f_k^{HE} : $N - 1$ fractions for the high energy component;
- Two spectral normalizations J_0^{LE} and J_0^{HE} ;
- Two spectral indexes γ^{LE} and γ^{HE} ;
- Two maximum rigidities $R_{\text{cut}}^{\text{LE}}$ and $R_{\text{cut}}^{\text{HE}}$.

The deviance of the spectrum has the same expression of eq. 3.14.

$$D_J = \sum_m \frac{(J_m^{\text{obs}} - J_m^{\text{exp}})^2}{\sigma_m^2} \quad (4.2)$$

In this case, the expected flux can be written as $J_m^{\text{exp}} = J_m^{\text{LE}} + J_m^{\text{HE}}$, while J_m^{obs} is the observed spectrum in the m -th energy bin.

An important point to note is that the two components are not fixed with respect to each other but the relative normalization between them can change. In formula 4.1, this is expressed by the two normalization factors $J_0^{\text{LE,HE}}$. The best relative normalization, spectral parameters and mass fraction, can be obtained by minimizing the χ^2 as in the previous chapter.

It is possible to define $t_1 = \sum_i (J_i^{\text{HE}})^2$, $t_2 = \sum_i (J_i^{\text{LE}})^2$, $t_3 = \sum_i J_i^{\text{HE}} J_i^{\text{obs}}$, $t_4 = \sum_i J_i^{\text{LE}} J_i^{\text{obs}}$, $t_5 = \sum_i J_i^{\text{LE}} J_i^{\text{HE}}$,

where the index i refers to the energy bin. The two normalization factors can be expressed such as:

$$\begin{aligned} J_0^{\text{HE}} &= \frac{t_2 t_3 - t_4 t_5}{t_1 t_2 - (t_5)^2} \\ J_0^{\text{LE}} &= \frac{t_1 t_4 - t_3 t_5}{t_1 t_2 - (t_5)^2} \end{aligned} \quad (4.3)$$

In the following I will focus on the technical issues encountered in the implementation of the extended combined fit and its importance compared to the combined fit above the ankle.

4.2.2 Technical issues

Since the number of parameters has doubled with respect to the above-ankle fit case and the minimization is more difficult and computationally demanding, there is a higher risk of getting stuck in a local minimum in the spectral parameters space, from which the minimizer cannot escape.

For this reason, the combined fit procedure is performed more than once, changing each time the initial values for the spectral parameters and assigning them random values in the ranges of interest. As a first step the ranges for the variables γ^{LE} , $\log_{10}(R_{\text{cut}}^{\text{LE}}/V)$, γ^{HE} and $\log_{10}(R_{\text{cut}}^{\text{HE}}/V)$ are defined, then a random starting point within them is selected and the fit is performed, saving the best fit values. Using this procedure several minima are found and the best is chosen.

This procedure, starting from certain reasonable values of spectral parameters, allows us to rely on the true minimum for a defined scenario not dependent on the initial condition of the fit. At this stage we can focus on different scenarios explored with the extended combined fit.

4.3 Results

In this section, the results of the extended combined fit are illustrated.

In subsection 4.3.1 a first attempt to extend the energy range of the fit is presented: in this case the structure is simply duplicated introducing an additional extra-galactic component. Both components are made of all nuclear species, accelerated with different spectral parameters.

In section 4.3.2 it is discussed how the end of the galactic spectrum influences the results of the extended combined fit. Following other works in literature [84, 2], the galactic flux is identified with the heavy component of KASCADE-GRANDE (K-G) measurements.

In section 4.3.3 a fit is performed using only protons in the low energy component. This is due to the fact that we want to mimic the interactions at the sources: in some astrophysical scenarios, the nucleus-gamma interactions with photons permeating the environment surrounding the sources can create a copious flux of escaping light particles.

In this case the normalization and the cutoff of the galactic component are fitted. Two scenarios are going to be tested: one in which a single rigidity cutoff for the two components is fitted and a second one in which the proton contribution has a different rigidity cutoff compared to the high energy fluxes.

4.3.1 Combined fit using two extra-galactic populations

As a first approach, a duplication of the combined fit structure was performed. The implemented model consists of two independent components, capable to accelerate all the nuclear species with different spectral parameters. This implementation corresponds to the astrophysical hypothesis of two independent class

of extra-galactic sources; in addition, the end of the galactic spectrum is supposed to be subdominant in this case. The two population are identical when the fit starts; assigning different ranges to the spectral parameters it is possible to remove this degeneracy.

For this test, we will use is TALYS as the photo-disintegration cross section model and the Gilmore EBL model (STG). The hadronic interaction model used is EPOS-LHC; in addition, a flat evolution of the sources is considered, including the overdensity of the local sources (detailed in section 3.5.3). For this particular case, we assume the source evolution to be the same for both components.

The best fit parameters are shown in tab 4.1 (left case), referring to the low and high energy component with “LE” and “HE”. The fitted spectrum and composition are shown in 4.3 and 4.4. In figure 4.3(top) the measured energy spectrum is plotted along with the best fit function and with the partial spectra corresponding to the contribution from each representative mass at the sources, while on the bottom the predicted energy fluxes at the Earth are grouped according to the mass number of the particles reaching the top of atmosphere.

Many interesting features can be noted:

Parameter	OD		NO OD	
	LE	HE	LE	HE
$I_{\text{H}}(\%)$	49 ± 0.1	$O(10^{-9})$	49.5 ± 0.3	$O(10^{-6})$
$I_{\text{He}}(\%)$	8 ± 0.1	27.8 ± 0.1	5.8 ± 0.1	25 ± 0.3
$I_{\text{N}}(\%)$	43 ± 0.3	70.4 ± 10	44.7 ± 0.1	60.8 ± 0.3
$I_{\text{Si}}(\%)$	$O(10^{-10})$	$O(10^{-6})$	$O(10^{-10})$	13 ± 0.1
$I_{\text{Fe}}(\%)$	$O(10^{-10})$	1.8 ± 0.6	$O(10^{-10})$	1.2 ± 0.01
γ	3.46 ± 0.1	-1.96 ± 0.1	3.5 ± 0.1	-2.21 ± 0.1
$\log_{10}(R_{\text{cut}}/V)$	19.6 ± 1.5	18.15 ± 0.01	21 ± 4	18.12 ± 0.01
D_{J}	39(24)		37.2(24)	
$D_{X_{\text{max}}}$	514.2 (329)		522.4 (329)	
D_{tot}	553.3(353)		559.6(353)	

Table 4.1: Best fit values for the extended combined fit with and without overdensity correction.

- The high-energy component consists of a hard injection spectrum ($\gamma \simeq -2$) and a low energy cutoff at the sources. For this low value, the observed suppression of the spectrum at the highest energies can be addressed to the rigidity cutoff at the acceleration rather than to propagation energy losses.
- On the other side, the low-energy component presents an extremely soft injected energy spectrum, with a spectral index larger than 3. Its rigidity cutoff is rather high ($\log_{10}(R_{\text{cut}}/V) \simeq 21$) with a large uncertainty, which can be explained by the fact that the suppression of such component is mainly due to the propagation effects, making the exact value of the maximum energy at sources almost irrelevant and allowing for a non-negligible amount of protons in the ankle region.

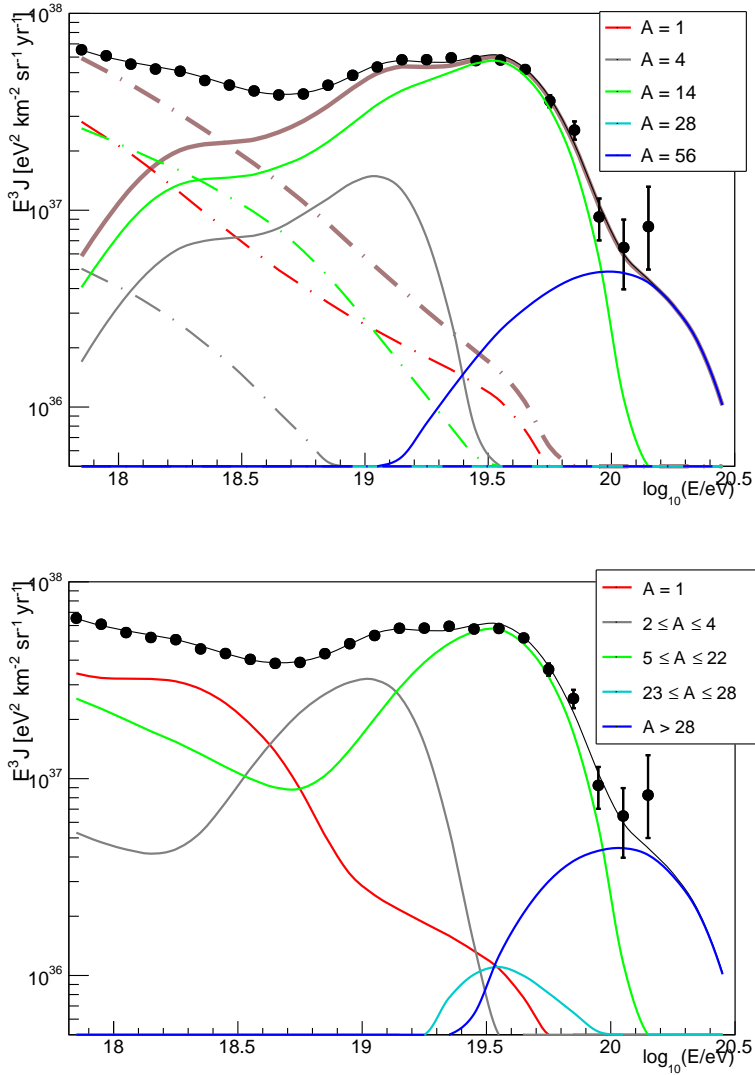


Figure 4.3: Spectrum of two components at Earth. Top: The dash-dotted lines represent the low energy component, while the solid lines represent the high energy component. The sum of each independent component is drawn in brown, while the solid black line is the sum of the two components. Each curve corresponds to one representative elements at the sources for both solid and dashed lines.

Bottom: The all-particle best fit function and the partial spectra related to different detected mass groups.

In the top panel of figure 4.5, the injection spectra given by the best fit solution are shown for all the representative masses grouped at Earth and for both populations of sources. Concerning the high-energy component, the abundance of nuclear elements at the sources is dominated by intermediate-mass nuclei (He and N), with a small contribution from Fe nuclei. On the other hand, there is no significant contribution from H, since all the protons reaching Earth are either

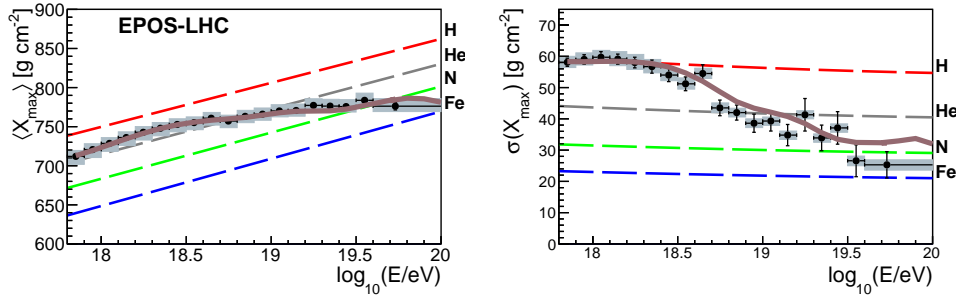


Figure 4.4: Average and standard deviation of the X_{\max} distribution at each energy, as measured by Auger black points; grey bands are systematic uncertainties and predicted by EPOS-LHC for various pure compositions (thin lines) and for the composition predicted by our model at the best fit (thick brown line). The mass numbers are grouped as follows: $A = 1$ (red), $2 \leq A \leq 4$ (grey), $5 \leq A \leq 22$ (green), $23 \leq A \leq 38$ (cyan), $A \geq 39$ (blue).

secondary particles or primary ones injected by the low-energy component. In fact, the low-energy population of sources exhibits a mass composition dominated by light elements (mainly H and N, with a smaller amount of He).

The relative abundances of the partial spectra at Earth are plotted in 4.5 (bottom panel). It is worth to notice that no mass information is available for the energies above $10^{19.7}$ eV (as indicated by the dashed lines). According to the best fit, a very low (below few %) contribution from masses with $A \leq 4$ is required at the highest energies.

The spectral index for the high energy component is $\gamma \simeq -2$; this value is different compared to the results presented in the previous chapter (table 3.6) and to the one published in [2]. One could conclude that the low energy component might affect the fit above the ankle; however, it is known that in the negative γ region, the overall flux is shaped by the fractions, rather than the spectral parameters. This explains why in this case the sensitivity to the spectral index becomes poor [2], as already outlined in the combined fit paper and in the previous section.

For the sake of completeness, in table 4.1 (last two columns) we report the fit results obtained in the reference scenario without the overdensity correction. The deviance is only slightly worsened when the overdensity correction is not applied: this is almost exclusively due to the increase of $D_{X_{\max}}$, as D_J is basically unchanged. Also, the parameter values are not significantly modified.

When the overdensity correction is taken into account, the low-energy component is almost unchanged: as expected, the increased number of local sources affects only the fit at the highest energies. On the other hand, the effect on the high-energy component is qualitatively in agreement with the one observed in the previous chapter (fit above the ankle).

This case is taken as reference and the parameter space was further explored: for example, by changing the models for photo-disintegration, hadronic interaction and source evolution, the role of the systematic uncertainties has been explored.

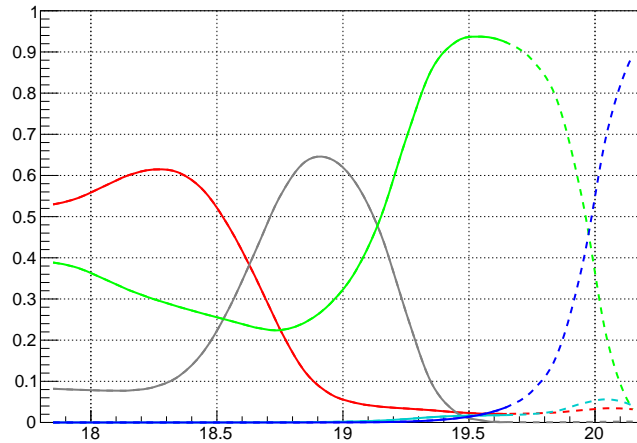
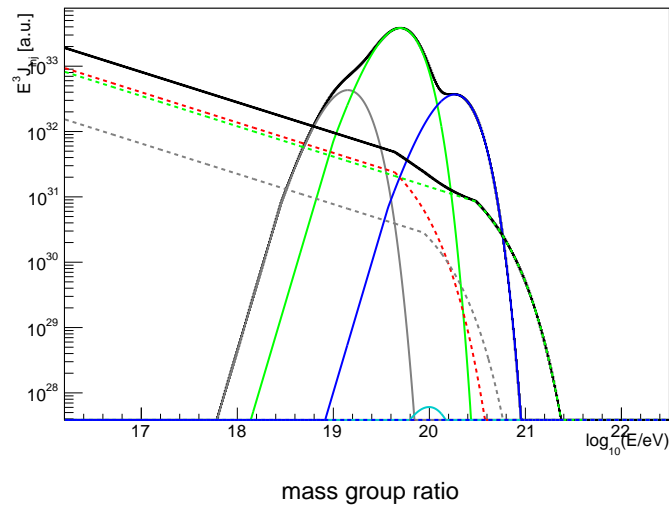


Figure 4.5: On the top: injection spectra at sources multiplied by E^3 for the low-energy (dashed line) and the high-energy (continuous line) components. The legenda is the same of figure 4.3 (left panel).

On the bottom: relative abundances at the top of atmosphere as a function of the energy. The dashed lines highlight the energy region $E > 10^{19.7}$ eV where there is no mass composition information. The mass numbers are grouped as in figure 4.3 (bottom panel).

A more detailed study can be found in E. Guido PhD thesis [112].

4.3.2 Including the galactic component

In the scenario explored in the previous section, a description of the Auger energy spectrum and composition was provided at $E \geq 6 \cdot 10^{17}$ eV using only two extra-galactic components. In this section I test the influence of the end of the galactic component on the combined fit.

The standard version of the SuperNova remnant (SNR) paradigm suggests that SNRs may accelerate cosmic rays up to rigidity $R \sim (3 - 5) \cdot 10^6$ GV, which leads to iron nuclei with maximum energy $7.8 \cdot 10^{16} - 1.3 \cdot 10^{17}$ eV. This range of energies should also correspond to the end of galactic CRs. On the other hand, it has been speculated that some rare but more energetic SN events may give rise to CRs with even larger energies [120], although there may be severe theoretical difficulties in understanding how to achieve such high energies [79]. In this section I report the modelling of the galactic component according to the KASCADE-Grande (K-G) measurements [121], as was already done in other works [2, 84]. In the energy region $10^{17} - 10^{18}$ eV the KASCADE-Grande collaboration distinguishes two different components. In [122, 121], the presence of two separate cosmic rays components is discussed: one light, so called “electron-rich” and the other heavy, called “electron poor”, with different spectra. The technique employed to derive the all-particle energy spectrum and the abundance of “light” and “heavy” primaries is based on the correlation between the number of charged particles (N_{ch}) with energy $E > 3$ MeV, and muons (N_{μ}) with kinetic energy $E > 230$ MeV on an event-by-event basis. The basic idea that motivates their studies is that the total number of secondary particles at observation level is related to the primary energy while the energy sharing between the electromagnetic and the hadronic (i.e. muonic) shower components is related to the primary mass. Therefore, the primary energy $\log_{10}(E/\text{GeV})$ is assumed to be proportional to the shower size $\log_{10}(N_{\text{ch}})$:

$$\log_{10}(E/\text{GeV}) = [a_{\text{H}} + (a_{\text{Fe}} - a_{\text{H}}) \cdot k] \cdot \log_{10}(N_{\text{ch}}) + b_{\text{H}} + (b_{\text{Fe}} - b_{\text{H}}) \cdot k \quad (4.4)$$

with k :

$$k = \frac{\log_{10}(N_{\text{ch}}/N_{\mu}) - \log_{10}(N_{\text{ch}}/N_{\mu})_{\text{H}}}{\log_{10}(N_{\text{ch}}/N_{\mu})_{\text{Fe}} - \log_{10}(N_{\text{ch}}/N_{\mu})_{\text{H}}} \quad (4.5)$$

In this way, it is possible to calculate the primary energy per individual shower on the basis of the reconstructed N_{ch} and N_{μ} . The k parameter is, by definition, a number centered around 0 for H initiated showers and 1 for Fe ones if expressed as a function of N_{ch} . The separation into mass groups was chosen for k values between CNO and Si initiated showers, based on Monte-Carlo simulations.

The heavy component is shown in 4.6 (left panel) and depends on the hadronic interaction model used. In [122], this is parametrized using a normalization factor, two spectral indexes γ_1 and γ_2 and an energy break E_b , as written in equation 4.6.

$$J(E) = J_0^{\text{G}} \cdot \begin{cases} E^{-\gamma_1} & E \leq E_b \\ E^{-\gamma_2} & E > E_b \end{cases} \quad (4.6)$$

Because the heavy component is less abundant than the other component and it seems to decrease at energy $E \simeq 10^{18}$ eV, this component can be identified as

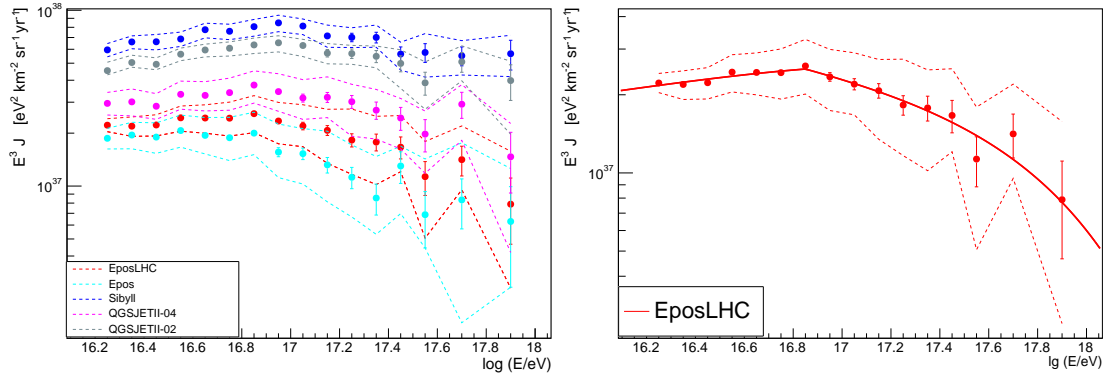


Figure 4.6: On the left: Heavy component of K-G as shown in [122] for different hadronic models. On the right: fit of the K-G data (EPOS-LHC) using the equation 4.6.

the galactic component we want to introduce in our fit.

Unfortunately for our purposes, the Auger measurements and the K-G ones overlap only in a small energy range, because the K-G data end at 10^{18} eV. Since our assumption is that the heavy component of K-G coincides with the galactic component and it is expected that the galactic component decreases with the energy, it is reasonable to include an exponential cutoff, expressed in equation 4.7, in the expression 4.6,

$$f_{\text{cut}}(E, E_{\text{cut}}^G) = \exp\left(-\frac{E}{E_{\text{cut}}^G}\right) \quad (4.7)$$

where we assume $E_{\text{cut}}^G = 10^{18}$ eV.

Therefore, I perform a fit of the K-G data using the equation 4.6 with an exponential cutoff; on the right panel of figure 4.6 this is shown (red line) in the case EPOS-LHC is assumed as hadronic interaction model.

Param.	value
J_0^G ($\text{eV}^{-1}\text{km}^{-2}\text{s}^{-1}\text{sr}^{-1}$)	$(7.61 \pm 0.04) \cdot 10^{-14}$
γ_1	2.86 ± 0.01
γ_2	3.19 ± 0.04
$\log_{10}(E_b/\text{eV})$	16.85 ± 0.001

Table 4.2: Best fit parameters for the electron-poor component fit shown in figure 4.6 (right).

In order to investigate what role the galactic component plays in the fit above $10^{17.8}$ eV, the same fit detailed in the previous section was performed taking into account the galactic component. Because the K-G collaboration does not provide a specific atomic mass of the heavy component, the mass of the galactic component is fixed and, for simplicity, is assumed to be made by a single atomic mass. Three different fits were performed, assuming the galactic component consists entirely of iron, silicon or nitrogen.

The results are shown in table 4.3. Note that for all the results presented in this and in the following sections, we use STG configuration, using EPOS-LHC as the hadronic interaction model, including overdensity correction (the same scenario of the previous section).

	Iron		Silicon		Nitrogen	
	LE	HE	LE	HE	LE	HE
$I_H(\%)$	39.5 ± 0.1	$O(10^{-9})$	48.2 ± 0.1	$O(10^{-9})$	56.1 ± 0.1	$O(10^{-9})$
$I_{He}(\%)$	46.3 ± 1	21.9 ± 0.1	28.6 ± 0.5	23.9 ± 1	9 ± 0.3	25.6 ± 0.1
$I_N(\%)$	14.1 ± 1	75.8 ± 2	23.2 ± 0.5	74 ± 14	34.8 ± 0.3	72.3 ± 2
$I_{Si}(\%)$	$O(10^{-9})$	$O(10^{-9})$	$O(10^{-9})$	$O(10^{-9})$	$O(10^{-9})$	$O(10^{-9})$
$I_{Fe}(\%)$	$O(10^{-9})$	2.3 ± 0.6	$O(10^{-9})$	2 ± 0.8	$O(10^{-9})$	2 ± 0.7
γ	3.25 ± 0.03	-1.64 ± 0.12	3.26 ± 0.02	-1.84 ± 0.1	3.31 ± 0.03	-1.99 ± 0.1
$\log_{10}(R_{\text{cut}}/V)$	21 ± 2	18.17 ± 0.01	20.8 ± 1.6	18.15 ± 0.01	19.5 ± 0.4	18.14 ± 0.01
D_J	52.4(24)		45(24)		41.4(24)	
$D_{X_{\text{max}}}$	768.8 (329)		533.3 (329)		512.5 (329)	
D_{tot}	821.2(353)		578.3(353)		553.9(353)	

Table 4.3: Best fit parameters for the extended combined fit using two extra-galactic components and including the galactic one.

An important aspect to note is the following: if it is assumed a galactic component made of heavy elements, the fit is worse compared to the previous section; instead, in the case where we assume a galactic component made of nitrogen, this is not distinguishable from the case presented in the previous section. In other words, comparing the results in the last column of table 4.3 with 4.1(left case), if one assumes two independent extra-galactic components with or without a galactic component, the fit is not able to prefer one scenario to the other. The spectral parameters are quite similar, the only difference can be seen in the mass fraction of the low energy component: in fact, the fit adjusts the mass fraction, increasing or decreasing the nitrogen fraction in absence or presence of the galactic component. Looking at the two composition fits (figures 4.4 and 4.7 (bottom)), the two plots seem indistinguishable.

A sizeable amount of medium-mass elements such as nitrogen at these energies might seem surprising; at this energies the galactic component is supposed to be almost exhausted for energetic reasons and hence dominated by heavy elements, while the extra-galactic one, being at its onset, would be dominated by light elements. However, scenarios have been proposed in which the galactic flux at these energies would mostly originate from Wolf-Rayet stars, dominantly emitting medium-mass elements. Considering that the number of Wolf-Rayet stars in our Galaxy is $\simeq 1200$, this corresponds to $\simeq 1$ Wolf-Rayet explosion in every 7 supernova explosions occurring in the Galaxy, it was found that such a galactic contribution of cosmic rays is expected to be dominant between 10^{17} and 10^{18} eV [123].

We conclude that the two astrophysical scenarios both fit equally well the Auger data up to $E = 10^{17.8}$ eV.

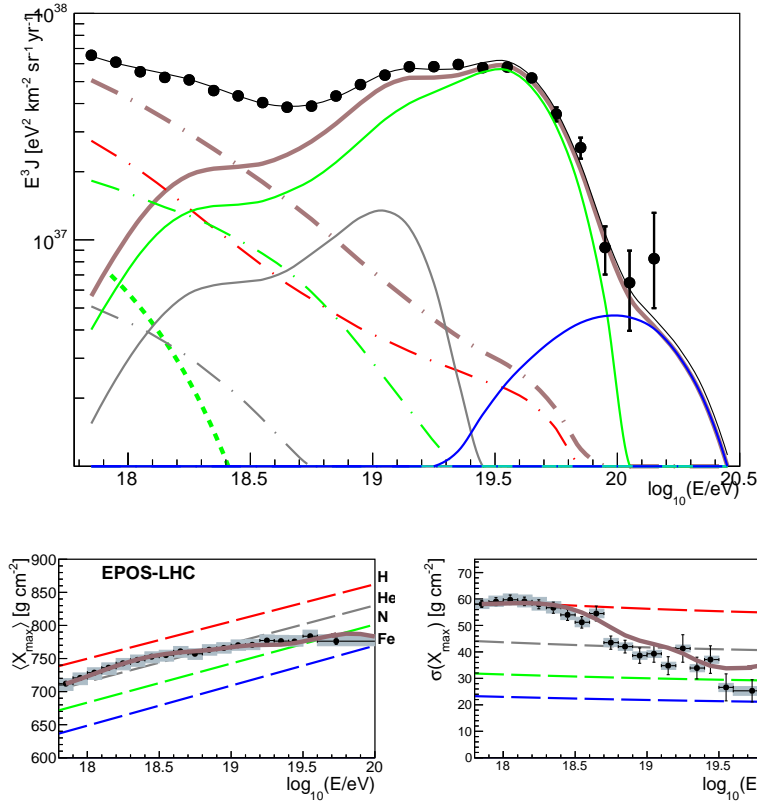


Figure 4.7: Top: Spectrum of two components at the Earth. The dash-dotted lines represent the low energy component, while the solid lines represent the high energy component. The sum of each independent component is drawn in brown, while the solid black line is the sum of the two components. The color legend is the same of figure 4.3 (bottom). The green dashed line represents the galactic component in the nitrogen case.

Bottom: average and standard deviation of X_{max} distribution at each energy, as measured by Auger (black points; grey bands are systematic uncertainties) and predicted by EPOS-LHC for various pure compositions (thin lines) and for the composition predicted by our model at the best fit (thick brown line).

4.3.3 Low energy component made of protons

The fit performed using two complete extra-galactic components (subsection 4.3.1) is capable to explain the Auger spectrum and composition starting from $6 \cdot 10^{17}$ eV using two completely independent extra-galactic components. In 4.3.2 it was shown how, taking into account the end of the galactic spectrum, a heavy galactic component is strongly disfavoured, while the best fit was found with an intermediate-mass component, in our case made of nitrogen. The fit is not able to distinguish this case from the case presented in 4.3.1. At this stage we want to test a different scenario, inspired by the disintegration of nuclei in an environment surrounding the source.

In fact, while getting accelerated in a magnetic environment confining them, cos-

mic rays can interact with the radiation. The ejection spectra of the particles and the amount of the different ejected nuclei can thus differ from the spectrum resulting from the acceleration process for the injected nuclei. In particular, neutrons escaping from the sources will decay into protons on their way to Earth, so that the ejection spectrum of the neutrons can be absorbed into the one of the protons. Several recent studies have focused on this, with different approaches and for different source characteristics (see next chapter).

Therefore, in this case we assume the presence of a low-energy component, which injects only protons and contributes to the low energy region.

At the same time, because we expect that a low energy component fully made of protons cannot fit the mass measurements, as already shown in section 4.1, we choose to fit the normalization of the galactic component (the parameter J_0^G in equation 4.6) and the cutoff energy E_{cut}^G reported in equation 4.7.

In order to mimic source mechanism effects, two different spectral indexes and a single rigidity cutoff are fitted, as it would be expected if the two populations are produced in the same sources.

For this reason the fitted parameters are:

- A single rigidity cutoff, two spectral indexes and two normalizations for both extra-galactic components;
- 4 parameters for the high energy component (for 5 mass fractions above the ankle), such as standard combined fit presented in the previous section. We do not fit any mass parameter for the low energy component because we are considering only protons below the ankle;
- The normalization factor J_0^G and the cutoff E_{cut}^G of a galactic component modelled according to eq. 4.6 including an exponential cutoff.

Also, in this case, a study of the result of the fit as a function of the galactic mass has been done. Here we report only the case in which this is assumed to consist purely of nitrogen, which is the best in terms of deviance, as shown in the previous section.

The K-G data we are taking into account are those one presented in the right figure of figure 4.6, obtained using the hadronic interaction model EPOS-LHC. We present both the fitted value J_0^G and the ratio J_0^G/J_0^{KG} , where J_0^{KG} is the nominal value obtained by the K-G data fit, shown in tab 4.2.

The results are reported in the second and third columns of table 4.4. The parameters at the best fit present the same features of other cases (i.e. hard injection spectrum at the high energies while soft injection spectrum for protons), while the deviance is significantly worse.

One could ask at this point if this scenario can be improved using two independent rigidity cutoffs, as already shown in the previous section. This corresponds to the hypothesis of two classes of sources with different spectral parameters and different mass composition at the escape. The results are shown in the last two columns of table 4.4, while spectrum and X_{max} moments for the two cases are shown in figure 4.8.

Parameter	Single cutoff		Two cutoffs	
	LE	HE	LE	HE
$I_{\text{H}}(\%)$	1 (fixed)	4.7 ± 0.01	1 (fixed)	$O(10^{-9})$
$I_{\text{He}}(\%)$	0	29.1 ± 2	0	27.4 ± 0.1
$I_{\text{N}}(\%)$	0	65 ± 5	0	70.6 ± 12
$I_{\text{Si}}(\%)$	0	$O(10^{-9})$	0	$O(10^{-9})$
$I_{\text{Fe}}(\%)$	0	1.1 ± 0.5	0	2 ± 2
γ	3.05 ± 0.04	-1.67 ± 0.1	3.34 ± 0.06	-1.66 ± 0.1
$\log_{10}(R_{\text{cut}}/V)$	18.2 ± 0.2		21.4 ± 1.6	18.18 ± 0.01
$\log_{10}(J_0^{\text{G}}/\text{eV}^{-1}\text{km}^{-2}\text{s}^{-1}\text{sr}^{-1})$	-12.85 ± 0.3		-12.85 ± 0.3 (1.88)	
$(J_0^{\text{G}}/J_0^{\text{KG}})$	1.88		1.88	
$\log_{10}(E_{\text{cut}}^{\text{G}}/\text{eV})$	18.57 ± 0.01		18.53 ± 0.03	
D_{J}	78.9(24)		39.4(24)	
$D_{X_{\text{max}}}$	536.7 (329)		530.2 (329)	
D_{tot}	615.6(353)		569.6(353)	

Table 4.4: Best fit parameters for the extended combined fit using using a sub-ankle contribution made of protons. The galactic component is included, in this case assumed to consist entirely of nitrogen, fitting the galactic normalization and cutoff.

Similar to what we found in the case with two extra-galactic components (section 4.3.1), the high-energy LE component has a very low and negative spectral index, while the low-energy light component injects particles with a very soft spectral index $\gamma \sim 3$.

As shown in figure 4.8, the galactic component is dominant only in the first energy bins included in the fit, since above $\sim 10^{18}$ eV, the extra-galactic contribution dominates. If compared with the case with two extra-galactic components (table 4.1), it is clear that the main differences with it is a predicted mass composition dominated by N instead of H at the lowest energies, due to the pure nitrogen of the galactic component. However, comparing the deviance with respect to previous cases, it is possible to affirm that the agreement to the experimental data is not as good as the other cases, for both choices of $R_{\text{cut}}^{\text{LE}}$.

Finally, some further questions can be raised. In table 4.4, the ratio $J_0^{\text{G}}/J_0^{\text{KG}}$ was shown, which represents how much the normalization of the K-G flux is increased in order to fit the data. It is obtained that the required galactic component is roughly two times more abundant than the K-G data, which is not in the agreement with the systematic uncertainties reported by the K-G collaboration [122] and presented in figure 4.6.

At the same time, this scenario suggests a high value for the galactic cutoff, at an energy higher than the last experimental point. One could ask if it is physically reasonable to assume a galactic flux so abundant even at the highest energies.

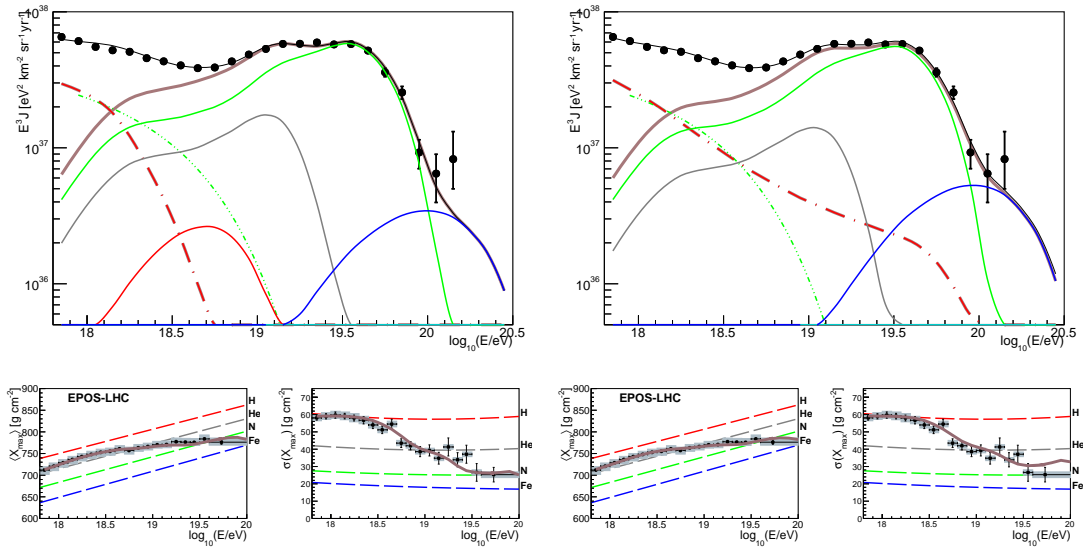


Figure 4.8: Top: spectrum of two components at the Earth using one (left) or two (right) rigidity cutoffs. The dash-dotted lines represent the low energy component, while the solid lines represent the high energy component. The sum of each independent component is drawn in brown, while the solid black line is the sum of the two components. The color legend is the same of figure 4.3 (bottom). The green dashed line represents the galactic component in the nitrogen case. Bottom: average and standard deviation of X_{\max} distribution in the two cases, together with the Auger data (black points; grey bands are systematic uncertainties) and predicted by EPOS-LHC for various pure compositions (thin lines) and for the composition predicted by our model at the best fit for the two cases (thick brown line).

To summarize, it is possible to affirm that the results found in the last column of table 4.4 are comparable to that one using the two extra-galactic components (see section 4.3.1) at the price of overestimating the galactic contribution.

4.4 Quality of the fit

Despite the three explored scenarios present differences, some common points can be underlined:

- The HE component requires an hard injection spectrum: this is qualitatively consistent with the ones obtained for the fit above the ankle. It is possible to deduce that the additional component below the ankle does not spoil the main features of the fit shown in the previous chapter;
- The LE component requires a soft injection spectrum: this could be explained by a source interaction model, as described in the next chapter;

- The fit is not able to distinguish between a galactic and an extra-galactic contribution at low energies. Nonetheless, the intermediate composition is favoured.
- The presence of an iron component at low energies is strongly disfavoured.

As outlined in the previous chapter, in the limit of large statistics, the probability distribution of D_{\min} is a χ^2 distribution [106]. All the presented cases have similar deviances; if we just consider the overall χ^2 per degree of freedom n , any of the tested scenarios produces a $\chi^2/n \simeq 1$.

Another possibility concerns to determine the probability distribution function of L_{\max} (or D_{\min}) by means of a Monte Carlo study. So, once found a minimization, we can make the model fluctuate and in this way we will have a deviance distribution. The **p-value** is defined as the integral of the distribution above the value found by the minimization.

The obtained p-value for the case tested in 4.3.1 is $2 \cdot 10^{-4}$, and also the other two models present similar values. It means commonly that our model is not well describing the experimental data.

Nonetheless, looking at the partial p-value for spectrum and composition in

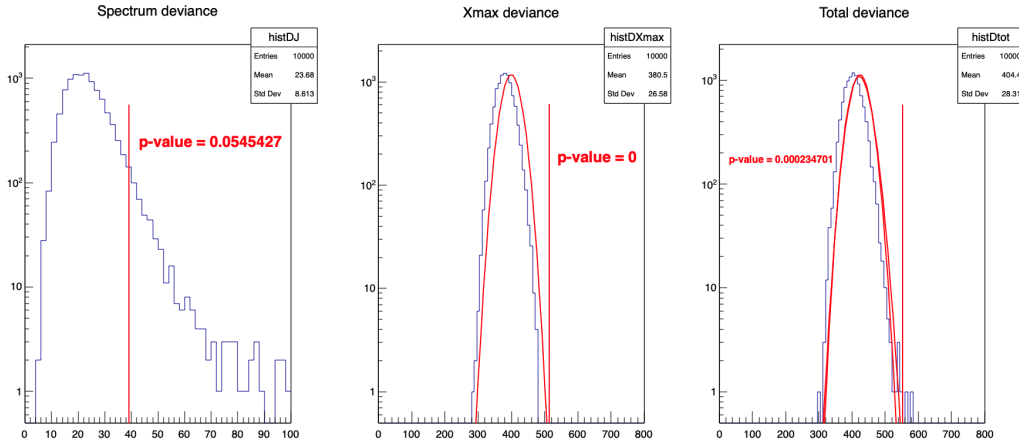


Figure 4.9: Distributions of D_J , $D_{X_{\max}}$ and D_{tot} in the mock data sets generated from the best-fit model predictions. The vertical red lines represent the corresponding values of D_J , $D_{X_{\max}}$ and D_{tot} of the found best fit.

figure 4.9, it is evident how the p-value from the spectrum deviance has a more reasonable value, while the bad result obtained in the X_{\max} deviance distribution (p-value = 0 for 10^4 randomizations) influences the total result. This is still an open problem: note that, while the spectrum used in this analysis is published [64], the X_{\max} analysis is still going on.

In addition, probably not all the systematical uncertainties have been explored and taken into account in this fit: this aspect is still under investigation in the collaboration.

4.5 Crosscheck on the errors

As already explained in the previous chapter, the used minimizer is Minuit, and in particular, we make use of its main algorithm, called **MIGRAD**. The errors shown in this work are those one calculated by MIGRAD in the assumption of χ^2 behaviour for all the parameters. In fact, given a certain parameter θ , for a χ^2 , the errors can be defined such as:

$$\sigma_{\theta}^2 \sim 2 \left[\frac{\delta^2 \chi^2}{\delta \theta^2} \right]_{\theta=\bar{\theta}}^{-1} \quad (4.8)$$

Because our fit cannot be considered in large sample limit, a crosscheck on the error values is needed. The uncertainty calculation is performed with the **Bootstrap method** [124]. Therefore the fit is performed many times, randomizing the experimental data: concerning the spectrum, each point can fluctuate following a Gaussian distribution.

Instead, the X_{\max} distributions are randomized filling histograms where each X_{\max} bin content is treated as a Poisson variable.

This procedure is applied for the fit without galactic contribution (the case explored in section 4.3.1). Performing the fit with the randomization of the experimental data, many best fit parameters are obtained. The distribution of spectral parameters, the mass fractions and their correlations after data randomization are shown in figure 4.10. From these distributions, the mean and the standard deviation are reported in table 4.5, where we present the spectral parameters and the mass fraction f at a fixed energy $E_0 = 10^{18}$ eV.

Looking at figure 4.10, it can be noticed that a strong correlation is present be-

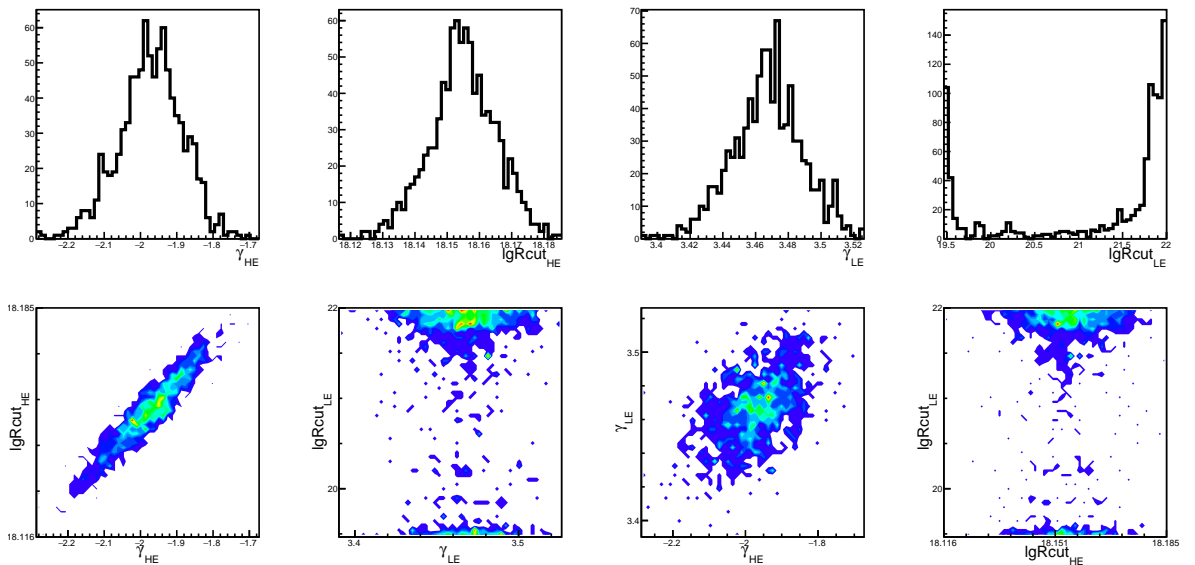


Figure 4.10: On the top: distributions of the spectral parameters in the mock traces. On the bottom: correlation between the four spectral parameters.

tween the spectral parameters ($\rho = 0.94$) concerning the HE component (bottom-left panel), similar to what was found in the single component case.

There is also correlation between the two spectral indexes, γ^{HE} and γ^{LE} (third panel to the bottom), where the correlation factor is $\rho = 0.49$.

An interesting result regards the behaviour of the spectral parameter $R_{\text{cut}}^{\text{LE}}$. In fact the low energy flux is suppressed by the interaction through the extra-galactic space rather than limited by the flux at the source. This creates a degeneracy in its distribution, which, as can be seen in figure 4.10 (top-right panel), has not a gaussian shape. It is possible to see two peaks: one at low energies, which corresponds to a local minimum, and a second peak at $E > 10^{19}$ eV. In this region the deviance is roughly the same for every value of $R_{\text{cut}}^{\text{LE}}$. In fact, the same fit was performed removing the cutoff to the low energy component and it was found the same result in terms of deviance and best fit parameters. Due to this degeneracy, also, it is affected by a huge statistic error.

From the parameter distributions it is also possible to infer information about the asymmetric errors, considering the 68% quantiles are obtained for each fitted fraction, which represents the area of the distribution of $\pm \sigma$ around the median. The asymmetric errors are reported on table 4.5 (**emin** and **emax**): we can notice that the error bars are comparable between them, so the gaussian approximation is justified. In addition, they are on the same order of magnitude of those one reported by Minuit. The two methods (MIGRAD and bootstrap) are in agreement concerning the parameter errors.

Parameter	Mean	std dev	median	emin	emax
γ^{HE}	-1.9769	± 0.0875	-1.9717	-0.0893	+0.0824
$\log_{10}(R_{\text{cut}}^{\text{HE}}/V)$	18.1542	± 0.0106	18.1545	-0.0104	+0.0100
γ^{LE}	3.4673	± 0.0210	3.4679	-0.0203	+0.0203
$\log_{10}(R_{\text{cut}}^{\text{LE}}/V)$	21.2134	± 0.8478	21.5271	-1.9903	+0.4069
f_{H}^{HE}	0.0306	± 0.0939	0.0000	-0.0000	+0.0011
$f_{\text{He}}^{\text{HE}}$	0.9527	± 0.0923	0.9824	-0.0046	+0.0024
f_{N}^{HE}	0.0166	± 0.0028	0.0167	-0.0025	+0.0025
$f_{\text{Si}}^{\text{HE}}$	0.0000	± 0.0000	0.0000	-0.0000	+0.0000
$f_{\text{Fe}}^{\text{HE}}$	0.0000	± 0.0000	0.0000	-0.0000	+0.0000
f_{H}^{LE}	0.4979	± 0.0040	0.4979	-0.0030	+0.0025
$f_{\text{He}}^{\text{LE}}$	0.0670	± 0.0072	0.0671	-0.0049	+0.0051
f_{N}^{LE}	0.4350	± 0.0042	0.4352	-0.0040	+0.0039
$f_{\text{Si}}^{\text{LE}}$	0.0000	± 0.0000	0.0000	-0.0000	+0.0000
$f_{\text{Fe}}^{\text{LE}}$	0.0000	± 0.0000	0.0000	-0.0000	+0.0000

Table 4.5: Errors obtained with the bootstrap methods for the case presented in section 4.3.1.

4.6 Expected neutrino fluxes

In this section we will summarize the expected neutrino fluxes associated with different scenarios explored in this thesis.

Neutrinos can be produced by the interactions of charged cosmic rays, both with radiation fields in the acceleration sites and with background radiation (the CMB photons and, with a much lower probability, the EBL ones) during the propagation in the intergalactic medium. The processes by which neutrinos are produced are shown in eq. 4.9. The decay of charged pions generated through the photo-pion production and of their daughter muons produce neutrinos with energies of the order of 10^{15} eV and 10^{18} eV in the case of interactions with EBL and CMB photons, respectively. On the other hand, the beta decay of neutrons and unstable nuclei generated in photo-hadronic interactions produces neutrinos with energies of the order of 10^{14} eV and 10^{16} eV in the case of interactions with EBL photons and with CMB ones, respectively.

$$\begin{aligned}
 p + \gamma &\longrightarrow n + \pi^+, \quad \pi^\pm \longrightarrow \mu^\pm + \nu_\mu(\bar{\nu}_\mu), \quad \mu^\pm \longrightarrow e^\pm + \nu_e(\bar{\nu}_e) + \bar{\nu}_\mu(\nu_\mu) \\
 n &\longrightarrow p + e^- + \bar{\nu}_e, \quad (A, Z) \longrightarrow (A, Z \pm 1) + e^\mp + \bar{\nu}_e(\nu_e)
 \end{aligned} \tag{4.9}$$

Neutrinos propagate through the intergalactic space undergoing only adiabatic energy losses due to the expansion of the Universe, hence their energy spectrum at Earth is expected to be also affected by the presence of sources beyond $z_{\max} = 1$ (few Gpc) and by their cosmological evolution. For this reason, the flux of predicted cosmogenic neutrinos associated with the best fit results of each chosen scenario can be compared with the measured fluxes (or, at higher energies, with the estimated upper limits) and such comparison could possibly constrain the cosmological evolution of sources.

The emissivity evolution for redshifts $z \leq 1$ can be parameterized as $S(z) \propto (1+z)^m$. As a first simple approach, we chose to use a continuation of such parameterization also above $z = 1$. The flux of cosmogenic neutrinos associated to the best fit results obtained in the reference scenario with the overdensity correction is shown in figure 4.11 (left plot). Since the number of expected neutrinos increases with z_{\max} , it is clear that, as expected, sources beyond $z = 1$ produce a non-negligible contribution to the total flux of cosmogenic neutrinos reaching the Earth's upper atmosphere.

The Pierre Auger Observatory is sensitive to neutrinos with energies above 10^{17} eV [125], which correspond to the energy range for neutrinos coming from the photo-pion production of UHECRs on the CMB photons. No neutrinos were observed so far, hence a 90% C.L. integrated upper limit has been set to $4.4 \cdot 10^{-9}$ GeV cm⁻² s⁻¹ sr⁻¹. It is clear that the predicted flux of neutrinos produced in the UHECRs propagation (namely **cosmogenic** neutrinos) obtained assuming no source evolution is about two orders of magnitude lower than the 90% C.L. integrated limit, even with $z_{\max} = 6$ (see left panel of figure 4.11), hence no constraints can be imposed. In fact, the energy cutoff of the nuclei from the fit is very low (of the order of few $\sim 10^{18}$ eV), hence, even if a non-negligible amount of protons is injected at sources (e.g. less than 10%), the photo-pion production can occur only on the EBL photons, which contribute to the neutrinos flux at

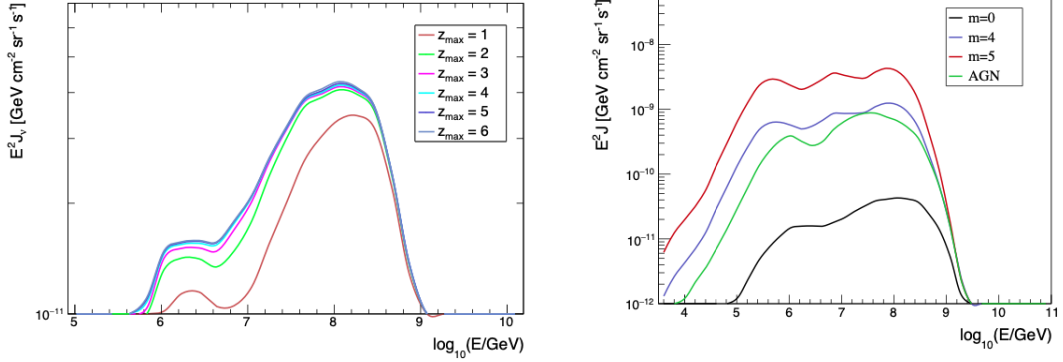


Figure 4.11: Left: The predicted flux of cosmogenic neutrinos for the above the ankle combined fit associated with the best fit results obtained for the SPG scenario with the over-density correction and no source evolution. Each curve refers to a different value of maximum redshift z_{max} from 1 to 6 in steps of 1. Right: the predicted flux of cosmogenic neutrinos for the combined fit above the ankle corresponding to the best fit results obtained making different assumptions on the source evolution [112].

lower energies and to a lesser extent because of the greater interaction length. However, the number of predicted neutrinos reaching Earth increases in the case of positive source evolution. The flux of expected cosmogenic neutrinos obtained for different source evolutions, with the assumption $z_{max} = 6$, is shown in 4.11(right).

In figure 4.12, the predicted spectrum of neutrinos obtained for $m = 5$ and $z_{max} = 6$ is compared with the 90% C.L. integrated limit provided by Auger for energies above 0.1 EeV. Even if the total number of neutrinos reaching Earth has

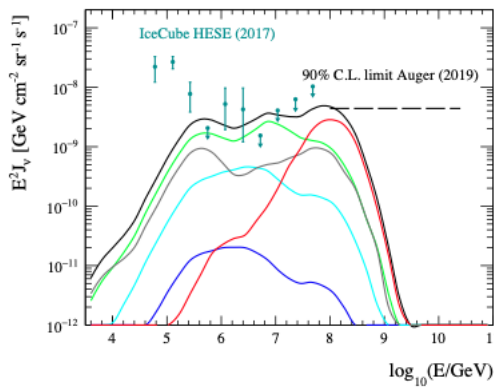


Figure 4.12: The predicted spectrum of neutrinos obtained with $m = 5$ along with the curves corresponding to the contributions from each injected representative mass to the total flux of neutrinos at Earth (color code as figure 3.12) [112].

significantly increased, such flux is below the limits. Since most of the predicted neutrinos have energies below the region where Auger could detect them, also the measurements and the upper limits provided by IceCube up to 10^{17} eV are drawn for comparison.

At this point it would be interesting to compute the expected neutrino fluxes in the extended combined fit.

As seen also for the single component case, this strongly depends on the assumed source evolution. In [112] the effect of the source evolution in the reference (STG) scenario has been studied considering different cases related to various source candidates. Since there is no physical reason to assume that the two populations of sources have the same evolution with redshift, they performed the fit assuming all their possible combinations. In particular, Star Formation (SF) objects and AGN, which have a positive source evolution for $z < 1$, have been considered as shown in eq. 4.10 and 4.11, respectively. As concerns the negative source evolution scenario, we assume a constant $m = -3$, which is approximately the expected value for Tidal Disruption Events (TDEs) [126], while for the other case:

$$S_{\text{SFR}}(z) \propto \begin{cases} (1+z)^{3.4} & z \leq 1 \\ 2^{3.7} \cdot (1+z)^{-0.3} & 1 < z \leq 4 \\ 2^{3.7} \cdot 5^{3.2} \cdot (1+z)^{-3.5} & z > 4 \end{cases} \quad (4.10)$$

$$S_{\text{AGN}}(z) \propto \begin{cases} (1+z)^5 & z \leq 1.7 \\ 2.7^5 & 1.7 < z \leq 2.7 \\ 2.7^5 \cdot 10^{2.7-z} & z > 2.7 \end{cases} \quad (4.11)$$

The results thus obtained are summarised in figure 4.13, where the total deviance is shown as a function of the source evolution of the high-energy population for each possible source evolution of the low-energy population, taking into account the systematic uncertainties from the X_{max} scale [112].

First of all, we note that all scenarios with an AGN-like evolution for the high-

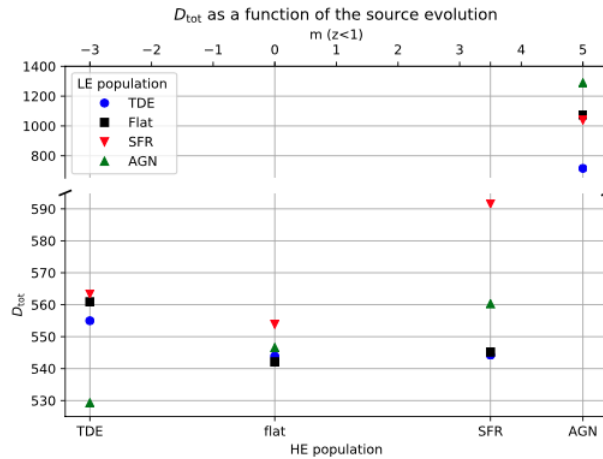


Figure 4.13: The total deviance for all the possible combinations of source evolution of the two populations. The different markers refer to fixed evolutions of the low-energy population, as written in the legend: for each one the total deviance is plotted as a function of the evolution of the high-energy population [112].

energy component can be rejected, since they cause a severe worsening of the fit.

Besides, also choosing a SFR-like evolution for the low-energy population produce in general a worsening of the goodness-of-fit regardless of the assumption on the high-energy population; however, for a negative or flat source evolution of the high-energy component the deviance is still similar to the one obtained in the reference case and such scenarios cannot be discarded.

Finally, also the fluxes of neutrinos corresponding to different source evolution configurations have been calculated: they were compared to the measurements provided by IceCube [127] below 10^{17} eV and to the Auger upper limit and expected sensitivity of GRAND [128] at higher energies. In all the considered configurations the high-energy population, being characterized by a very hard injection spectrum with a relatively low rigidity cutoff, does not provide any significant contribution to the flux of neutrinos, regardless of the chosen source evolution. On the other hand, as can be seen in figure 4.14, the low-energy population always produces a peak in the neutrino flux at $\sim 10^{16}$ eV, mainly due to the photo-pion production of protons on the EBL; unfortunately, such a predicted flux is below the measurements. A second peak at ($\sim 10^{18}$ eV) is expected, due to the interactions of protons with the CMB, in the cases where a very large rigidity cutoff is estimated for the low-energy component. Nevertheless, it is important to stress that the very large uncertainties on the energy cutoff value also strongly affect the predicted flux of neutrinos, so that the whole high-energy peak is actually encompassed within the 1σ error bands on the flux (grey band in figure 4.14).

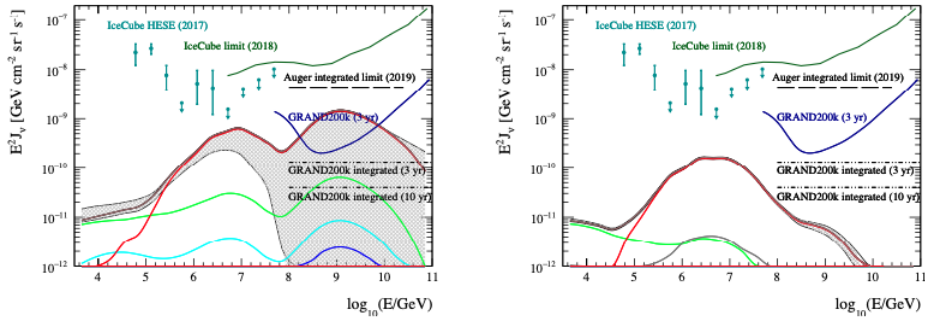


Figure 4.14: The predicted flux of neutrinos (single flavour) corresponding to the best fit results obtained with the AGN evolution for the low energy component and TDE evolution for the high energy component (best configuration in figure 4.13) (left) and in the case with no source evolution (right). The total fluxes are shown along with the contributions from each injected representative mass to the total flux of neutrinos at Earth (color code as in figure 3.12). A comparison with current results and future detectors sensitivity is also shown [112].

Therefore, at this stage, the neutrino fluxes predicted for the simple two-component scenario proposed here are not guaranteed to put any constraints on our model. Possibly, with the next-generation neutrino detectors, such as GRAND, one can exclude regions in the neutrino flux plots and therefore constrain the maximal energy of the low-energy component.

5.1 Source interaction model

In the previous chapter, an extended combined fit above $10^{17.8}$ eV of the spectrum and composition measured by the Pierre Auger Observatory was shown. From this analysis it appears that the Auger data can be fitted using two populations: one with a hard injection spectrum at high energies and a second one with a soft injection spectrum at low energies. In this chapter, we want to investigate the interactions that might take place in the source environment in order to motivate the results of the extended combined fit. These requirements favor source environments which are optically thick to nuclei-photon interactions but simultaneously optically thin to proton-photon interactions [129].

In an environment with a photon field, the photo-disintegration process generally acts as a high-pass filter, permitting the highest energy cosmic ray nuclei to escape unscattered while the lower energy ones are disintegrated inside the source region, generating nucleons with energy $1/A$ of the original nucleus of mass A [3]. The basic setup of our phenomenological model is drawn in figure 5.1.

In a first moment we study these interactions in a generic source. As a second step, this assumption is left and a potentially interesting class of sources is studied: the Starburst Galaxies (SBG). Starting from the hypothesis that the UHECRs are produced in a SBG prototype, the escaping fluxes are propagated through the extra-galactic space, taking into account a diffuse flux from identical sources uniformly distributed, and then compared to the Auger energy spectrum and composition. In addition, the effect of the hadronic interactions in the environment surrounding the sources will be taken into account. This inclusion represents a new contribution to UHECR propagation codes.

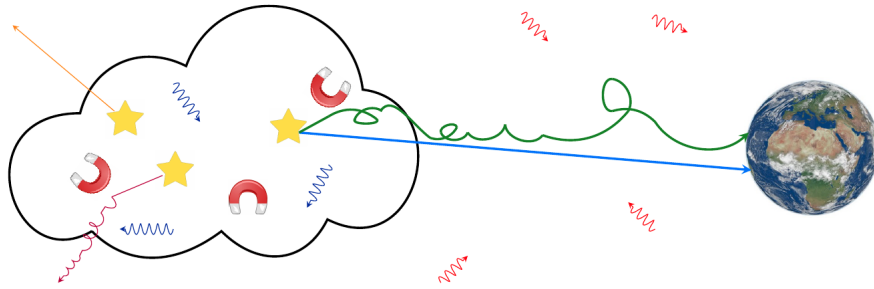


Figure 5.1: Illustration of the source-propagation model: Sources inject cosmic rays with a power law in energy, into a surrounding region of radiation and turbulent magnetic fields. After propagation through this local environment and then intergalactic space, these cosmic rays and their secondary products are detected at Earth.

5.2 The UFA model

There are several works [130, 131, 132] that consider UHECR sources embedded by photon fields in the presence of a magnetic field. Here we illustrate the procedure and the results of the Unger-Farrar-Anchordoqui (**UFA**) model [3] because it is fundamental to the understanding of this work. In their **source-propagation model**, particles are propagated inside and then outside the source, in order to compare the expected energy spectrum and composition with the measured ones.

The essential hypotheses of this model are:

- A fast acceleration mechanism and a low photon density inside the accelerator region;
- No energy is lost except through nucleus-photon interactions, and a nucleus loses one or more nucleons by photo-disintegration or undergoes photo-pion production;
- A leaky box model is assumed: this means that a particle, propagated through the environment surrounding the source, can either interact or escape. The interaction and escape rate are called τ_{int} and τ_{esc} .
- τ_{int} and τ_{esc} are independent of the position in the source environment and depend only on the energy, mass and charge of the nucleus.

In order to quantify what is the fraction of particles escaping without interaction, the key quantity to know is the ratio between the escape and the interaction times, but not the absolute value of either.

In this analysis several photon fields have been considered, with the different shapes shown in figure 5.2 (left panel). It is concluded that the position of the peak, called ϵ_0 , is the most important parameter. In the UFA analysis a broken

power law (cyan solid line in figure 5.2) is used:

$$n(\epsilon) = \begin{cases} (\epsilon/\epsilon_0)^\alpha & \epsilon > \epsilon_0 \\ (\epsilon/\epsilon_0)^\beta & \epsilon < \epsilon_0 \end{cases} \quad (5.1)$$

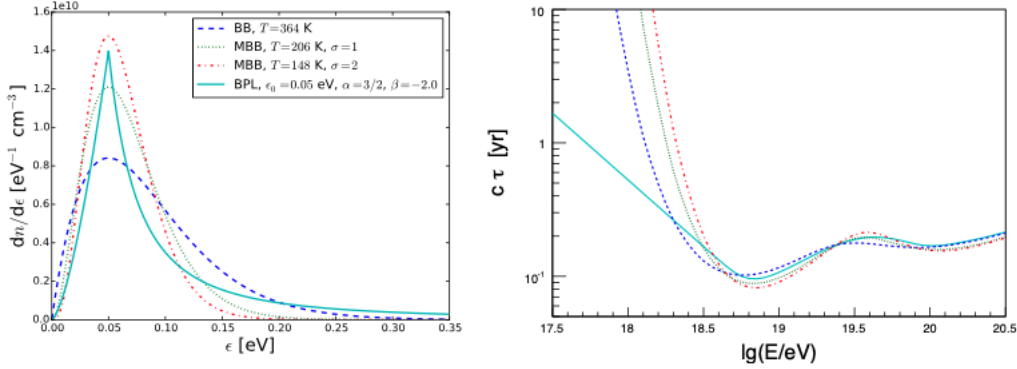


Figure 5.2: On the left: different photon spectrum used in [3]: broken power law (solid cyan), black body (dashed blue), modified black bodies (dashed green and red).

On the right: interaction time for each photon field in the case of silicon nuclei.

In the right panel of figure 5.2 the interaction times related to the tested photon fields are shown. They used numerical integration of TALYS and SOPHIA [33] for the photo-disintegration and photo-pion cross section. Note that, in case a broken power law is used, the interaction time assumes a W – shape, with two dips in correspondence of the two resonances for photo-disintegration and photo-pion production.

Concerning the escape time, it was chosen to use a power law on rigidity, to mimic the diffusion of particles in a magnetic field.

$$\tau_{\text{esc}} = \tau_0 (EZ^{-1}/E_0)^\delta \quad (5.2)$$

where τ_0 is a normalization factor and $\delta = -0.77$. The value of this source parameter was chosen in order to maximize the agreement with the experimental data at Earth, within a source-propagation model.

Using the interaction and escape time shown in the left panel of figure 5.3, nuclei are propagated through the source environment: for simplicity it was assumed to inject only a single nuclear species, in this case ^{28}Si , and fix the injection spectral index to $\gamma = 1$, such that particles are accelerated following:

$$J(E) = J_0 \left(\frac{E}{E_0} \right)^{-\gamma} \cdot f_{\text{cut}}(E, E_{\text{cut}}) \quad (5.3)$$

using the cutoff shape reported in 5.4:

$$f_{\text{cut}}(E, E_{\text{cut}}) = \begin{cases} 1 & E \leq E_{\text{cut}} \\ \exp\left(-\frac{E}{E_{\text{cut}}}\right) & E > E_{\text{cut}} \end{cases} \quad (5.4)$$

with $E_{\text{cut}} = 10^{18.5}$ eV. It is important to stress that the injected fluxes (equation 5.3) are propagated first inside and then outside the environment surrounding the source. This is a difference compared to the combined fit analysis, where we assume point-like sources and the spectral index γ refers to the fluxes ejected from the sources and the interactions inside them are neglected.

The escaping fluxes from the source are shown on the right panel of figure 5.3. The particles escaping the source environment are then propagated through the

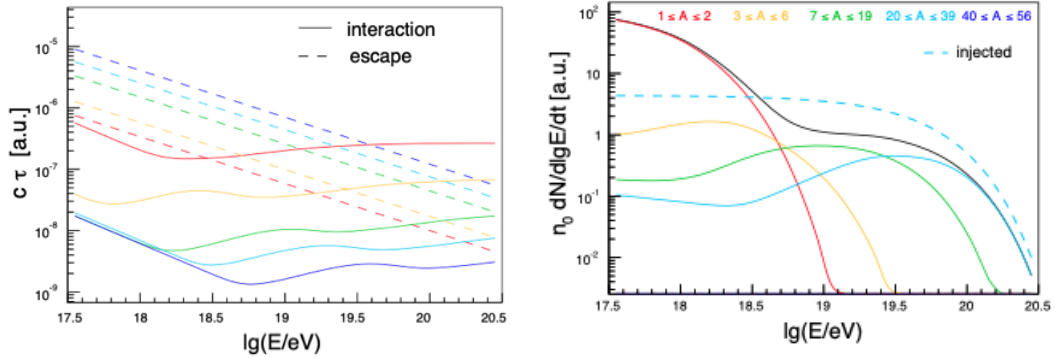


Figure 5.3: Left: Interaction and escape times for $A = 1, 4, 14, 28, 56$. Right: Injected ^{28}Si (dashed cyan) and escaping CR fluxes (red: $1 \leq A \leq 2$, yellow: $3 \leq A \leq 5$, green: $7 \leq A \leq 19$, cyan: $20 \leq A \leq 39$, blue: $40 \leq A \leq 56$), while the thin black solid line denotes the sum of all escaping nuclei. From [3].

intergalactic medium. In addition, a galactic component is considered at low energy, as an exponential function.

The resulting spectra after the propagation in the extra-galactic space are shown in figure 5.4. Tuning opportunely some parameters, such as the peak energy of the photon field density ϵ_0 , the maximal energy E_{cut} , the injected mass A , the power law of the escape δ and the ratio between interaction and escape time, this model well describes the Auger data.

5.2.1 Comparison to UFA model

An initial step of this work involves reproducing the UFA results. In order to do so, I adapted the SimProp code to include interactions inside the source environment. This is a difference with respect to the UFA work, where the extra-galactic propagation was taken into account using the propagation code *CRPropa* [91, 92, 93].

The inverse of the interaction time can be written such as [27]:

$$\frac{1}{\tau_{\text{int}}} = \frac{1}{2\Gamma^2} \int_{\epsilon'_{\text{min}}}^{2\Gamma\epsilon} \int_{\epsilon'=0}^{+\infty} \frac{n_\gamma(\epsilon)}{\epsilon^2} d\epsilon \sigma(\epsilon') \epsilon' d\epsilon' \quad (5.5)$$

The two integrals over the photon field and cross section are computed separately in SimProp: this helps to calculate the interaction time for different photon fields.

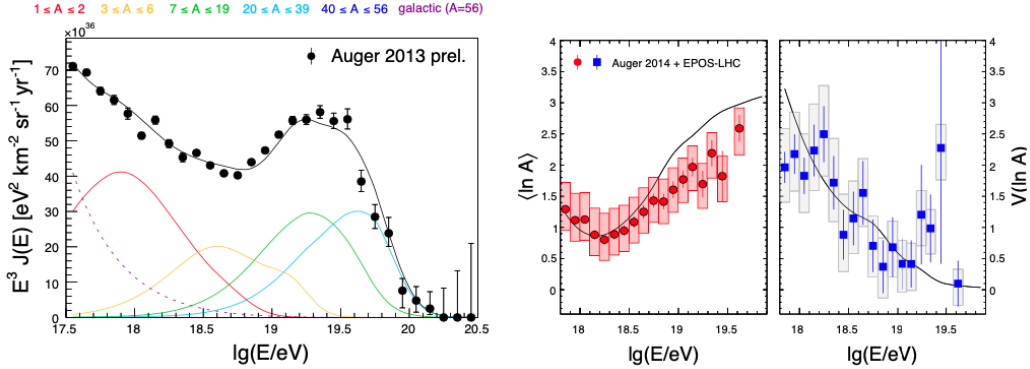


Figure 5.4: Cosmic rays spectrum and composition at Earth. The data points are from the Pierre Auger Observatory, the error bars denote the statistical uncertainties and the shaded boxes illustrate the experimental systematic uncertainties of the composition. The composition estimates are based on an interpretation of air shower data with the hadronic model EPOS-LHC; the UFA authors choose to fit $\langle \ln A \rangle$ (in red) and its variance $V(\langle \ln A \rangle)$ (in blue). The lines denote the predictions corresponding to this model [3].

In the left panel of figure 5.5, I show the photon fields that I have implemented in a modified version of SimProp, hereafter called *in-source-SimProp*, reproducing the ones shown in fig 5.2. Using the equations 5.5 and 5.2, I have calculated both the interaction and escape times (right panel of figure 5.5). At this stage we have all the ingredients necessary to reproduce UFA results: 10^6 ^{28}Si nuclei are injected with a random energy sampled from a flat distribution between 17.5 and 20.5 in $\log_{10}(E/\text{eV})$. In addition, the spectral index and the maximal energy were chosen to be in agreement to what was used in UFA model, such as the photo-disintegration cross section model (TALYS) and the EBL model (Gilmore). The results are shown in figure 5.6, in which the comparisons between the timescales (left) and the ejected spectra (right) are performed; in the right panel the ejected spectra are normalized superimposing the injected spectra (dashed cyan lines) in the two cases.

From the left panel of figure 5.6, one can see that the results of this work and the UFA ones present some differences, especially for heavy nuclei. The differences seen in the interaction times can be addressed to the different treatment of the photo-disintegration process regarding the TALYS cross section model. In SimProp, only two photo-disintegration processes are implemented for the TALYS cross section model: nucleon ejection and α -particle ejection. The interaction rates for these processes are taken to be the sum of all actual processes weighted by the number of nucleons and α -particles ejected, respectively. This ensures that the numbers of free nucleons and of α -particles at Earth are reproduced in good approximation. However, this can create some differences in the comparison of the interaction lengths with the UFA model, where the branching ratios from TALYS are directly used for the emission of the available channels.

There are also differences in the treatment of the TALYS cross section as implemented in the two approaches, as can be seen in the escape fluxes (see figure 5.6,

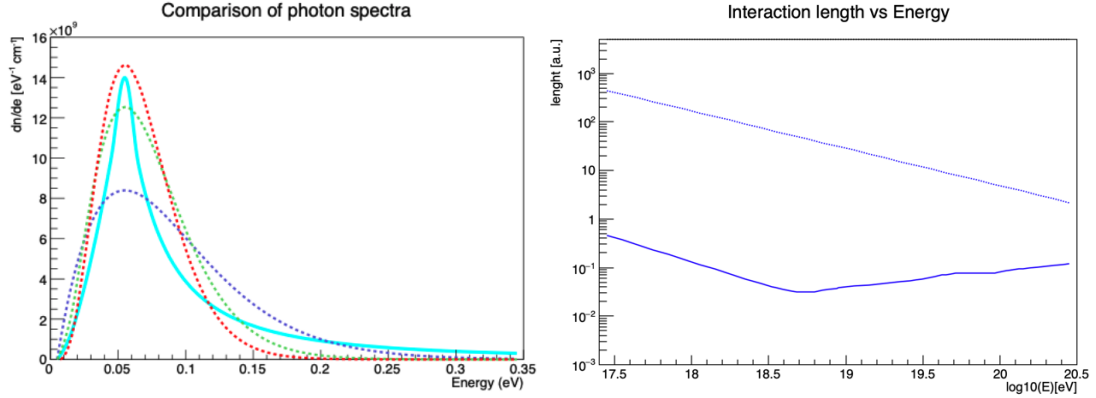


Figure 5.5: Left: Photon fields as shown in figure 5.2 computed in in-source-SimProp. As in the UFA case: broken power law (solid cyan), black body (dashed blue), modified black bodies (dashed green and red). Right: Interaction (solid line) and escape times (dashed lines) for iron nuclei assuming a broken power law spectrum.

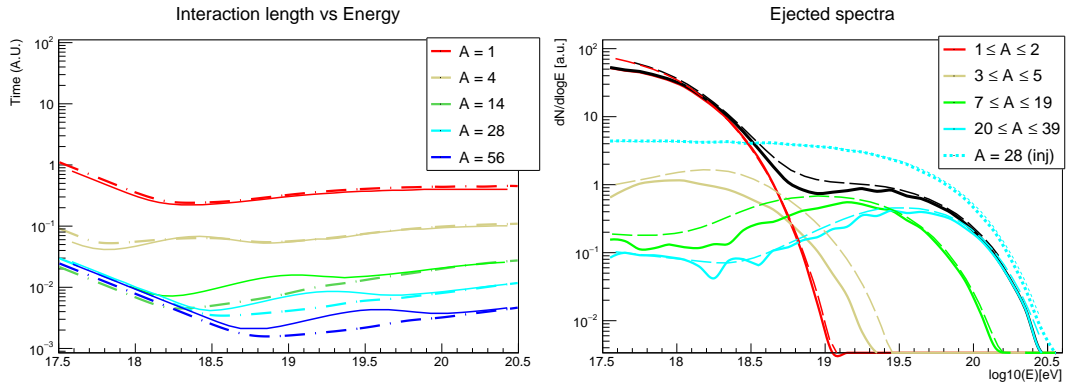


Figure 5.6: Left: Comparison between the interaction times for UFA paper (dot-dashed lines) and the ones obtained in in-source-SimProp (solid lines). Right: Escaping fluxes at the sources for UFA paper (dot-dashed lines) and my work (solid lines). The black lines represent the sum of each contributions. The fluctuations in the solid lines can be attributed to statistical reasons.

right). The most important differences can be seen in the flux of the nitrogen and helium groups, showing that the UFA model disintegrates these primaries less efficiently with respect to the cross section model in SimProp. This is due to the simplified interaction scheme used in the UFA model for the in-source interactions, where only single nucleon emission is used for photo-disintegration. The proton flux at the escape is similar for the two models, due to the slight overestimate of disintegration of helium nuclei in protons by SimProp [87]. Propagating the escaping fluxes through the Universe and taking into account the same evolution of the sources used in UFA, namely SFR (equation 4.11), in figure 5.7 I show the propagated fluxes at Earth. The solid lines represent this

work while the dot-dashed lines represent the UFA cases.

In addition to the propagated fluxes, a galactic component is taken into account,

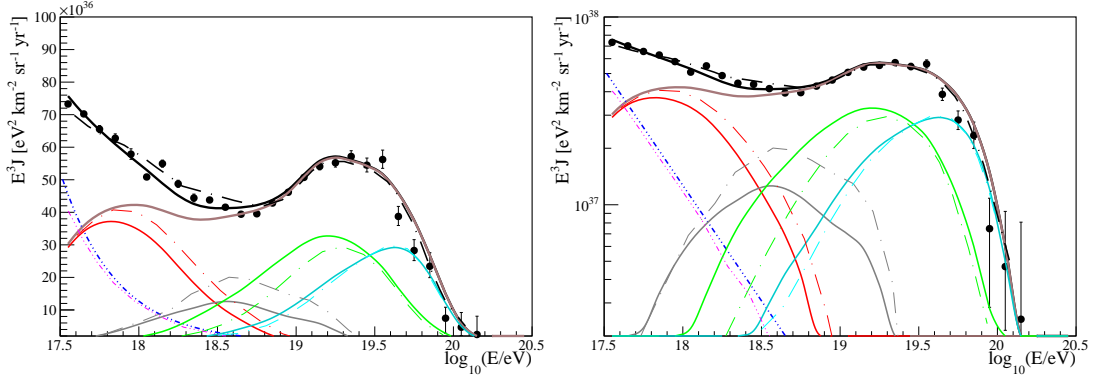


Figure 5.7: Spectrum at Earth in linear (left) and log scale (right). In this case the solid lines represent our case, the dot-dashed lines represent the UFA reference scenario. The color legend is the same of figure 4.3 (bottom). In pink the galactic component for the UFA case, in blue in this work.

as in the UFA model. It is important to stress that the galactic component plays an important role in this model in the description of the low-energy part of the spectrum. Because of the differences in the propagated fluxes, I choose to use the galactic component fitting only the normalization and using the same spectral index as the one used in UFA (dashed blue line in figure 5.7). I found that it is necessary to increase the normalization of the galactic component by a factor ~ 1.25 with respect to UFA model using the same shape.

The spectra at Earth show that the UFA+CRPropa model used for the propagation in the extra-galactic space induce more efficient disintegrations in the silicon and nitrogen groups, whose fluxes are smaller at Earth with respect to what found in our model. This can be explained with the fact that we are grouping the nuclei at the escape and thus, for instance, propagating the nitrogen group at the escape as pure nitrogen. With this procedure we associate to nitrogen particles the interaction lengths of lighter particles, that are larger and thus we induce a smaller number of interactions in our model, resulting in a larger flux of intermediate mass particles. The differences in the helium flux are similar to what found already in [96], due to the different implementation of the helium production in CRPropa and SimProp, and including also the effect of the differences of the heavier mass groups.

At this stage, one could investigate if this galactic component used in the UFA model, represented by a power law, could be in agreement with the data measured in that range. Because in different works this was identified as the electron-poor component of Cascade-Grande experiment [122], as shown in section 4.3.2, the comparison between the K-G data and the UFA galactic component at low

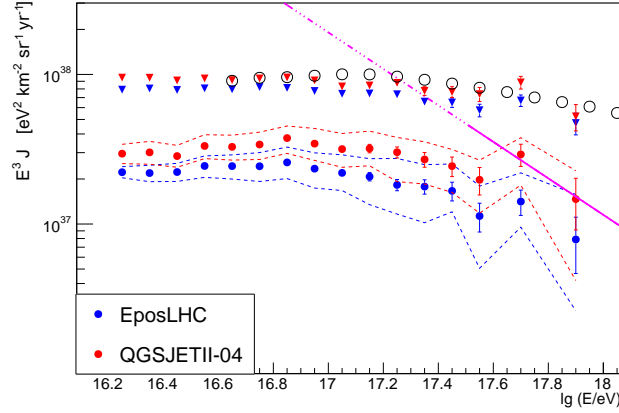


Figure 5.8: Cascade-Grande electron poor component (coloured dots) and total flux (triangles) for two different hadronic interaction models. The empty black dots are the Auger data (ICRC2019) while, in pink, the UFA galactic component extrapolated to lower energies, represented by a solid line up to the energy in which it is used in UFA paper ($E = 10^{17.5}$ eV).

energies is shown in figure 5.8. From the comparison one can notice that the galactic component is very abundant compared to the measurements of K-G. This shape of the galactic component will be used in the following sections, varying the normalization in order to be in agreement with the experimental data.

5.3 Astrophysical input: application of the source interaction model to starburst galaxies

5.3.1 Motivation

Starburst galaxies (SBGs) are unique objects in the Universe characterized by a high rate of supernova explosions and star formation rate which can often be as high as $\sim 10^2 M_{\odot} \text{yr}^{-1}$ [133]. As reported in [134], the higher the rate of star formation the greater the infrared luminosity, and according to [135], a corresponding increment of the rate of supernovae ($\mathcal{R}_{\text{SN}} \sim 0.1 \div 1 \text{yr}^{-1}$) is often observed. Such a high supernova rate makes SBGs very promising factories for cosmic rays.

In several SBGs, the star forming region is observed to be localized in the central part of the galaxy with typical radial extension of $R \sim 0.2\text{--}0.5$ kpc. These objects are referred to as starburst nuclei (SBNi) and their interstellar medium (ISM) is naturally expected to be highly perturbed with a strong level of turbulence.

The starburst environment also exhibits additional extreme conditions such as a particle densities higher than $n_{\text{ISM}} \sim 10^2 \text{cm}^{-3}$ (see also [137, 138]), magnetic



Figure 5.9: Picture of Messier 82 (M82), also known as cygar Galaxy. M82 is a starburst galaxy approximately 12 million light-years away in the constellation Ursa Major. From [136].

field (B) at the level of $\sim 0.1 \div 1$ mG (see [139]) and infrared energy density (U_{RAD}) often higher than 10^3 eV cm $^{-3}$. The superposition of several supernovae and the intense star forming activity is capable to launch a powerful wind with estimated velocity (v_{W}) of about $\sim 10^2 \div 10^3$ km s $^{-1}$ [140, 141, 142]. The high level of turbulence in such a crowded environment suggests that PeV and sub-PeV CR protons might lose a considerable part of their energy before escaping SBN due to $p-p$ interaction, while the main leading mechanism for the particle escape would be played by the wind-advection [143, 144, 145]. Recent investigations on SBGs and their superwind bubbles [146, 147, 148] proposed that CRs can be accelerated up to hundreds of PeV and, under certain conditions, also up to some EeV. These particles would still lose part of their energy via $p-p$ and $p-\gamma$ interactions, but their energy would efficiently allow them to diffuse away from the starburst surroundings.

We choose to use SBGs to test our source interaction model, supported also by the following reasons:

- On one hand, there are models in which the SBGs can accelerate cosmic rays up to EeV energies [146, 147, 148].
- On the other hand, the Pierre Auger collaboration has found a correlation of UHECRs above 39 EeV with a catalogue of 17 SBGs, as shown in chapter 2 [69].

I am going to apply the source interaction model to a SBG prototype.

As in the previous section, in order to perform a propagation inside and then outside the sources, some steps are needed:

- The calculation of the interaction and escape probability have to be performed. It is assumed that the two probabilities do not depend on the position of the particles in the environment but just on the energy, mass and charge of the particle;
- If the probability of escape is greater than that of interaction, the particle is not propagated anymore in the cascade; otherwise, the particle loses energy and mass according to the dominant process and all the secondary products are propagated in the following steps.
- This procedure is performed for a certain number of steps; after that, all the particles not escaped are considered trapped at source.

First of all it is important to highlight the difference compared to the UFA model: also in this case a leaky box model is considered, but the interaction and the escape times taken into account are different. In fact, in the UFA case, the photon spectrum and its temperature were chosen just to fit the data and the escape time was modelled simply as a power law in rigidity. Instead, in the case of SBG, the parameters are derived from the phenomenology of the chosen source. In the following section, I will show what was chosen for interaction and escape times.

5.3.2 Escape time

In the source interaction for SBGs, the escape time was chosen to be the minimum between the advection and the diffusion time.

The advection time is the speed of wind v_W and the radius of the starburst nucleus R :

$$t_{\text{adv}} = \frac{R}{v_W} \quad (5.6)$$

Concerning diffusion process, these calculations can be derived by [149, 150]. The general formula for the diffusion time is

$$t_D = \frac{R^2}{D} \quad (5.7)$$

where R is the size of the starburst nucleus and D the diffusion coefficient. Its general form is given by

$$D = \frac{1}{3} \frac{R_L c}{F(k)} \quad (5.8)$$

where R_L is the Larmor radius of the particle, c is the speed of light and $F(k)$ is the wave energy density in the wavenumber dk at the resonant wavenumber k , such that:

$$\frac{\delta B^2(k)}{B^2} =: F(k)dk \quad (5.9)$$

gives the ratio of the energy densities (related to the magnetic field) per unit mode k . So a generic form of the energy density is considered:

$$F(k) = F(0) \cdot k^{1-d} \quad (5.10)$$

with $F(0) \equiv \text{const}$ and d is the turbulence index (for example $d = 5/3$ in case of a Kolmogorov turbulence). In order to find $F(0)$, we require

$$\int_{k_0}^{\infty} \frac{F(k)}{k} dk = \left(\frac{\delta B}{B} \right)^2 \quad (5.11)$$

$$\begin{aligned} \int_{k_0}^{\infty} \frac{F(k)}{k} dk = \left(\frac{\delta B}{B} \right)^2 &\Leftrightarrow F(0) \int_{k_0}^{\infty} k^{-d} dk = \left(\frac{\delta B}{B} \right)^2 \\ &\Leftrightarrow -F(0) \frac{k_0^{1-d}}{1-d} = \left(\frac{\delta B}{B} \right)^2 \end{aligned} \quad (5.12)$$

hence

$$F(0) = \left(\frac{\delta B}{B} \right)^2 \frac{d-1}{k_0^{1-d}} \quad (5.13)$$

Finally, we can write

$$F(k) = (d-1) \left(\frac{\delta B}{B} \right)^2 \left(\frac{k}{k_0} \right)^{1-d} \quad (5.14)$$

Now we consider

$$k = \frac{1}{R_L} \quad \text{and} \quad k_0 = \frac{1}{L_0}$$

where L_0 is the correlation length of the magnetic field. Substituting into equation (5.14), the form for the wave energy density becomes

$$F(k) = (d-1) \left(\frac{\delta B}{B} \right)^2 \left(\frac{R_L}{L_0} \right)^{1-d} \quad (5.15)$$

The final form of our diffusion coefficient in a turbulent magnetic field is given by:

$$D = \frac{1}{3} \frac{R_L c}{F(k)} = \frac{1}{3(d-1)} \left(\frac{\delta B}{B} \right)^{-2} L_0^{d-1} R_L^{2-d} c \quad (5.16)$$

Using a typical Kolmogorov slope $d = 5/3$, we get that the diffusion time scales as $E^{-1/3}$. When the energy increases, as shown in [151], the transport of charged particles in interplanetary space and the interstellar medium, including in regions of particle acceleration, is highly influenced by the presence of turbulent magnetic fields and their spectral distribution. The nature of particle transport in these fields also depends on particle energy. In general, higher energy particles, with a gyro-radius larger than the correlation length of the magnetic field, will sample many uncorrelated field lines within one gyration. For taking into account this effect, if the Larmor radius is greater than the correlation length of the magnetic field, the diffusion coefficient is estimated as $D = D_0(R_L/L_c)^2$, where D_0 is the value of the diffusion coefficient computed at the energy E_0 such that $R_L(E_0) = L_c$. If the diffusion time is smaller than R/c , the diffusion is ballistic and the

diffusion time becomes R/c .

In this work the parameters B , L_0 and $\frac{\delta B}{B}$ are not varied during the following analysis. It was chosen to use the nominal magnetic field of the benchmark SBG, M82, $B = 200 \mu\text{G}$; concerning the normalization of the diffusion coefficient, it was chosen $\frac{\delta B}{B} = 1$ as we expect for a turbulent magnetic field. Finally, the coherence length is set to $L_0 = 1 \text{ pc}$, which is the expected injection scale of the turbulence for young Supernovae in Starburst Galaxy.

As it is possible to see from figure 5.10, we observe that the advection time is constant with respect to the masses and the energy of the primary particles (pink dashed line), while the diffusion times show three distinct regimes for the five injected masses considered.

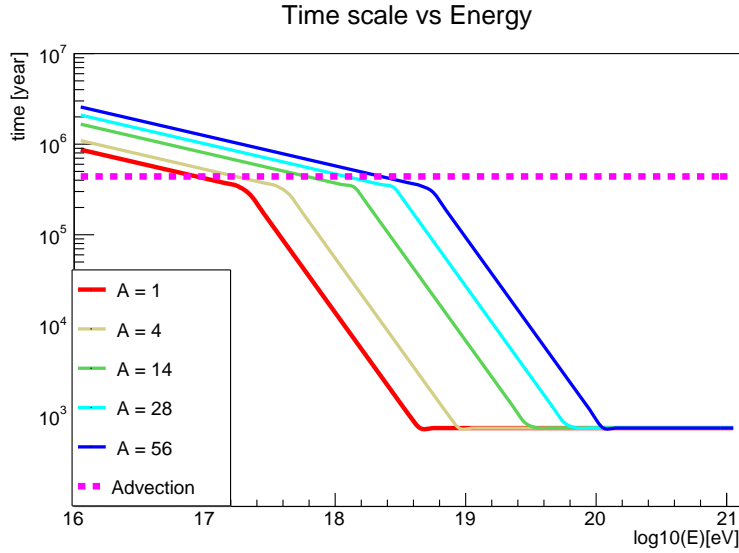


Figure 5.10: Diffusion and advection time in in-source-SimProp. The pink dashed line refers to the advection time, while the other lines refer to the diffusion time.

5.3.3 Interaction time

In [145] the SBG photon spectrum is approximated using two black bodies on visible and infrared energies. To be more precise, the infrared (IR) background is usually modelled such as modified black body (or diluted black body), as proposed by [152]:

$$n_{\text{IR}}(E) = C \cdot \frac{8\pi}{(hc)^3} \frac{E^2}{e^{E/kT} - 1} \left(\frac{E}{E_0} \right)^\sigma \quad (5.17)$$

This functional shape allows the infrared spectrum to be a pure black body above the energy E_0 , whereas at lower energies it reduces to a grey body spectrum $\propto E^{2+\sigma}$, where the spectral index σ generally assumes values between 0 and 2.

The normalization C is obtained from a fit to the IR spectrum of SBGs. At this stage, I approximate the SBG photon field using two black bodies spectra, one in optical and one in the infrared range.

In order to find the correct normalization of the spectrum, we integrate the black body spectrum in energy and, knowing the energy density $U_{\text{RAD}} \simeq 10^3 \text{ eV cm}^{-3}$ [145], we can normalize the photon field in the following way:

$$\frac{1}{\pi^2} \frac{1}{(hc)^3} \int_0^\infty \frac{\varepsilon^2}{e^{\frac{\varepsilon}{kT}} - 1} \varepsilon d\varepsilon = \frac{4\pi}{(hc)^3} \cdot \frac{\pi^4 (kT)^4}{15} = I \quad (5.18)$$

$$n_\gamma(\varepsilon) = \left(\frac{U_{\text{RAD}}}{I} \right) \frac{1}{\pi^2} \frac{1}{(hc)^3} \cdot \frac{\varepsilon^2}{e^{\frac{\varepsilon}{kT}} - 1}$$

The interaction time can be written as in formula 5.5; it presents two dips in correspondence of each photon field, as can be seen in figure 5.11. Looking at

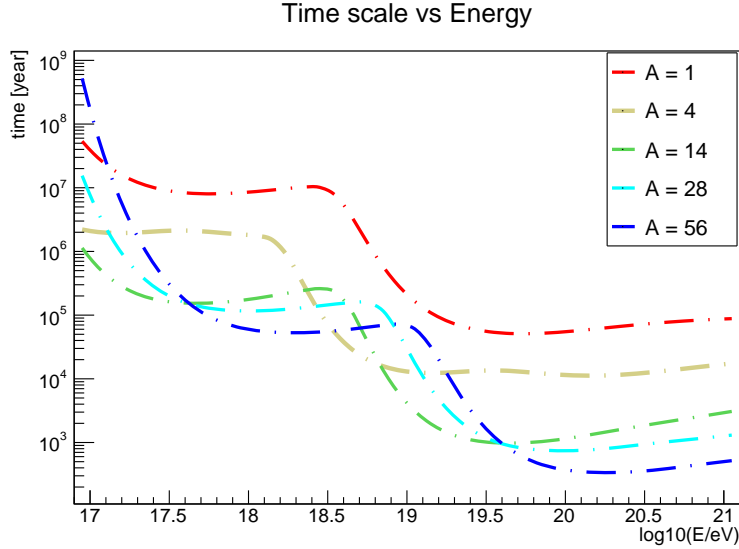


Figure 5.11: Photo-interaction times in in-source-SimProp for five different injected masses. It is possible to see two dips, in correspondence with the optical and infrared photon peaks.

heavy nuclei, the dip at low energies corresponds to the photo-disintegration on the visible light, while at higher energies the interaction time is dominated by the infrared spectrum. This can be easily understood taking into account the photon energy in the Nucleus Rest Frame:

$$\epsilon'_{\text{opt}} \simeq \Gamma \epsilon_{\text{opt}} \quad (5.19)$$

Being $\epsilon_{\text{opt}} \simeq 0.33 \text{ eV}$ and assuming the proton mass $m_p \simeq 10^9 \text{ eV}$, it is possible to calculate the Lorentz factor Γ for iron at 10^{18} eV for example.

$$\Gamma = \frac{10^{18} \text{ eV}}{m_p \cdot 56} \simeq 10^7 \quad (5.20)$$

This leads to $\epsilon'_{\text{opt}} \simeq 10 \text{ MeV}$, which roughly corresponds to the Giant Dipole Resonance. An analogous calculation can be performed for the infrared peak.

5.3.4 Source injection interface

After the implementation of the interactions in the source in in-source-SimProp, it was necessary to prepare an interface as intermediate step between the propagation inside and outside the source.

In fact, SimProp allows to inject particles following a pre-set parametric function within a given energy range. For this reason, once a certain number of events has been simulated, an interface is needed to:

- Read all the events written in the in-source-SimProp output file;
- Group the escaping events in some mass groups, as expressed figure 5.4 (left);
- Weight the events according to the chosen spectral parameters (according to the same procedure of the propagation matrix described in section 3.2.2).
- Write an output file with the escaping fluxes, which can be propagated through the extra-galactic space until reaching the Earth.

The procedure is analogue to the one explored in section 3.2.2; the main difference consists in the output. In this case, instead of a .txt files, a single histogram (*TH1D* in ROOT) for each mass group is created. In a second step, the propagation through the extra-galactic space is performed using propagation matrices already generated for the combined fit purposes. The whole procedure can be sketched in figure 5.12. It has the advantage to disentangle the parameters at the source and the accelerator features. In fact, in each simulation of in-source-SimProp, the parameters at the source are fixed, while the spectral parameters of the acceleration, such as the spectral index and the rigidity cutoff, are determined in the interface. This implies that, if we want to compare the ejected spectra using two different spectral indexes, a run of a new simulation is not needed.

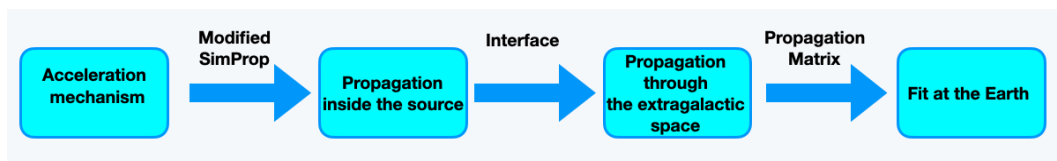


Figure 5.12: Scheme of the steps from the source to the comparison at Earth.

5.3.5 The benchmark case: M82

Inspired by [145], it was chosen to test the source interaction model assuming that all the sources have the same parameters of a reference SBG: M82.

As other different SBGs, the M82 spectrum can be described as the sum of different contributions detailed in figure 5.13. In order to model the photon field, we choose to take into account only two black bodies, one in the optical range with a peak at 0.33 eV (green line in figure 5.13) and one in the infrared range,

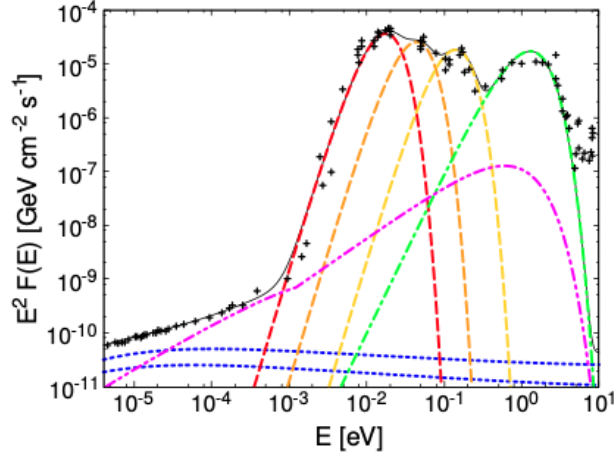


Figure 5.13: Multiwavelength spectrum of M82 as shown in [145]: thermal dust modified black bodies (red, orange and yellow dashed) and optical star black body (green dot-dashed). In addition, also the free-free absorption (magenta line) and synchrotron emission (blue lines) are plotted.

with the peak at $3 \cdot 10^{-3}$ eV (red line in figure 5.13). Using the parameters detailed in [145], a calculation of the interaction and the escape time has been performed, as shown in the previous section. For the M82 case, the two times are shown in the left panel of figure 5.14. As in the UFA case, it was chosen to inject a single heavy mass ^{28}Si with a hard spectral index ($\gamma = 1$) in the starburst nucleus of M82. The ejected spectra from M82 are shown in the right panel of figure 5.14.

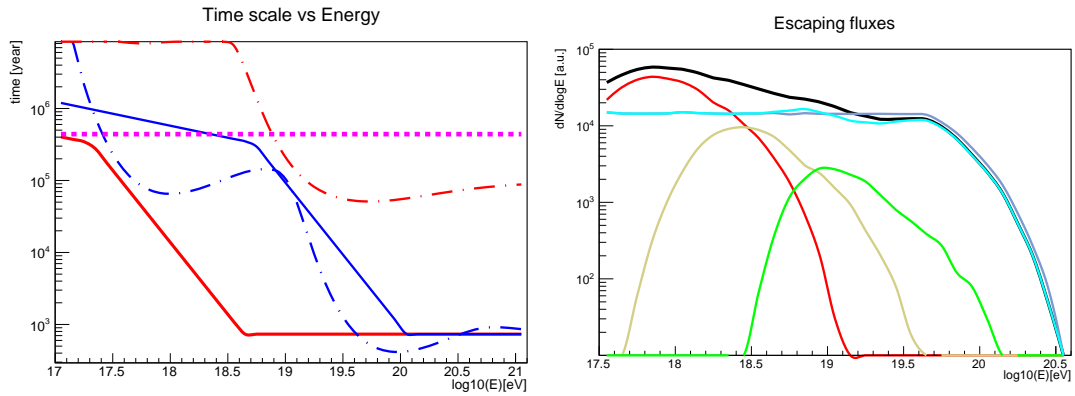


Figure 5.14: Left: timescale in M82 benchmark case: solid lines represent diffusion time, dashed pink line is the advection time, dot-dashed lines are photo-interaction time for protons (red) and iron (blue).

Right: escaping fluxes at the source using M82 parameters. The dotted grey line represent the injected spectrum (silicon nuclei), while the solid lines represent the escaping fluxes from the sources. The color legend is the same of figure 4.3 (bottom).

Looking at the ejected spectra (right panel of figure 5.14), it turns out that the photon field of M82 is not able to efficiently disintegrate all the injected silicon nuclei: the result is that the protons pile-up at low energies is not enough compared to the UFA model. In addition, the ankle-like feature visible in the UFA model and shown in figure 5.6 (right panel) here is not present. It is important to stress that the generic source in UFA model was proposed in order to fit spectrum and composition. In our case, a more realistic scenario does not provide a good agreement of the experimental data, being the parameters fixed at the source and not optimized.

Since we are interested in the comparison with the experimental data at Earth, it was chosen to see the effect of the extra-galactic propagation. Starting from a single source, we hypothesize that all the sources in the Universe are identical to M82 and equally distributed up to $z_{\max} = 6$, assuming a flat evolution of the sources ($m = 0$).

In order to describe the low energy part, a galactic component is also taken into account, using the same slope as the galactic component used in the UFA paper, and changing the normalization in order to minimize the deviance. Following the results shown in the extended combined fit (sec. 4.3.2), it is chosen to use a galactic component only made of nitrogen.

As shown in figure 5.15, propagating the escaping particles from the sources,

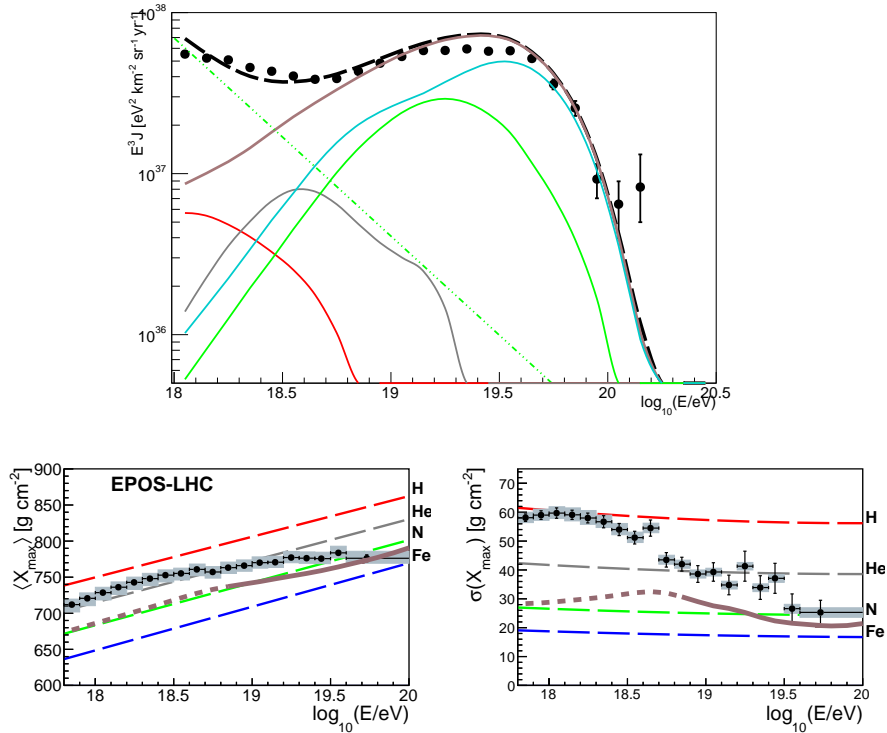


Figure 5.15: Spectrum and composition at Earth assuming M82 as source prototype. The color legend is the same of figure 4.3 (bottom). In the energy spectrum (top) the dashed green line refers to the used galactic component.

this scenario does not provide a good description of the energy spectrum and composition measured by Auger. In particular it is possible to notice that the composition is too heavy compared to the Auger data; in fact, the pile-up of protons at low energy, capable to justify the energy spectrum below the ankle in the UFA model (figure 5.4), here is not present. In addition, the galactic contribution (dashed green line in the top panel of figure 5.15) necessary to describe the Auger spectrum is so abundant to be even higher than the experimental data at low energies; this has also an effect on the composition, which in this case is compatible with pure nitrogen and therefore does not describe the experimental data.

For this reason, a scan over the possible parameter space is necessary. For instance, we expect that increasing the luminosity of the sources, the interaction probability will increase and the mass composition at the escape could be lighter.

5.3.6 Scan over the parameter space

It is possible at this point, moving from the M82 hypothesis, to search for a starburst prototype capable to describe the Auger data. Concerning the SBG parameters it is possible to vary:

- **The radius of the starburst nucleus R .** It was chosen a nominal value of 220 pc, but, following [145], it is known that SBG nuclei can extend up to 300 pc.
- **The infrared luminosity L_{IR} :** according to Fermi measurements [153], M82 is an average SBG; in fact, the observed infrared luminosity for SBG can be up to two order of magnitude more intense.

Concerning the acceleration mechanism, it is possible to vary:

- **Spectral parameters γ and R_{cut} :** The standard diffusive shock acceleration suggests a spectral index $\gamma \simeq 2$; in addition, other works [154, 155] conclude that the acceleration mechanism could lead to a hard injection spectrum $dN/dE \propto E^{-\gamma}$, with $\gamma = 1$. Concerning the rigidity cutoff, it was chosen a range between [18, 19] in $\log_{10}(R_{\text{cut}}/V)$, following the best fit results shown in the previous chapters.
- **Injected masses A :** following the UFA model, at this stage we inject just silicon ^{28}Si . Nonetheless, there is no reason to believe that a SBG can accelerate a single nuclear species. The effect of using two injected masses is shown in the following section;

In addition, other parameters have to be taken into account:

- **Photo-disintegration cross section model:** as shown in chapter 3, in SimProp [87], two photo-disintegration cross section models are implemented: TALYS [99, 100, 101] and PSB [97, 98]. Following the UFA scenario, it was chosen to use TALYS;

- **EBL model:** this is important for the extra-galactic propagation. SimProp offers two different model: Gilmore [95] and Dominguez [94]. Coherently with the analyses presented in the previous chapter, it was chosen to use the Gilmore model;
- **Evolution of the sources:** the evolution choice has an important effect on the ejected cosmic rays and also on the neutrino fluxes. Flat evolution ($m = 0$) or SFR evolution (see equation 4.11) are going to be considered.

In the M82 case the parameter choices are listed in tab. 5.1. In order to explore

Parameter	Range	M82
R/pc	[150,300]	220
$\log_{10}(L_{\text{IR}}/(\text{erg/s}))$	[44,46]	44
γ	[1,2]	1
$\log_{10}(R_{\text{cut}}/V)$	[18,19]	18.5
A	[1,56]	28
Photodis. cross section	TALYS, PSB	TALYS
EBL model	Gilmore, Dominguez	Gilmore
Evolution	Flat, SFR	Flat

Table 5.1: Parameter space for the M82 model.

the parameter space, starting from the M82 scenario (last column of tab 5.1), it was chosen to perform a scan in $\gamma - R_{\text{cut}}$ space, fixing all the other parameters, with the aim of reproducing spectrum and composition of ICRC2019 dataset starting from $10^{17.8}$ eV.

Together with the other parameters, also the hadronic interaction model is fixed to EPOS-LHC (as in the previous chapters) and the galactic component is taken into account with the same features described in the previous section (5.3.5).

In figure 5.16 we show a $\gamma - R_{\text{cut}}$ scan for four different IR luminosity: M82 luminosity and 10, 20 and 50 times M82 luminosity. On the z-axis we report the base-10 logarithm of the deviance of the energy spectrum and composition, defined as the sum of equations 3.14 and 3.17 described in chapter 3.

From the scan, we see that the best deviance is found in correspondence of the red cross ($\gamma = 1$, $\log_{10} R_{\text{cut}} = 10^{18.5}$ eV) for a luminosity ten times higher than M82. However, looking at the best case, the deviance is still very high (> 8000). This can be also noticed by the expected energy spectrum and composition of the best scenario, shown in figure 5.17. While the photo-interaction is improved by an order of magnitude, the proton pile-up is not sufficient to describe the low energy region of spectrum; for the same reason the $\sigma(X_{\text{max}})$ does not describe the data because of the excess of nitrogen from the galactic contribution.

At intermediate energies (i.e $10^{18.7}$ eV), the primary silicon nuclei are not disintegrated and they are still abundant, making it harder to accommodate the ankle feature. The abundance of heavy masses at low energies can be understood

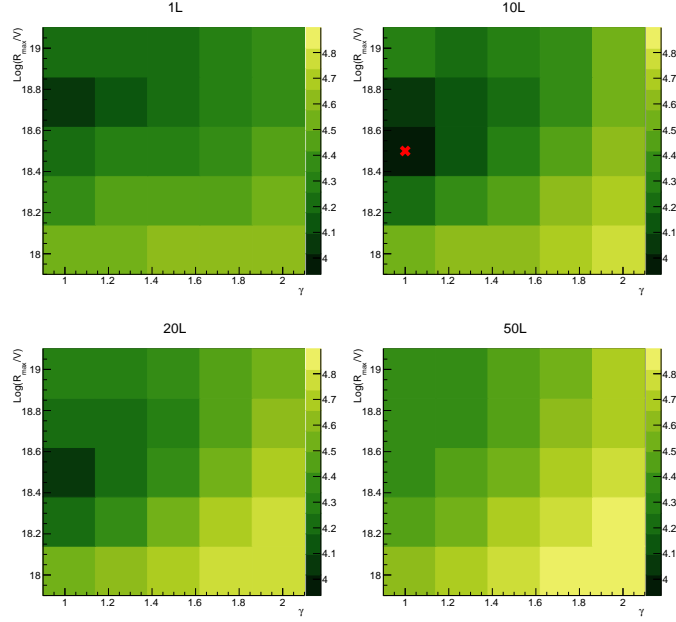


Figure 5.16: Scan in $\gamma - R_{\text{cut}}$ space for different luminosity. In the z axis we report $z = \log_{10}(D_{\text{tot}})$, where D_{tot} is defined by the sum of equations 3.14 and 3.17. The comparison is performed above $17.8 \log_{10}(E/\text{eV})$. Each panel refers to luminosity N times the M82 luminosity, such that $N \cdot L = N \cdot L_{\text{M82}}$. The red cross represents the point in the parameter space in which the best deviation is found.

by considering at the interaction times in figure 5.14. In fact, an accelerated particle should interact with the optical photon field rather than the infrared one within this energy range; but the optical photon field is less intense than the infrared one and, for this reason, in this configuration many heavy particles can escape from the source without interacting.

In order to improve this aspect, two paths can be followed: on the one hand accelerating light and heavy particles, such as protons and silicon nuclei. This methodology will be shown in the next subsection. On the other hand, a more detailed study of the interaction inside the sources will be provided in the next section, taking into account spallation processes.

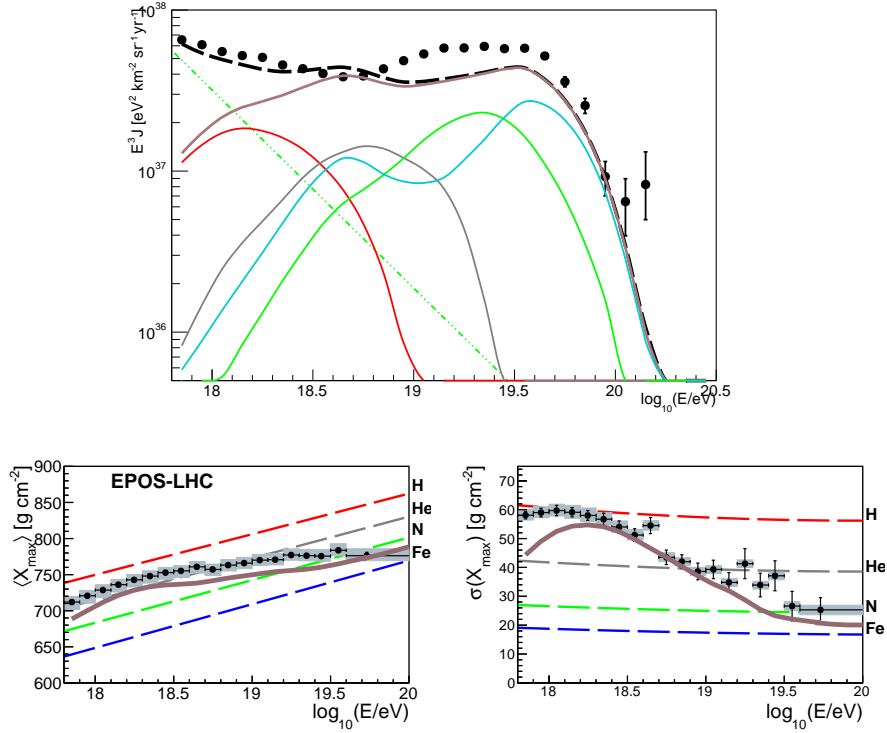


Figure 5.17: Spectrum and composition at Earth using the best configuration in the parameter space (figure 5.16). The color legend is the same of figure 4.3 (bottom). In the energy spectrum (top) the dashed green line refers to the used galactic component. In this scenario only silicon nuclei are injected at the source.

5.3.7 Injecting light and heavy masses

As previously outlined, there is no reason to believe that starburst galaxies can accelerate just silicon nuclei. To see how our results change with respect to the injected mass, it was chosen to test a case in which a source can accelerate both protons and silicon nuclei. This is motivated by the fact that, injecting only silicon nuclei, the energy spectrum and composition at Earth are not well described. In fact, silicon nuclei are not sufficiently disintegrated and the secondary protons are not numerous enough to describe the low energy portion of the spectra.

For these reasons:

- Two simulations have been performed, one in which silicon nuclei are injected, the other one in which only protons are injected in the source region;
- The two ejected spectra are summed together in the interface; it is assumed that the two injected species are accelerated with the same spectral index and the same rigidity cutoff. This implies that $E_{\max}^{\text{Si}} = Z^{\text{Si}} \cdot E_{\max}^{\text{p}}$, that is, what is expected if the acceleration mechanism is electromagnetic.

- Finally, the total spectrum is propagated through the Universe and compared to the experimental data.

In the interface we introduce a new parameter, called $K = \frac{J^P(E_0)}{J^{Si}(E_0)}$; it represents the ratio between the proton and the silicon nuclei injection spectra at a certain energy $E_0 < E_{\max}^P$. Therefore, fixing a certain luminosity, the parameter K can be varied in order to find the best agreement with the data.

For instance, fixing the luminosity to the M82 case (tab 5.1), it is possible to produce another $\gamma - R_{\text{cut}}$ scan, as shown in figure 5.18. Comparing this plot with that one presented in the previous subsection (figure 5.16), it is evident that we are improving the deviance of the energy spectrum and composition.

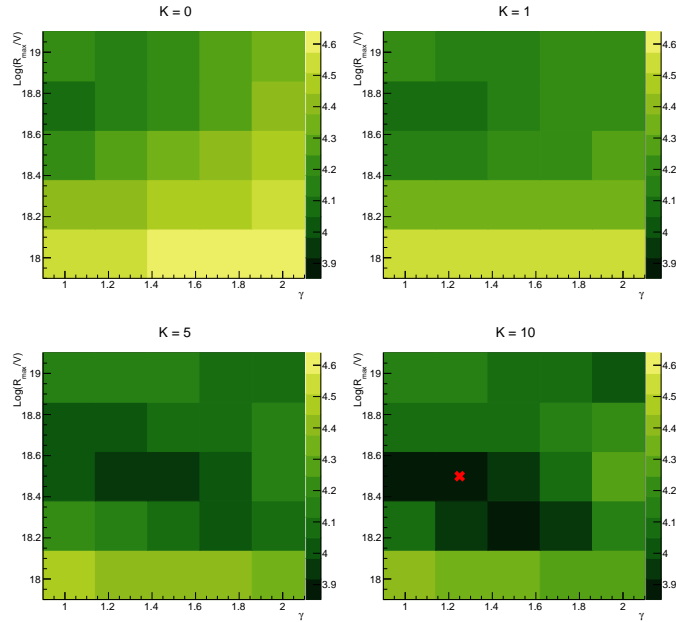


Figure 5.18: Scan in $\gamma - R_{\text{cut}}$ space using protons and silicon nuclei at the injection. In the z axis we report $z = \log_{10}(D_{\text{tot}})$, where D_{tot} is defined by the sum of equations 3.14 and 3.17. The comparison is performed above $17.8 \log_{10}(E/\text{eV})$. The red cross represents the point in the parameter space in which the best deviance was found.

In this case the best scenario was found for $K = 10$ (it means that for each silicon nucleus we are accelerating 10 protons), $\gamma = 1.25$, $\log_{10}(R_{\text{cut}}/\text{V}) = 18.5$. The plots of spectrum and composition corresponding to the best scenario are shown in figure 5.19. Comparing these results with the ones presented in the previous section, it is possible to affirm that a better deviance is obtained and, in addition, the description of the energy spectrum significantly improves.

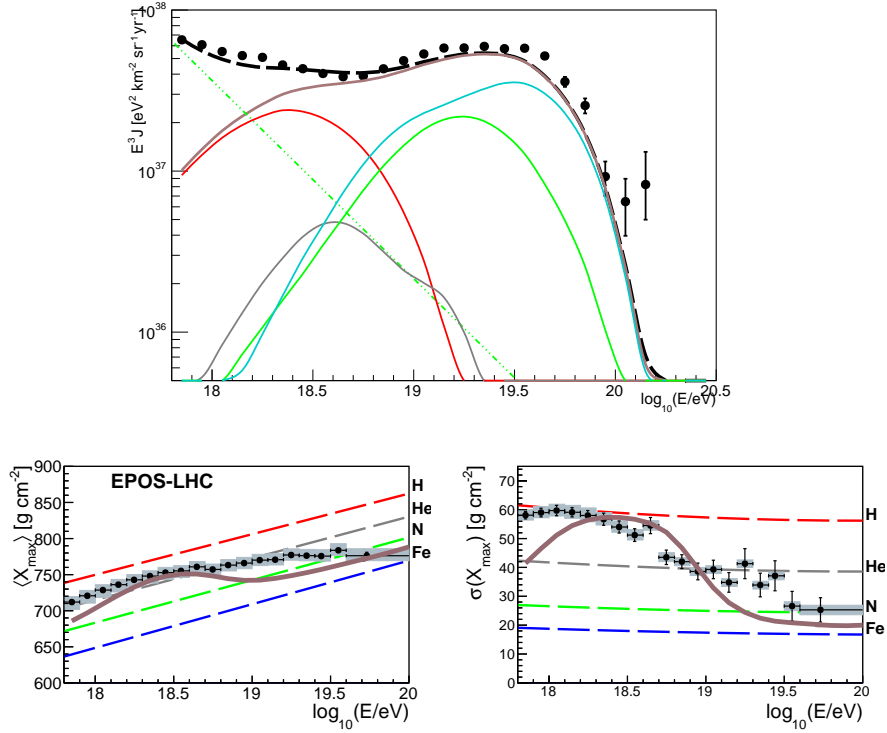


Figure 5.19: Spectrum and composition at Earth using the best configuration in the parameter space (figure 5.18). The color legend is the same of figure 4.3 (bottom). In the energy spectrum the dashed green line refers to the used galactic component.

Nonetheless, some open questions remain:

- The required galactic flux in this scenario is so abundant to coincide with the Auger data at $17.8 \log_{10}(E/\text{eV})$.
- Even using two injected masses, our model does not describe the X_{\max} distributions measured by Auger.

These results can suggest that, using these assumptions, our model is only partially able to reproduce Auger spectrum and composition. Note that a single galactic mass is used: looking in particular at the composition in figure 5.19, it is possible to conclude that the chosen galactic mass is too heavy to describe our data. A further investigation, using a mixed galactic component made of helium and nitrogen, can be performed in the future. In this work, instead, we want to improve our understanding of the processes inside the SBG. For this reason, a detailed study of the hadronic interaction processes has been performed. In the next section I will include the spallation processes inside in-source-SimProp and I will discuss how this interaction change my results with respect to the experimental data.

5.4 Hadronic interaction input: Including spallation mechanism

Spallation processes are negligible for the extra-galactic propagation, due to the low density of the gas; however, for propagation inside starburst galaxies, they have to be taken into account.

The computation of the spallation process is a new entry in SimProp. We base our analysis on the most recent hadronic model, **Sibyll 2.3d** [4], which is an event generator designed for Monte Carlo simulations of atmospheric cascades at ultra-high energies. The hadronic interaction cross section is calculated in the minijet model, while the Glauber scattering theory [156] is applied in hadron-nucleus collisions and extended with a semi-superposition approach [157] to nucleus-nucleus collisions.

At this stage this hadronic interaction model was not directly included inside in-source-SimProp. For this reason I introduce a parametric model: starting from Sibyll2.3d outcomes, it is possible to parametrize them as a function of the energy E and mass A of the interacting particle in order to describe the hadronic interaction in in-source-SimProp. In this section I am going to describe the parametric model while Sibyll2.3d will be included in in-source-SimProp in a second moment: a preliminary comparison is provided in section 5.4.1. The most important quantities in order to describe the spallation in our propagation code are:

- The inelastic spallation cross sections for proton-proton σ_{pp} and proton-nucleus interactions σ_{pA} ;
- The fragmentation of nuclei after their interaction with the protons of the ISM;
- The multiplicity of secondary particles for both proton-proton interaction and proton-nucleus interaction;

The Sibyll2.3d cross section is shown to be in agreement with the latest experimental data, as can be seen from figure 5.20. The cross section is a crucial quantity because, in the leaky box model, allows to calculate the interaction time for spallation, according to the following formula:

$$\tau_{\text{spal}} = \frac{1}{n_{\text{ISM}} \sigma c} \quad (5.21)$$

Where n_{ISM} is the proton density in the environment surrounding the starburst nucleus (in M82 $n_{\text{ISM}} = 125 \text{ cm}^{-3}$).

Using Sibyll2.3d, the cross section predictions for four nuclear species (H, He, O, and Fe) in a large energy range (from 10 to 10^9 GeV in the laboratory frame) have been provided. Starting from these outcomes, it is possible to parametrize the $p-A$ cross section dependence on energy and mass according to the following formula:

$$\log(\sigma/\text{mb}) = a_0 + a_1 \cdot \ln A + (b_0 + b_1 \cdot \ln A) \cdot L + (c_0 + c_1 \cdot \ln A) \cdot L^2 \quad (5.22)$$

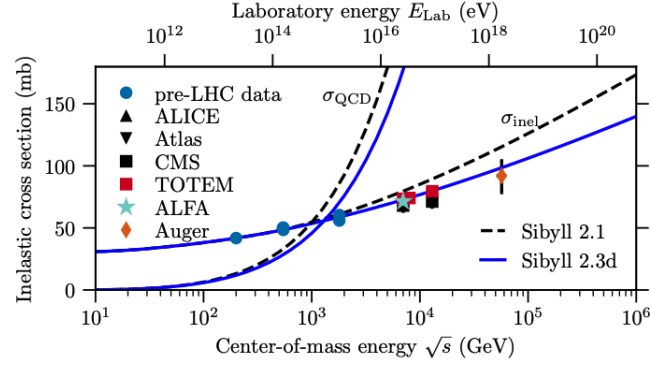


Figure 5.20: Inelastic proton–proton cross section according to Sibyll2.3d model [4].

Where $L = \log_{10}(E_p/\text{GeV})$ with E_p energy of the particle with mass A , while the parameter a_0 , a_1 , b_0 , c_0 and c_1 and b_1 are free parameters of the fit. Therefore it is possible to fit the Sibyll2.3d outcomes using equation 5.22. The results are shown in 5.21. We can conclude that our parametric model reasonably describes the Sibyll results.

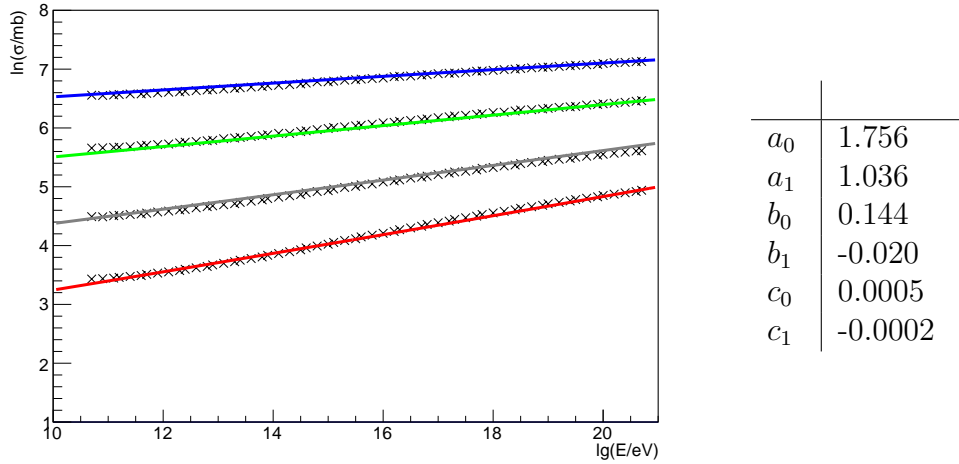


Figure 5.21: Left: Fit of the cross section following the equation 5.22: $\log(\sigma/\text{mb}) = a_0 + a_1 \cdot \ln A + (b_0 + b_1 \cdot \ln A) \cdot L + (c_0 + c_1 \cdot \ln A) \cdot L^2$. The crosses are the cross section values obtained by Sibyll2.3d. The coloured lines are the equation here reported for 4 different masses: ^1H (red), ^4He (grey), ^{16}O (green), ^{56}Fe (blue). Right: table of the best fit parameters.

A second important information concerns the disintegration of nuclei due to a hadronic interaction. The nucleons emitted by a nucleus due to a hadronic interaction depend on the mass and energy.

In the implementation of the fragmentation in our parametric model a simpli-

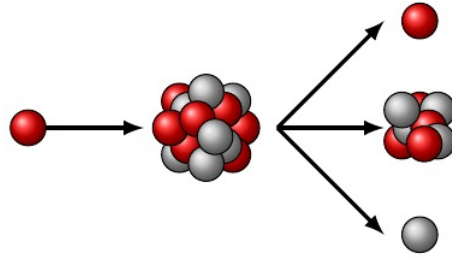


Figure 5.22: Sketch of disintegration due to hadronic interaction.

fication is assumed: a spallated nucleus A in the final state produces a single fragment with mass A_{frag} , while the other $A - A_{\text{frag}}$ nucleons are just single neutrons or protons propagating in the shower. In addition, all of them have the same Lorentz factor Γ . In order to know how many neutrons and protons are produced, using a SimProp routine, it is possible to determine what is the charge Z_{frag} corresponding to the most stable isotopes with mass A_{frag} . Knowing the final mass and charge, the number of protons and neutrons in the final state is automatically determined.

The same procedure detailed for the cross section was performed for the parameter A_{frag} : starting from Sibyll2.3d outcomes, A_{frag} was parametrized as a function of energy and mass. The results of the fit are presented in figure 5.23.

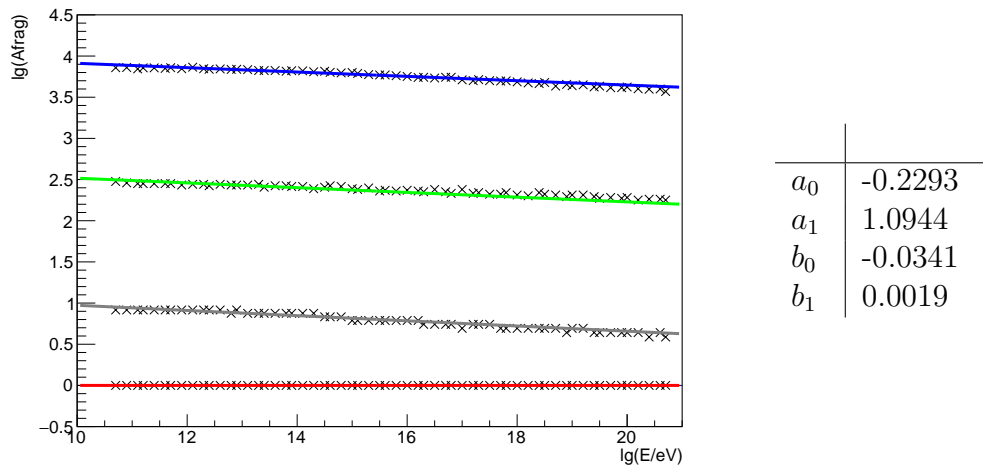


Figure 5.23: Left: Fit of the A_{frag} parameter using the formula:

$$\log(A_{\text{frag}}) = a_0 + a_1 \cdot \ln A + (b_0 + b_1 \cdot \ln A) \cdot L$$

The crosses are the A_{frag} values obtained by Sibyll2.3d. The coloured lines are the equation here reported for 4 different masses: ^1H (red), ^4He (grey), ^{16}O (green), ^{56}Fe (blue). Right: table of the best fit parameters.

Another important information concerns the secondary particles: at each

hadronic interaction, part of the energy is used for producing secondary particles, mostly pions and kaons, which can decay and produce photons and neutrinos. This information can be useful to improve the constrain capability of our model, looking at the expected neutrino fluxes at the sources and compared to the experimental data, following a multi-messenger approach.

In the parametric model it was assumed that all the secondaries produced in hadronic interactions are pions. This is a strong approximation; in section 5.4.1 a comparison between the parametric model and Sibyll is performed in order to quantify the weight of this assumption. Also in this case, from Sibyll2.3d the average number of produced charged secondaries (**nchd**) has been performed and then it parametrized as a function of energy and mass. The results are shown in figure 5.24.

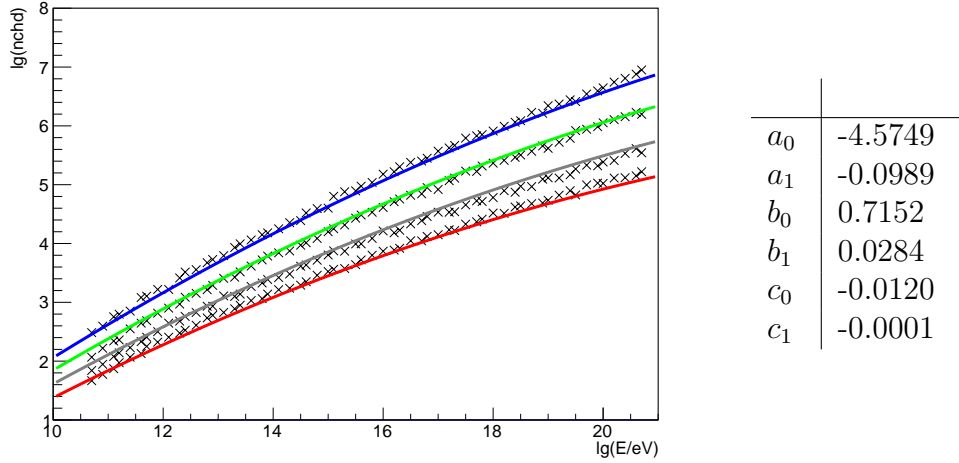


Figure 5.24: Left: Fit of the charged secondary particles following the equation: $\log(\text{nchd}) = a_0 + a_1 \cdot \ln A + (b_0 + b_1 \cdot \ln A) \cdot L + (c_0 + c_1 \cdot \ln A) \cdot L^2$. The crosses are the charged secondary particles obtained by Sibyll2.3d. The coloured lines are the equation here reported for 4 different masses: ^1H (red), ^4He (grey), ^{16}O (green), ^{56}Fe (blue). Right: table of the best fit parameters. .

Once the number of secondary particles has been estimated using the formula in figure 5.24, this is randomized according to a poissonian distribution.

In order to randomize the energy of the produced secondary particles, considering multiperipheral models [158], a general qualitative description of the momentum spectrum of secondaries, resulting from a collision of two hadrons at high energies, was provided considering a plateau in rapidity y . For this reason it was chosen to randomize the energy of the secondary particles according to a flat distribution in rapidity. For each rapidity, the particle momentum p is fixed by the relation:

$$p = \mu \sinh(y) \quad (5.23)$$

Where $\mu = \sqrt{(m^2 + p_T^2)} \simeq 0.38$ GeV is the pion transverse mass.

In general, it is possible to demonstrate [159] that, for a particle with energy E and mass m , the minimum and maximum rapidity y_0 and y_1 of the secondary particles can be written according to:

$$y_0 = \frac{b\mu}{m(1 - x_{\text{lead}})} \quad y_1 = \log \left(\frac{2(1 - x_{\text{lead}})E}{b\mu} \right) \quad (5.24)$$

where b is the coefficient in lns in the total pp multiplicity [160], being s the center of mass energy.

An important quantity for the hadronic interaction is x_{lead} , which is the fraction of energy of the interacting proton which is conserved in the final state. Following

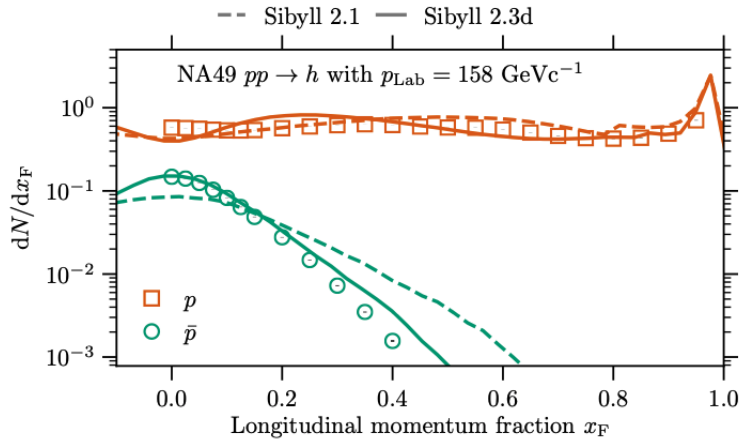


Figure 5.25: x_{Lead} distributions of secondary particles in $p - p$ interactions as measured by NA49. Taken from [4]

the observation of NA49 (figure 5.25), it was chosen to randomize it according to a flat distribution within the range $[0, 1]$.

Once a hadronic interaction happens, the rapidity and therefore the energy of the secondary particles, is chosen randomly in a range dictated by the equations in 5.24. Fixing the energy ($E = 10^{16}$ eV) and the mass ($A = 1$) of the interacting particle, the obtained rapidity distribution is reported in the left panel of fig. 5.26, while on the right panel the corresponding secondary energy distribution is plotted. Summing the energy of all the produced secondaries and including the energy of the leading proton in the final state, it is possible to affirm that the energy is statistically conserved.

At this point it is possible to perform a test between our parametric model and Sibyll2.3d in order to see how our assumptions influence the outcomes.

5.4.1 Comparison with Sibyll

While the parameteric model described in the previous section starts from Sibyll2.3d inputs, some simplifications have been assumed.

The main differences between our parametric model and Sibyll, and the corresponding effects, are the following:

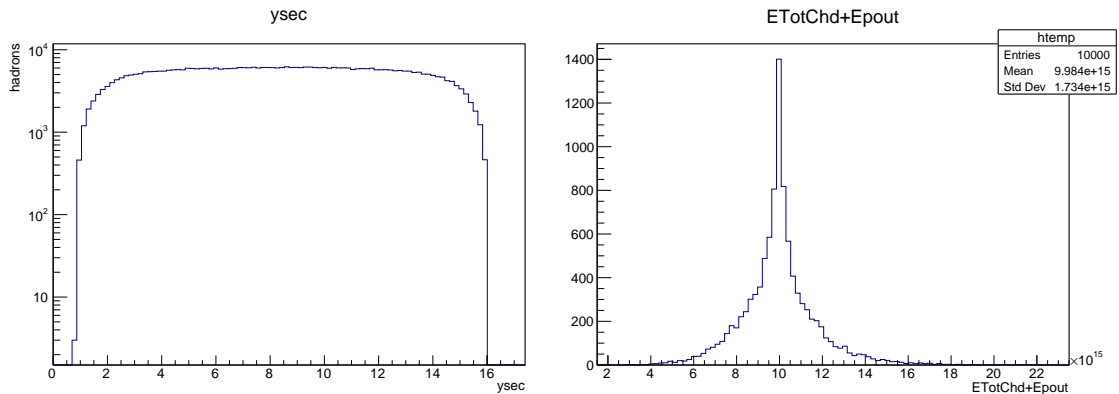


Figure 5.26: Rapidity and energy distribution for secondary of a $p - p$ interaction at 10^{16} eV varying x_{lead} between 0 and 1.

- From collider experiments [4], it seems that the secondary particles have a flat distribution in the central rapidity region, while at lower and higher rapidity the data are well described by two gaussian wings; in the parametric model described in the previous section only the flat region has been considered;
- Once the number of secondary particles have been estimated from the used parametrization, it is randomized according to a poissonian distribution. A more realistic model should randomize secondary particles following a negative binomial distribution [161], even if it is not expected to lead to significant differences.
- In our parametric model all the produced secondary particles are supposed to be pions, equally distributed between charged and neutral. In Sibyll2.3d, many other particles are produced: K , Σ , Λ , etc.. (even if with a lower probability).
- Using Sibyll2.3d, it was found that the fragments distribution is more complex than expected; how the approximation used in the parametric model (a single heavy fragment A_{frag} in the final state and $A - A_{\text{frag}}$ free nucleons) influences our results is still under investigation.

We have performed a comparison between Sibyll2.3d and the parametric model in order to evaluate the agreement.

Fixing a certain energy and mass of the target ($E = 10^{17}$ eV, $A = 28$), the comparison is performed in figure 5.27. The blue lines represent the particle fluxes from Sibyll, while the red lines come from our parametric model. On the left, the two rapidity distributions for secondaries are shown and it is possible to appreciate the discussed differences; on the right, the neutrino fluxes in the same case. It is possible to conclude that for our purposes the two models are qualitatively consistent with each other; nonetheless, it is important to stress that this is just a first implementation.

In order to better estimate the differences between the parametric model and Sibyll2.3d, instead of fixing the primary mass and energy, one has to include directly the hadronic interaction model inside in-source-SimProp. At this stage this is not released, but it seems to be the natural extension of this analysis.

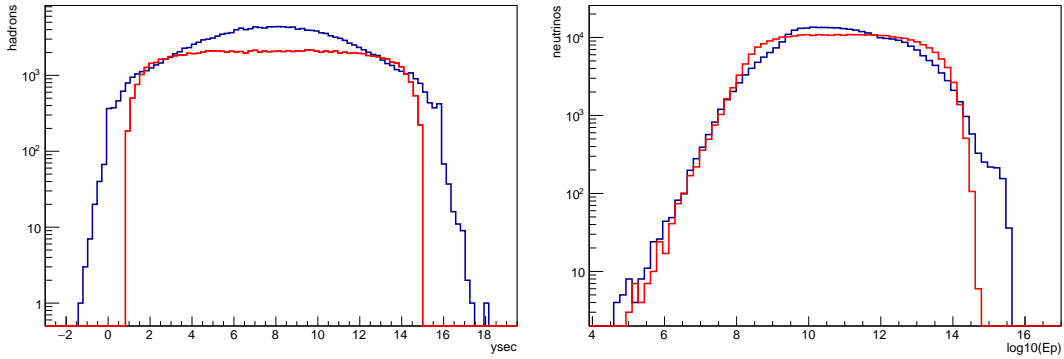


Figure 5.27: Left: hadrons rapidity distribution for Sibyll2.3d (blue) and my parametric model (red). Right: Neutrinos energy distributions for Sibyll2.3d (blue) and my parametric model (red).

5.4.2 Scan over the parameter space

With the inclusion of the hadronic interaction in in-source-SimProp a new interaction is taken into account in the competition among processes. The interaction time for the spallation process is shown in figure 5.28 (dashed lines). The spallation time decreases slowly as a function of energy. Note that, neglecting this interaction, in our parametric model light particles basically escape at energies below 10^{19} eV, because the optical field is not intense enough to make light particles interact. As shown in the previous section, this makes the description of the ankle more complicated. Including this new process we expect to disintegrate the primary particles in a more efficient way. For this reason we choose to inject just silicon nuclei at this stage.

It is possible to investigate the parameter space, following the procedure in section 5.3.6. However, in this case, an additional parameter has to be added in the table 5.1: the density of the interstellar medium n_{ISM} , that, as shown in equation 5.21, determines the spallation time. For the M82 case, n_{ISM} is assumed to be 125 cm^{-3} .

It was chosen to vary this parameter together with the infrared luminosity: this can be justified by the Kennicutt-Schmidt (KS) law [162], which relates the star formation rate (SFR) surface densities Σ_{SFR} and gas surface densities Σ_{gas} , according to the formula:

$$\Sigma_{\text{SFR}} = \Sigma_{\text{gas}}^N \quad (5.25)$$

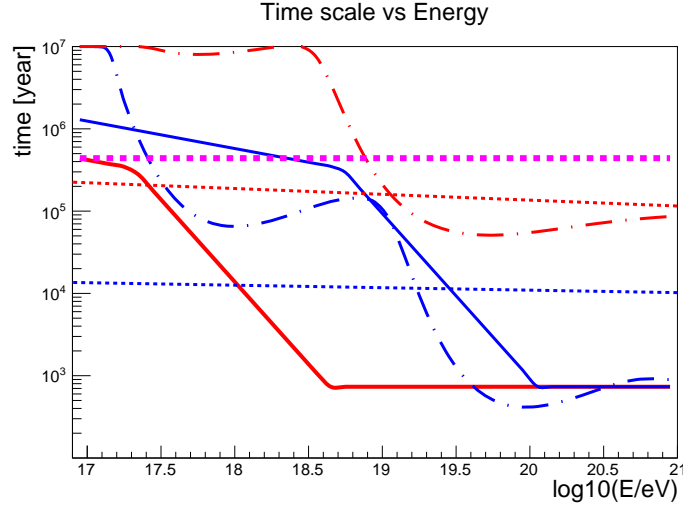


Figure 5.28: Timescales for M82 case: photo-hadronic interaction times (dashed-dot lines), spallation times (dashed lines) and diffusion times (solid lines) for protons (red) and iron nuclei (blue). The pink dashed line is the advection time.

with N between 1 and 2 (in [162] $N = 1.4$). However, a strong correlation is present, as shown in figure 5.29 (left). At the same time, in current analyses the

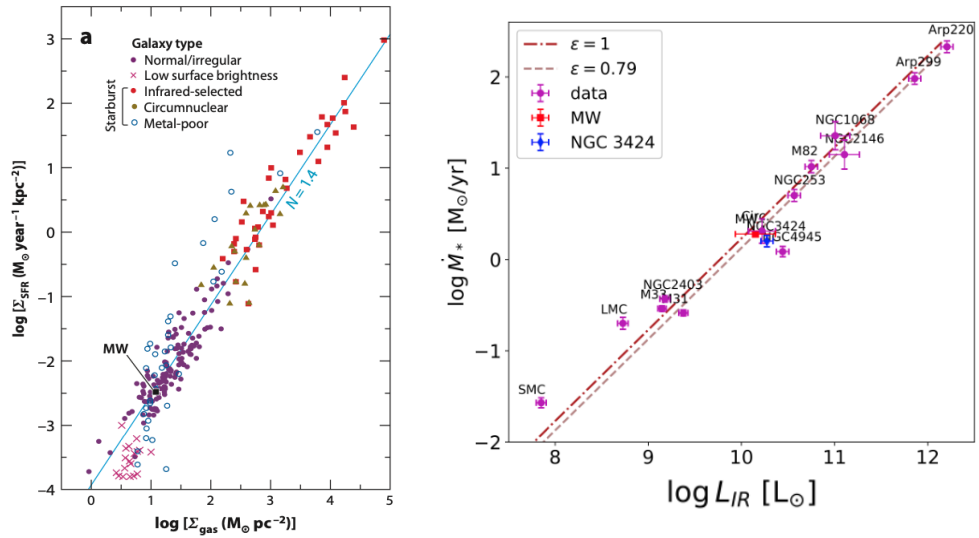


Figure 5.29: Left: KS law for different galaxy types [162].

Right: Correlation between infrared luminosity (L_{IR}) and star formation rate (in this paper indicated with M_*). The parameter ϵ is a proportional factor. From [163].

total IR luminosity L_{IR} is usually used as a proxy for the star formation rate [163], as shown on the right plot of figure 5.29. This suggests us to move together luminosity and density of the ISM.

The procedure detailed in section 5.3.6 is repeated. Chosen certain parameters at the sources and assuming a certain evolution of the sources, CR-nuclei are accelerated and propagated in the environment surrounding the source; the escaping fluxes travel through the extra-galactic space and are fitted to the energy spectrum and composition measured provided by the Pierre Auger Observatory. As shown in figure 5.30, the procedure is performed for two different evolutions of the sources: flat evolution and SFR. It is interesting to note that in this case,

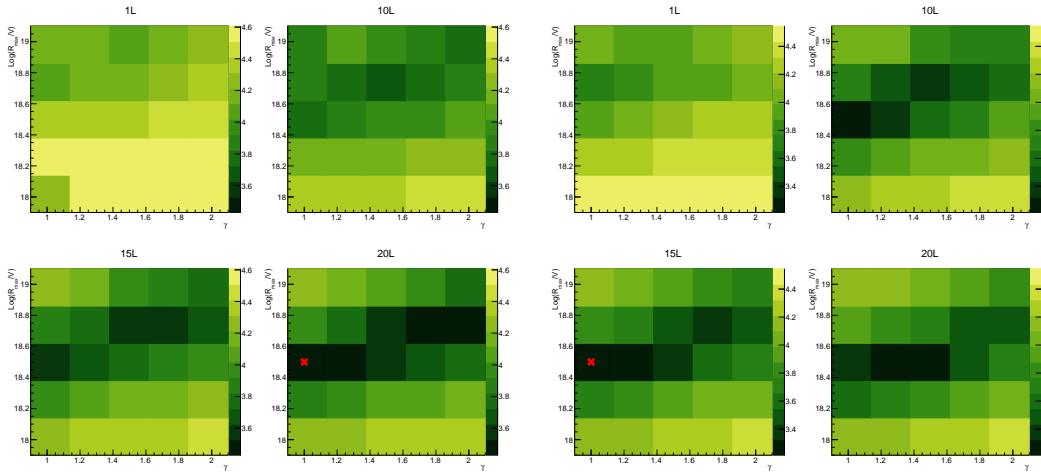


Figure 5.30: Left: Scan in $\gamma - R_{\text{cut}}$ space for flat evolution. Right: Scan in $\gamma - R_{\text{cut}}$ space for SFR evolution. In both cases $z = \log_{10}(D_{\text{tot}})$, where D_{tot} is defined by the sum of equations 3.14 and 3.17. The comparison is performed above $17.8 \log_{10}(E/\text{eV})$.

injecting just silicon nuclei, an intermediate luminosity configuration could lead to a better deviance compared to the case in which two masses were injected. The best cases are shown in figure 5.31 and 5.32. For the SFR best case ($\gamma = 1, \log_{10}(R_{\text{cut}}/V) = 18.5$) the best deviance of the analysis presented in this chapter is obtained. It can be noticed that, using a strong evolution, the best solution can be accommodated for a lower luminosity at the source and therefore less interactions in the environment surrounding the source.

Other tests have been performed and not presented in this thesis:

- Changing the injected mass A : an injected mass heavier than silicon nuclei does not provide a good agreement of the spectrum and especially of the composition measurements. Even pushing the luminosity towards the upper limit, our model is not able to disintegrate all the injected iron and, as shown in the previous chapter, the Auger data do not need iron to be. On the other hand, using a light injected mass could be a possible way to improve our description of the data, especially the mass composition at the energies above the ankle. In order to have a better agreement, it could be useful to take into account the overdensity correction used in the chapter 3 and 4.

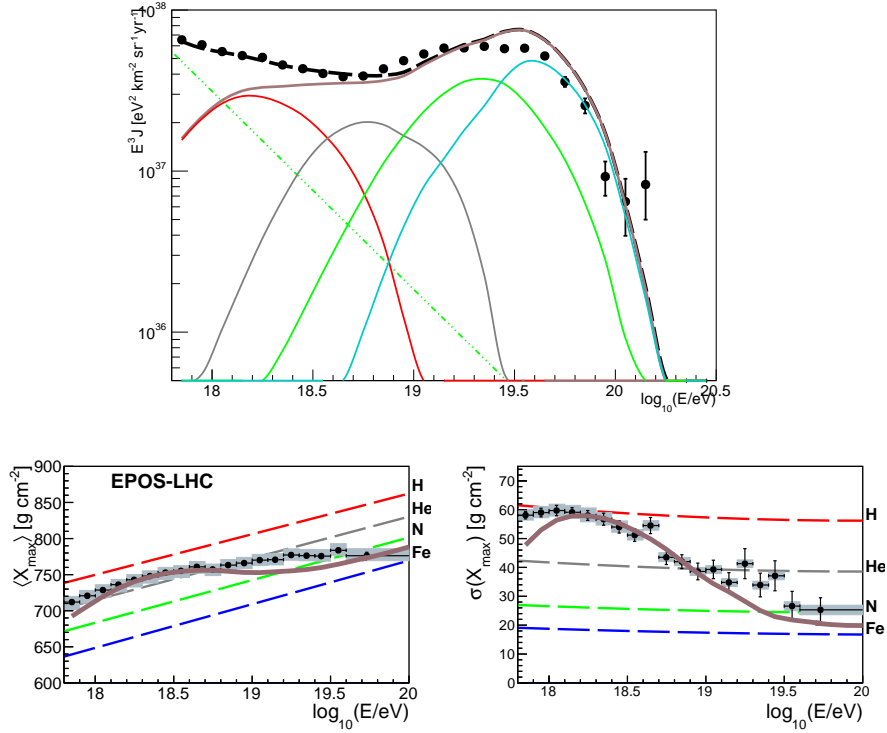


Figure 5.31: Spectrum and composition at Earth using the best configuration in the parameter space for flat evolution of the sources. The color legend is the same of figure 4.3 (bottom). In the energy spectrum (top) the dashed green line refers to the used galactic component.

- Changing the photo-disintegration cross section model (TALYS to PSB) or EBL model (Gilmore to Dominguez) does not improve the agreement with the Auger data;

In this last two section an investigation of the source-propagation model inside starburst galaxies was performed. Starting from a SBG prototype, a scan over the plausible parameter values at the source was provided; in particular it was shown how the IR luminosity plays an important role. A combination of masses was also tested in order to improve the agreement with spectrum and composition data.

A big improvement was achieved when the hadronic interactions have been taken into account: this represents a novelty to UHECR propagation codes. In particular, the best configuration was found using a SFR evolution of the source (equation 4.11) and for a luminosity 15 times higher with respect to M82. In order to improve the constraining capability of our model, one can compute the neutrino fluxes associated with a certain parameter choice and, in particular, at how the hadronic interactions can influence the expected neutrino fluxes from the sources.

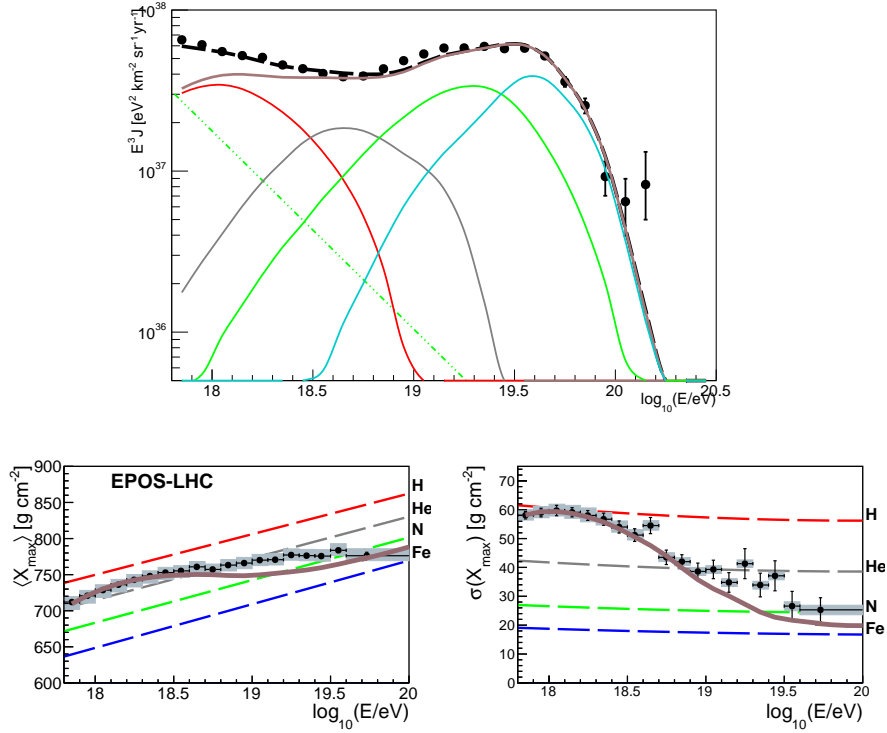


Figure 5.32: Spectrum and composition at Earth using the best configuration in the parameter space for SFR evolution of the sources. The color legend is the same of figure 4.3 (bottom). In the energy spectrum (top) the dashed green line refers to the used galactic component.

5.5 Expected neutrino fluxes

A great advantage of using a MonteCarlo code for the propagation of particles inside and outside sources, is that together with the escaping cosmic rays, all the secondary particles produced in the interactions with background photons and protons are automatically computed.

Therefore, assuming a certain configuration in the parameter space, it would be interesting to look at the associated neutrino fluxes, in order to compare it with the experimental results.

The Pierre Auger Observatory is sensitive to energies above 10^{17} eV [125]; since we expect neutrinos with energies below the region where Auger could detect them, in the following plots also the measurements and the upper limits provided by IceCube up to 10^{17} eV [127] are shown.

Neutrinos produced at the sources are weighted for the chosen spectral parameters, as the cosmic rays escaping fluxes, in the interface (see section 5.3.4) and then propagated through the Universe. For propagating neutrinos, we only consider the adiabatic energy loss defined in section 1.4.1.

In this analysis we are able to distinguish cosmogenic neutrino (coming from interactions with the CMB and EBL) to the neutrinos produced in interaction

with the photons surrounding the accelerator at the source and the neutrinos produced due to hadronic interactions.

In figure 5.33 we report the neutrino fluxes associated to the SFR evolution for the M82 case (left) and for the best case (shown in 5.32). In the plots with the grey line we report the cosmogenic neutrinos, in blue the neutrinos produced by photo-interactions in the source, in magenta the neutrinos due to hadronic interactions, in red the Auger limit and in orange that one expected by GRAND [128] after three years of operation, while the points refer to the High Energy Starting Events (HESE) published by IceCube [164].

In the M82 case, the expected neutrino flux is in agreement with the measured events and the estimated limits; however, in the case of the best scenario, the neutrino flux is an order of magnitude higher than the M82 case. This result can be expected because, in that case, the luminosity and the density of the ISM is higher by roughly an order of magnitude compared to the M82 scenario. The

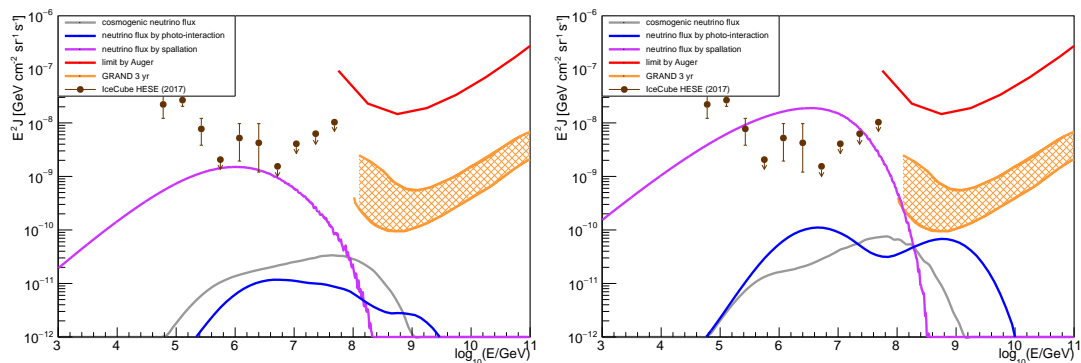


Figure 5.33: Neutrino fluxes for M82 case (left) and best case (right) according to a SFR evolution of the sources.

same considerations can be made for the case with flat source evolution, shown in figure 5.34, but in both cases the associated neutrino fluxes are less abundant than the SFR case.

We should consider whether or not these results are acceptable. It is clear that an expected neutrino flux more abundant than the measured one tends to exclude the configuration found in the parameter space, which fits best the Auger spectrum and composition. Nonetheless, some considerations have to be taken into account:

- In our model we assume all identical sources uniformly distributed up to $z = 6$. This is an approximation that affects the expected neutrino fluxes rather than the UHECRs fluxes, which are expected to be originated not far than $z = 1$.
- Another critical point regards the spatial distribution of photons and ISM: in this model we are assuming the density of ISM and photons constant in the whole SBN. This is not entirely true: in fact, observations suggest that

5.5. EXPECTED NEUTRINO FLUXES

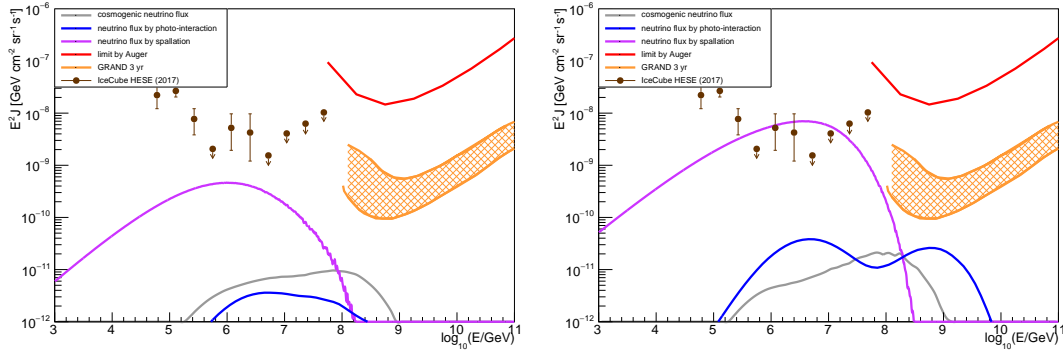


Figure 5.34: Neutrino fluxes for M82 case (left) and best case (right) according to a flat evolution of the sources.

the density decreases with respect of the distance from the center [165]. In this sense, taking into account that we are using the average photon density (and ISM density), the neutrino fluxes can be affected by some uncertainties due to this simplification.

- An important point to stress is that the implementation of the spallation processes is approximated. As already outlined in the previous sections, it is planned to improve the comparison with Sibyll2.3d.

For the listed considerations, it is possible to affirm that the expected neutrino fluxes are comparable to the experimental data and limits and cannot be used to exclude the configurations, found in section 5.4.2, which best fit the data.

We have thus demonstrated that the contribution of the hadronic processes to the production of secondary messengers is extremely important in some candidate sources. In fact, considering only $p - \gamma$ interactions, it was shown how the associated neutrino flux coming from the sources is of the same order of magnitude of the cosmogenic neutrino flux found in the previous chapter. Both of them are way below the limits set by Auger and IceCube. Instead, once taken into account also the hadronic interactions, the most important contribution of the neutrino fluxes comes from these interactions. Increasing by several order of magnitudes, the expected neutrino flux can be used to constrain plausible scenarios that describe the UHECR data.

We thus have demonstrate that a source-propagation model can describe UHE-CRs energy spectrum and composition and, at the same time, be consistent with the measured neutrino fluxes, completing the multi-messenger picture.

Conclusions and future prospects

In the analysis illustrated in this work we show different approaches to provide an astrophysical interpretation of the energy spectrum and composition measured by the Pierre Auger Observatory above $10^{17.8}$ eV. To this aim, it was fundamental to study the impact of propagation in the sources and in the intergalactic medium on the accelerated particles.

The first part of my analysis concerns the fit of spectrum and composition above $10^{18.7}$ eV using a single population of extra-galactic point-like sources, capable to accelerate nuclei according to a power-law energy spectrum with a rigidity-dependent cutoff at the source, taking into account only the effect of propagation in the extra-galactic space (propagation model).

To this point, a preliminary technical work was performed: the first part of my thesis work concerns the reorganization of the internal structure of the combined fit of energy spectrum and composition measured by the Pierre Auger Observatory. The combined fit code has been divided in several different classes in C++, trying to follow the path of a single particle from its emission until its detection. The results are consistent with the ones obtained in previous studies by the Pierre Auger Collaboration [2]. Using the latest dataset, the spectral index which minimizes the deviance is very hard, with $\gamma \simeq -1$; in correspondence, the fitted maximum rigidity is quite low ($\log_{10}(R_{\text{cut}}/V) = 18.2$), showing that the fluxes are suppressed mostly by the maximum acceleration of the sources rather than propagation effects. The composition at sources is dominated by intermediate-mass elements.

As a natural extension of this work, we chose to fit data down to $10^{17.8}$ eV. Different scenarios appear to be able to describe our data: a natural extension consists of simply duplicating the preexisting structure introducing an additional extra-galactic component. Both components can be composed by all nuclear species with different spectral parameters.

It is also investigated how the end of the galactic spectrum influences the results of the extended combined fit. According to other works in literature [84, 2], the galactic flux is identified with the heavy component of KASCADE-GRANDE

(K-G) measurements.

Another step consists in the fit using only protons in the low energy component and taking into account the galactic contribution. This is due to the fact that we want to mimic the interactions at the sources.

We found that a galactic component made of heavy elements is strongly disfavoured by the composition data, while the best fit were found attributing on intermediate-mass to the galactic spectrum. The presence of a galactic intermediate-mass contribution, in our fit represented by nitrogen, is difficult to accommodate with respect to the standard SNRs acceleration. Nonetheless, such a scenario could be explained by considering an additional galactic contribution provided by the Wolf-Rayet stars [123], which could actually accelerate nitrogen nuclei up to energies of the order of 10^{18} eV. The composition and anisotropies studies that will be performed by the Pierre Auger Collaboration in this energy range can help to understand if a galactic component with these features is reasonable.

In all the explored scenarios, the high-energy component presents a hard injection spectrum, in agreement with the one found in the combined fit above the ankle; therefore it is possible to affirm that the high-energy component is not spoiled by the extension of the fit to lower energies.

Instead, the low-energy component presents an extremely soft spectral index ($\gamma > 3$), and a rigidity cutoff with a high value and great uncertainties. As a consequence, this additional component presents protons up to very high energies. The possible presence of such a subdominant light contribution at the highest energies implies that some nearby sources could be investigated searching for anisotropies in the arrival directions at the highest energies. In order to justify the softness of the low-energy component spectral index, photo-disintegration processes occurring in the acceleration sites have to be taken into account.

Motivated by the results in the propagation model, the last part of this work concerns the study of UHECR interactions in the environment surrounding the sources. It was shown how the post-processing of UHECRs via photo-disintegration in an environment surrounding the source can naturally explain the entire energy spectrum and composition, in the context of a source-propagation model. In these models, the spectrum and composition above the ankle are predominantly dictated by the accelerator and propagation to Earth, while the cosmic rays below the ankle are predominantly protons from nucleons knocked off higher energy nuclei in the region surrounding the accelerator in presence of a magnetic field [3].

Starting from a reference model [3], I choose to implement the interactions in the source environment in SimProp [87], a MonteCarlo code used for the extragalactic propagation of UHECRs.

At this point the hypothesis of generic sources is left and we study in detail a potentially interesting class of sources, for both theoretical and experimental reasons: Starburst Galaxies (SBG). An improvement compared to the previous scenario regards the detailed description of the escaping processes: diffusion and advection. We choose to use two black bodies to model the photons in a SBG

prototype: M82. At this stage only the photo-interactions are taken into account. Therefore, it is assumed all the sources to be identical to M82, capable to accelerate a single nuclear species (silicon nuclei): a diffuse flux from these sources uniformly distributed is taken into account and then compared to the Auger energy spectrum and composition. It turns out that particles accelerated in the M82 environment are free to escape and there are not enough interactions to find a good agreement with the experimental data at Earth.

It is possible to scan the values of some parameter at the source, such as the radius of the starburst nucleus or the infrared luminosity. For each choice of parameter values at the source, particles are propagated in the environment surrounding the source. The escaping fluxes are therefore propagated through the extra-galactic space and finally fitted to the energy spectrum and mass composition measured by the Pierre Auger Observatory. The case of using two different masses at the injection, namely proton and silicon nuclei, is also explored: an improvement of the deviance of both energy spectrum and composition is observed with respect to the only silicon nuclei case.

In the second part of my work on source interactions, the effect of the hadronic interactions in the environment surrounding the sources have been studied. Therefore, starting from the most current hadronic interaction model available, namely Sibyll2.3d [4], I implement a parametric model in order to take into account these new interactions in the modified version of SimProp. This inclusion represents a new contribution to UHECR propagation codes. In particular, the fragmentation of nuclei when they interact with a proton of the interstellar medium and the study of the distribution of the emitted secondary particles were introduced. A comparison with the Sibyll2.3d code is also provided. A scan over the parameter space is performed taking into account spallation processes in order to find which configuration could fit best spectrum and composition measurements: a better agreement is found with respect to the case in which the spallation processes are neglected.

Finally, the neutrino fluxes associated with the case which fits best the spectrum and composition are reported. We show that, taking into account only $p - \gamma$ interactions, the neutrino fluxes produced in the sources are comparable to the cosmogenic ones. Instead, considering also the hadronic interactions, the neutrino fluxes increase by several order of magnitudes and can be compared to the fluxes measured at Earth, improving the constraining capability of our model and completing the multi-messenger picture.

Possible extension of these analyses concerns:

- The implementation of a hadronic interaction model inside the propagation code. Including, in our case, Sibyll2.3d inside SimProp, implies releasing all the assumptions used in the parametric model. This could represent a new contribution for the UHECR propagation codes; a possible further step could be implementing different hadronic interaction models in order to estimate which one provides the best agreement with the experimental data.

- Another possible extension of this work could be to connect my modified version of SimProp with the combined fit. This improvement will directly link parameters at the source with the energy spectrum and composition measured by Auger. Instead of scanning each parameter space, as was done in this work, it would be interesting to directly fit the parameters at the source, such as the spectral index or the mass composition, with the experimental data.
- In addition, the possibility to produce and propagate photons inside the sources seems to be a natural extension: such as the neutrino fluxes, the expected photon fluxes can be compared to the experimental data, improving in this way the constrain capability of our model.
- In this thesis we have mainly focused on SBG as potential accelerators of UHECRs; nonetheless, a detail study can be performed to other interesting source classes, once known the plausible ranges of their parameters (such as luminosity, ISM density, etc..)
- A fundamental concept developed in this work concerns that, fitting together energy spectrum and composition, one can remove degeneracy and improve an astrophysical model capable to describe the data. A great improvement could be including the UHECRs arrival direction provided by the Pierre Auger Observatory. This approach could allow us to relax the assumption of sources identical and uniformly distributed and directly link our source-propagation model to specific sources. A similar work, assuming in this case point-like sources, is ongoing inside the Collaboration [166].

Finally, the upgrade of the Pierre Auger Observatory will provide us more constraining data, such that we will find the answers for the open questions reported in the Introduction and will solve the puzzle of UHECRs, one of the most intriguing open problems of modern astrophysics.

First, we parametrize the X_{\max} distribution before detector effects as a Gumbel function [107]

$$g(X_{\max} | \lg E, A) = \frac{\lambda^\lambda}{\sigma \Gamma(\lambda)} \exp\left(-\lambda \frac{X_{\max} - \mu}{\sigma} - \lambda \exp\left(-\frac{X_{\max} - \mu}{\sigma}\right)\right) \quad (5.26)$$

The values of μ, σ, λ were obtained by fitting this Gumbel parametrization to X_{\max} distributions obtained via CONEX simulations [108]. When detectors effects are taken into account, we refer to acceptance and resolution.

Acceptance

A gumbel distribution probability function has to be multiplied by the acceptance function $\mathcal{A}(X_{\max}, E)$, i.e. the probability that if a shower with energy E and maximum depth X_{\max} occurs within the detector area it will be detected, using parametrization from [118]:

$$\mathcal{A}(X_{\max}, E) = \begin{cases} \exp\left(-\frac{x_1 - X_{\max}}{\lambda_1}\right) & X_{\max} < x_1 \\ 1 & x_1 \leq X_{\max} \leq x_2 \\ \exp\left(-\frac{X_{\max} - x_2}{\lambda_2}\right) & X_{\max} > x_2 \end{cases} \quad (5.27)$$

where x_1, λ_1, x_2 and λ_2 are calculated as a function of E .

Resolution

In a second moment, we convolve the result by the detector resolution function, parameterized as in [118] with the central values for the parameters:

$$\mathcal{R}(X_{\max}^{\text{rec}} - X_{\max} | E) = f \cdot G(X_{\max}^{\text{rec}} | X_{\max}, \sigma_1) + (1 - f) \cdot G(X_{\max}^{\text{rec}} | X_{\max}, \sigma_2) \quad (5.28)$$

where $G(x | \mu, \sigma)$ is a Gaussian distribution with mean μ and standard deviation σ , and the parameters f, σ_1 and σ_2 are function of E and are tabulated.

The two probabilities are reported in figure 5.35. The probability that an event with energy E and mass number A is detected with reconstructed maximum depth X_{rec} is then

$$\mathcal{G}(X_{\text{rec}}|E, A) = \int_0^{+\infty} \mathcal{R}(X_{\text{max}}^{\text{rec}} - X_{\text{max}}|E) \mathcal{A}(X_{\text{max}}, E) g_m(X_{\text{max}}|\lg E, A) dX_{\text{max}} \quad (5.29)$$

Computing $\mathcal{A}(X_{\text{max}}, E) g_m(X_{\text{max}}|\lg E)$ at the center of the bin X_i of the X_{max} bins, we use:

$$\mathcal{G}(X_j|E, A) = \sum_i \mathcal{A}(X_i, E) g_m(X_{\text{max}}|\lg E, A) \int_{X_j - X_i - 0.5\Delta X}^{X_j - X_i + 0.5\Delta X} \mathcal{R}(X|E) dX \quad (5.30)$$

where $\Delta X = 20 \text{ g/cm}^2$ is the bin width, and the sum extends from the third bin below that of the observed event with the lowest X_{max} to the third bin above that of the event with the highest X_{max} .

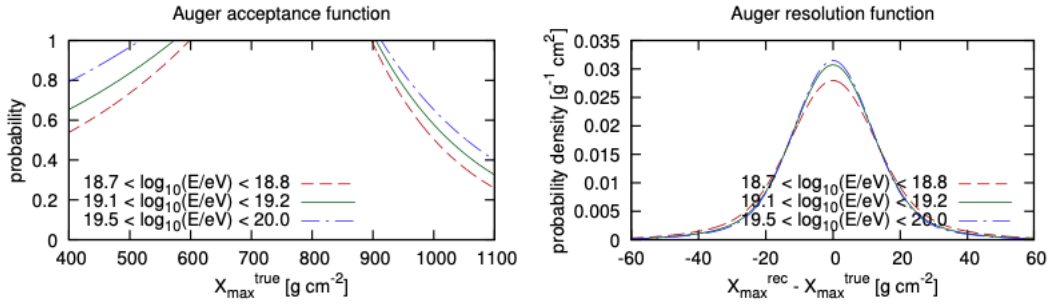


Figure 5.35: Detector acceptance and resolution functions in three different $\log_{10}(E/\text{eV})$ bins.

Gumbel parametrization

Sibyll2.3d	a_0	a_1	a_2	b_0	b_1	b_2
μ	785.852	-15.5994	-1.06906	60.5929	-0.786014	0.200728
σ	41.0345	-2.17329	-0.306202	-0.309466	-1.16496	0.225445
λ	0.799493	0.235235	0.00856884	0.0632135	-0.0012847	0.000330525
EPOS-LHC	a_0	a_1	a_2	b_0	b_1	b_2
μ	775.457	-10.3991	-1.75261	58.5306	-0.827668	0.231144
σ	32.2632	3.94252	-0.864421	1.27601	-1.81337	0.231914
λ	0.641093	0.219762	0.171124	0.0726131	0.0353188	-0.0131158
QGSJet II-04	a_0	a_1	a_2	b_0	b_1	b_2
μ	758.65	-12.3571	-1.24539	56.5943	-1.01244	0.228689
σ	35.4234	6.75921	-1.46182	-0.796042	0.201762	-0.0142452
λ	0.671545	0.373902	0.075325	0.0304335	0.0473985	-0.000564531

Sibyll2.3d	c_0	c_1	c_2
μ	-0.689462	-0.294794	0.0399432
EPOS-LHC	c_0	c_1	c_2
μ	-1.40781	0.225624	-0.10008
QGSJet II-04	c_0	c_1	c_2
μ	-0.534683	-0.17284	-0.019159

Table 5.2: Gumbel distribution parameters for the X_{\max} distributions with different hadronic interaction models. The meaning of the parameters can be found in [107].

Bibliography

- [1] Alexander Aab et al. “The Pierre Auger Cosmic Ray Observatory”. In: *Nucl. Instrum. Meth.* A798 (2015), pp. 172–213. DOI: [10.1016/j.nima.2015.06.058](https://doi.org/10.1016/j.nima.2015.06.058). arXiv: [1502.01323](https://arxiv.org/abs/1502.01323).
- [2] A. Aab et al. “Combined fit of spectrum and composition data as measured by the Pierre Auger Observatory”. In: *Journal of Cosmology and Astroparticle Physics* 2017.04 (Apr. 2017), pp. 038–038. ISSN: 1475-7516. DOI: [10.1088/1475-7516/2017/04/038](https://doi.org/10.1088/1475-7516/2017/04/038). URL: <http://dx.doi.org/10.1088/1475-7516/2017/04/038>.
- [3] Michael Unger, Glennys R. Farrar, and Luis A. Anchordoqui. “Origin of the ankle in the ultrahigh energy cosmic ray spectrum, and of the extragalactic protons below it”. In: *Phys. Rev.* D92.12 (2015), p. 123001. DOI: [10.1103/PhysRevD.92.123001](https://doi.org/10.1103/PhysRevD.92.123001). arXiv: [1505.02153](https://arxiv.org/abs/1505.02153) [[astro-ph.HE](https://arxiv.org/abs/1505.02153)].
- [4] Felix Riehn et al. “Hadronic interaction model sibyll 2.3d and extensive air showers”. In: *Physical Review D* 102.6 (Sept. 2020). ISSN: 2470-0029. DOI: [10.1103/physrevd.102.063002](https://doi.org/10.1103/physrevd.102.063002). URL: <http://dx.doi.org/10.1103/PhysRevD.102.063002>.
- [5] T. Wulf. “Beobachtungen u ber die Strahlung hoher Durchdringungsfähigkeit auf dem Eiffelturm”. In: *Phys. Z.* 11 (1910), pp. 811–813.
- [6] D. Pacini. “La radiazione penetrante alla superficie ed in seno alle acque”. In: *Nuovo Cimento VI/3* (1912), pp. 93–100. arXiv: [1002.1810](https://arxiv.org/abs/1002.1810).
- [7] Victor F. Hess. “Über Beobachtungen der durchdringenden Strahlung bei sieben Freiballonfahrten”. In: *Phys. Z.* 13 (1912), pp. 1084–1091.
- [8] E. S. Seo et al. “Measurement of Cosmic-Ray Proton and Helium Spectra during the 1987 Solar Minimum”. In: *Astrophys. J.* 378 (Sept. 1991), p. 763. DOI: [10.1086/170477](https://doi.org/10.1086/170477).
- [9] N. L. Grigorov et al. “Energy Spectrum of Primary Cosmic Rays in the 10^{11} - 10^{15} eV According to the Data of Proton-4 Measurements.” In: International Cosmic Ray Conference 1 (Jan. 1971), p. 170. URL: <https://ui.adsabs.harvard.edu/abs/1971ICRC....1..170G>.

BIBLIOGRAPHY

- [10] M. Nagano et al. “Energy spectrum of primary cosmic rays above 10^{17} eV determined from the extensive air shower experiment at Akeno”. In: *J. Phys. G* 18 (1992), pp. 423–442. DOI: [10.1088/0954-3899/18/2/022](https://doi.org/10.1088/0954-3899/18/2/022).
- [11] T. Antoni et al. “KASCADE measurements of energy spectra for elemental groups of cosmic rays: Results and open problems”. In: *Astroparticle Physics* 24.1-2 (Sept. 2005), pp. 1–25. ISSN: 0927-6505. DOI: [10.1016/j.astropartphys.2005.04.001](https://doi.org/10.1016/j.astropartphys.2005.04.001). URL: <http://dx.doi.org/10.1016/j.astropartphys.2005.04.001>.
- [12] J. Abraham et al. “Observation of the Suppression of the Flux of Cosmic Rays above $4 \cdot 10^{19}$ eV”. In: *Physical Review Letters* 101.6 (Aug. 2008). ISSN: 1079-7114. DOI: [10.1103/physrevlett.101.061101](https://doi.org/10.1103/physrevlett.101.061101). URL: <http://dx.doi.org/10.1103/PhysRevLett.101.061101>.
- [13] S. Yoshida et al. “The Cosmic ray energy spectrum above 3×10^{18} -eV measured by the Akeno Giant Air Shower Array”. In: *Astropart. Phys.* 3 (1995), pp. 105–124. DOI: [10.1016/0927-6505\(94\)00036-3](https://doi.org/10.1016/0927-6505(94)00036-3).
- [14] R. U. Abbasi et al. “First Observation of the Greisen-Zatsepin-Kuzmin Suppression”. In: *Physical Review Letters* 100.10 (Mar. 2008). ISSN: 1079-7114. DOI: [10.1103/physrevlett.100.101101](https://doi.org/10.1103/physrevlett.100.101101). URL: <http://dx.doi.org/10.1103/PhysRevLett.100.101101>.
- [15] James J. Beatty and Stefan Westerhoff. “The Highest-Energy Cosmic Rays”. In: *Annual Review of Nuclear and Particle Science* 59.1 (2009), pp. 319–345. DOI: [10.1146/annurev.nucl.58.110707.171154](https://doi.org/10.1146/annurev.nucl.58.110707.171154). URL: <https://doi.org/10.1146/annurev.nucl.58.110707.171154>.
- [16] Enrico Fermi. “On the origin of the cosmic radiation”. In: *Physical Review* 75.8 (1949), p. 1169.
- [17] Malcolm S. Longair. *High Energy Astrophysics*. Cambridge University Press.
- [18] A. M. Hillas. “The Origin of Ultra-High-Energy Cosmic Rays”. In: 22 (Jan. 1984), pp. 425–444. DOI: [10.1146/annurev.aa.22.090184.002233](https://doi.org/10.1146/annurev.aa.22.090184.002233). URL: <https://ui.adsabs.harvard.edu/abs/1984ARA&A..22..425H>.
- [19] S. I. Ginzburg and V. L. Syrovatskii. *The Origin of Cosmic Rays*. 1964.
- [20] B. L. Fanaroff and J. M. Riley. “The Morphology of Extragalactic Radio Sources of High and Low Luminosity”. In: *Monthly Notices of the Royal Astronomical Society* 167.1 (Apr. 1974), 31P–36P. ISSN: 0035-8711. DOI: [10.1093/mnras/167.1.31P](https://doi.org/10.1093/mnras/167.1.31P). eprint: <https://academic.oup.com/mnras/article-pdf/167/1/31P/8079923/mnras167-031P.pdf>. URL: <https://doi.org/10.1093/mnras/167.1.31P>.
- [21] Antoine Letessier-Selvon and Todor Stanev. “Ultrahigh energy cosmic rays”. In: *Rev. Mod. Phys.* 83 (3 Sept. 2011), pp. 907–942. DOI: [10.1103/RevModPhys.83.907](https://doi.org/10.1103/RevModPhys.83.907). URL: <https://link.aps.org/doi/10.1103/RevModPhys.83.907>.

BIBLIOGRAPHY

- [22] C. Megan Urry and Paolo Padovani. In: 107 (Sept. 1995), p. 803. DOI: [10.1086/133630](https://doi.org/10.1086/133630). URL: <https://doi.org/10.1086/133630>.
- [23] Attilio Ferrari. “Acceleration of ultra-high-energy cosmic rays (UHECR) in clusters of galaxies.” In: *National Radio Astronomy Observatory Workshop 16* (Jan. 1986), pp. 207–212. DOI: <https://ui.adsabs.harvard.edu/abs/1986NRAOW..16..207F>.
- [24] G. Ghisellini et al. “Ultra-high energy cosmic rays, spiral galaxies and magnetars”. In: *Monthly Notices of the Royal Astronomical Society: Letters* 390.1 (Oct. 2008), pp. L88–L92. ISSN: 1745-3933. DOI: [10.1111/j.1745-3933.2008.00547.x](https://doi.org/10.1111/j.1745-3933.2008.00547.x). URL: <http://dx.doi.org/10.1111/j.1745-3933.2008.00547.x>.
- [25] Kumiko Kotera and Angela V. Olinto. “The Astrophysics of Ultrahigh-Energy Cosmic Rays”. In: *Annual Review of Astronomy and Astrophysics* 49.1 (Sept. 2011), pp. 119–153. ISSN: 1545-4282. DOI: [10.1146/annurev-astro-081710-102620](https://doi.org/10.1146/annurev-astro-081710-102620). URL: <http://dx.doi.org/10.1146/annurev-astro-081710-102620>.
- [26] Edward W Kolb and Michael Stanley Turner. *The early universe*. Frontiers in Physics. Boulder, CO: Westview Press, 1990. DOI: [10.1201/9780429492860](https://doi.org/10.1201/9780429492860). URL: <https://cds.cern.ch/record/206230>.
- [27] G.R. Blumenthal. In: *Phys. Rev. D* 1 (1970), p. 1596. DOI: [10.1103/PhysRevD.1.1596](https://doi.org/10.1103/PhysRevD.1.1596).
- [28] Daniel Mazin, Denis Bastieri, and Riccardo Rando. “Constraints on Extragalactic Background Light from Cherenkov telescopes: status and perspectives for the next 5 years”. In: *AIP Conference Proceedings* (2009). DOI: [10.1063/1.3125771](https://doi.org/10.1063/1.3125771). URL: <http://dx.doi.org/10.1063/1.3125771>.
- [29] Veniamin Berezhinsky, Askhat Gazizov, and Svetlana Grigorieva. “On astrophysical solution to ultrahigh energy cosmic rays”. In: *Physical Review D* 74.4 (Aug. 2006). ISSN: 1550-2368. DOI: [10.1103/physrevd.74.043005](https://doi.org/10.1103/physrevd.74.043005). URL: <http://dx.doi.org/10.1103/PhysRevD.74.043005>.
- [30] R. Aloisio, V. Berezhinsky, and S. Grigorieva. “Analytic calculations of the spectra of ultra high energy cosmic ray nuclei. II. The general case of background radiation”. In: *Astroparticle Physics* 41 (Jan. 2013), pp. 94–107. ISSN: 0927-6505. DOI: [10.1016/j.astropartphys.2012.06.003](https://doi.org/10.1016/j.astropartphys.2012.06.003). URL: <http://dx.doi.org/10.1016/j.astropartphys.2012.06.003>.
- [31] Denise Boncioli, Anatoli Fedynitch, and Walter Winter. “Nuclear Physics Meets the Sources of the Ultra-High Energy Cosmic Rays”. In: *Scientific Reports* 7.1 (July 2017). ISSN: 2045-2322. DOI: [10.1038/s41598-017-05120-7](https://doi.org/10.1038/s41598-017-05120-7). URL: <http://dx.doi.org/10.1038/s41598-017-05120-7>.
- [32] Armando Di Matteo. “Ultra-high-energy cosmic ray phenomenology: Monte Carlo simulations and experimental data”. PhD thesis. 2015.

BIBLIOGRAPHY

- [33] A. Mücke et al. “Monte Carlo simulations of photohadronic processes in astrophysics”. In: *Computer Physics Communications* 124.2-3 (Feb. 2000), pp. 290–314. ISSN: 0010-4655. DOI: [10.1016/S0010-4655\(99\)00446-4](https://doi.org/10.1016/S0010-4655(99)00446-4). URL: [http://dx.doi.org/10.1016/S0010-4655\(99\)00446-4](http://dx.doi.org/10.1016/S0010-4655(99)00446-4).
- [34] W. Heitler. *The quantum theory of radiation*. Vol. 5. International Series of Monographs on Physics. Oxford: Oxford University Press, 1936.
- [35] Antoine Letessier-Selvon and Todor Stanev. “Ultrahigh energy cosmic rays”. In: *Rev. Mod. Phys.* 83 (3 Sept. 2011), pp. 907–942. DOI: [10.1103/RevModPhys.83.907](https://doi.org/10.1103/RevModPhys.83.907). URL: <http://link.aps.org/doi/10.1103/RevModPhys.83.907>.
- [36] J. Matthews. “A Heitler model of extensive air showers”. In: *Astroparticle Physics* 22.5-6 (Jan. 2005), pp. 387–397. DOI: [10.1016/j.astropartphys.2004.09.003](https://doi.org/10.1016/j.astropartphys.2004.09.003). URL: <https://ui.adsabs.harvard.edu/abs/2005APh...22..387M>.
- [37] D. Heck et al. “CORSIKA: A Monte Carlo code to simulate extensive air showers”. In: (Feb. 1998).
- [38] D. Kuempel, K.-H. Kampert, and M. Risse. “Geometry reconstruction of fluorescence detectors revisited”. In: (2007). arXiv: [0708.3976](https://arxiv.org/abs/0708.3976) [astro-ph].
- [39] J. Abraham et al. “The Fluorescence Detector of the Pierre Auger Observatory”. In: *Nucl. Instrum. Meth.* A620 (2010), pp. 227–251. DOI: [10.1016/j.nima.2010.04.023](https://doi.org/10.1016/j.nima.2010.04.023). arXiv: [0907.4282](https://arxiv.org/abs/0907.4282).
- [40] T. K. Gaisser and A. M. Hillas. “Reliability of the Method of Constant Intensity Cuts for Reconstructing the Average Development of Vertical Showers”. In: International Cosmic Ray Conference 8 (Jan. 1977), p. 353. URL: <https://ui.adsabs.harvard.edu/abs/1977ICRC...8..353G>.
- [41] John Linsley. “Structure of Large Air Showers at Depth 834 G cm⁻² Fluctuations”. In: International Cosmic Ray Conference 12 (Jan. 1977), p. 62. URL: <https://ui.adsabs.harvard.edu/abs/1977ICRC...12...62L>.
- [42] Guus Van Aar. “On the nature and origin of Ultra-High-Energy cosmic rays”. PhD thesis. 2016. URL: https://www.nikhef.nl/pub/services/biblio/theses_pdf/thesis_G_van_Aar.pdf.
- [43] “HEAT – a low energy enhancement of the Pierre Auger Observatory”. In: *Astrophysics and Space Sciences Transactions* 7.2 (May 2011), pp. 183–186. ISSN: 1810-6536. DOI: [10.5194/astra-7-183-2011](https://doi.org/10.5194/astra-7-183-2011). URL: <http://dx.doi.org/10.5194/astra-7-183-2011>.
- [44] Federico Sánchez. “The AMIGA detector of the Pierre Auger Observatory: overview”. In: 3 (Aug. 2011), pp. 149–152. DOI: [10.7529/ICRC2011/V03/0742](https://doi.org/10.7529/ICRC2011/V03/0742).

BIBLIOGRAPHY

- [45] J. Abraham et al. “A study of the effect of molecular and aerosol conditions in the atmosphere on air fluorescence measurements at the Pierre Auger Observatory”. In: *Astroparticle Physics* 33.2 (Mar. 2010), pp. 108–129. ISSN: 0927-6505. DOI: [10.1016/j.astropartphys.2009.12.005](https://doi.org/10.1016/j.astropartphys.2009.12.005). URL: <http://dx.doi.org/10.1016/j.astropartphys.2009.12.005>.
- [46] Tim Huege. “Radio detection of cosmic rays with the Auger Engineering Radio Array”. In: *EPJ Web of Conferences* 210 (2019). Ed. by I. Lhenry-Yvon et al., p. 05011. ISSN: 2100-014X. DOI: [10.1051/epjconf/201921005011](https://doi.org/10.1051/epjconf/201921005011). URL: <http://dx.doi.org/10.1051/epjconf/201921005011>.
- [47] I. Allekotte et al. “The surface detector system of the Pierre Auger Observatory”. In: *Nuclear Instruments and Methods in Physics Research Section A: Accelerators, Spectrometers, Detectors and Associated Equipment* 586.3 (Mar. 2008), pp. 409–420. ISSN: 0168-9002. DOI: [10.1016/j.nima.2007.12.016](https://doi.org/10.1016/j.nima.2007.12.016). URL: <http://dx.doi.org/10.1016/j.nima.2007.12.016>.
- [48] J. Abraham et al. “Trigger and aperture of the surface detector array of the Pierre Auger Observatory”. In: *Nuclear Instruments and Methods in Physics Research Section A: Accelerators, Spectrometers, Detectors and Associated Equipment* 613.1 (Jan. 2010), pp. 29–39. ISSN: 0168-9002. DOI: [10.1016/j.nima.2009.11.018](https://doi.org/10.1016/j.nima.2009.11.018). URL: <http://dx.doi.org/10.1016/j.nima.2009.11.018>.
- [49] *Pierre Auger Observatory website*. URL: <https://www.auger.org/index.php/gallery>.
- [50] D. Newton, J. Knapp, and A. Watson. “The optimum distance at which to determine the size of a giant air shower”. In: *Astroparticle Physics* 26.6 (Jan. 2007), pp. 414–419. ISSN: 0927-6505. DOI: [10.1016/j.astropartphys.2006.08.003](https://doi.org/10.1016/j.astropartphys.2006.08.003). URL: <http://dx.doi.org/10.1016/j.astropartphys.2006.08.003>.
- [51] C. Bonifazi. “The angular resolution of the Pierre Auger Observatory”. In: *Nuclear Physics B - Proceedings Supplements* 190 (May 2009), pp. 20–25. ISSN: 0920-5632. DOI: [10.1016/j.nuclphysbps.2009.03.063](https://doi.org/10.1016/j.nuclphysbps.2009.03.063). URL: <http://dx.doi.org/10.1016/j.nuclphysbps.2009.03.063>.
- [52] J. Hersil et al. “Observations of Extensive Air Showers near the Maximum of Their Longitudinal Development”. In: *Phys. Rev. Lett.* 6 (1961), pp. 22–23. DOI: [10.1103/PhysRevLett.6.22](https://doi.org/10.1103/PhysRevLett.6.22).
- [53] Valerio Verzi for the Pierre Auger Collaboration. “Measurement of the energy spectrum of ultra-high energy cosmic rays using the Pierre Auger Observatory.” In: *Proc. 36rd ICRC* (Madison, 2019). URL: <https://pos.sissa.it/358/450/>.

BIBLIOGRAPHY

- [54] A. Aab et al. “Energy estimation of cosmic rays with the Engineering Radio Array of the Pierre Auger Observatory”. In: *Physical Review D* 93.12 (June 2016). ISSN: 2470-0029. DOI: [10.1103/physrevd.93.122005](https://doi.org/10.1103/PhysRevD.93.122005). URL: <http://dx.doi.org/10.1103/PhysRevD.93.122005>.
- [55] J. Abraham et al. “The Fluorescence Detector of the Pierre Auger Observatory”. In: *Nucl. Instrum. Meth. A* 620 (2010), pp. 227–251. DOI: [10.1016/j.nima.2010.04.023](https://doi.org/10.1016/j.nima.2010.04.023). arXiv: [0907.4282](https://arxiv.org/abs/0907.4282) [astro-ph.IM].
- [56] Antonella Castellina. “Highlights from the Pierre Auger Observatory (ICRC2019)”. In: *PoS ICRC2019* (2020), p. 004. DOI: [10.22323/1.358.0004](https://doi.org/10.22323/1.358.0004). arXiv: [1909.10791](https://arxiv.org/abs/1909.10791) [astro-ph.HE].
- [57] F. D. Kahn and I. Lerche. “Radiation from Cosmic Ray Air Showers”. In: *Proceedings of the Royal Society of London Series A* 289.1417 (Jan. 1966), pp. 206–213. DOI: [10.1098/rspa.1966.0007](https://doi.org/10.1098/rspa.1966.0007).
- [58] G A Askaryan. “Excess negative charge of electron-photon shower and the coherent radiation originating from it. Radio-recording of shower under the ground and the moon.” In: *J. Phys. Soc. Japan* Vol: 17: Suppl. A-III (Jan. 1962). URL: <https://www.osti.gov/biblio/4754120>.
- [59] Stefan Jansen. “Radio for the masses: Cosmic ray mass composition measurements in the radio frequency domain”. PhD thesis. Nijmegen U., 2016.
- [60] Romain Gaior. “Detection of Cosmic Rays using Microwave Radiation at the Pierre Auger Observatory”. In: International Cosmic Ray Conference 33 (Jan. 2013), p. 2037. URL: <https://ui.adsabs.harvard.edu/abs/2013ICRC...33.2037G>.
- [61] Daniele Martello. “The Pierre Auger Observatory status and the Auger-Prime upgrade program”. In: ed. by B. Pattison. Vol. 145. 2017, p. 05001. DOI: [10.1051/epjconf/201614505001](https://doi.org/10.1051/epjconf/201614505001).
- [62] Alexander Aab et al. “The Pierre Auger Observatory Upgrade - Preliminary Design Report”. In: (Apr. 2016). arXiv: [1604.03637](https://arxiv.org/abs/1604.03637) [astro-ph.IM].
- [63] Antonella Castellina. “The dynamic range of the AugerPrime Surface Detector: technical solution and physics reach”. In: ed. by Darko Veberic. Vol. ICRC2017. 2018, p. 397. DOI: [10.22323/1.301.0397](https://doi.org/10.22323/1.301.0397).
- [64] A. Aab et al. “Features of the Energy Spectrum of Cosmic Rays above 2.5×10^{18} eV Using the Pierre Auger Observatory”. In: *Phys. Rev. Lett.* 125 (12 Sept. 2020), p. 121106. DOI: [10.1103/PhysRevLett.125.121106](https://doi.org/10.1103/PhysRevLett.125.121106). URL: <https://link.aps.org/doi/10.1103/PhysRevLett.125.121106>.
- [65] A. Aab et al. “Measurement of the cosmic-ray energy spectrum above $2.5 \cdot 10^{18}$ eV using the Pierre Auger Observatory”. In: *Physical Review D* 102.6 (Sept. 2020). ISSN: 2470-0029. DOI: [10.1103/physrevd.102.062005](https://doi.org/10.1103/physrevd.102.062005). URL: <http://dx.doi.org/10.1103/PhysRevD.102.062005>.

BIBLIOGRAPHY

- [66] Alexey Yushkov for the Pierre Auger Collaboration. “Mass composition of cosmic rays with energies above $10^{17.2}$ eV from the hybrid data of the Pierre Auger Observatory”. In: *Proc. 36rd ICRC* (Madison, 2019). URL: <https://pos.sissa.it/358/482/>.
- [67] Alexander Aab et al. “Observation of a Large-scale Anisotropy in the Arrival Directions of Cosmic Rays above 8×10^{18} eV”. In: *Science* 357.6537 (2017), pp. 1266–1270. DOI: [10.1126/science.aan4338](https://doi.org/10.1126/science.aan4338). arXiv: [1709.07321](https://arxiv.org/abs/1709.07321) [[astro-ph.HE](#)].
- [68] A. Aab et al. “Large-scale cosmic-ray anisotropies above 4 EeV measured by the Pierre Auger Observatory”. In: *Astrophys. J.* 868.1 (2018), p. 4. DOI: [10.3847/1538-4357/aae689](https://doi.org/10.3847/1538-4357/aae689). arXiv: [1808.03579](https://arxiv.org/abs/1808.03579) [[astro-ph.HE](#)].
- [69] Lorenzo Caccianiga for the Pierre Auger Collaboration. “Anisotropies of the highest energy cosmic-ray events recorded by the Pierre Auger Observatory in 15 years of operation”. In: *Proc. 36rd ICRC* (Madison, 2019). URL: <https://pos.sissa.it/358/206/>.
- [70] John P. Huchra et al. “The 2MASS Redshift Survey—Description and Data Release”. In: 199.2, 26 (Apr. 2012), p. 26. DOI: [10.1088/0067-0049/199/2/26](https://doi.org/10.1088/0067-0049/199/2/26). arXiv: [1108.0669](https://arxiv.org/abs/1108.0669) [[astro-ph.CO](#)]. URL: <https://ui.adsabs.harvard.edu/abs/2012ApJS..199...26H>.
- [71] W. H. Baumgartner et al. “The 70 months SWIFT-BAT all-sky hard x-ray survey”. In: *The Astrophysical Journal Supplement Series* 207.2 (July 2013), p. 19. ISSN: 1538-4365. DOI: [10.1088/0067-0049/207/2/19](https://doi.org/10.1088/0067-0049/207/2/19). URL: <http://dx.doi.org/10.1088/0067-0049/207/2/19>.
- [72] M. Ajello et al. “3FHL: The Third Catalog of Hard Fermi -LAT Sources”. In: *The Astrophysical Journal Supplement Series* 232.2 (Sept. 2017), p. 18. ISSN: 1538-4365. DOI: [10.3847/1538-4365/aa8221](https://doi.org/10.3847/1538-4365/aa8221). URL: <http://dx.doi.org/10.3847/1538-4365/aa8221>.
- [73] M. Ackermann et al. “GeV Observation of star-forming galaxies with the fermi large area telescope”. In: *The Astrophysical Journal* 755.2 (Aug. 2012), p. 164. ISSN: 1538-4357. DOI: [10.1088/0004-637x/755/2/164](https://doi.org/10.1088/0004-637x/755/2/164). URL: <http://dx.doi.org/10.1088/0004-637x/755/2/164>.
- [74] Julia K. Becker et al. “Cosmic Rays VI - Starburst galaxies at multiwavelengths”. In: (Jan. 2009). arXiv: [0901.1775](https://arxiv.org/abs/0901.1775) [[astro-ph.HE](#)].
- [75] Kenneth Greisen. “End to the Cosmic-Ray Spectrum?” In: *Phys. Rev. Lett.* 16 (17 Apr. 1966), pp. 748–750. DOI: [10.1103/PhysRevLett.16.748](https://doi.org/10.1103/PhysRevLett.16.748). URL: <https://link.aps.org/doi/10.1103/PhysRevLett.16.748>.
- [76] G. T. Zatsepin and V. A. Kuzmin. “Upper limit of the spectrum of cosmic rays”. In: *JETP Lett.* 4 (1966), pp. 78–80.
- [77] J. Linsley. In: *Proceedings of the 8th ICRC, Jaipur* 4 (1963), p. 77.

BIBLIOGRAPHY

- [78] Olivier Deligny. “Cosmic rays around 10^{18} eV: Implications of contemporary measurements on the origin of the ankle feature”. In: *Comptes Rendus Physique* 15.4 (2014). Ultra-high-energy cosmic rays: From the ankle to the tip of the spectrum, pp. 367–375. ISSN: 1631-0705. DOI: <https://doi.org/10.1016/j.crhy.2014.02.009>. URL: <https://www.sciencedirect.com/science/article/pii/S1631070514000280>.
- [79] K. M. Schure and A. R. Bell. “Cosmic ray acceleration in young supernova remnants”. In: *Monthly Notices of the Royal Astronomical Society* 435.2 (Aug. 2013), pp. 1174–1185. ISSN: 0035-8711. DOI: [10.1093/mnras/stt1371](https://doi.org/10.1093/mnras/stt1371). URL: <http://dx.doi.org/10.1093/mnras/stt1371>.
- [80] Alexander Aab et al. “Evidence for a mixed mass composition at the ‘ankle’ in the cosmic-ray spectrum”. In: *Phys. Lett.* B762 (2016), pp. 288–295. DOI: [10.1016/j.physletb.2016.09.039](https://doi.org/10.1016/j.physletb.2016.09.039). arXiv: [1609.08567](https://arxiv.org/abs/1609.08567) [astro-ph.HE].
- [81] V. Berezhinsky. “UHECR: Signatures and models”. In: *EPJ Web of Conferences* 53 (2013). Ed. by K.-H. Kampert et al., p. 01003. ISSN: 2100-014X. DOI: [10.1051/epjconf/20135301003](https://doi.org/10.1051/epjconf/20135301003). URL: <http://dx.doi.org/10.1051/epjconf/20135301003>.
- [82] Roberto Aloisio et al. “Signatures of the transition from galactic to extragalactic cosmic rays”. In: *Physical Review D* 77.2 (Jan. 2008). ISSN: 1550-2368. DOI: [10.1103/physrevd.77.025007](https://doi.org/10.1103/physrevd.77.025007). URL: <http://dx.doi.org/10.1103/PhysRevD.77.025007>.
- [83] R. Aloisio et al. “A dip in the UHECR spectrum and the transition from galactic to extragalactic cosmic rays”. In: *Astroparticle Physics* 27.1 (Feb. 2007), pp. 76–91. ISSN: 0927-6505. DOI: [10.1016/j.astropartphys.2006.09.004](https://doi.org/10.1016/j.astropartphys.2006.09.004). URL: <http://dx.doi.org/10.1016/j.astropartphys.2006.09.004>.
- [84] R. Aloisio, V. Berezhinsky, and P. Blasi. “Ultra high energy cosmic rays: implications of Auger data for source spectra and chemical composition”. In: *Journal of Cosmology and Astroparticle Physics* 2014.10 (Oct. 2014), pp. 020–020. ISSN: 1475-7516. DOI: [10.1088/1475-7516/2014/10/020](https://doi.org/10.1088/1475-7516/2014/10/020). URL: <http://dx.doi.org/10.1088/1475-7516/2014/10/020>.
- [85] Dan Hooper and Andrew M. Taylor. “On the heavy chemical composition of the ultra-high energy cosmic rays”. In: *Astroparticle Physics* 33.3 (Apr. 2010), pp. 151–159. ISSN: 0927-6505. DOI: [10.1016/j.astropartphys.2010.01.003](https://doi.org/10.1016/j.astropartphys.2010.01.003). URL: <http://dx.doi.org/10.1016/j.astropartphys.2010.01.003>.
- [86] Noemie Globus, Denis Allard, and Etienne Parizot. “A complete model of the cosmic ray spectrum and composition across the Galactic to extragalactic transition”. In: *Physical Review D* 92.2 (July 2015). ISSN: 1550-2368. DOI: [10.1103/physrevd.92.021302](https://doi.org/10.1103/physrevd.92.021302). URL: <http://dx.doi.org/10.1103/PhysRevD.92.021302>.

-
- [87] Roberto Aloisio et al. “SimProp v2r4: Monte Carlo simulation code for UHECR propagation”. In: *Journal of Cosmology and Astroparticle Physics* 2017.11 (Nov. 2017), pp. 009–009. ISSN: 1475-7516. DOI: [10.1088/1475-7516/2017/11/009](https://doi.org/10.1088/1475-7516/2017/11/009). URL: <http://dx.doi.org/10.1088/1475-7516/2017/11/009>.
- [88] R. Aloisio et al. “SimProp: a simulation code for ultra high energy cosmic ray propagation”. In: *Journal of Cosmology and Astroparticle Physics* 2012.10 (Oct. 2012), pp. 007–007. ISSN: 1475-7516. DOI: [10.1088/1475-7516/2012/10/007](https://doi.org/10.1088/1475-7516/2012/10/007). URL: <http://dx.doi.org/10.1088/1475-7516/2012/10/007>.
- [89] R. Aloisio et al. “SimProp v2r2: a Monte Carlo simulation to compute cosmogenic neutrino fluxes”. In: (2015). arXiv: [1505.01347](https://arxiv.org/abs/1505.01347) [[astro-ph.HE](#)].
- [90] Roberto Aloisio et al. “SimProp v2r3: Monte Carlo simulation code of UHECR propagation”. In: (2016). arXiv: [1602.01239](https://arxiv.org/abs/1602.01239) [[astro-ph.HE](#)].
- [91] Eric Armengaud et al. “CRPropa: A numerical tool for the propagation of UHE cosmic rays, γ -rays and neutrinos”. In: *Astroparticle Physics* 28.4-5 (Dec. 2007), pp. 463–471. ISSN: 0927-6505. DOI: [10.1016/j.astropartphys.2007.09.004](https://doi.org/10.1016/j.astropartphys.2007.09.004). URL: <http://dx.doi.org/10.1016/j.astropartphys.2007.09.004>.
- [92] Rafael Alves Batista and Günter Sigl. “Diffusion of cosmic rays at EeV energies in inhomogeneous extragalactic magnetic fields”. In: *Journal of Cosmology and Astroparticle Physics* 2014.11 (Nov. 2014), pp. 031–031. ISSN: 1475-7516. DOI: [10.1088/1475-7516/2014/11/031](https://doi.org/10.1088/1475-7516/2014/11/031). URL: <http://dx.doi.org/10.1088/1475-7516/2014/11/031>.
- [93] Rafael Alves Batista et al. “CRPropa 3: a public astrophysical simulation framework for propagating extraterrestrial ultra-high energy particles”. In: *Journal of Cosmology and Astroparticle Physics* 2016.05 (May 2016), pp. 038–038. ISSN: 1475-7516. DOI: [10.1088/1475-7516/2016/05/038](https://doi.org/10.1088/1475-7516/2016/05/038). URL: <http://dx.doi.org/10.1088/1475-7516/2016/05/038>.
- [94] A. Domínguez et al. “Extragalactic background light inferred from AEGIS galaxy-SED-type fractions”. In: *Monthly Notices of the Royal Astronomical Society* 410.4 (Oct. 2010), pp. 2556–2578. ISSN: 0035-8711. DOI: [10.1111/j.1365-2966.2010.17631.x](https://doi.org/10.1111/j.1365-2966.2010.17631.x). URL: <http://dx.doi.org/10.1111/j.1365-2966.2010.17631.x>.
- [95] F. W. Stecker and M. H. Salamon. “Photodisintegration of Ultra-High-Energy Cosmic Rays: A New Determination”. In: *The Astrophysical Journal* 512.2 (Feb. 1999), pp. 521–526. ISSN: 1538-4357. DOI: [10.1086/306816](https://doi.org/10.1086/306816). URL: <http://dx.doi.org/10.1086/306816>.
- [96] R. Alves Batista et al. “Effects of uncertainties in simulations of extragalactic UHECR propagation, using CRPropa and SimProp”. In: *Journal of Cosmology and Astroparticle Physics* 2015.10 (Oct. 2015), pp. 063–063. ISSN: 1475-7516. DOI: [10.1088/1475-7516/2015/10/063](https://doi.org/10.1088/1475-7516/2015/10/063). URL: <http://dx.doi.org/10.1088/1475-7516/2015/10/063>.
-

BIBLIOGRAPHY

- [97] J. L. Puget, F. W. Stecker, and J. H. Bredekamp. “Photonuclear interactions of ultrahigh energy cosmic rays and their astrophysical consequences.” In: 205 (Apr. 1976), pp. 638–654. DOI: [10.1086/154321](https://doi.org/10.1086/154321). URL: <https://ui.adsabs.harvard.edu/abs/1976ApJ...205..638P>.
- [98] F. W. Stecker and M. H. Salamon. “Photodisintegration of Ultra-High-Energy Cosmic Rays: A New Determination”. In: *The Astrophysical Journal* 512.2 (Feb. 1999), pp. 521–526. ISSN: 1538-4357. DOI: [10.1086/306816](https://doi.org/10.1086/306816). URL: <http://dx.doi.org/10.1086/306816>.
- [99] A. J. Koning, S. Hilaire, and M. C. Duijvestijn. “TALYS: Comprehensive Nuclear Reaction Modeling”. In: American Institute of Physics Conference Series 769 (May 2005). Ed. by Robert C. Haight et al., pp. 1154–1159. DOI: [10.1063/1.1945212](https://doi.org/10.1063/1.1945212). URL: <https://ui.adsabs.harvard.edu/abs/2005AIPC..769.1154K>.
- [100] A.J. Koning and D. Rochman. “Modern Nuclear Data Evaluation with the TALYS Code System”. In: 113.12 (Dec. 2012). ISSN: 0090-3752. DOI: [10.1016/J.NDS.2012.11.002](https://doi.org/10.1016/J.NDS.2012.11.002).
- [101] S. Hilaire A. Koning and S. Goriely. *TALYS 1.6 User Manual*. URL: https://tendl.web.psi.ch/tendl_2019/talys.html.
- [102] J. Allison et al. “Geant4 developments and applications”. In: *IEEE Transactions on Nuclear Science* 53.1 (2006), pp. 270–278. DOI: [10.1109/TNS.2006.869826](https://doi.org/10.1109/TNS.2006.869826).
- [103] T. Pierog et al. “EPOS LHC: Test of collective hadronization with data measured at the CERN Large Hadron Collider”. In: *Physical Review C* 92.3 (Sept. 2015). ISSN: 1089-490X. DOI: [10.1103/physrevc.92.034906](https://doi.org/10.1103/physrevc.92.034906). URL: <http://dx.doi.org/10.1103/PhysRevC.92.034906>.
- [104] S. Ostapchenko. “Monte Carlo treatment of hadronic interactions in enhanced Pomeron scheme: QGSJET-II model”. In: *Physical Review D* 83.1 (Jan. 2011). ISSN: 1550-2368. DOI: [10.1103/physrevd.83.014018](https://doi.org/10.1103/physrevd.83.014018). URL: <http://dx.doi.org/10.1103/PhysRevD.83.014018>.
- [105] Eun-Joo Ahn et al. “Cosmic ray interaction event generator SIBYLL 2.1”. In: *Physical Review D* 80.9 (Nov. 2009). ISSN: 1550-2368. DOI: [10.1103/physrevd.80.094003](https://doi.org/10.1103/physrevd.80.094003). URL: <http://dx.doi.org/10.1103/PhysRevD.80.094003>.
- [106] G. Cowan. *Statistical data analysis*. Oxford University Press, USA, 1998. URL: <https://www.bibsonomy.org/bibtex/2d60dc4e2f14d9ce5de3fbb8e298e13d2/peter.ralph>.
- [107] Manlio De Domenico et al. “Reinterpreting the development of extensive air showers initiated by nuclei and photons”. In: *Journal of Cosmology and Astroparticle Physics* 2013.07 (July 2013), pp. 050–050. ISSN: 1475-7516. DOI: [10.1088/1475-7516/2013/07/050](https://doi.org/10.1088/1475-7516/2013/07/050). URL: <http://dx.doi.org/10.1088/1475-7516/2013/07/050>.

BIBLIOGRAPHY

- [108] T. Pierog et al. “First results of fast one-dimensional hybrid simulation of EAS using CONEX”. In: *Nucl. Phys. B Proc. Suppl.* 151 (2006). Ed. by P. K. F. Grieder, B. Pattison, and L. K. Resvanis, pp. 159–162. DOI: [10.1016/j.nuclphysbps.2005.07.029](https://doi.org/10.1016/j.nuclphysbps.2005.07.029). arXiv: [astro-ph/0411260](https://arxiv.org/abs/astro-ph/0411260).
- [109] F. James. “MINUIT Function Minimization and Error Analysis: Reference Manual Version 94.1”. In: (1994).
- [110] URL: <https://www.auger.unam.mx/AugerWiki/Phenomenology/CombinedFitDataSets>.
- [111] Jose Bellido. “Depth of maximum of air-shower profiles at the Pierre Auger Observatory: Measurements above $10^{17.2}$ eV and Composition Implications”. In: *The Pierre Auger Observatory: Contributions to the 35th International Cosmic Ray Conference (ICRC 2017)*. 2017, pp. 40–47. URL: http://inspirehep.net/record/1618417/files/1617990_40-47.pdf.
- [112] Eleonora Guido. “Constraining UHECR source scenarios with a combined fit of the energy spectrum and X_{\max} distributions from $10^{17.8}$ eV to the highest energies.” PhD thesis. 2021.
- [113] Pedro Abreu et al. “Interpretation of the Depths of Maximum of Extensive Air Showers Measured by the Pierre Auger Observatory”. In: *JCAP* 1302 (2013), p. 026. DOI: [10.1088/1475-7516/2013/02/026](https://doi.org/10.1088/1475-7516/2013/02/026). arXiv: [1301.6637](https://arxiv.org/abs/1301.6637) [[astro-ph](https://arxiv.org/abs/astro-ph).HE].
- [114] Francesco Fenu. “The cosmic ray energy spectrum measured using the Pierre Auger Observatory”. In: vol. ICRC2017, p. 486. DOI: [10.22323/1.301.0486](https://doi.org/10.22323/1.301.0486).
- [115] Q. Luce. “Etude des Rayons Cosmiques d’Ultra-Haute Energie avec l’Observatoire Pierre Auger: del’extraction du signal a l’interpre tation du spectre en energie”. PhD thesis. 2018.
- [116] J. J. Condon, A. M. Matthews, and J. J. Broderick. “Radio Sources in the Nearby Universe”. In: *The Astrophysical Journal* 872.2 (Feb. 2019), p. 148. ISSN: 1538-4357. DOI: [10.3847/1538-4357/ab0301](https://doi.org/10.3847/1538-4357/ab0301). URL: <http://dx.doi.org/10.3847/1538-4357/ab0301>.
- [117] Hylke B. J. Koers and Peter Tinyakov. “Flux calculations in an inhomogeneous Universe: weighting a flux-limited galaxy sample”. In: *Monthly Notices of the Royal Astronomical Society* 399.2 (Oct. 2009), pp. 1005–1011. ISSN: 1365-2966. DOI: [10.1111/j.1365-2966.2009.15344.x](https://doi.org/10.1111/j.1365-2966.2009.15344.x). URL: <http://dx.doi.org/10.1111/j.1365-2966.2009.15344.x>.
- [118] A. Aab et al. “Depth of maximum of air-shower profiles at the Pierre Auger Observatory. I. Measurements at energies above $10^{17.8}$ eV”. In: *Physical Review D* 90.12 (Dec. 2014). ISSN: 1550-2368. DOI: [10.1103/physrevd.90.122005](https://doi.org/10.1103/physrevd.90.122005). URL: <http://dx.doi.org/10.1103/PhysRevD.90.122005>.
- [119] Private communication with S. Marafico.

- [120] Vladimir Ptuskin, Vladimir Zirakashvili, and Eun-Suk Seo. “Spectrum of galactic cosmic rays accelerated in supernova remnants”. In: *The Astrophysical Journal* 718.1 (June 2010), pp. 31–36. ISSN: 1538-4357. DOI: [10.1088/0004-637x/718/1/31](https://doi.org/10.1088/0004-637x/718/1/31). URL: <http://dx.doi.org/10.1088/0004-637X/718/1/31>.
- [121] W. D. Apel et al. “Ankle-like feature in the energy spectrum of light elements of cosmic rays observed with KASCADE-Grande”. In: *Physical Review D* 87.8 (Apr. 2013). ISSN: 1550-2368. DOI: [10.1103/physrevd.87.081101](https://doi.org/10.1103/physrevd.87.081101). URL: <http://dx.doi.org/10.1103/PhysRevD.87.081101>.
- [122] Mario Bertaina et al. “KASCADE-Grande energy spectrum of cosmic rays interpreted with post-LHC hadronic interaction models”. In: *PoS ICRC2015* (2016), p. 359. DOI: [10.22323/1.236.0359](https://doi.org/10.22323/1.236.0359).
- [123] S. Thoudam et al. “Cosmic-ray energy spectrum and composition up to the ankle: the case for a second Galactic component”. In: *Astronomy & Astrophysics* 595 (Oct. 2016), A33. ISSN: 1432-0746. DOI: [10.1051/0004-6361/201628894](https://doi.org/10.1051/0004-6361/201628894). URL: <http://dx.doi.org/10.1051/0004-6361/201628894>.
- [124] B. Efron. “Bootstrap Methods: Another Look at the Jackknife”. In: *Annals Statist.* 7.1 (1979), pp. 1–26. DOI: [10.1214/aos/1176344552](https://doi.org/10.1214/aos/1176344552).
- [125] A. Aab et al. “Probing the origin of ultra-high-energy cosmic rays with neutrinos in the EeV energy range using the Pierre Auger Observatory”. In: *Journal of Cosmology and Astroparticle Physics* 2019.10 (Oct. 2019), pp. 022–022. ISSN: 1475-7516. DOI: [10.1088/1475-7516/2019/10/022](https://doi.org/10.1088/1475-7516/2019/10/022). URL: <http://dx.doi.org/10.1088/1475-7516/2019/10/022>.
- [126] Daniel Biehl et al. “Tidally disrupted stars as a possible origin of both cosmic rays and neutrinos at the highest energies”. In: *Scientific Reports* 8.1 (July 2018). ISSN: 2045-2322. DOI: [10.1038/s41598-018-29022-4](https://doi.org/10.1038/s41598-018-29022-4). URL: <http://dx.doi.org/10.1038/s41598-018-29022-4>.
- [127] M. G. Aartsen et al. “Differential limit on the extremely-high-energy cosmic neutrino flux in the presence of astrophysical background from nine years of IceCube data”. In: *Physical Review D* 98.6 (Sept. 2018). ISSN: 2470-0029. DOI: [10.1103/physrevd.98.062003](https://doi.org/10.1103/physrevd.98.062003). URL: <http://dx.doi.org/10.1103/PhysRevD.98.062003>.
- [128] Jaime Álvarez-Muñiz et al. “The Giant Radio Array for Neutrino Detection (GRAND): Science and Design”. In: *Sci. China Phys. Mech. Astron.* 63.1 (2020), p. 219501. DOI: [10.1007/s11433-018-9385-7](https://doi.org/10.1007/s11433-018-9385-7). arXiv: [1810.09994](https://arxiv.org/abs/1810.09994) [astro-ph.HE].
- [129] D. Biehl et al. “Cosmic-Ray and Neutrino Emission from Gamma-Ray Bursts with a Nuclear Cascade”. In: *A & A* 611.A101 (2018), p. 31. arXiv: [1705.08909](https://arxiv.org/abs/1705.08909).

BIBLIOGRAPHY

- [130] D. Allard and R. J. Protheroe. “Interactions of UHE cosmic ray nuclei with radiation during acceleration: consequences for the spectrum and composition”. In: *A & A* 502.3 (2009), pp. 803–815. DOI: <https://doi.org/10.1051/0004-6361/200911839>.
- [131] N. Globus et al. “UHECR acceleration at GRB internal shocks”. In: *Monthly Notices of the Royal Astronomical Society* 451.1 (2015), pp. 751–790. DOI: <https://doi.org/10.1093/mnras/stv893>.
- [132] A.D. Supanitsky, A. Cobos, and A. Etchegoyen. “Origin of the light cosmic ray component below the ankle”. In: *Phys. Rev. D* 98 (2018), p. 103016. DOI: <https://doi.org/10.1103/PhysRevD.98.103016>.
- [133] Y. Gao and P. M. Solomon. “The Star Formation Rate and Dense Molecular Gas in Galaxies”. In: *The Astrophysical Journal* 606 (May 2004), pp. 271–290. DOI: [10.1086/382999](https://doi.org/10.1086/382999). eprint: [astro-ph/0310339](https://arxiv.org/abs/astro-ph/0310339). URL: <http://adsabs.harvard.edu/abs/2004ApJ...606..271G>.
- [134] G. H. Rieke et al. “Determining star formation rates for infrared galaxies”. In: *The Astrophysical Journal* 692.1 (Feb. 2009), pp. 556–573. DOI: [10.1088/0004-637x/692/1/556](https://doi.org/10.1088/0004-637x/692/1/556). URL: <https://doi.org/10.1088/0004-637x/692/1/556>.
- [135] F. Mannucci et al. “The infrared supernova rate in starburst galaxies”. In: *Astronomy and Astrophysics* 401 (Apr. 2003), pp. 519–530. DOI: [10.1051/0004-6361:20030198](https://doi.org/10.1051/0004-6361:20030198). eprint: [astro-ph/0302323](https://arxiv.org/abs/astro-ph/0302323). URL: <http://adsabs.harvard.edu/abs/2003A%5C%26A...401..519M>.
- [136] NASA website. URL: <https://www.nasa.gov/feature/goddard/2017/messier-82-the-cigar-Galaxy>.
- [137] Robert C. Kennicutt Jr. “The Global Schmidt law in star forming galaxies”. In: *Astrophys. J.* 498 (1998), p. 541. DOI: [10.1086/305588](https://doi.org/10.1086/305588). arXiv: [astro-ph/9712213](https://arxiv.org/abs/astro-ph/9712213) [astro-ph].
- [138] N. M. Förster Schreiber et al. “Near-Infrared Integral Field Spectroscopy and Mid-Infrared Spectroscopy of the Starburst Galaxy M82”. In: *The Astrophysical Journal* 552 (May 2001), pp. 544–571. DOI: [10.1086/320546](https://doi.org/10.1086/320546). eprint: [astro-ph/0101153](https://arxiv.org/abs/astro-ph/0101153). URL: <http://adsabs.harvard.edu/abs/2001ApJ...552..544F>.
- [139] T. A. Thompson et al. “Magnetic Fields in Starburst Galaxies and the Origin of the FIR-Radio Correlation”. In: *The Astrophysical Journal* 645 (July 2006), pp. 186–198. DOI: [10.1086/504035](https://doi.org/10.1086/504035). eprint: [astro-ph/0601626](https://arxiv.org/abs/astro-ph/0601626). URL: <http://adsabs.harvard.edu/abs/2006ApJ...645..186T>.
- [140] E. R. Seaquist and N. Odegard. “A nonthermal radio halo surrounding M82”. In: *The Astrophysical Journal* 369 (Mar. 1991), pp. 320–330. DOI: [10.1086/169764](https://doi.org/10.1086/169764). URL: <http://adsabs.harvard.edu/abs/1991ApJ...369..320S>.

BIBLIOGRAPHY

- [141] C. W. Engelbracht et al. “Extended Mid-Infrared Aromatic Feature Emission in M82”. In: *The Astrophysical Journal Letters* 642.2 (2006), p. L127. URL: <http://stacks.iop.org/1538-4357/642/i=2/a=L127>.
- [142] D. K. Strickland and T. M. Heckman. “Supernova Feedback Efficiency and Mass Loading in the Starburst and Galactic Superwind Exemplar M82”. In: *The Astrophysical Journal* 697 (June 2009), pp. 2030–2056. DOI: [10.1088/0004-637X/697/2/2030](https://doi.org/10.1088/0004-637X/697/2/2030). arXiv: [0903.4175](https://arxiv.org/abs/0903.4175) [astro-ph.CO]. URL: <http://adsabs.harvard.edu/abs/2009ApJ...697.2030S>.
- [143] Tova M. Yoast-Hull et al. “Winds, Clumps, and Interacting Cosmic Rays in M82”. In: *Astrophys. J.* 768 (2013), p. 53. DOI: [10.1088/0004-637X/768/1/53](https://doi.org/10.1088/0004-637X/768/1/53). arXiv: [1303.4305](https://arxiv.org/abs/1303.4305) [astro-ph.HE].
- [144] X. Wang and B. D. Fields. “Are starburst galaxies proton calorimeters?” In: *MNRAS* 474 (Mar. 2018), pp. 4073–4088. DOI: [10.1093/mnras/stx2917](https://doi.org/10.1093/mnras/stx2917). arXiv: [1612.07290](https://arxiv.org/abs/1612.07290) [astro-ph.HE]. URL: <http://adsabs.harvard.edu/abs/2018MNRAS.474.4073W>.
- [145] Enrico Peretti et al. “Cosmic ray transport and radiative processes in nuclei of starburst galaxies”. In: *Mon. Not. Roy. Astron. Soc.* 487.1 (2019), pp. 168–180. DOI: [10.1093/mnras/stz1161](https://doi.org/10.1093/mnras/stz1161). arXiv: [1812.01996](https://arxiv.org/abs/1812.01996) [astro-ph.HE].
- [146] Gustavo E. Romero, Ana Laura Müller, and Markus Roth. “Particle acceleration in the superwinds of starburst galaxies”. In: *Astron. Astrophys.* 616 (2018), A57. DOI: [10.1051/0004-6361/201832666](https://doi.org/10.1051/0004-6361/201832666). arXiv: [1801.06483](https://arxiv.org/abs/1801.06483) [astro-ph.HE].
- [147] L. A. Anchordoqui. “Acceleration of ultrahigh-energy cosmic rays in starburst superwinds”. In: *Physical Review D* 97.6, 063010 (Mar. 2018), p. 063010. DOI: [10.1103/PhysRevD.97.063010](https://doi.org/10.1103/PhysRevD.97.063010). arXiv: [1801.07170](https://arxiv.org/abs/1801.07170) [astro-ph.HE]. URL: <http://adsabs.harvard.edu/abs/2018PhRvD..97f3010A>.
- [148] Enrico Peretti et al. “Particle acceleration and multi-messenger emission from starburst-driven galactic winds”. In: (2021). arXiv: [2104.10978](https://arxiv.org/abs/2104.10978) [astro-ph.HE].
- [149] Pasquale Blasi. “The origin of galactic cosmic rays”. In: *The Astronomy and Astrophysics Review* 21.1 (Nov. 2013). ISSN: 1432-0754. DOI: [10.1007/s00159-013-0070-7](https://doi.org/10.1007/s00159-013-0070-7). URL: <http://dx.doi.org/10.1007/s00159-013-0070-7>.
- [150] Andrej Dundovic et al. “Novel aspects of cosmic ray diffusion in synthetic magnetic turbulence”. In: *Physical Review D* 102.10 (Nov. 2020). ISSN: 2470-0029. DOI: [10.1103/physrevd.102.103016](https://doi.org/10.1103/physrevd.102.103016). URL: <http://dx.doi.org/10.1103/PhysRevD.102.103016>.
- [151] P. Subedi et al. “Charged Particle Diffusion in Isotropic Random Magnetic Fields”. In: *The Astrophysical Journal* 837 (2017), pp. 140–150. arXiv: [1612.09507](https://arxiv.org/abs/1612.09507).

BIBLIOGRAPHY

- [152] Min S. Yun and C. L. Carilli. “Radio-to-Far-Infrared Spectral Energy Distribution and Photometric Redshifts for Dusty Starburst Galaxies”. In: *The Astrophysical Journal* 568 (2002), pp. 88–98. DOI: [10.1086/338924](https://doi.org/10.1086/338924).
- [153] M. Ajello et al. “The γ -Ray Emission of Star-forming Galaxies”. In: *The Astrophysical Journal* 894.2 (May 2020), p. 88. ISSN: 1538-4357. DOI: [10.3847/1538-4357/ab86a6](https://doi.org/10.3847/1538-4357/ab86a6). URL: <http://dx.doi.org/10.3847/1538-4357/ab86a6>.
- [154] Pasquale Blasi, Richard I. Epstein, and Angela V. Olinto. “Ultrahigh-energy cosmic rays from young neutron star winds”. In: *Astrophys. J. Lett.* 533 (2000), p. L123. DOI: [10.1086/312626](https://doi.org/10.1086/312626). arXiv: [astro-ph/9912240](https://arxiv.org/abs/astro-ph/9912240).
- [155] Kumiko Kotera, Elena Amato, and Pasquale Blasi. “The fate of ultrahigh energy nuclei in the immediate environment of young fast-rotating pulsars”. In: *JCAP* 08 (2015), p. 026. DOI: [10.1088/1475-7516/2015/08/026](https://doi.org/10.1088/1475-7516/2015/08/026). arXiv: [1503.07907](https://arxiv.org/abs/1503.07907) [[astro-ph.HE](https://arxiv.org/abs/1503.07907)].
- [156] R. J. Glauber and G. Matthiae. “High-energy scattering of protons by nuclei”. In: *Nucl. Phys. B* 21 (1970), pp. 135–157. DOI: [10.1016/0550-3213\(70\)90511-0](https://doi.org/10.1016/0550-3213(70)90511-0).
- [157] J. Engel et al. “Nucleus-nucleus collisions and interpretation of cosmic ray cascades”. In: *Phys. Rev. D* 46 (1992), pp. 5013–5025. DOI: [10.1103/PhysRevD.46.5013](https://doi.org/10.1103/PhysRevD.46.5013).
- [158] Carleton E. DeTar. “Momentum Spectrum of Hadronic Secondaries in the Multiperipheral Model”. In: *Phys. Rev. D* 3 (1 Jan. 1971), pp. 128–144. DOI: [10.1103/PhysRevD.3.128](https://doi.org/10.1103/PhysRevD.3.128). URL: <https://link.aps.org/doi/10.1103/PhysRevD.3.128>.
- [159] Thomas K. Gaisser, Ralph Engel, and Elisa Resconi. *Cosmic Rays and Particle Physics*. 2nd ed. Cambridge University Press, 2016. DOI: [10.1017/CB09781139192194](https://doi.org/10.1017/CB09781139192194).
- [160] K. Gottfried. “Space-Time Structure of Hadronic Collisions and Nuclear Multiple Production”. In: *Phys. Rev. Lett.* 32 (17 Apr. 1974), pp. 957–961. DOI: [10.1103/PhysRevLett.32.957](https://doi.org/10.1103/PhysRevLett.32.957). URL: <https://link.aps.org/doi/10.1103/PhysRevLett.32.957>.
- [161] Premomoy Ghosh. “Negative binomial multiplicity distribution in proton-proton collisions in limited pseudorapidity intervals at LHC up to $s = 7$ TeV and the clan model”. In: *Physical Review D* 85.5 (Mar. 2012). ISSN: 1550-2368. DOI: [10.1103/physrevd.85.054017](https://doi.org/10.1103/physrevd.85.054017). URL: <http://dx.doi.org/10.1103/PhysRevD.85.054017>.
- [162] Robert C. Kennicutt and Neal J. Evans. “Star Formation in the Milky Way and Nearby Galaxies”. In: *Annual Review of Astronomy and Astrophysics* 50.1 (Sept. 2012), pp. 531–608. ISSN: 1545-4282. DOI: [10.1146/annurev-astro-081811-125610](https://doi.org/10.1146/annurev-astro-081811-125610). URL: <http://dx.doi.org/10.1146/annurev-astro-081811-125610>.

BIBLIOGRAPHY

- [163] P. Kornecki et al. “ γ -ray/infrared luminosity correlation of star-forming galaxies”. In: *Astronomy & Astrophysics* 641 (Sept. 2020), A147. ISSN: 1432-0746. DOI: [10.1051/0004-6361/202038428](https://doi.org/10.1051/0004-6361/202038428). URL: <http://dx.doi.org/10.1051/0004-6361/202038428>.
- [164] R. Abbasi et al. *The IceCube high-energy starting event sample: Description and flux characterization with 7.5 years of data*. 2020. arXiv: [2011.03545](https://arxiv.org/abs/2011.03545) [[astro-ph.HE](https://arxiv.org/abs/2011.03545)].
- [165] M. S. Westmoquette et al. In: *The Astrophysical Journal* 706.2 (Nov. 2009), pp. 1571–1587. ISSN: 1538-4357. DOI: [10.1088/0004-637x/706/2/1571](https://doi.org/10.1088/0004-637x/706/2/1571). URL: <http://dx.doi.org/10.1088/0004-637x/706/2/1571>.
- [166] T. Bister or the Pierre Auger Collaboration. “A combined fit of energy spectrum, shower depth distribution and arrival directions to constrain astrophysical models of UHECR sources”. In: *Proc. 37rd ICRC* (Berlin, 2021).

Aknowledgements

Aknowledgements

Only my name is on the first page of this work but I would not have been to write it without the help and support from a lot of people.

First of all, I would like to thank my supervisors, Prof. Sergio Petrera and Dr. Denise Boncioli, whose ideas and coaching were essential. Working on technical problems during my PhD was challenging but also frustrating at times. At the end it worked out, thanks to your ideas, guidance and persistence. Your open style of communication sparked many discussions that led to interesting ideas; one day I hope to be as good of a scientist as you are.

I want to thank the whole L'Aquila group working on the Pierre Auger Collaboration for their support and fruitful discussions.

This thesis would also not be complete without the feedback I received from my referees: many thanks to Maurizio Spurio, Silvia Mollerach and Andrea Chiavassa for your work.

Another important person (a friend!) to thank for his support is definitely Enrico Peretti: thank you for your patience and for your out of the box point of view.

I want to thank Dr. Eleonora Guido for the many discussions we have had during the last three years, specifically crosschecking everything that can be crosschecked. Thank you a lot for your patience, I hope to work again with you in the future

Another two people to thank inside the Pierre Auger Collaboration are Gialex and Roberta: thanks for your personal support during my PhD.

I want to thank also Prof. Jonathan Biteau for trusting me and for allowing me to do what I like most for the next two years.

Concerning every-day life, I want to thank my flatmate and friend Austin:

Aknowledgements

thanks for all for stimulating discussions, for the dinners and movie nights and for all the fun we had together. Hope to see you soon, in Sicily, in an Abruzzo sheep farm, in route 66, or wherever.

Living in a city like L'Aquila cannot be easy. I want to thank all the people who shared with me this experience: Ambra, Cristina, Francesca, Giuseppe, Giorgio, Mattia, Michele, Valentina. Alessia deserves a special mention for sharing with me the last period during the pandemic: your support was fundamental in order to not become crazy.

A great privilege that I had during my experience in L'Aquila city was to be part of a local basketball team. This was a great honor and it was super fun: for this reason thanks to Fabio (the captain), Matteo, Gimmy, Cola, Claudio, Cristian, Angelo, Francesco, Piergiorgio, Kuks, Mauro and Valerio.

Figures 1.8, 5.1 and 5.22 of this thesis are produced by Silvia. Thank you for sharing with me a big part of this experience and for supporting me during the gloomiest and darkest times.

Despite not being in L'Aquila, the Sicilian friends need to be in this list: Coco, Gabriele and Pesce (the party), Luca, Domenico, Mirko, Irma, Francesca, Fabrizio, Claudia, Eliana. Thanks a lot for being part of my life since I don't remember when.

Last but not least: thanks for all my family for their love and infinite support.

